UNIVERSIDAD POLITÉCNICA DE MADRID

ESCUELA TÉCNICA SUPERIOR DE INGENIEROS INDUSTRIALES

PASSIVITY-BASED MULTILATERAL CONTROL FOR DELAYED TELEOPERATION

DOCTOR OF PHILOSOPHY

AUTOMATION AND ROBOTICS

Michael Panzirsch

Octubre 1, 2018

UNIVERSIDAD POLITÉCNICA DE MADRID

ESCUELA TÉCNICA SUPERIOR DE INGENIEROS INDUSTRIALES

DLR - GERMAN AEROSPACE CENTER

ROBOTICS AND MECHATRONICS CENTER

PASSIVITY-BASED MULTILATERAL CONTROL FOR DELAYED TELEOPERATION

DOCTOR OF PHILOSOPHY

AUTOMATION AND ROBOTICS

Author: Michael Panzirsch
Mechanical Engineer

Advisors: Prof. Manuel Ferre Pérez
Universidad Politécnica de Madrid

Dr. Jordi Artigas Esclusa
DLR - German Aerospace Center

Octubre 1, 2018

PASSIVITY-BASED MULTILATERAL CONTROL FOR DELAYED TELEOPERATION

Autor: Michael Panzirsch

Tribunal:

Presidente	Prof. Claudio Rossi
Secretario:	Prof. José Mariá Cogollor Delgado
Vocal A:	Prof. Alin Albu-Schäffer
Vocal B:	Prof. Jee-Hwan Ryu
Vocal C:	Prof. Raúl Marín Prades
Suplente A:	Prof. José María Azorín Poveda
Suplente B:	Prof. Antonio Giménez Fernández

Acuerdan otorgar la calificación de:

Madrid, 1 de octubre de 2018

Acknowledgments

First of all, I would like to express my deep gratitude to my research supervisors, Professor Manuel Ferre and Jordi Artigas, for their patient guidance, enthusiastic encouragement and useful critiques of this thesis. Thanks to the unconditional support of Rosa Marà Ortiz, the accomplishment of an international dissertation was a trouble-free experience. I would like to express my great appreciation and deep respect to Professor Gerd Hirzinger and Professor Alin Albu-Schäffer for the establishment and direction of the Robotics and Mechatronics Center that provides extraordinary opportunities in terms of hardware and individual development to its scientists. Furthermore, I would like to thank Professor Jee-Hwan Ryu most sincerely for our profound discussions on passivity and time domain control in particular.

Also, I would like to offer my special thanks to my colleagues at the Robotics and Mechatronics Center and the telepresence laboratory especially. My grateful thanks are directed at Christian Ott, Ribin Balanchandran, Thomas Hulin and Philipp Kremer that inspired me with discussions and advices in control theory and rendered essential assistance at the maintenance of the robot hardware. Not least, I am especially grateful for the assistance given by Bernhard Weber in the statistical analysis of this research.

I wish to thank my parents and sisters for their support and encouragement throughout my educational career. My sincere thanks go to my wife Maria and my children for bringing joy in my life that supported me spiritually throughout this work. Children open up our minds and forgotten perspectives that enrich our life and often reveal alternative paths. The deepest inspiration was conveyed by my uncle who was the prototype of an educated person and a role model to me. To him I dedicate this thesis.

Michael Panzirsch.

Abstract

Today, robots are a mature and save tool in automated production lines as well as in collaboration with human workers. Over the past few years, the progress in robotic technologies such as higher computational performance, the development of smarter sensors and impedance controlled light weight robots, has paved the path for robots to new fields of application. Besides space and the nuclear industry, new markets for robots, e.g. in medicine and industrial maintenance have evolved. Since unstructured, dynamic and narrow environments present a challenge for autonomous systems, there is still a high demand for teleoperation systems that give a human operator access to the control of a robot (slave) via haptic input device (master).

Besides acoustic and visual feedback, the haptic control loop providing a sense of touch to the operator is crucial in teleoperation systems. Modern control techniques enhanced the transparency, i.e. the quality of immersion into the slaves environment that the human operator perceives via his/her interaction device. Via telemanipulation it became feasible to use robots for plant maintenance or complex constructional tasks e.g. in the nuclear industry.

Still, the performance of such so-called bilateral teleoperation systems is limited in several situations. Multiple cooperative robotic agents, autonomous or teleoperated, can achieve a common objective more effectively. Also, in terms of reliability, adaptability and ergonomics multi-robot or multilateral control systems respectively can bring obvious benefits.

The basic contribution of this thesis is the development of a modular control framework that allows for an uncomplicated stability analysis for a large variety of multilateral setups thanks to its modularity. The control approach is passivity based which is a widely used stability criterion particularly in the presence of time delay in the communication channel. In a second set of contributions, new control architectures are developed that aim the performance increase in terms of accuracy of position and perceived impedances in the multilateral coupling. In this context, new time domain control approaches for delayed systems, measured force feedback and an extended model-mediated rate control concept are proposed and validated. The third set of contributions of haptic augmentation concepts builds up on these developments. The virtual grasping point concept and a haptic intention augmentation approach are introduced that promise the increase of precision in cooperative tasks and the manipulation of large or flexible objects. Additionally, a role distribution is proposed that promises to increase the system performance in these scenarios and allows for haptic training applications.

The work is original in that a large part of the presented approaches brings benefit compared to the state of the art also when applied in standard bilateral setups and in that novel multilateral applications and haptic augmentation concepts are introduced. All

discussed concepts are evaluated through real robotic experiments in the course of this thesis and the generality of the modular approach is validated in various applications. Experimental results of task allocation and virtual grasping point concepts, the control of cooperative slave robots as well as rate controlled wheeled mobile robots are presented in real multi-degree of freedom setups. A user study serves the objective evaluation of a set of haptic augmentation approaches. Furthermore, the effects of time delay and a novel haptic intention augmentation approach are demonstrated in a scenario involving a cosmonaut on the International Space Station.

Resumen

Hoy en día los mecanismos robóticos son una herramienta madura y segura en el campo de la automatización, así como en la colaboración con trabajadores. En los últimos años el progreso de las tecnologías robóticas ha logrado una mayor eficiencia computacional, desarrollo de sensores más inteligentes y mecanismos robóticos ligeros controlados por impedancia, dando lugar así a nuevos campos de aplicación. Donde, además de las conocidas industrias espaciales y nucleares, se han creado y evolucionado nuevos mercados para robots, como por ejemplo el campo de la medicina y el mantenimiento industrial. Ya que estos requieren un sistema robótico para entornos no estructurados, restringidos y dinámicos. No obstante este tipo de entornos continúan suponiendo un reto para los sistemas autónomos, existiendo así una alta demanda actual de sistemas de tele-operación, los cuales permiten a un operador humano controlar un sistema robótico (esclavo) a través de un dispositivo de entrada háptico (maestro). Adicionalmente, en este sistema de tele-operación, el operador cuenta con sistemas de retroalimentación del entorno, ya sea acústico, visual o de tacto, donde el bucle de control háptico resulta ser primordial para proporcionar una sensación de contacto crucial en la operación.

Por otro lado, las técnicas de control modernas han conseguido mejorar la transparencia, es decir, la calidad de inmersión en el entorno del esclavo que el operador humano percibe a través de su dispositivo de interacción. De este modo, mediante el uso de la tele-manipulación, se ha vuelto posible el uso de sistemas robóticos para mantenimiento de plantas o trabajos complejos de construcción, como en la industria nuclear. Pero aun, la eficiencia de los así conocidos sistemas de operación bilateral están limitados en varias situaciones. Agentes robóticos de cooperación múltiple, ya sea autónomos o teleoperados, pueden alcanzar un objetivo común más fácilmente. Así también, en términos de fiabilidad adaptabilidad y ergonomía de multirobots, o sistemas de control multilateral, respectivamente, puede traer apreciables beneficios.

La contribución básica de esta tesis es el desarrollo de un sistema de control modular que permita un análisis de estabilidad simple enfocado a una gran variedad de configuraciones multilaterales gracias a su modularidad. El control ha sido basado en pasividad, el cual es un criterio de estabilidad ampliamente usado particularmente en presencia de retardos en el canal de comunicación. En un segundo conjunto de contribuciones, se han desarrollado nuevas arquitecturas de control con la finalidad de incrementar la eficiencia, en términos de precisión de la posición y en la impedancia percibida de un acoplamiento multilateral. En este contexto, han sido propuesto y validados nuevos enfoques de control para sistemas con retardo en el dominio del tiempo, medición de retroalimentación por fuerza y un amplio concepto del control de velocidad. El tercer conjunto de aportaciones está enfocado a incrementar la sensación háptica, las cuales surgen a partir de los desarrollos antes mencionados. El concepto de punto de agarre virtual y la aproximación

del realce de la intención háptica son introducidos, ya que ambos aseguran incrementar la precisión en tareas de cooperación y en la manipulación de objetos grandes y flexibles. Adicionalmente, una distribución de roles se ha propuesto con el fin de incrementar la eficiencia del sistema en estos escenarios y permitir así, aplicaciones de entrenamiento háptico.

El trabajo es original, ya que gran parte de los métodos presentados traen beneficios, en comparación con métodos del estado del arte, aun cuando son aplicadas en configuraciones bilaterales estándar, además de aportar novedosas aplicaciones multilaterales y conceptos de realce háptico. Por otro lado, todos los conceptos discutidos son evaluados a través de experimentos robóticos en campo en el curso de esta tesis y la generalidad del enfoque modular es validada en varias aplicaciones. Los resultados de los experimentos en tareas de asignación y los conceptos del punto de agarre virtual, el control cooperativo de robots esclavos, así como también robots móviles con ruedas controladas por velocidad son presentados en configuraciones reales de múltiples grados de libertad. Un estudio de usuario otorga una evaluación objetiva de un grupo de métodos de aumentación háptica. Además, los efectos de retardo, y un novedoso y aumentado enfoque en la intención háptica son demostrados en un escenario con un cosmonauta en la Estación Espacial Internacional.

Contents

Acknowledgements **iii**

Abstract **v**

Resumen **vii**

1 Introduction **1**
1.1 Motivation . . . 2
1.2 Multiple Agent Configurations and Applications . . . 3
1.3 Main contributions . . . 5
1.4 Outline . . . 6

2 Background on Multilateral Teleoperation **9**
2.1 Bilateral Teleoperation . . . 9
2.2 Multilateral Scenarios and Related Functionalities . . . 24
2.3 Control Approaches for Multilateral Teleoperation . . . 26
2.4 Taxonomy of Multilateral Control Approaches . . . 44
2.5 Conclusions from Background . . . 51

3 The MPMT: A Methodology for Passivity-Based Multilateral Teleoperation **53**
3.1 A Suitable Control Approach . . . 53
3.2 Multilateral Passivity Principle . . . 58
3.3 The MPMT Framework . . . 60
3.4 Experimental Analysis of the Multilateral Coupling . . . 71
3.5 Discussion on the MPMT Design . . . 76

4 Passive Coupling Architectures for the MPMT **77**
4.1 Time Delay . . . 77
4.2 Measured Force Feedback . . . 102
4.3 3-Channel Architecture . . . 110
4.4 4-Channel Architecture . . . 117
4.5 Model-Mediated Teleoperation for Rate Control Setups . . . 125
4.6 Discussion on Passive Coupling Architectures . . . 139

5 Haptic Augmentation based on the MPMT **141**
5.1 Virtual Grasping Points . . . 142
5.2 Role Distribution of Agents . . . 174

5.3 Haptic Intention Augmentation 186
5.4 Discussion on Haptic Augmentation 195

6 Experimental Applications **197**
6.1 Telemanipulation with Virtual Grasping Points (N:1) 197
6.2 Cooperative Manipulation with Haptic Intention Augmentation (N:N) . . 212
6.3 Model-Mediated Teleoperation of WMR (1:N) 216
6.4 Discussion on the Experimental Evaluation 223

7 Conclusion **225**

A Experimental Setups **227**
A.1 1DoF Master-Slave-System 227
A.2 7DoF DLR Light Weight Robots 228
A.3 HUG - Space Justin 230
A.4 Omega.7 - HUG 231
A.5 Space Link Setup 231
A.6 Lightweight Rover Unit 233

Chapter 1

Introduction

Several elaborated technologies as telecommunication allow a person to exert influence in a remote environment. More modern approaches as web conferencing or augmented reality conferencing can be regarded as modes of telepresence which means that the participants gain the appearance of being present in a distant location. The degree of transparency, i.e. the quality of immersion, in telepresence technologies is limited as a person will presumably in the long term be able to distinguish between telepresence and real presence in an environment. The highest transparency can be achieved via telerobotics as the most sophisticated mode of telepresence that involves a telemanipulator (also slave robot) allowing mechanical interaction with the remote environment [34]. Aside from the mechanical interfaces, visual and acoustic feedback is required. Referring to the haptic channel, a teleoperator involves besides the telemanipulator, the control and communication infrastructure as well as the haptic interface (also master). The achievable performance of a teleoperator depends strongly on the quality of the master and slave devices in terms of workspace, friction as well as resolution of the sensors. The intuitiveness of teleoperation depends e.g. on network characteristics, workspace mapping, field of view, quality of haptic feedback and so forth [19]. Through the master device, a human operator is able to control the motion of mobile robots or to telemanipulate objects with the help of stationary slave robots. Impedance controlled light weight robots, higher computational performance and modern control techniques lead the teleoperation technology to market maturity in the last decade. Especially in harmful environments as nuclear power plants or space, telepresence technologies are applied. Besides industry, also the health-care sector employs telepresence systems e.g. as service robots for doctor-patient conversation [49] or in minimally invasive surgery [76].

In the context of Industry 4.0, teleoperation pushes the concept of the Internet of Things (IoT) to the next level. Through the IoT, smart devices are connected worldwide such that they can sense one another and communicate. Still, in this fourth industrial revolution the main application of the IoT are the remote open-loop control of devices and the gathering of Big Data. E.g. the settings of household appliances may be checked and changed remotely, its firmware is automatically upgraded and the devices may place an order autonomously. In comparison, teleoperation or more precisely, the kinematic coupling in a closed-loop control setup, presents one of the most complicated interactions within the IoT.

1.1 Motivation

A variety of jobs in industry as well as in the health care sector expose employees to danger. Workers on an oil platform [79], astronauts in space as well as doctors in quarantine facilities bear the risk of harm. Therefore, robotic setups were developed with specific focus on teleoperation in the past few years. Regarding space and industry, thus, besides physical risks also costs [13] could be reduced since repeating human transport costs (e.g. extra vehicular activities in space or flights to an oil platform) can be reduced to a minimum. Especially the processes of surgeons require high precision causing an enormous workload and reduced period of deep concentration [28]. The introduction of tremor filters as well as the micro-manipulation capabilities in teleoperation systems led to the preference of the application of surgical robots instead. Further advantages of telerobotic systems result from the feasibility of scaling between master and slave devices [147]. Via the scaling of forces a teleoperation system allows the manipulation of far heavier objects compared to direct manipulation. This raises new possibilities in industry as well as in the health-care sector where nurses could be spared from lifting heavy patients [52], an in the long run harmful workload.

Exemplary, the Ebola outbreak in 2014 hit besides civil victims about 50 p.c. of the nursing workers and varying parts of other health worker positions that overall have a 20 to 30 times higher probability of getting infected compared to the general adult population (preliminary data of [118]). The epidemic was not restricted to West Africa. Among others, one nurse assistant was infected in a quarantine facility in Madrid [108]. Different tasks, as temperature, oxygen [125] and blood pressure measurements or even blood sampling [18], that expose the health workers under unnecessary risks can be performed with existing telerobotic systems. An obvious field of telerobotics that increases the cost efficiency is the on orbit servicing. The Hubble Space Telescope had an initially planned cost of $5 billion dollar. Several manned maintenance missions were necessary after the launch of the space telescope which raised the costs up to $10 billion dollar [13]. Teleoperation technology will help to reduce these costs immensely in future. Besides teleoperatod manipulators, also mobile robot technology developed for space applications such as planetary exploration can be applied in the civil sector. The use of mobile robots is recommendable for the exploration of disaster areas. Since such territory is mostly unstructured, autonomous functions are limited. Thus, a human operator and the teleoperation technology are required. Also, food supply trucks sent to war zones can be teleoperated to avoid preventable risks for humans.

These scenarios include tasks that require an enormous grade of dexterity. The comparatively new concept of multilateral teleoperation extends the capabilities of the standard bilateral teleoperation scheme. Besides the master and the slave robot, an arbitrary number of robots can be introduced into the setup. These robots may serve as master or slave devices. The resulting network can be designed to improve the precision and the robustness as well as the handling and the load capacities of the robotic system.

Various procedures in industry as well as in the health-care sector are hardly feasible via bilateral teleoperation and may be eased employing additional robots. Multilateral robotic setups that allow the training of novel surgeons and multilateral haptic augmentation approaches likewise, have the potential to enhance the performance especially with respect to precision in robotic surgery. The multilateral cooperation of slave robots on the other hand not only eases constructional tasks involving heavy and bulky objects

drastically, but also leads to higher reliability [84]. Thereby, multilateral systems do not necessarily lead to higher costs since in such setups e.g. one master instead of two can be applied to control two slave robots. Also, the complexity of the master hardware can even be reduced due to different multilateral augmentation approaches.

The following section presents further applications of multilateral teleoperation that emphasize the usefulness of the technology in more detail.

1.2 Multiple Agent Configurations and Applications

Multilateral architectures cover a broad range of applications. The capabilities reach from haptic training and haptic augmentation algorithms in dual-user systems or single-user systems respectively to frameworks that allow the parallel control of a number n of slave robots. In the following, the capabilities are categorized with reference to the number of agents which can e.g. represent a human operator with the master device or the slave robot in its environment. Note that a multi-master system does not necessarily require more than one human operator. This thesis focuses electronically coupled multilateral systems (i.e. coupled via control algorithms). Robots that are coupled purely mechanically via a cooperatively grasped object for example are not considered.

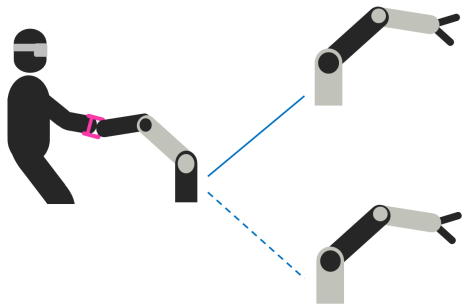

Figure 1.2.1: Single-Master-Multi-Slave: Sequential Setup

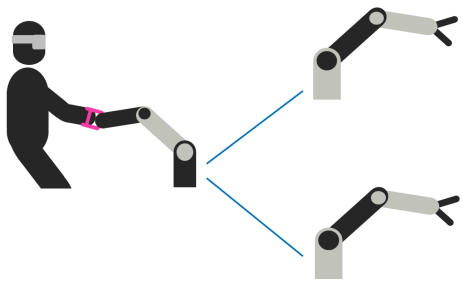

Figure 1.2.2: Single-Master-Multi-Slave: Synchronous Motion Setup

1.2.1 Single-Master-Multi-Slave (1:N Approach)

A 1:N approach with one single master and multiple slave robots (SMMS) can be realized in two fundamentally different ways. A sequentially designed setup gives e.g. a nurse access to several clinical robots in different hospital rooms (compare Fig. 1.2.1). Similarly, a doctor requires only one master input device to control a variety of care robots for elderly persons in their remote homes. This sequential 1:N approach does not require multilateral but only bilateral electronic coupling and is therefore not considered in the course of this thesis. The synchronous control of two slave robots as presented in Fig. 1.2.2 is another simple Single-Master-Multi-Slave setup. In contrast, one master device can also be used to operate two slave robots in a parallel framework as depicted in Fig. 1.2.3. E.g. two aerial robots can be electronically coupled in a fix distance such that a grasped bulky object can be teleoperated via one single master device. Also, in

a search and rescue scenario, a locally computed model of a remotely controlled mobile robot and its circumjacent terrain can be added to a standard bilateral architecture, such that the human operator receives merged information of the actual non-perfect feedback of the model and delayed feedback from the real robot (compare Fig. 1.2.4). Also this multilaterally extended model-mediated teleoperation can be regarded as a parallel setup.

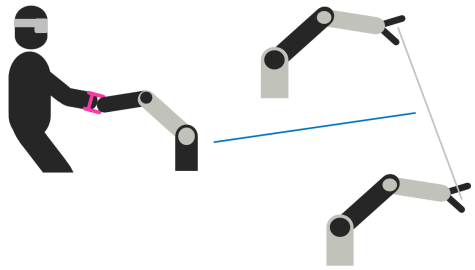

Figure 1.2.3: Single-Master-Multi-Slave: Cooperative Manipulation Setup

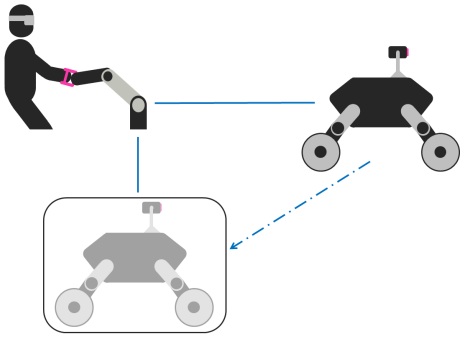

Figure 1.2.4: Single-Master-Multi-Slave: Extended Model-Mediated Setup

1.2.2 Multi-Master-Single-Slave (N:1 Approach)

Multiple masters and one single slave (MMSS) can be controlled by one or more human operators in a N:1 approach. Two surgeons may use one input device each to control a surgical robot cooperatively in a training scenario as depicted in Fig. 1.2.5. Such a system can be tuned in a way that a novice surgeon cannot affect the slave behavior but only perceive haptically the interactions of the slave. Later on, a more experienced trainee can gain gradually more control on the slave robot whereas the authority of the mentor surgeon is decreased. Another application of the N:1 approach is the use of two master devices by one human operator to control a single slave robot (compare Fig. 1.2.6). The replacement of a pipe e.g. on an oil platform via a simple bilateral teleoperator is a demanding task, especially if the pipe is long and the grasping point is distant from the plug-in position. A multilateral setup can be designed such that a second master device allows to control an additional interaction point on the pipe, easing the procedure significantly. Through this concept, among others, the rotational precision in teleoperation systems can be enhanced. Therefore, MMSS systems hold promise in a variety of applications ranging from constructional tasks to medical ultrasonics.

1.2.3 Multi-Master-Multi-Slave (M:N Approach)

The extension to setups with multiple masters and multiple slaves (MMMS) is denoted M:N approach in the following. Besides the diverse options to merge SMMS and MMSS architectures as depicted in Fig. 1.2.7, M:N systems can be found in cooperative teleoperator systems. For example, two separately controlled teleoperation systems that manipulate one object conjointly can be regarded as a MMMS system. Two engineers that want to assemble a windshield into a car in such a setup cooperatively need a good

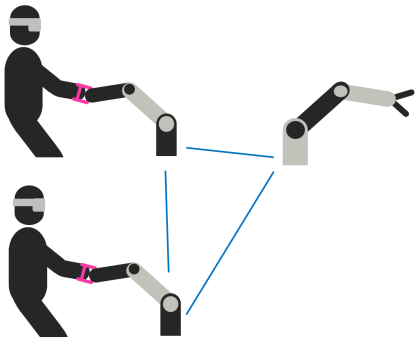

Figure 1.2.5: Multi-Master-Single-Slave: Training Setup

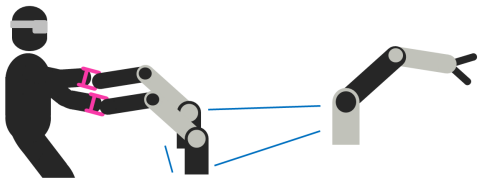

Figure 1.2.6: Multi-Master-Single-Slave: Rotational Precision Setup

intention awareness for the cooperating engineer. This intention awareness can be improved haptically by displaying the interaction force of one operator with his/her input device to the other operator in an electronically coupled teleoperation system (compare Fig. 1.2.8).

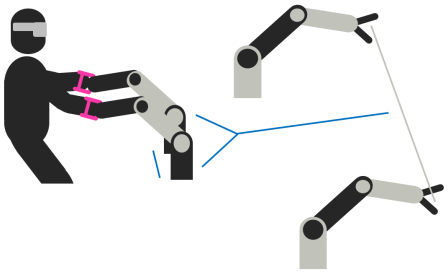

Figure 1.2.7: Multi-Master-Multi-Slave: Rotational Precision Setup for Cooperative Manipulation

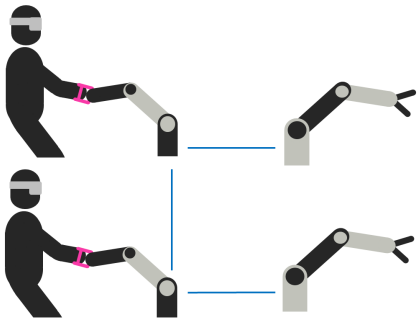

Figure 1.2.8: Multi-Master-Multi-Slave: Intention Augmentation Setup

1.3 Main contributions

The main contributions of this thesis are:

- MPMT Concept: The central development of this thesis is a Methodology for Passivity-Based Multilateral Teleoperation (MPMT). In Section 3.3, the basic framework of the MPMT is designed based on three main modules in the network representation. The MPMT concept is generated to match the requirements derived from the literature review with special focus on the modularity and adaptability of the control approach. The passivity criterion confers this quality to the MPMT since stability can be guaranteed by the passivity of its modules.

- Track Modules: The central module of the MPMT is the track that establishes the coupling of two agents. In order to allow for control structures that can deal with low-quality communication channels and/or promise higher system transparency, a variety of passive tracks are developed in Chapter 4. In Section 4.1, two novel approaches are presented that guarantee the track's passivity despite time delay. A comparison underlines the advantages of one novel approach in terms of transparency. Novel methods for passivity control of measured force feedback, 3-, 4-*Channel* and rate control architectures are introduced in Section 4.2 to 4.4.

- Augmentation Concepts: Another contribution of this thesis is the approach of haptic augmentation (Chapter 5). Haptic augmentation comprises a variety of concepts that extend the usability and applicability of low-cost as well as complex haptic input devices or facilitate the cooperation of human operators. The virtual grasping point approach, introduced in Section 5.1, e.g. simplifies the manipulation of bulky objects, enhances the capabilities of underactuated devices and allows for the control of kinematically coupled slave robots. In contrast, the role distribution of agents (Section 5.2) enables training applications or a Cartesian task allocation. Finally, a haptic intention augmentation, presented in Section 5.3, can be designed in the MPMT framework, promising advantages of teleoperative cooperation even in comparison with real interactions.

- Validation by Experiments and Applications: All control approaches developed within this thesis are validated via experiments employing real hardware. Besides this control specific evaluation, a set of the proposed concepts is validated in realistic scenarios. Experiments and a user study on the performance increase related to the virtual grasping point and Cartesian task allocation method are presented in Section 6.1. Furthermore, the haptic intention augmentation is evaluated in a setup with real space link to the ISS and an operator in a microgravity condition (Section 6.2). Another application focuses the control of a mobile robot through an extended model-mediated teleoperation approach in Section 6.3.

1.4 Outline

Chapter 2 presents the fundamentals of bilateral and multilateral control. At first, system representations that have been applied in the literature on multilateral control are introduced. Building up on that, the state of the art of bilateral and multilateral teleoperation is summarized. Additionally, the available literature is allocated to specific categories such that the universality of the approaches concerning multilateral control can be evaluated.

The design concept of the MPMT is developed in Chapter 3. In the first step, the requirements are drawn from the objectives of various applications of multilateral teleoperation and the analysis of the categorization of the state of the art in Chapter 2. Afterward, the basic multilateral control framework and its main modules are established based on the passivity principle of multilateral systems. Also, a primary experimental evaluation of the multilateral control structure is conducted.

Novel concepts extending basic bilateral control architectures are introduced in Chapter 4. Three approaches considering time delay in the communication channel are pre-

sented. Furthermore, it is shown, how passivity can be guaranteed in case of different coupling signals. Also, the approach is applied in the teleoperation of both, position-controlled robotic manipulators and rate-controlled mobile robots.

In Chapter 5, the idea of haptic augmentation is explained and implemented for different multilateral scenarios. The first part presents the virtual grasping point concept for different multilateral systems with multiple degrees of freedom (DoF). In the second part, the role distribution among agents for training scenarios and a Cartesian task allocation are introduced. Lastly, a haptic intention augmentation approach is designed that is meant to ease the cooperation of two humans through two telemanipulators.

Besides control specific experiments in the Chapters 3 to 5, experiments focusing realistic applications are presented in Chapter 6. The virtual grasping point and the Cartesian task allocation concept are evaluated in experiments and a user study. Finally, the haptic intention augmentation concept is tested in an experiment with a space link to the International Space Station (ISS). A third application presents an extended model-mediated rate control of a wheeled mobile robot (WMR) with fictitious force feedback.

The conclusion of the thesis and an outlook to related future research is given in Chapter 7.

Chapter 2

Background on Multilateral Teleoperation

The first step in the controller development of a robotic system is the design of the interaction structure between the different agents which can e.g. represent a human operator with the master device or the slave robot in its environment. Based on this, a signal flow diagram needs to be set up that considers the desired interaction and the control interfaces (commanded values, force feedback) of the agents. The most common bilateral couplings are introduced with the respective signal flow diagram. In order to analyze the system's behavior concerning stability, robustness and transparency different system representations can be applied. In this chapter, common modeling concepts of mechanical and electrical systems will be introduced. Based on that, the state of the art of control approaches applied in multilateral applications is provided. Also, the challenges of teleoperation demanding for multilateral control are discussed and a literature review and taxonomy analysis of multilateral control approaches and applications concludes this chapter.

2.1 Bilateral Teleoperation

2.1.1 Motivation and Applications

This section extends the motivation of Section 1.1 considering the social and economic aspects with the technical advantages and challenges, bilateral teleoperation brings. Besides the fundamental visual feedback that provides a 3D-View on the slave environment recorded by a pair of stereo cameras, teleoperation systems require an audio channel for acoustic feedback. The haptic channel that is focused in this thesis considers the position or rate control of the slave in the forward direction on the one hand and on the other hand the force feedback to the master device in the backward direction.

If the master and slave devices have different workspaces, a scaling or the indexing

method [77] has to be implemented that extends the workspace of the master virtually via the repetitive uncoupling from the slave position control. Furthermore, the control of stationary robotic manipulators, where generally the tool center point TCP is controlled, can be differentiated from the control of mobile robots. Mobile robots can be position, rate or even acceleration controlled. The lateral motion of the robot can be intuitively controlled via the instantaneous center of rotation [130], a yaw-rate command or analogous to cars via a curvature command [130].

In order to provide a sense of touch to the human operator, force feedback is required. The focus of this thesis lies on the kinesthetic feedback whereas the tactile feedback is neglected. Considering the control of stationary robots, the force feedback can be calculated from the impedance type position controller, measured by a force sensor close to the slave tool tip or designed as a fictitious force of a virtual environment. Since the force feedback leads to a closed haptic control loop, the stability in the haptic channel has to be assured.

Still, the transparency and thus the sense of touch is limited by the dynamic properties of the haptic device. High masses and friction in the user interface vanish the precise force perception by the operator. If a surgeon has to accelerate the mass of the master and to work against friction, the tissue properties in the slave environment can not be well sensated.

For example, the grasping of free floating satellites [6] teleoperated from ground requires an impedance matching that damps out oscillatory kinetic energy that is only feasible with force feedback. In such feedback systems, a time delay in the communication channel introduces a severe destabilizing effect into the respective system. In the telemanipulation of objects located in the geostationary earth orbit, the consideration of time delay (600ms roundtrip) in the stability analysis is crucial. The so-called model-mediated control promises to compensate for the effect of delay to some extent through integration of a local (master side) model of the slave and its environment. Such models can be generated by 3D-sensors at the slave. To enhance the geometric model, the slave's force sensor can be used to observe the physical properties of the objects. Still, the imperfectness of the models presents a big limitation of this concept.

The visual feedback is the most crucial one, but it is most heavily restricted by the data transfer rate. This is due to the fact that an adequate number of frames per second (fps) leads to a high amount of transmitted data in contrast to the haptic channel although that is transferred optimally at one kilohertz (khz) frequency. Especially in the presence of time delay, the visual and haptic communication channels have to be synchronized to improve the operator's immersion.

Force feedback displayed to operators of mobile robots can provide information e.g. on the street wheel contact or the distance to obstacles. The immersion in the case of dynamic unmanned ground vehicles (UGV) as wheeled mobile robots or unmanned air vehicles (UAV) can further be improved by vestibular feedback provided by robotic motion simulators. A comparatively new field of research considers the control of robotic manipulators attached to UAVs enabling aerial manipulation.

2.1.2 System Description

Bilateral teleoperation can be designed with a variety of architectures that differ mainly in the signals that are exchanged via the communication channel between master and

slave. The architecture depicted in the signal flow diagram Fig. 2.1.1 is called PF_{comp} (position - computed force), since a position and velocity respectively are sent from master to slave and the computed controller force is fed back to the master device. The signal flow diagram is a system representation that is very close to the implementation of the respective teleoperation setup.

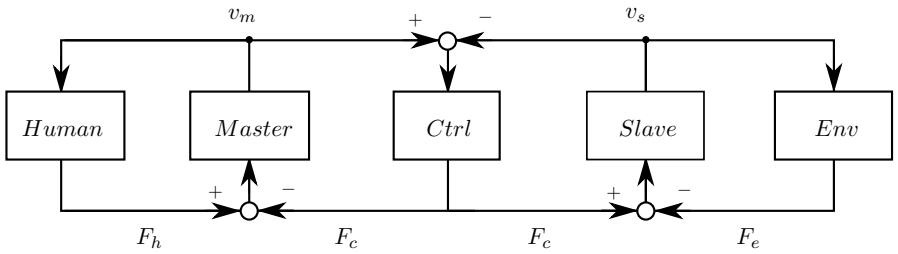

Figure 2.1.1: Signal Flow Diagram of the PF_{comp} Architecture without Delay
A signal flow diagram depicts the control structure of a teleoperation setup. A human operator controls a slave robot in its environment via a master input device. A controller compares the velocities and positions of the devices to generate a force F_c that assures the position tracking of master and slave device. The human applies a force F_h on the master and the environmental force F_e acts on the slave.

The architecture of Fig. 2.1.1 establishes a haptic link between two impedance type devices which have a position/velocity output and receive force commands. In [47, 3], impedance and admittance displays are compared considering teleoperation and virtual reality applications respectively. Impedance controlled devices [133] are in general lightweight and backlash free and able to display low masses [3]. Impedance type setups require besides low impedances, a high back-drivability [47] which can be improved e.g. by feedforward compensation [42, 53]. A common drawback of impedance type displays is a decreased performance at high forces, high mass and high stiffness [175]. In contrast, admittance type devices receive a position/velocity command and have a force output [51, 103, 2, 175]. These displays are typically industrial robots with high inertia, high friction, low back-drivability and low compliance [23, 146, 3]. Admittance controlled devices are not able to render low masses, but to render very high stiffnesses and minimal friction [175].

Although the devices are called impedance displays, the hardware (master m and slave s) has to be integrated into the control loop in admittance causality $Y(s)$

$$v_i(s) = Y_i(s)F_i(s) = Z_i^{-1}(s)F_i(s), \tag{2.1}$$

($i \in \{m, s\}$) whereas the human operator (h) and the environment (e) are integrated in impedance causality Z_h, Z_e

$$F_j(s) = Z_j(s)v_j(s), \tag{2.2}$$

with $j \in \{h, e\}$. Note that in this thesis only impedance type devices are applied. The master and slave devices are generally modeled as continuous

$$Z_i(s) = M_i s + B_i, \tag{2.3}$$

($i \in \{m, s\}$) or discrete mass-damper systems:

$$Y_i(z) = \frac{z^2}{(\frac{M_i}{T_s^2} + \frac{B_i}{T_s})z^2 - (2\frac{M_i}{T_s^2} + \frac{B_i}{T_s})z + \frac{M_i}{T_s^2}}. \tag{2.4}$$

A PI controller acting on the difference of slave velocity v_s and reference velocity v_m serves the position following of the two devices. The proportional part acts as a damper whereas the integral part has a spring like behavior. The controller contains damping B_c and stiffness parameters K_c respectively. The same holds for the environment impedance Z_e:

$$Z_c(s) = B_c + \frac{K_c}{s}, \tag{2.5}$$

$$Z_e(s) = B_e + \frac{K_e}{s}. \tag{2.6}$$

The discrete equations are:

$$Z_c(z) = \frac{(K_c + \frac{B_c}{T_s})z - \frac{B_c}{T_s}}{z}, \tag{2.7}$$

$$Z_e(z) = \frac{(K_e + \frac{B_e}{T_s})z - \frac{B_e}{T_s}}{z}. \tag{2.8}$$

The human operator can be considered as a continuous mass-spring-damper system:

$$Z_h(s) = M_h s + B_h + \frac{K_h}{s}. \tag{2.9}$$

The discrete model equation of the human operator is:

$$Z_h(z) = \frac{(K_h + \frac{M_h}{T_s^2} + \frac{B_h}{T_s})z^2 - (2\frac{M_h}{T_s^2} + \frac{B_h}{T_s})z + \frac{M_h}{T_s^2}}{z^2}. \tag{2.10}$$

Figure 2.1.2 presents a PF_{comp} architecture with delay in the communication channel. The velocity of the master v_m is sent to the controller located on the slave side of the communication channel with time delay T_i ($e^{-T_i s}$, $i \in \{1, 2\}$). The delayed controller force F_c^{del} is sent back to the master device.

The transmission line can also be modeled in the frequency domain [59, 20] via the 2-port form of the lossy telegrapher's equation:

$$F_c^{del}(s) = \cosh(\kappa(s)l)F_c(s) + Z(s)\sinh(\kappa(s)l)v_m^{del}(s), \tag{2.11}$$

$$v_m(s) = Y(s)\sinh(\kappa(s)l)F_c(s) + \cosh(\kappa(s)l)v_m^{del}(s), \tag{2.12}$$

with the length l of the transmission line, the propagation constant $\kappa(s)$ and the line impedance Z and admittance Y

$$\kappa(s) = \sqrt{(L_{TL}s + R_{TL})(C_{TL}s + G_{TL})}, \tag{2.13}$$

$$Z(s) = \sqrt{\frac{L_{TL}s + R_{TL}}{C_{TL}s + G_{TL}}}, \tag{2.14}$$

$$Y(s) = 1/Z(s). \tag{2.15}$$

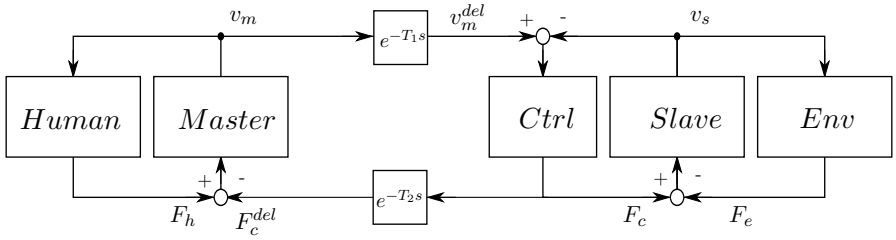

Figure 2.1.2: Signal Flow Diagram of the PF_{comp} Architecture with Delay
For instance, due to communication over long distances, a delay $e^{-T_i s}$ $(i \in \{1, 2\})$ has to be considered in the communication channel. For the sake of controllability, the controller is positioned on the slave side of the communication channel. Therefore, the delayed master velocity v_m^{del} and the delayed controller force F_c^{del} arrives at the slave and master side of the communication channel respectively.

The line parameters (inductance L_{TL}, resistance R_{TL}, capacitance C_{TL} and conductance G_{TL}) are defined per unit length. With the resistance R_{TL} and the conductance G_{TL}, ohmic and dielectric losses are modeled. Note that in a lossless transmission line $R_{TL} = G_{TL} = 0$ holds.

From the Laplace Transformation

$$F(s) = \int_{0^-}^{\infty} f(t)e^{-st}\mathrm{d}t, \tag{2.16}$$

the Laplace Transform of a time delay T can be identified as

$$\mathcal{L}(f(t-T)\gamma(t-T)) = \int_{0^-}^{\infty} (f(t-T)\gamma(t-T))e^{-st}\mathrm{d}t = e^{-Ts}F(s), \tag{2.17}$$

since

$$\gamma(t-T) = \begin{cases} 0, & t < T \\ 1, & t \geq T. \end{cases} \tag{2.18}$$

Note that the delay in the communication channel T_1 and T_2 will be neglected in the following analysis. Analyzing Fig. 2.1.1 of a PF_{comp} architecture, the following system equations can be derived under negligence of the time delay:

$$F_c(s) = K_c(\frac{v_m(s)}{s} - \frac{v_s(s)}{s}) + B_c(v_m(s) - v_s(s)), \tag{2.19}$$

$$F_e(s) = K_e(x_0 - \frac{v_s(s)}{s}) + B_e v_s(s), \tag{2.20}$$

$$v_m(s) = Z_m^{-1}(s)(F_h(s) - F_c(s)) = \frac{F_h(s) - F_S(s)}{M_m s + B_m}, \tag{2.21}$$

$$v_s(s) = Z_s^{-1}(s)(F_c(s) - F_e(s)) = \frac{F_c(s) - F_e(s)}{M_s s + B_s}, \tag{2.22}$$

with the center x_0 of the environmental stiffness K_e. Thus, the transfer function $T(s)$ from $F_h(s)$ to $v_s(s)$

$$v_s(s) = T(s)F_h(s) \tag{2.23}$$

results in

$$T(s) = \frac{K_c + B_c s}{(\frac{K_e + \frac{B_e}{s} + \frac{(K_c + B_c s)(B_m + M_m s)}{K_c + B_c s + B_m s + M_m s^2}}{B_s + M_s s} + 1)(B_s + M_s s)(K_c + B_c s + B_m s + M_m s^2)}. \quad (2.24)$$

A stability analysis should consider different types of environments. Free motions ($Z_e = 0$) as well as very stiff environments ($K_e > 10000N/m$) as the most critical cases should be analyzed.

As mentioned above, different bilateral architectures can be designed that differ in the amount and type of signals that are exchanged through the communication channel. Other architectures require additional sensors or controllers but promise better performance in different applications. In order to increase the transparency of the teleoperator, the force measured in the interaction of slave and environment can be fed back to the master in a PF_{meas} architecture. This type of bilateral system is depicted in Fig. 2.1.3. The measured force feedback promises to display interaction forces of higher frequencies to the human operator at the master device and low resistance due to zero feedback in free motion.

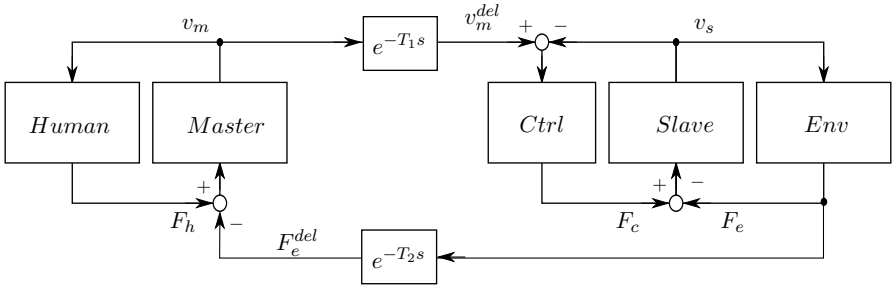

Figure 2.1.3: Signal Flow Diagram of the PF_{meas} Architecture with Delay
In the PF_{meas} architecture, the force F_e measured at the interaction of slave and environment is fed back to the master device. This bilateral architecture promises higher transparency than the PF_{comp} architecture since the measured forces contain information of higher frequency.

In the so called PP architecture (compare Fig. 2.1.4), the positions of the devices are exchanged via the communication channel, such that on each side one controller serves the position following of the two devices. Note that in case of unique controller parameterization and zero delay, the PP architecture equals the PF_{comp} architecture.

The PF_{meas} and PF_{comp} architecture can be merged to a 3-*Channel* architecture with hybrid force feedback (see Fig. 2.1.5). The computed and measured force feedback is scaled by the factors λ_c and λ_e respectively. In bilateral systems, higher fidelity can be achieved via the combination of computed and measured force feedback compared to systems with pure computed or measured force feedback [155, 46].

The 4-*Channel* architecture presented in Fig. 2.1.6 extends the 3-*Channel* version by a feed forward of the measured human interaction force to the slave. In theory, the bilateral system can reach perfect transparency in this architecture [171]. The computed and measured force feedback is scaled by the factors λ_c^m and λ_e respectively. The forces sent to the slave robot are scaled by λ_c^s and λ_h.

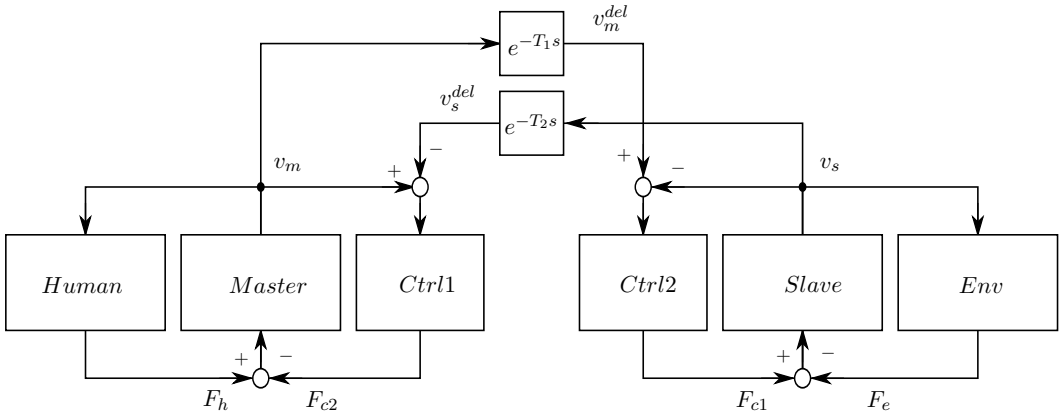

Figure 2.1.4: Signal Flow Diagram of the PP Architecture with Delay
Two positions and velocities respectively are exchanged through the communication channel in the PP Architecture. On each side of the channel, a controller generates a force to assure position tracking of the master and slave device. In case of zero delay and unitary controller parametrization, the PP architecture and the PF_{comp} architecture equal.

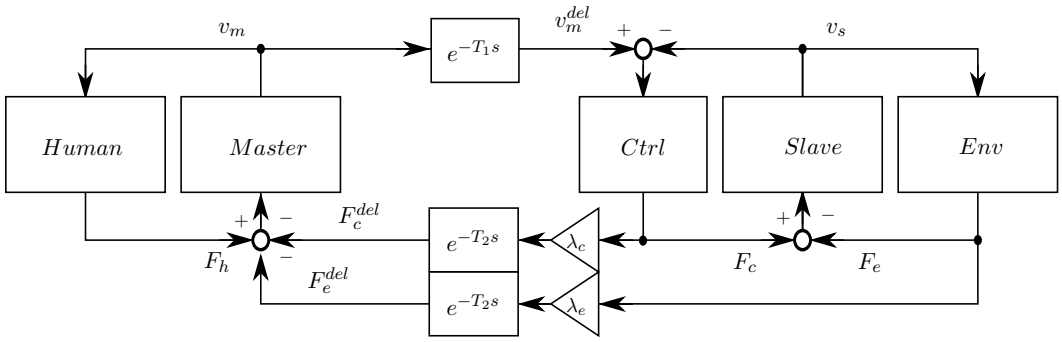

Figure 2.1.5: Signal Flow Diagram of a 3-*Channel* Architecture with Delay
In one type of 3-*Channel* architecture, the computed F_c and measured forces F_e are fed back to the master device. Two scaling factors need to be introduced to limit and to weight the feedback forces. This 3-*Channel* architecture fuses the benefits of PF_{comp} and PF_{meas} architecture: High frequency forces of the interaction with the environment and feedback on the slave dynamics in free motion are displayed at the master device.

2.1.3 System Representations

This section introduces different system modeling concepts and the analogies of the mechanical and electrical domains which are required to analyze a mechanical system with the help of the network representation. Note that the following selection of system representations concentrates on approaches that have been applied also to multilateral control concepts in literature.

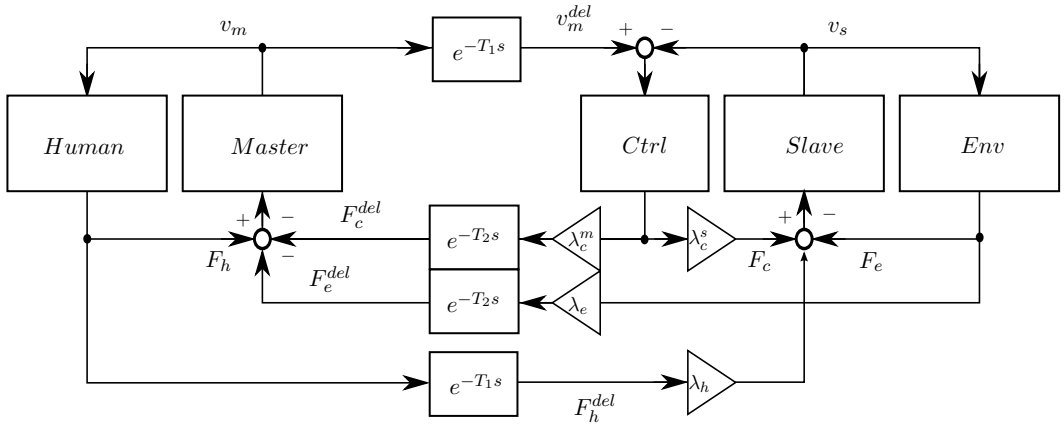

Figure 2.1.6: Signal Flow Diagram of a 4-*Channel* Architecture with Delay
Theoretically, the 4-*Channel* architecture enables the design of a absolute transparent system. In addition to the signals exchanged in the 3-*Channel* architecture, the interaction force F_h of human and master is sent to the slave device. The human and the computed force need to be scaled to limit the force that accelerates the slave robot.

2.1.3.1 Immittance Matrix

A bilateral teleoperation system can be considered as a 2-port network with an impedance matrix Z or a hybrid matrix H ([43], Fig. 2.1.7)

$$\begin{bmatrix} F_1(s) \\ F_2(s) \end{bmatrix} = \begin{bmatrix} Z_{11}(s) & Z_{12}(s) \\ Z_{21}(s) & Z_{22}(s) \end{bmatrix} \begin{bmatrix} v_1(s) \\ v_2(s) \end{bmatrix} \quad \text{and}$$
$$\begin{bmatrix} F_1(s) \\ -v_2(s) \end{bmatrix} = \begin{bmatrix} H_{11}(s) & H_{12}(s) \\ H_{21}(s) & H_{22}(s) \end{bmatrix} \begin{bmatrix} v_1(s) \\ F_2(s) \end{bmatrix}.$$

The elements of these matrices are transfer functions $T(s)$

$$T(s) = \frac{Y(s)}{U(s)} \tag{2.25}$$

that allow the stability analysis in the frequency domain. A transfer function $T(s)$ gives a relation between the input $U(s)$ of a system and its output $Y(s)$ in the Laplace domain.

The parameters of the impedance matrix Z, admittance matrix Y and the hybrid matrix H have the following relation:

$$Y(s) = \begin{bmatrix} \frac{Z_{22}(s)}{det(Z(s))} & -\frac{Z_{12}(s)}{det(Z(s))} \\ -\frac{Z_{21}(s)}{det(Z(s))} & \frac{Z_{11}(s)}{det(Z(s))} \end{bmatrix}, \tag{2.26}$$

$$H(s) = \begin{bmatrix} \frac{det(Z(s))}{Z_{22}(s)} & \frac{Z_{12}(s)}{Z_{22}(s)} \\ -\frac{Z_{21}(s)}{Z_{22}(s)} & \frac{1}{Z_{22}(s)} \end{bmatrix}. \tag{2.27}$$

If the 2-port contains the master and slave devices, the forces F_1 and F_2 equal the interaction force of human F_h and environment F_e with the respective hardware. The

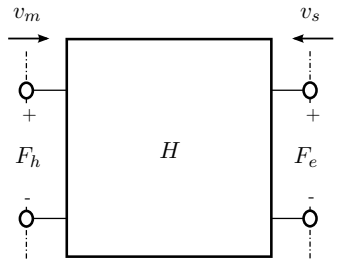

Figure 2.1.7: 2-port of a H-Matrix Representation
A 2-port network with hybrid matrix H or impedance matrix Z can represent a bilateral teleoperator with controller, communication channel. Also, the master and/or slave hardware can be considered within the 2-port. The terminations of the 2-port are the human operator with or without master device and the environment with or without slave robot. The ports of the network are power-correlated such that an effort F_i an a flow v_i can be measured at port i.

velocities v_1 and v_2 are the master v_m and slave velocity v_s. The hybrid matrix H of a PF_{comp} architecture is

$$\begin{bmatrix} F_h(s) \\ -v_s(s) \end{bmatrix} = \begin{bmatrix} Z_m(s) + \frac{Z_c(s)Z_s(s)}{Z_s(s)+Z_c(s)} & -\frac{Z_c(s)}{Z_s(s)+Z_c(s)} \\ -\frac{Z_c(s)}{Z_s(s)+Z_c(s)} & \frac{1}{Z_s(s)}(1 - \frac{Z_c(s)}{Z_s(s)+Z_c(s)}) \end{bmatrix} \begin{bmatrix} v_m(s) \\ F_e(s) \end{bmatrix}. \quad (2.28)$$

The master and slave impedance are $Z_i(s) = M_i s + B_i$ ($i \in \{m, s\}$) and the PI controller impedance is $Z_c(s) = B_c + K_c \frac{1}{s}$, with mass M, damping B and stiffness K.

In the following $R^z_{ij} = Re(Z_{ij})$, $X^z_{ij} = Im(Z_{ij})$, $R^h_{ij} = Re(H_{ij})$ and $X^h_{ij} = Im(H_{ij})$.

2.1.3.2 Linear Fraction Representation

The Linear Fraction Representation (compare Fig. 2.1.8) is useful to visualize the signal flow with consideration of modeled uncertainties. Therefore, it is applied e.g. for $\mathcal{H}^\infty$ control. The control matrix K uses the measured signals v to generate a control input u to the plant P. The virtual inputs w and outputs z are added. It can be shown [159] that a closed-loop transfer function from the disturbances w to the error signals z can

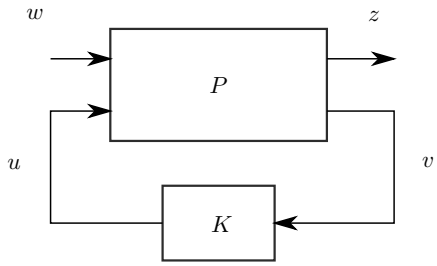

Figure 2.1.8: Linear Fraction Representation of a General Control Configuration [159]
To model uncertainties, the linear fraction representation as a type of signal flow diagram can be applied e.g. for $\mathcal{H}^\infty$ control. The disturbances w lead to the error signals z. u and v are the plant input and output.

be presented in the fractional representation

$$z = F_l(P, K) \tag{2.29}$$

$$F_l(P, K) = P_{11} + P_{12}K(I - P_{22}K)^{-1}P_{21}. \tag{2.30}$$

In [66], the slave and environment were considered as the plant P, the slave velocity v_s as plant output v and the controller F_C as the plant input u. The transfer function of plant P results as

$$P = \frac{1}{Z_s + Z_e}. \tag{2.31}$$

2.1.3.3 Circuit Theory and Network Representation

In order to apply tools of the electrical circuit theory in the analysis of the mechanical teleoperation system, the representation of the teleoperator as an electric circuit or network needs to be found. Here, first, the electrical analogs of the mechanical elements of a teleoperator are presented to design the network representation of a teleoperator in the next step.

Mechanical Electrical Analogy A quantity that has mathematically, but not physically an identical behavior as another quantity is called analogous quantity or analog [36]. Those quantities can be signals, elements or systems. Analogies can be found e.g. for the lumped elements of the mechanical and electrical domain. Lumped elements represent a specific physical property concentrated between its two ends. With reference to these ends or terminals across and through variables can be found that define the exchange of energy of the element. Note that the through variables are equal at both terminals. A pair of through and across variables complement each other such that the instantaneous power can be calculated by the product of the so-called power-conjugated pairs $F(t)v(t)$ and $V(t)I(t)$ respectively. Power-conjugated pairs belong to a common energy domain and consist of one effort e and one flow f variable. The flow variables are derivatives of a state variable i.e. an extensive quantity that depends on the amount of matter. The effort variables are intensive quantities and independent of the amount of mass or volume. The potential E_{pot} and kinetic E_{kin} energies stored in the mechanical

	Electrical		Mechanical	
Effort e	Voltage V		Force F	
Flow f	Current I		Velocity v	
Derivative	Inductor L	$V(t) = L\frac{dI(t)}{dt}$	Mass M	$F(t) = M\frac{dv(t)}{dt}$
Proportional	Resistor R	$V(t) = RI(t)$	Damper B	$F(t) = Bv(t)$
Integrative	Capacitor C	$V(t) = \frac{1}{C}\int I(\tau)d\tau$	Spring K	$F(t) = K\int v(\tau)d\tau$

Table 2.1: Analogies

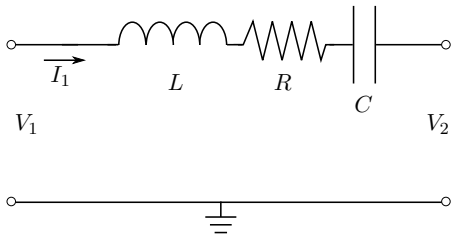

Figure 2.1.9: 2-port of a RLC Circuit

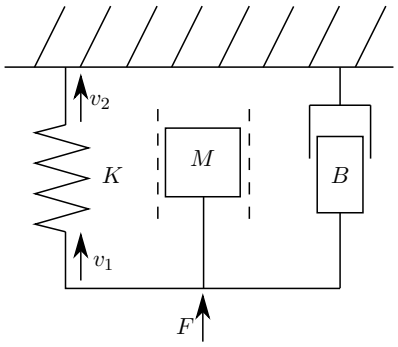

Figure 2.1.10: Mass, Damper and Spring Diagram

system

$$E_{pot}(t) = \frac{1}{2}Kx(t)^2 = \frac{1}{2}K\int_0^t v(\tau)d\tau^2 = \frac{1}{2}\frac{f(t)^2}{K}, \tag{2.32}$$

$$E_{kin}(t) = \frac{1}{2}Mv(t)^2, \tag{2.33}$$

correlate to the energy stored in electric E_{el} and magnetic E_{mag} fields

$$E_{el}(t) = \frac{1}{2}CV(t)^2, \tag{2.34}$$

$$E_{mag}(t) = \frac{1}{2}LI(t)^2. \tag{2.35}$$

RLC circuit Fig. 2.1.9 and Fig. 2.1.10 present an RLC-circuit and an analogous mechanical diagram. The analogies between mass and inductance, stiffness and capacitor as well as damper and resistor is noted in Table 2.1. Since the world's mass is very high, the velocity v_2 can be assumed to be zero. The mechanical elements K, M and B have the same velocity v_1, just as the same current I_1 flows through R, C and L.

Via the analogies, the mechanical system can be represented as an electrical system consisting of lumped elements such that all network elements are physically separable. The result is a linear network since the element impedances as mass, stiffness and damping don't vary in time.

Network Subsystems The simplest form of an element in the network representation [5] is the so-called 1-port as depicted in Fig. 2.1.11. This subsystem can be considered as a black box that has a pair of terminals called a port. In order to fulfill the port condition, the ingoing signal f_1 has to equal the outcoming signal f_1' at the other terminal of the pair. Note that any two-pole circuit is a 1-port as it always meets the port condition [11].

Fig. 2.1.12 presents a 2-port subsystem with two pairs of terminals. The conformance of the port condition depends on the external connections of the 2-port. The power conjugated signals voltage and current can be measured at the ports of a subsystem such that the energy behavior of the network elements can be observed at the ports.

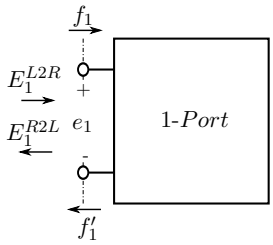

Figure 2.1.11: Energy Flow at a 1-port Network
The network representation of a system can consist of several n-port subsystems. At each port an effort e and a flow f can be measured such that a power or energy respectively can be calculated. Through consideration of the power sign, the flow direction (left to right L2R or right to left R2L) of the power can be determined. A 1-port has one port interface with two poles. The indices of the energies indicate the flow direction and the port at which the energy is measured.

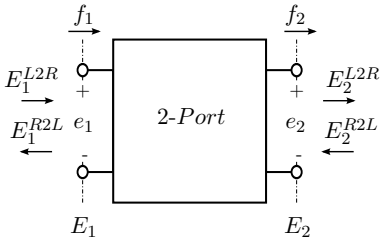

Figure 2.1.12: Energy Flow at a 2-port Network
A 2-port network has two port interfaces with two poles each. The indices of the energies indicate the flow direction of the power or energy respectively and the port at which the energy is measured. The input energy can be transmitted through the port or reflected such that it can exit at both ports.

The power P_i flowing at port 1 and port 2 ($i \in \{1, 2\}$) of a 2-port (see Fig.2.1.12) can be observed as:

$$P_1(t) = f_1(t)e_1(t),$$
$$P_2(t) = f_2(t)e_2(t).$$

The power can be split into the flow directions as:

$$P_i^{L2R}(t) = \begin{cases} P_i(t), & \text{if } P_i(t) > 0 \\ 0, & \text{if } P_i(t) < 0, \end{cases}$$
$$P_i^{R2L}(t) = \begin{cases} 0, & \text{if } P_i(t) > 0 \\ -P_i(t), & \text{if } P_i(t) < 0, \end{cases}$$

with the power P_i^j flowing at port 1 or 2 in left to right (L2R) or right to left (R2L) direction ($j \in \{\text{L2R}, \text{R2L}\}$) respectively. By integration over time, the in/out flowing

energy E_i^j on the left/right side can be calculated:

$$E_i^{L2R}(t) = \int_0^t P_i^{L2R}(\tau)\, d\tau \tag{2.36}$$

$$E_i^{R2L}(t) = \int_0^t P_i^{R2L}(\tau)\, d\tau. \tag{2.37}$$

PI controller The PI controller in Fig. 2.1.13 as a mechanical system can be easily transduced into its electrical analogon (see Fig. 2.1.14). The spring equals a capacitor and the damping a resistor such that $F_1 = F_2$. Note that the parallel structure in the mechanical domain is converted into a series connection in the electrical domain, whereas a series mechanical system results in a parallel electrical one.

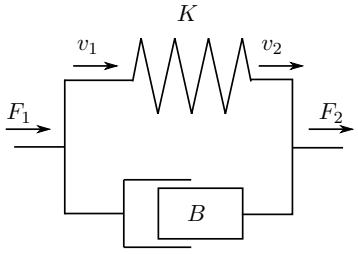

Figure 2.1.13: Mechanical Representation of a PI controller
The PI controller consists of a spring K and a damping element B. In a teleoperation system, the terminations are moved with the master velocity $v_1 = v_m$ and the slave velocity $v_2 = v_s$ respectively. The computed controller force F_c equals F_1 and F_2.

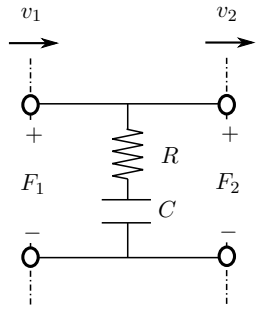

Figure 2.1.14: Electrical Representation of a PI controller
The spring can be represented as a capacitor C and the damper as a resistor R in the electrical domain assuming lumped elements. Since the efforts F_1 and F_2 both equal the controller force F_c, the PI network has a parallel structure.

Application to Bilateral Teleoperation The network representation is the central modeling tool in this thesis. The standard bilateral teleoperation scheme without time delay (see Fig. 2.1.15) is transduced into the network representation in the next step. Based on the impedance models in equation (2.3)-(2.9), the one degree of freedom (DoF) teleoperator of the mechanical domain in Fig. 2.1.16 can be found. The human mass is connected via a spring and damper to the world's mass that is assumed to be infinitely high such that its velocity is zero. The human input force F_0 as well as the human impedance (M_h,B_h,K_h) and the controller forces act on the master mass M_m that is affected by a damping B_m. The right part of the PI's spring damper system is connected to the slave mass M_s and the environmental stiffness and damping. Via the analogies introduced before, the electrical representation depicted in Fig. 2.1.17 can be found. The currents of human operator and master device I_m are equal. This holds also for the environmental and the slave current I_s. This correlates with the position or velocities respectively in the mechanical domain (see Fig. 2.1.16). The voltage across human

operator and master or the environment and the slave respectively correspond to the forces acting in Fig. 2.1.15.

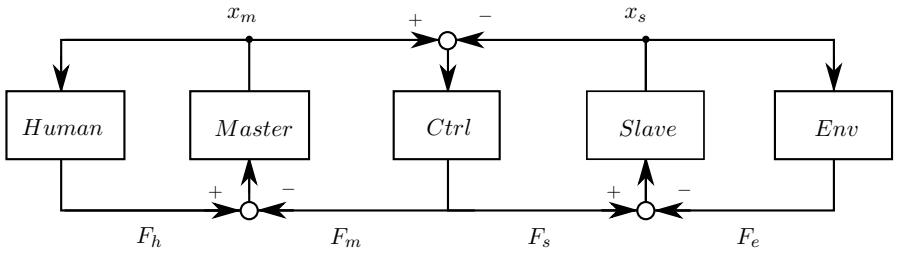

Figure 2.1.15: Signal Flow Diagram of a Bilateral Teleoperator without Delay

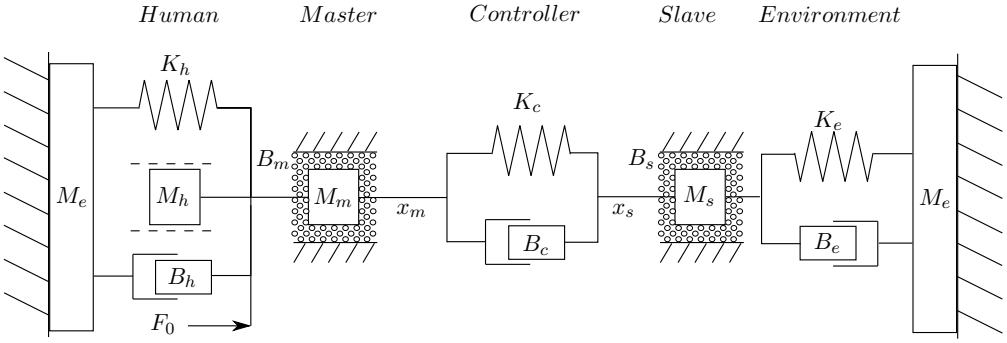

Figure 2.1.16: Mechanical 1DoF Model of a Bilateral Teleoperator
The human is coupled to the world mass. The slave interacts with an object that has damping B_e and stiffness properties K_e and is fixed to the world mass. The operator that applies a force F_0 on the master device, is modeled as a system with mass M_h, damping B_h and stiffness K_h. The master and slave device are modeled as masses M_i with Coulomb friction B_i ($i \in \{m, s\}$) and the controller has a spring and damping element.

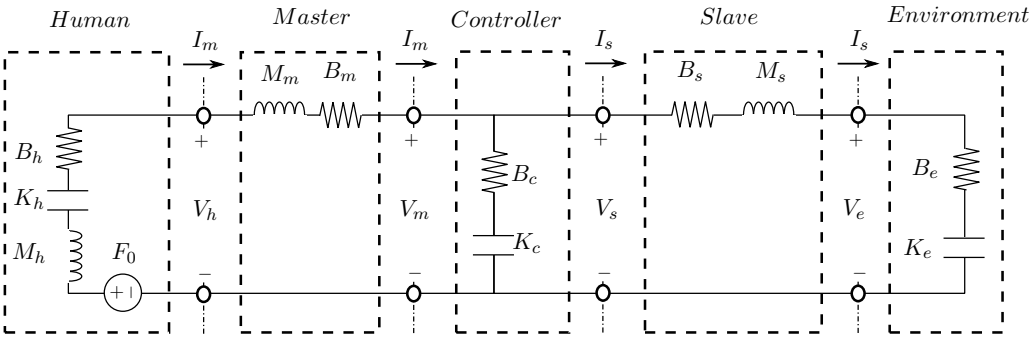

Figure 2.1.17: Electrical 1DoF Model of a Bilateral Teleoperator
The network representation can be deduced from the mechanical scheme considering the mechanical electrical analogies. Human operator and master as well as slave and environment are connected serially since they move with the same velocity and thus the same current I_m and I_s respectively flows through them. The human and environment are the terminations of the electrical network.

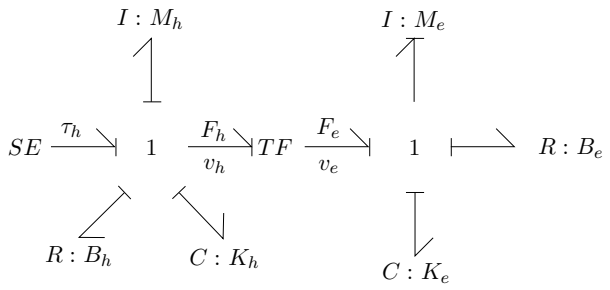

Figure 2.1.18: Bond Graph of Ideal Operation
In the energy-based bond graph representation, half arrow links represent a bond with effort and flow variable that points in the direction of power flow. The short perpendicular line at one end of the bond arrow (causal stroke) indicates the effort flow direction. The side opposite to the causal stroke defines the effort source. SE denotes a source of effort and the transformer TF models a power-conserving coordinate transformation.

2.1.3.4 Bond Graph

Bond Graphs are a powerful tool for energy-based modeling of physical systems [131]. A bond graph as depicted in Fig. 2.1.18 is a structure with half arrow links representing a bond with effort and flow variable and pointing in the direction of power flow. A causal stroke (a short perpendicular line at one end of the bond arrow) indicates the effort flow direction. The side opposite to the causal stroke defines the effort source. E.g. F_h is independent from the transformer TF whereas v_h is a dependent output of TF. Fig. 2.1.18 presents an ideal (transparent) system, in which an operator interacts directly with the environment $F_e = F_h$ and $v_h = v_e$. K_j, M_j and B_j ($j \in \{h, e\}$)) are the stiffness, inertia, and damping parameters of the operator arm (op) and the environment (e) respectively. The operator's muscles produce a force τ_h and SE denotes a source of effort.

The components I and C model the energy storage of inertia and stiffness elements, while the damping is represented by an R component. The 1-junction represents a summation of efforts, and the transformer TF models a power-conserving coordinate transformation.

The interaction of an operator with impedance type master is depicted in Fig. 2.1.19. Fig. 2.1.20 presents a slave-environment interaction. The effort sources producing τ_m and τ_s can be implemented as an intrinsically passive spring (see Section 2.3.2.5) connecting master and slave (compare Fig. 2.1.2). A communication channel can be integrated via the method presented in Section 2.3.2.2.

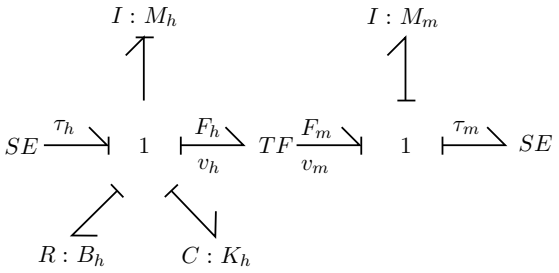

Figure 2.1.19: Bond Graph of Human-Master Interaction

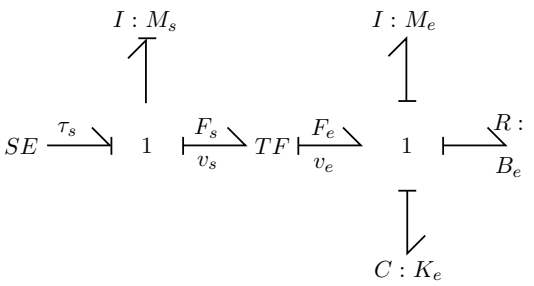

Figure 2.1.20: Bond Graph of Slave-Environment Interaction

2.2 Multilateral Scenarios and Related Functionalities

Bilateral teleoperation systems gained market maturity in various fields of application. Still the range of application can be extended to areas that require higher performance in terms of ergonomics, dexterity and reliability. These parameters depend strongly on the types and the quality of robots and haptic interfaces being used. Also, the price of the hardware limits the application of robotic systems in industry. This problem can be solved to some extent by increasing adaptability of the systems. Several of these necessary steps to novel robotic applications can be pushed by multilateral control concepts.

Multilateral systems involve at least three agents. An agent can be a human operator with the master input device, a slave with its environment or an artificial intelligent agent. In multilateral applications, a general bilateral teleoperation system consisting of one master input device and one slave robot is extended with n agents. All agents can be electronically coupled with each other. I.e., each of the agents is coupled directly or indirectly via another agent to each other agent through a controller. Each agent can receive information on the position or the environmental interaction of one or more other agents. Also, each agent can have an effect on the position of one or more other agents. Note that in some literature the term multilateral is used for systems in which two remotely controlled slave robots controlled via two separate bilateral teleoperation setups cooperate with each other [21]. Such systems that are not multilaterally electronically coupled and bilateral systems that interact with a human in the slave environment [134] are not in the scope of this thesis.

On one side, additional devices need to be added to increase dexterity and accuracy of telerobotic systems, on the other side, thanks to novel approaches cheaper devices can be applied in multilateral control reducing the effective costs of additional devices. Note that some applications, as haptic training setups or cooperative robots manipulating heavy loads are only feasible via multilateral control.

Different control objectives or features in multilateral architectures require specific coupling architectures. Therefore, different multilateral coupling types and the related applications are discussed more in detail in the following.

For example, the interaction of two input devices controlling one robot can be designed in a way to achieve higher precision and intuitivity or more accurate force or torque feedback. In bilateral systems, the master device controls the TCP of a slave robot. In a multilateral manner, a second input device can provide a control interface

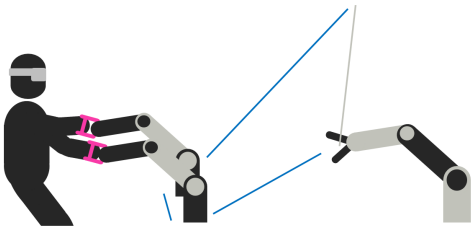

Figure 2.2.1: Multi-Master-Single-Slave: Virtual Grasping Point Concept

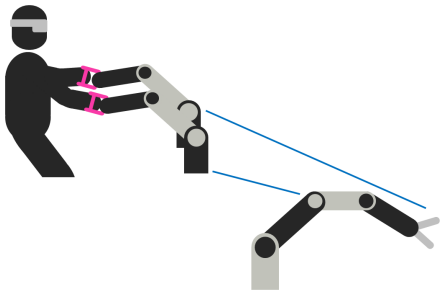

Figure 2.2.2: Multi-Master-Single-Slave: Nullspace Control

to a different point of interaction in the slave environment as depicted in Fig. 2.2.1 (virtual grasping point method, see Section 5.1.1). Especially, if this point is distant from the slave TCP the manipulation performance can be increased. Such additional virtual grasping points can be defined through the projection of the endeffector frames and the transformation of the wrenches of the coupling controller. Similar, asymmetric N:1 setups enable two simple input devices to control a slave robot that has more degrees of freedom (DoF) than one single master device. A coupling of two master devices without torque feedback can provide a feeling for the rotatory interaction of the slave robot through counteracting forces on the two input devices (compare Section 5.1.2). Another important functionality in multilateral teleoperation of mobile robots are rate control interfaces. In this work, a multilaterally extended model-mediated teleoperation scenario is introduced in which the operator receives force feedback from the remote slave side and a local model. In such setups, the operator can command the longitudinal velocity and the yaw-rate of the robot such that the control loop differs gravely from position controlled manipulators.

Trilateral training systems with authority allocation that have been first presented in the year 2005 by the authors of [111] have been realized with a variety of control approaches [60, 63, 35, 139] and patented in 2013 [75]. A mentor coupled as a third agent to the trainee and the slave robot is able to supervise the manipulation. A scaling acting on the control signals of the three agents allows to give the trainee progressively higher control on a slave robot. For instance, if the feedback force of the trainee to the slave is decreased by the scaling factor, the slave motion is less influenced by the trainee actions. These haptic setups promise a faster training compared to orally guided alternatives. A technique which is similar to the scaling in the training scenario can be applied to realize a Cartesian task allocation that allows the distribution of roles to two master devices that control one slave robot (compare Section 5.2.2). In the aforementioned virtual grasping point method, the point of interaction with the environment can be distant from the slave hand and is therefore controlled by a second master device. Since this master is coupled directly to a virtual grasping point in the point of interaction, it should gain higher influence on the position of this point. In the Cartesian task allocation method, this is realized through a scaling of forces. In another N:1 setup, an expert operator can change the Nullspace configuration of a redundant robotic manipulator [97, 98, 100] via

his/her second input device (compare Fig. 2.2.2. Thus, the size of the slave robot does not necessarily need to be adapted to the narrowness of its environment since collisions can be prevented. Also, singularities can be avoided and the workspace can be optimized with respect to load capacities or dexterity directly by the knowledge of the expert.

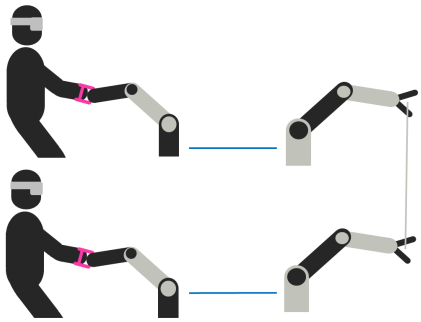

Figure 2.2.3: Multi-Master-Single-Slave: Cooperation of two Separate Teleoperators

In a reverse concept (1:N), one single master can be used to control an object that is cooperatively grasped by two slave robots [55, 96]. This is reasonable especially in scenarios that require the manipulation of objects that are too bulky or heavy for one single robot. The master controls a virtual grasping point in the slave robots' environment which has a fix kinematic coupling to the slaves' TCPs. In contrast, this task becomes more complicated when using two separate teleoperators to manipulate a cooperatively grasped object (compare Fig. 2.2.3) since the motion synchronization of the two slave robots becomes more demanding.

Besides these applications involving three agents, Multi-Master-Multi-Slave systems evolving from a combination of the aforementioned approaches are reasonable. Telerehabilitation systems with an arbitrary number of participants interacting in virtual environments, as implemented by the authors of [85, 16], present other typical applications of M:N setups.

Further novel concepts and applications aiming for an increase in ergonomics and transparency are presented in the course of this thesis.

2.3 Control Approaches for Multilateral Teleoperation

This section recapitulates fundamental control concepts for bilateral teleoperation systems with focus on approaches that have been applied in the literature on multilateral control. With reference to the overview presented in [176], the relation between different control approaches is pointed out.

2.3.1 $\mathcal{L}^p$ Stability

The research of [97, 98, 100, 99, 101] is based on the $\mathcal{L}^p$ stability (also Input-Output-Stability) principle. The $\mathcal{L}^p$ norm is defined as

$$\|x\|^p = \left(\int_0^\infty |x(\tau)|^p \, d\tau \right)^{1/p} \tag{2.38}$$

for $p \in [1, \infty)$. The $\mathcal{L}^\infty$ norm is defined as

$$\|x\|^\infty = \sup_{t \geq 0} |x(t)| \, . \tag{2.39}$$

The extended norms $\mathcal{L}^{pe}$ and $\mathcal{L}^{\infty e}$ are equivalent to $\mathcal{L}^p$ and $\mathcal{L}^\infty$, but defined for a time $0 \leq \tau \leq t$. In [56], the $\mathcal{L}^p$-stability is described by the convolution of two functions $u, h : \mathbb{R}^+ \to \mathbb{R}$

$$y(t) = u(t)h(t) = \int_0^\infty h(t-\tau)u(\tau)d\tau = \int_0^\infty u(t-\tau)h(\tau)d\tau \tag{2.40}$$

with the input u and output y. This system is $\mathcal{L}^p$-stable if for some constant $c \geq 0$

$$u \in \mathcal{L}^p \Rightarrow y \in \mathcal{L}^p \quad \text{and} \quad ||y||^p \leq c||u||^p. \tag{2.41}$$

A system has a finite $\mathcal{L}^2$-gain and is thus $\mathcal{L}^2$-stable if for an input signal $u \in \mathcal{L}^{2e}$

$$\sqrt{\int_0^t \|y\|^2 \, d\tau} \leq \nu \sqrt{\int_0^t \|u\|^2 \, d\tau} + b \tag{2.42}$$

holds for $t \geq 0$ with a finite $\mathcal{L}^2$-gain ν and an offset b. Note that $\mathcal{L}^\infty$ stability is also known as bounded-input bounded-output (BIBO) stability.

The $\mathcal{L}^p$ stability is applied in the analysis of various multilateral control strategies. In [100], the local master and slave controllers as well as the trilateral control structure have been analyzed with the help of input-output stability. The input-output stability proof in [98] is based on the analysis in [29, 71]. Also the consensus algorithms of [112, 78] make use of $\mathcal{L}^p$ stability (see Section 2.3.6).

2.3.2 Passivity

A system is passive if it does not generate energy. I.e. not more energy can be extracted from the system than has been injected and than has been available at time $t = 0$ (refer to [73] for more detail):

$$E(t) \leq \int_0^t w(\tau)d\tau + E^0. \tag{2.43}$$

E^0 is the energy that was initially stored in the system. The supply rate $w(t) = w(u(t)y(t))$ is a function of the inputs $u(t)$ and outputs $y(t)$ [181]. In general, systems that fulfill equation (2.43) are called dissipative [181, 74, 176] and conservative if equation (2.43) holds with equality. In passive systems, the supply rate is $w(t) = u(t)y(t)$, the dimension of inputs $u(t)$ and outputs $y(t)$ equal and equation (2.43) have to be fulfilled

[74]. In this work, input u and output signals y are power correlated effort e and flow f or more precisely force and velocity signals.

Another term applied for passivity analysis is the scattering matrix S which is an operator that maps the sum of effort e and flow f into their difference:

$$e(s) - f(s) = S(s)(e(s) + f(s)).$$

In a 2-port network the following relation between scattering matrix S and the hybrid matrix H holds:

$$S(s) = \begin{pmatrix} 1 & 0 \\ 0 & -1 \end{pmatrix} (H(s) - I)(H(s) - I)^{-1}.$$

A system is passive if and only if the scattering transform has a $\mathcal{L}^2$-gain ≤ 1 which means $\|S(s)\| \leq 1$ (see Section 2.3.1, [176]).

A 2-port subsystem (compare Section 2.1.3.3) is passive if the following condition holds:

$$E_1^{L2R}(t) - E_1^{R2L}(t) + E_2^{R2L}(t) - E_2^{L2R}(t) + E^0 \geq 0, \tag{2.44}$$

where E^0 is the initially stored energy in the system. Note that the delay will be considered in Section 4.1. Assuming that E^0 is zero, the conditions (2.45) and (2.46) meet the passivity criterion (2.44).

$$E_1^{L2R}(t) - E_2^{L2R}(t) \geq 0 \tag{2.45}$$

$$E_2^{R2L}(t) - E_1^{R2L}(t) \geq 0 \tag{2.46}$$

If the conditions (2.45) and (2.46) are fulfilled, less energy is leaving than entering the 2-port in both directions, i.e. more energy has been dissipated than generated and thus, the 2-port is passive.

The following control methods are based on the passivity criterion. Note that all passivity-based methods require that the terminations are passive. The terminations of the 2-port are the master and slave devices, together with the human operator and the environment respectively (compare Fig. 2.1.17). This requirement is discussed in detail in Section 3.3.2.

2.3.2.1 Raisbeck Passivity Criterion

The well known Raisbeck passivity criterion [137, 15] which relates to the hybrid 2-port matrix requires:

$$R_{11}^h \geq 0, \tag{2.47}$$

$$R_{22}^h \geq 0, \tag{2.48}$$

$$R_{11}^h R_{22}^h - (\frac{R_{12}^h + R_{21}^h}{2})^2 - (\frac{X_{12}^h - X_{21}^h}{2})^2 \geq 0, \tag{2.49}$$

where R is the real and X is the imaginary part of the Z matrix elements. A linear 2-port is proven passive, if a teleoperator fulfills the inequalities (2.47)-(2.49), the poles of H_{ij}

are not in the right half plane, the poles on the imaginary axis are simple and if for the residues k_{ij}^h of H_{ij} holds: $k_{11}^h \geq 0$, $k_{22}^h \geq 0$ and $k_{11}^h k_{22}^h - k_{12}^h k_{21}^h \geq 0$ with $k_{21}^h = k_{12}^{h*}$ where k_{12}^{h*} is the complex conjugate of k_{12}^h.

In [86], the Raisbeck criterion, that has been extended to n-port networks in [104], was applied to a trilateral system. The Z-matrix elements then have to fulfill the following requirements:

- The Z-matrix elements may not have poles in the right-half of the complex plane.
- The poles on the imaginary axis are simple. For the residues k_{mm} at these poles holds:

$$\begin{aligned} &k_{mm} \geq 0, \text{m=1,2,3,} \\ &\frac{k_{11}k_{22} - k_{12}k_{21}}{k_{11}} \geq 0, \\ &\frac{k_{11}k_{33} - k_{13}k_{31}}{k_{11}} - \frac{k_{11}k_{23} - k_{21}k_{13}}{k_{11}k_{22} - k_{12}k_{21}} \frac{k_{11}k_{32} - k_{31}k_{12}}{k_{11}} \geq 0. \end{aligned}$$

- The following conditions for the real and imaginary part are satisfied:

$$\begin{aligned} &R_{mm}^z \geq 0, \qquad \text{m=1,2,3} \\ &4R_{11}^z R_{22}^z - (R_{12}^z + R_{21}^z)^2 - (X_{12}^z - X_{21}^z)^2 \geq 0, \\ &4R_{11}^z R_{22}^z R_{33}^z - R_{33}^z((R_{12}^z + R_{21}^z)^2 + (X_{12}^z - X_{21}^z)^2) - R_{22}^z((R_{13}^z \\ &+ R_{31}^z)^2 + (X_{13}^z - X_{31}^z)^2) - R_{11}^z((R_{23}^z + R_{32}^z)^2 + (X_{23}^z - X_{32}^z)^2) \\ &+ (R_{23}^z + R_{32}^z)(R_{13}^z + R_{31}^z)(R_{12}^z + R_{21}^z) + (R_{12}^z + R_{21}^z) \\ &(X_{13}^z - X_{31}^z)(X_{23}^z - X_{32}^z) - (R_{13}^z + R_{31}^z)(X_{12}^z - X_{21}^z) \\ &(X_{23}^z - X_{32}^z) + (R_{23}^z + R_{32}^z)(X_{13}^z - X_{31}^z)(X_{12}^z - X_{21}^z) \geq 0. \end{aligned}$$

2.3.2.2 Wave Variables

The wave variables method [5] is an approach to guarantee passivity specifically of the communication channel (or transmission line). This method is closely related to the scattering matrix.

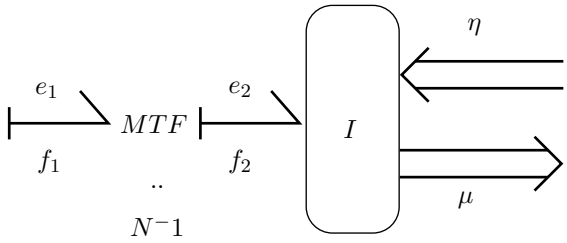

Figure 2.3.1: Bond Graph of the Impedance Adaption of the Transmission Line [166]
Here, the left part of the transmission line with modulated transformer MTF is depicted. The MTF serves the impedance decomposition of the transmission line. The so called scattering variables μ and η are transmitted as waves through the transmission line.

The so called scattering variables μ and η transmitted in the transmission line are visualized in a bond graph in Fig. 2.3.1. This figure presents the left part of the transmission line with the modulated transformer MTF that serves the impedance decomposition

of the transmission line as explained later. The departing wave of one side has to be connected to the incoming wave of the other side [166]. In [109], the wave variables μ_i, η_i ($i \in \{m, s\}$ master m, slave s, Fig. 2.3.2) are defined analogous to the scattering variables by:

$$\mu_m = \frac{bv_m + F_m}{\sqrt{2b}}, \qquad \eta_m = \frac{F_m - bv_m}{\sqrt{2b}}$$
$$\mu_s = \frac{F_s - bv_s}{\sqrt{2b}}, \qquad \eta_s = \frac{F_s + bv_s}{\sqrt{2b}}$$

such that the power variables v_i, F_i can be calculated from the wave variables

$$F_m = bv_m + \sqrt{2b}\eta, \qquad v_s = \frac{\sqrt{2b}\mu_s - F_s}{b}.$$

The strictly positive parameter b is the characteristic impedance of the communication channel (compare MTF) and has direct influence on the system behavior (see Section 2.3.2.5 for more detail). A position drift resulting from time-varying delay can be compensated by the method proposed in [185].

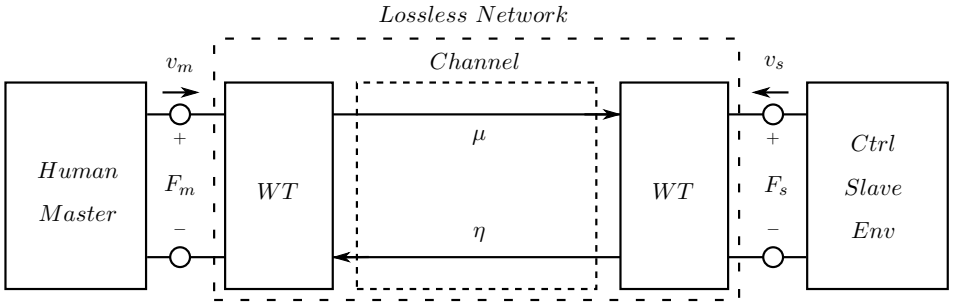

Figure 2.3.2: Bilateral Teleoperator with Wave Variables Approach in Network Representation The departing wave (scattering variables μ and η) of one side of the transmission line has to be connected to the incoming wave of the other side. The wave transformer (WT) transform the velocity and force signals into scattering variables and vice versa.

The wave variables method was applied to multilateral systems in [78, 58, 168]. The application is equivalent to the bilateral case. Still, the passivity of the overall system under negligence of time delay has to be proven. For instance, the passivity of the measured force feedback architecture can not simply be followed from the computed force feedback. This can be analyzed in the specific network representation of the measured force feedback architecture [180, 124]. Note that the majority of the haptic augmentation concepts developed for the MPMT in this thesis (see Section 5) can be combined with the wave variables concept.

2.3.2.3 Time Domain Passivity Approach

Another well-known approach, that was developed to ensure stability despite time delay in the communication channel, is the Time Domain Passivity Approach (TDPA [45], [144]) that allows the dissipation of undesired energy in the time domain. Therefore, the TDPA provides passivity observers (PO) that measure the power flowing at the

subsystem ports analogously to Equ. 2.36 and Equ. 2.37. The network representation (introduced in Section 2.1.3.3) is a crucial tool to analyze where the respective energies have to be measured in the signal flow diagram. Fig. 2.3.3 depicts a TDPA setup for 2-port subsystems. If the passivity observers recognize that an excessive amount of energy $E_{obs}(k)$ of time step k has been generated by the 2-port in a specific direction of energy flow, this energy can be dissipated by so-called passivity controllers (PC) in the respective direction. The calculation of $E_{obs}(k)$ depends on the application of the TDPA and is therefore presented in the respective later sections.

Passivity Controller Depending on the signal output of the 2-port, an admittance type PC that varies the velocity or an impedance type PC that varies the forces has to be applied. The energy that needs to be dissipated in the current time step $W(k)$ needs to consider the energy that has already been dissipated $W_{diss}(k-1)$.

$$W(k) = E_{obs}(k) - W_{diss}(k-1). \tag{2.50}$$

After the dissipation through passivity controllers, the dissipated energy $W_{diss}(k)$ needs to be updated:

$$W_{diss}(k) = W_{diss}(k-1) + W(k). \tag{2.51}$$

Admittance Type PC The admittance type PC dissipates energy by a variation of the velocity v_3:

$$v_4(k) = v_3(k) + v_{PC}(k) = v_3(k) + \beta(k)F_3(k) \quad \text{with} \tag{2.52}$$

$$\beta(k) = \begin{cases} \frac{-W(k)}{T_S F_3(k)^2} & \text{if } W(k) < 0 \\ 0 & \text{if } W(k) \geq 0. \end{cases} \tag{2.53}$$

T_S is the sample time of the system. Since the velocity is altered by the admittance type PC, the position information is affected by errors. Position drift compensations that eliminate this effect have been proposed in [8, 17]. The authors of [8] designed a PC that injects energy during passivity gaps observed by the POs. In [25], a multi-DoF admittance type PC has been proposed for a non teleoperation scenario.

Impedance Type PC The impedance type PC dissipates energy by a variation of the force F_2:

$$F_1(k) = F_2(k) + F_{PC}(k) = F_2(k) + \alpha(k)v_2(k) \quad \text{with} \tag{2.54}$$

$$\alpha(k) = \begin{cases} \frac{-W(k)}{T_S v_2(k)^2} & \text{if } W(k) < 0 \\ 0 & \text{if } W(k) \geq 0. \end{cases} \tag{2.55}$$

The PC leads to forces with high frequencies due to sudden force changes. The authors of [143] proposed an additional passive virtual mass-spring system to circumvent this effect. The virtual mass-spring system acts as a low-pass filter of force and velocity in both directions such that passivity is maintained. In [124], the TDPA, that was originally

developed for the communication delay, was applied to guarantee passivity of measured force feedback.

Different approaches for the multi-DoF case have been proposed for impedance type PCs. The authors of [135] mapped the force of the PC into the direction of the feedback force. In [119], the mass matrix was applied in a joint space and a Cartesian space approach to realize PC damping depending on the kinetic energy. Furthermore, an approach was presented that dissipated a part of the excessive energy in the Nullspace of a redundant robot.

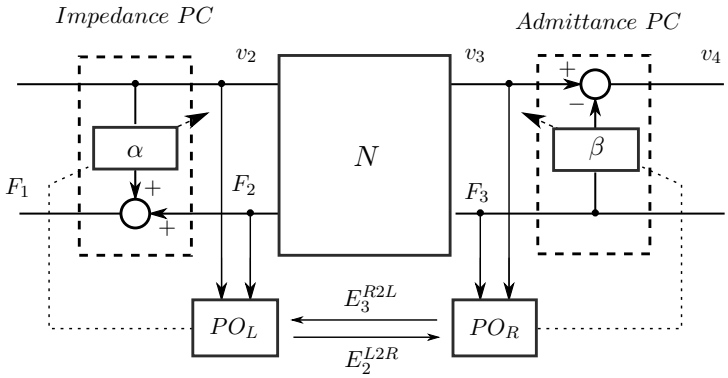

Figure 2.3.3: Time Domain Passivity Approach
The TDPA provides admittance and impedance type passivity controllers (PC) that vary the velocity or force respectively via a variable damping (α, β). Passivity observers (PO) calculate the energy that is generated by the network N to determine the amount of energy that has to be dissipated by the PCs to maintain passivity.

Time Delay Control with Time Delay Power Networks The consideration of time delay is the main motivation for the use of passivity control in multilateral teleoperation since the communication channel presents an active subsystem [5] with short phases of dissipation.

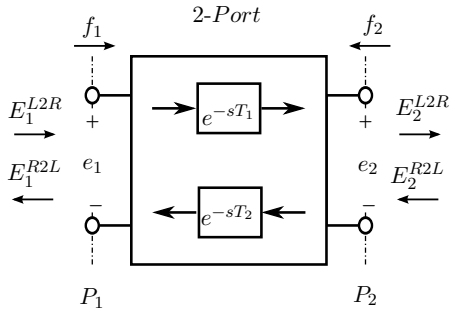

Figure 2.3.4: Energy Flow at a 2-port Network with Time Delay

Delayed Energy Transfer First, the energy transfer in a 2-port containing delay (see Fig. 2.3.4) has to be analyzed. Based on the 2-port energy analysis of Sections 2.1.3.3 and 2.3.2, the energies E_i^j flowing at port 1 and 2 ($i \in \{1, 2\}$) from left to right

(L2R) or right to left (R2L, ($j \in \{L2R, R2L\}$)) respectively through the 2-port can be computed through integration of the positive defined power P over time:

$$E_1^j(t) = \int_0^t P_1^j(\tau)\, d\tau,$$

$$E_2^j(t) = \int_0^t P_2^j(\tau)\, d\tau.$$

As these energies are observed in the two directions of a track separately and as they are affected by time delay, the passivity condition (2.44) has to be reformulated:

$$E_1^{L2R}(t - T_1) - E_2^{L2R}(t) + E_2^{R2L}(t - T_2) - E_1^{R2L}(t) \geq 0. \tag{2.56}$$

As the energies are purely increasing over time, the equation can be split up into the conditions

$$E_1^{L2R}(t - T_1) - E_2^{L2R}(t) \geq 0, \tag{2.57}$$

$$E_2^{R2L}(t - T_2) - E_1^{R2L}(t) \geq 0. \tag{2.58}$$

Thus, the observed time delayed energy difference E_{obs} results in

$$E_{obs}^{L2R}(t) = E_1^{L2R}(t - T_1) - E_2^{L2R}(t), \tag{2.59}$$

$$E_{obs}^{R2L}(t) = E_2^{R2L}(t - T_2) - E_1^{R2L}(t). \tag{2.60}$$

System Description The most frequently used time domain passivity approach is based on Time Delay Power Networks (TDPN, [9]) which are the central element representing the communication channel 2-port (compare Fig. 2.3.4) of the TDPN-approach.

The network representations of a PF_{comp} and a PP architecture with TDPN approach are presented in Fig. 2.3.5 and Fig. 2.3.6 respectively. The track is split up into its two directions of energy flow. As the TDPNs represent the communication channel, one TDPN is located next to each dependent source (F_6 and v_1 in Fig. 2.3.5). The TDPN concept is crucial to assure the power consistency of the transmitted signals in the communication channel. In the PP architecture of Fig. 2.3.6, the TDPNs indicate that e.g. the energy input E_4^{R2L} has to be calculated from the flow v_4 and effort F_4 which equals the delayed effort $F_3(t - T_1)$.

$$F_4(t) = F_3(t - T_1).$$

This power relation is not obvious in the signal flow diagram (compare Fig. 2.1.4), but only in the representation of the PP architecture in the electrical domain. In case without time domain passivity control, the force F_3 is not relevant for the control of the slave and would not be transmitted through the communication channel therefore. The $TDPN1$ of the PF_{comp} architecture has the conjugate pairs

$$TDPN1: \begin{cases} \langle F_2(t), v_2(t) \rangle & \text{at the left side, where } F_2(t) = F_6(t - T_2) \\ \langle F_3(t), v_2(t - T_1) \rangle & \text{at the right side, where } F_3(t) = F_6(t) \end{cases}$$

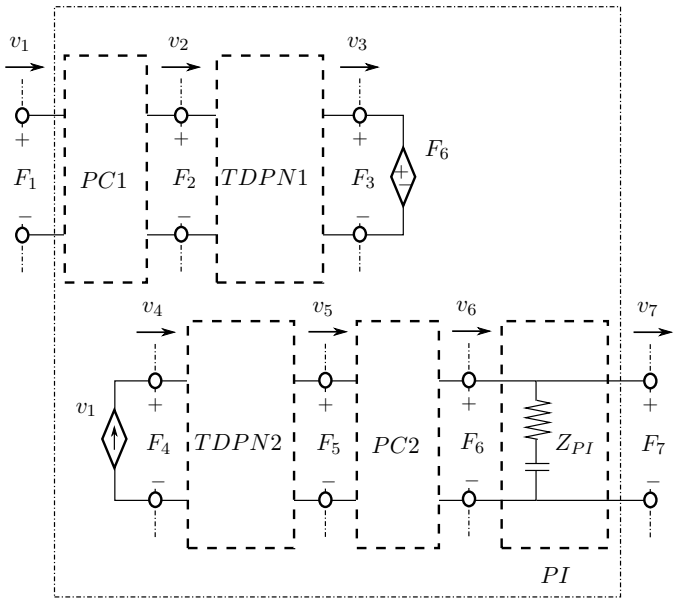

Figure 2.3.5: Track with PF_{comp} Architecture and TDPN Approach
The presented network is a track that connects two robotic agents with a PI controller and a communication channel represented by the TDPN subsystems. A master and operator at port 1 and a slave with environment at port 7 respectively terminate the network (not visualized). The network is split up into two circuits such that the effort source F_6 introduces the feedback force into the master side circuit and the flow source v_1 determines the flow in the slave side circuit. The upper circuit accounts for the $R2L$ energy flow direction and the lower circuit for the $L2R$ energy flow direction respectively. This splitting is necessary, especially for more complicated architectures (as PP or PF_{meas} architecture) to assure the power consistency of the network ports of the TDPNs. Two PCs terminate the TDPNs in the relevant energy flow direction to assure the passivity of the communication channels.

The $TDPN2$ of the PF_{comp} architecture has the conjugate pairs

$$TDPN2\text{:}\begin{cases} \langle F_4(t), v_1(t)\rangle & \text{at the left side, where } F_4(t) = F_5(t-T_2) \\ \langle F_5(t), v_1(t-T_1)\rangle & \text{at the right side} \end{cases}$$

Passivity Control In each direction two POs observe the energy behavior of the TDPNs. For the PF_{comp} architecture the POs are located at port 2 and 3 (R2L) and port 4 and 5 (L2R) respectively such that the energy generated in the TDPNs (including the communication channel with time delay) can be measured. Two PCs added next to TDPN1 and TDPN2 dissipate this energy in the corresponding direction of energy flow. The $PC1$ has impedance causality whereas the $PC2$ is of admittance type.

The observed time delayed energy difference E_{obs} in the PF_{comp} Architecture can be found as

$$E_{obs}^{R2L,TDPN1}(t) = E_3^{R2L}(t-T_2) - E_2^{R2L}(t), \tag{2.61}$$
$$E_{obs}^{L2R,TDPN2}(t) = E_4^{L2R}(t-T_1) - E_5^{L2R}(t). \tag{2.62}$$

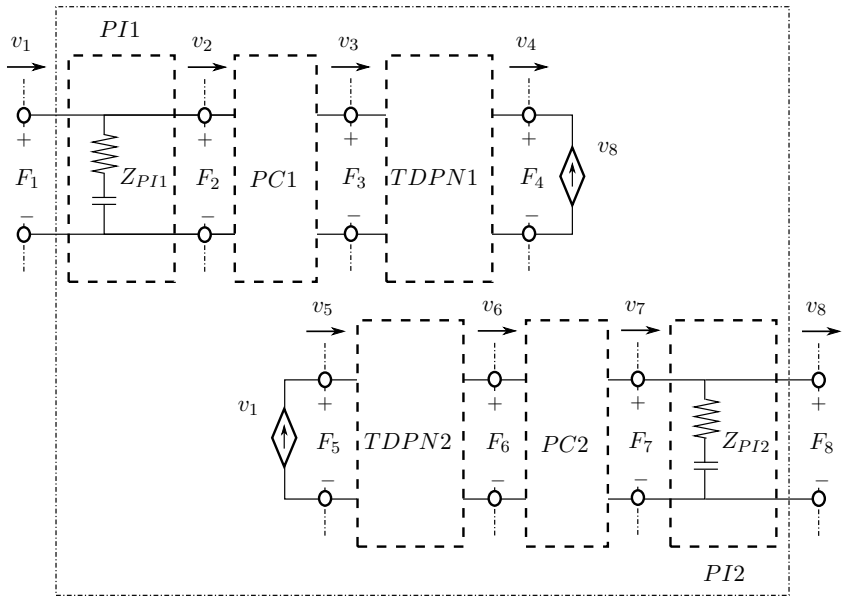

Figure 2.3.6: Track with PP Architecture and TDPN Approach
In the PP architecture, there is one PI controller in each circuit. Since positions are exchanged through the communication channel, a flow source v_8 feeds the slave velocity back to the controller of the master side circuit. Two PCs terminate the TDPNs in the relevant energy flow direction to assure the passivity of the communication channels.

$E_{obs}^{R2L,TDPN1}$ has to be dissipated by $PC1$ under consideration of v_2. $E_{obs}^{L2R,TDPN2}$ has to be dissipated by $PC2$ under consideration of F_5. The functionality of the PC types have been presented in Section 2.3.2.3.

Note that both PCs in the PP architecture are of admittance type. The TDPN approach is compared in Section 4.1.3 with more recent developments in TDPA-based time delay control. Therefore, experiments employing the TDPN approach are presented in Section 4.1.3.

Application in Multilateral Setups In multilateral systems, the TDPA has been applied to stabilize systems with delayed communication [121] and to guarantee passivity in systems with measured force feedback [124]. Since the TDPA is in combination with the MPMT a central instrument of this thesis, improvements and comparisons of the respective achievable transparency are performed in Chapter 4. Note that the novel concepts of this thesis are not only beneficial to multilateral but also to bilateral systems.

2.3.2.4 Methodology for Passivity-Based Multilateral Teleoperation

The focus of this thesis is the development of a generic and modular, passivity-based control concept for multilateral teleoperation. The resulting Methodology for Passivity-based Multilateral Teleoperation (MPMT) is designed with the help of the network representation. The MPMT will be thoroughly introduced in Chapter 3, but is mentioned here, since related literature [121, 127, 124] is considered in the literature review of Section 2.4.

2.3.2.5 Intrinsically Passive Controller

The author of [166] introduced an intrinsically passive controller (IPC) for the coupling of mechanical systems through a spatial spring. The design of the system is based on the bond graph and the port-Hamiltonian approach. The port-Hamiltonian approach is a representation of a dynamical system considering the total energy H in a system in Hamiltonian equations and port interfaces similar to the network representation.

Physical systems are connected via a power port similar to the network representation. With a vector space V for twists and its dual space V^* of wrenches the power P can be calculated:

$$P := V \times V^*.$$

The vector space V and its dual space V^* are $\mathbf{se}(3)$ (a Lie algebra of the Lie group SE(3), the special euclidean group used for rigid body kinematics that preserve orientation as translations and rotations). In teleoperation setups (see Fig. 2.1.19 and Fig. 2.1.20), the master and slave devices can be considered as two port controlled Hamiltonian systems [166]. The elements of the robots' ports are $(\dot{q}, \tau)$ the differentiated current configuration q and the joint torques τ. The other IPC ports are connected to a pair of interaction twists T_i and wrenches W_i. In [165], the differential equation of an IPC is defined as:

$$\dot{x} = (J(x) - R(x))\frac{\partial H_c}{\partial x} + g(x) \begin{pmatrix} \dot{q} \\ T_1 \\ \vdots \\ T_n \end{pmatrix}, \tag{2.63}$$

$$\begin{pmatrix} \tau \\ W_1 \\ \vdots \\ W_n \end{pmatrix} = g^T(x)\frac{\partial H_c}{\partial x} + B(x) \begin{pmatrix} \dot{q} \\ T_1 \\ \vdots \\ T_n \end{pmatrix}. \tag{2.64}$$

H_c is the internal energy function. $R(x)$ considers the dissipating elements. The network structure is described by the skew-symmetric Poisson tensor $J(x)$ and $g(x)$ determines the relation between the system and the external elements. The standard port-controlled generalized Hamiltonian system leads to a direct feed through of s^+ to s^- (the scattering variables in the transmission line, Section 2.3.2.2), which leads to wave reflections and thus potentially to instability in case of delay. Therefore, the extended form of the port-controlled Hamiltonian system with dissipation (PHCD, Equ. 2.64) contains the feed-through matrix B that allows the impedance matching to the impedance of the line (B=Z). To assure stability despite time delay, the wave variables method can be applied (compare Section 2.3.2.2). The change in internal energy $\dot{H}$ consists of supplied and dissipated power [165]:

$$\dot{H} = y^T u - (\frac{\partial H}{\partial x})^T R(x) \frac{\partial H}{\partial x}$$

Assuming that the energy supply to the system of robot and IPC is zero, the amount of energy in the system is $H_c + H_r$, with the IPC energy H_c and the robot's mechanical energy H_r. As this energy can not increase, the system is passive in any situation.

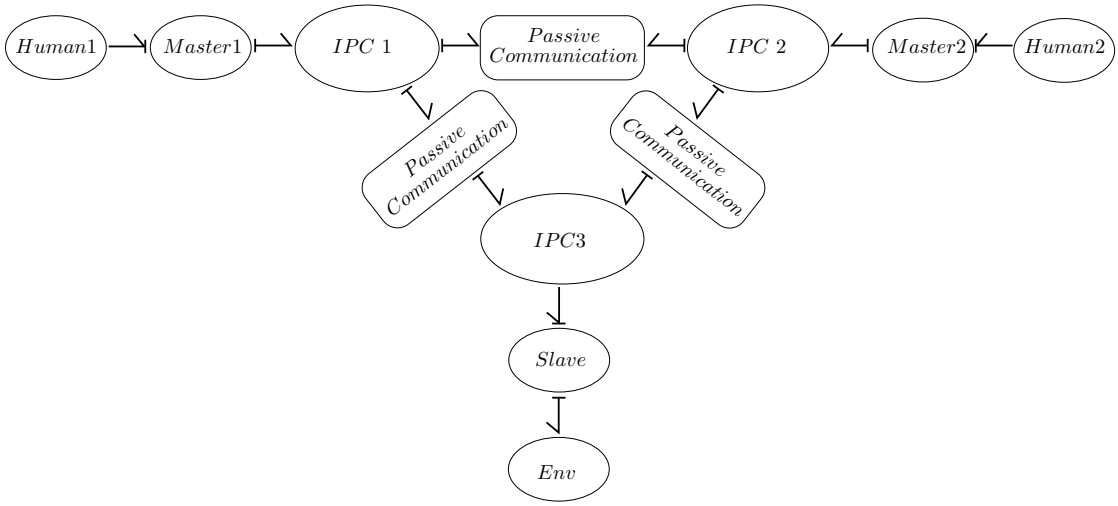

Figure 2.3.7: Bond Graph Representation of a Trilateral Teleoperation System
Three spatial springs connect all three devices. Within the bond graph representation, the passivity of the communication channel can be guaranteed for example through the wave variables approach.

A multilateral bond graph with IPC is depicted in Fig. 2.3.7. The authors of [32] argued based on the application of an IPC that the whole multilateral teleoperation system is passive. No time delay has been considered in that work.

2.3.2.6 Passive Decomposition

The method of passive decomposition in multilateral systems was developed specifically for 1:N setups with cooperatively grasping slaves. Through passive decomposition, a setup with multiple cooperatively grasping slaves can be simplified to a bilateral teleoperator. In [82], the dynamics of multiple slaves is decomposed into a shaped and a locked system while preserving energetic passivity. The locked system represents the overall behavior of the multiple slaves, whereas the shape system describes the cooperative grasping aspect. Thus, the slave robots can be regarded as a passive termination in the network representation of the bilateral teleoperator. In [82], stability in the case of time delay has been preserved by the wave variables method.

2.3.3 Absolute Stability

The absolute stability criterion allows the analysis of linear networks with passive terminations. In [40], it was shown that reciprocal networks ($R_{21} = R_{12}$,$X_{21} = X_{12}$) that are stable under all passive terminations are always passive. Llewellyn [94] showed that non-reciprocal networks need not be passive to be stable [15].

2.3.3.1 Llewellyn

Similar to the Raisbeck criterion, Llewellyn presented the less conservative absolute stability approach [94, 1] with the following conditions:

$$R_{11}^h \geq 0, \tag{2.65}$$

$$R_{22}^h \geq 0, \tag{2.66}$$

$$-\frac{Re(H_{21}H_{12})}{|H_{21}H_{12}|} + 2\frac{R_{11}^h R_{22}^h}{|H_{21}H_{12}|} \geq 1. \tag{2.67}$$

Furthermore, H_{11} and H_{22} must not have poles in the right half plane and the poles of H_{11} and H_{22} have to be simple and to have real positive residues. If these conditions hold for a given 2-port and if the terminations of the 2-port are passive, the system is absolutely stable.

A 3-port of a trilateral teleoperation network has been reduced to a 2-port in [68], such that the Llewellyn criterion for bilateral systems could be applied under consideration of specific environmental impedances. The Llewellyn criterion has been extended to the multilateral case in [126, 86]. In [86], it was shown that under the symmetrization condition

$$Z_{13}Z_{21}Z_{32} - Z_{12}Z_{23}Z_{31} = 0,$$

the following conditions fulfill the requirements for absolute stability:

- The Z-matrix elements may not have poles in the right-half of the complex plane.
- The poles on the imaginary axis are simple. For the residues k_{mm} at these poles holds:

$$\begin{aligned}
&k_{mm} \geq 0, \text{m=1,2,3} \\
&\frac{k_{11}k_{22} - k_{12}k_{21}}{k_{11}} \geq 0, \\
&\frac{k_{11}k_{33} - k_{13}k_{31}}{k_{11}} - \frac{k_{11}k_{23} - k_{21}k_{13}}{k_{11}k_{22} - k_{12}k_{21}} \frac{k_{11}k_{32} - k_{31}k_{12}}{k_{11}} \geq 0.
\end{aligned}$$

- The following conditions for the real and imaginary part are satisfied:

$$\begin{aligned}
&R_{mm}^z \geq 0, \text{m=1,2,3} \\
&R_{11}^z R_{22}^z - \frac{|Z_{12}Z_{21}| + Re(Z_{12}Z_{21})}{2} \geq 0, \\
&R_{11}^z R_{22}^z R_{33}^z - R_{11}^z \frac{|Z_{23}Z_{32}| + Re(Z_{23}Z_{32})}{2} \\
&- R_{22}^z \frac{|Z_{13}Z_{31}| + Re(Z_{13}Z_{31})}{2} \\
&- R_{33}^z \frac{|Z_{12}Z_{21}| + Re(Z_{12}Z_{21})}{2} \\
&+ 2Re(\sqrt{Z_{12}Z_{21}})Re(\sqrt{Z_{13}Z_{31}})Re(\sqrt{Z_{23}Z_{32}}) \geq 0.
\end{aligned}$$

The Llewellyn conditions are according to Haykin [48] equal to the Raisbeck conditions for symmetric 2-port systems. The authors of [85] showed that this holds also for symmetric 3-ports:

$$Z_{12} = Z_{21}, Z_{13} = Z_{31}, Z_{23} = Z_{32}.$$

In trilateral systems, absolute stability can only be guaranteed for such symmetric systems [85]. As discussed in Section 3.1.2, this symmetrization condition leads to some limitations.

2.3.3.2 Zeheb-Wallach

In contrast to the Llewellyn criterion, the Zeheb-Wallach method [187] to analyze absolute stability considers e.g. specific terminations like inductors or capacitors. This method was extended to suite a teleoperation system in [138].

In [139], the Zeheb-Wallach method was applied to prove absolute stability of a trilateral system. The presented extension of the Zeheb-Wallach criterion allows also for poles on the imaginary axis. Note that this absolute stability approach avoids the symmetrization condition of the Llewellyn criterion.

2.3.4 Lyapunov's Direct Method

In the following, Lyapunov's direct method also known as Lyapunov's second method will be briefly recapitulated [56].

Considering an ordinary differential equation $\dot{x} = f(t, x), x(t_0) = x_0$, an equilibrium state x_e can be described by

$$f(t, x_e) \equiv 0, \quad \forall \ t \geq t_0.$$

This equilibrium is said to be stable if for a maximum distance δ ($|x_0 - x_e| < \delta$) the system state x remains in a boundary ϵ around x_e ($|x(t; t_0, x_0) - x_e| < \epsilon$) for all $t \geq 0$. If $lim_{t\to\infty}|x(t; t_0, x_0) - x_e| = 0$, the equilibrium state is asymptotically stable.

To evaluate the stability, a system can be described via a positive definite Lyapunov function $V(t, x) : \mathbb{R}^+ \times \mathbb{B}(r) \mapsto \mathbb{R}$ (for some $r > 0$ and $\mathbb{B}(r) = \{x \in \mathbb{R}^n \ \mid \ |x| < r\}$) with the time derivative

$$\dot{V} = \frac{\partial V}{\partial t} + (\nabla V)^T f(t, x),$$

with the gradient ∇V of V with respect to x ($\nabla V = [\frac{\partial V}{\partial x_1}, \frac{\partial V}{\partial x_2}, ..., \frac{\partial V}{\partial x_n}]^T$).

Then $x_e = 0$ is stable if $\dot{V} \leq 0$ and x_e is uniformly asymptotically stable if V is decrescent [56] and $\dot{V} < 0$. In general, in Lyapunov analyses, free systems with zero input ($u = 0$) are investigated. This corresponds to the assumption of passive terminations in passivity-based approaches.

Several publications consider the Lyapunov criterion in multilateral approaches. The stability of the overall multilateral control structures in [168, 41] has been proven via the Lyapunov analysis. Also, for the stability proof of the higher order sliding mode controller in [148] and the adaptive fuzzy control in [91], a Lyapunov function was applied.

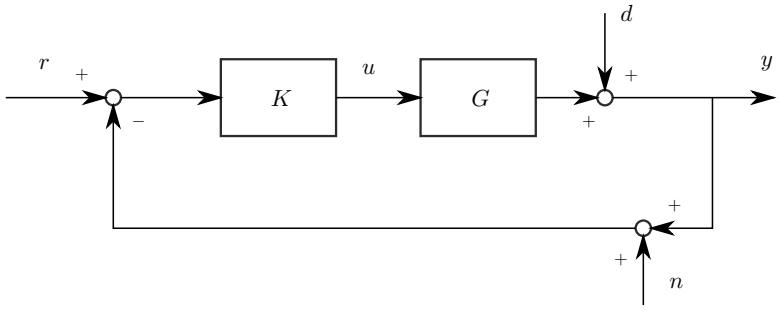

Figure 2.3.8: One Degree of Freedom Feedback Configuration [159]
The input r drives the interconnection of plant G and controller K which is influenced by the output disturbances d and the measurement noise n. The signals u serve the control of the output y.

2.3.5 $\mathcal{H}^\infty$ Control

In [186], the $\mathcal{H}^\infty$ control method for the synthesis of a controller was introduced with focus on the sensitivity minimization of a single-input-single-output (SISO) system. $\mathcal{H}^\infty$ control has been applied to bilateral teleoperation e.g. in [184, 150]. $\mathcal{H}^\infty$ describes the norm of the Hardy space $\mathcal{H}^p$, a subset of the Lebesgue ($\mathcal{L}^p$) space

$$\|f\|_{\mathcal{H}^\infty} = \sup_{|z|<1} |f(z)| \,. \tag{2.68}$$

The idea of $\mathcal{H}^\infty$ control is the consideration of known model uncertainties in an extended transfer function. The $\mathcal{H}^\infty$-Norm equals the maximal value of the amplitude frequency response of the respective transfer function.

$\mathcal{H}^\infty$ control aims at the minimization of the $\mathcal{H}^\infty$-Norms of $F_l(P, K)$ (compare Section 2.1.3.2). An alternative to $\mathcal{H}^\infty$ optimal control is the so-called mixed-sensitivity $\mathcal{H}^\infty$ control. Mixed-sensitivity approach (or robust performance problem) means that the sensitivity function S as well as a closed-loop transfer function KS and the complementary transfer function T are shaped in correspondence. In a feedback configuration (see Fig. 2.3.8, [159]), a sensitivity function $S = (I+GK)^{-1}$ and the closed-loop transfer function $T = \frac{GK}{I+GK} = I - S$ can be formulated. The standard form of the S/T mixed sensitivity approach with the weights W_i ($i \in \{1, 2\}$) for uncertainties and error dynamics is depicted in Fig. 2.3.9. The S/T mixed sensitivity minimization problem allows the shaping of T to achieve the desired tracking performance. A stabilizing controller minimizing

$$\left\| \begin{bmatrix} W_1 S \\ W_2 T \end{bmatrix} \right\|_\infty \tag{2.69}$$

needs to be found therefore. W_i produce the error signals z_i.

The $\mathcal{H}^\infty$ control approach with S/T Mixed Sensitivity Optimization in standard form has been applied to the trilateral system in [66]. A sensitivity and a complementary

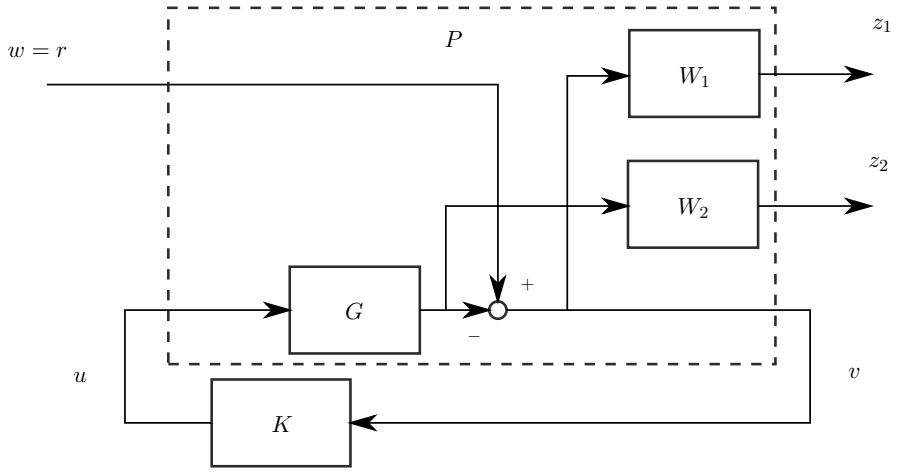

Figure 2.3.9: S/T Mixed Sensitivity Optimization in Standard Form [159]
In the mixed-sensitivity approach, the sensitivity function S as well as a closed-loop transfer function KS and the complementary transfer function T of a feedback configuration are shaped in correspondence to achieve the desired tracking performance. Uncertainties and error dynamics can be considered in the weights W_i ($i \in \{1, 2\}$).

sensitivity transfer function

$$S = \frac{1}{1 + G_s K},$$
$$T = \frac{G_s K}{1 + G_s K}$$

were considered. The transfer function G_s included the slave robot admittance and the environmental impedance model. A gain $K = K_{\mathcal{H}^\infty}$ on the slave side controller had to be found such that stability to uncertainties and tracking performance was ensured. The uncertainties in the environment and operator hand impedance and variations in a dominance factor were represented by the weight W_1. The specification of the desired sensitivity function or the slave closed-loop error dynamics were considered via the weight W_2:

$$||W_1 T||_\infty < 1, \tag{2.70}$$
$$||W_2 S||_\infty < 1. \tag{2.71}$$

2.3.6 Laplacian consensus algorithm

The information or communication graph of a robotic control system can be defined by the Laplacian matrix L

$$l_{ij} = \begin{cases} \sum_{k=1}^{\mathbb{N}} a_{ik} & i = j \\ -a_{ij} & i \neq j, \end{cases} \tag{2.72}$$

with $a_{ij} = 1$ if $j \in \mathcal{N}_i, a_{ij} = 0$ otherwise. The authors of [117] showed that in a strongly connected graph (requiring $rank(L) = n - 1$ and one zero eigenvalue of L) a consensus problem solves globally asymptotically. For this proof the spectral properties of a graph Laplacian are considered. Stability can be proven via the Geršgorin disk theorem.

Laplacian Consensus Algorithm with Consensus Filters Based on the Laplacian consensus algorithm, consensus filters can be developed that average the input signals applied to every node in a connected graph. In [172], a multilateral teleoperation control system was designed based on acceleration and force consensus filters. The acceleration consensus algorithm acting as a second order consensus filter has a PD-like structure:

$$\ddot{x}_i = \sum_{v_j \in \mathbb{N}_i} K(x_j - x_i) + \sum_{v_j \in \mathbb{N}_i} B(\dot{x}_j - \dot{x}_i) + u_i \tag{2.73}$$

$$\tag{2.74}$$

with damping B and stiffness K. The force tracking in such a system can be achieved if the input u is a function of the sum of interaction forces F_i in the system or with a force consensus filter.

In [172], experiments based on this control method with different network topologies have been examined (Fig. 2.3.10 - Fig. 2.3.12). The network topology is designed through the Laplacian matrix in equation (2.72).

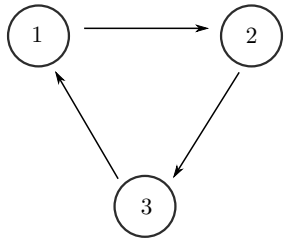

Figure 2.3.10: Ring Network

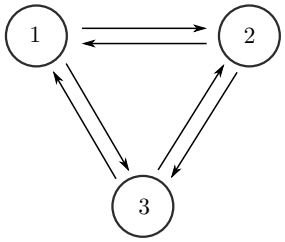

Figure 2.3.11: Connected Network

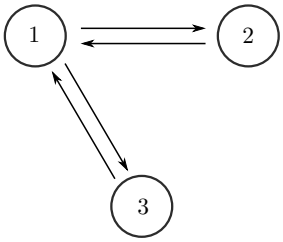

Figure 2.3.12: Hub Network

Adaptive Control with Laplacian Consensus Algorithm The authors of [112] presented an approach that allows the synchronization of agents through an adaptive controller with consideration of constant unknown time delay. The work generalizes the results gained in [22, 114] to Nonidentical Euler-Lagrange systems. The approach focuses the state synchronization of master and slave robots in free motion considering constant delay. State synchronization means:

$$\lim_{t\to\infty} \|q_m(t-T) - q_s(t)\| = \lim_{t\to\infty} \|\dot{q}_m(t-T) - \dot{q}_s(t)\| = 0$$
$$\lim_{t\to\infty} \|q_s(t-T) - q_m(t)\| = \lim_{t\to\infty} \|\dot{q}_s(t-T) - \dot{q}_m(t)\| = 0,$$

with the generalized coordinates q and the delay T. The bilateral control approach proposed in [22] has been proven to be $\mathcal{L}^2$-stable such that the robots synchronize their states. The authors also presented how this approach is related to the scattering transformation considering time delay.

In [114], it was shown that the adaptive controller for teleoperators with constant time-delays presented in [22] tends to drive to zero position when gravity forces are non-zero. Therefore, new control laws were introduced, that consider the errors e instead of q. The authors generalized in [112] the results of [114, 116] considering constant unknown time delay and to the synchronization of a multilateral network with n

agents/nonidentical Euler-Lagrange-systems. Furthermore, the approach allows a nonlinear coupling via nonlinear spring and damper systems. The approach is applicable to all connected communication graphs. I.e. there is a network node that is connected to all other nodes. In order to consider delays, the weighted Lyapunov-Krasovskii functional was applied. Two problem formulations are considered: The tracking synchronization (TSP) that yields that the position difference of agents and trajectory converges to zero ($\lim_{t\to\infty} |x_i(t) - x_d(t)| = 0$) and the consensus problem (CP) that ensures that without reference signal the agents position reaches a consensus position ($\lim_{t\to\infty} q_i(t) = q_c$). In case of time delay a term adding damping from the neighboring agents had to be considered in the controller equation.

2.3.7 Sliding Mode Control

The authors of [132] proposed a sliding-mode controller (SMC) for bilateral teleoperation with time delay that is robust to model uncertainties. SMC introduces a discontinuous control signal to alter the dynamics of a nonlinear system. In [132], this signal controls the slave robot along a sliding surface s_d

$$s_d(t) = \dot{x}_s(t) - K_p \dot{x}_m(t-T) + \lambda(x_s(t) - K_p x_m(t-T)) \tag{2.75}$$

with delay T, constant gain K_p and the strictly positive constant λ, designed to achieve the system's desired behavior. The control input at the slave contains a term $M_s\lambda(\dot{x}_s(t) - K_p\dot{x}_m(t-T_1))$ for the tracking of the sliding surface and a saturation term $K_{gain} sat(\frac{s_d}{\Phi})$ that compensates the time delay effect. K_{gain} is a nonlinear gain, $sat()$ is a saturation function and Φ reduces the chattering of the control input as a boundary layer thickness.

In the multilateral teleoperation setup of [148], a higher order sliding mode with the sliding surface $\mathbf{I}_e \in \mathbb{R}^n$ is utilized:

$$I_e = \bar{M}_s \ddot{\tilde{x}}_s + \bar{B}_s \dot{\tilde{x}}_s + \bar{K}_s \tilde{x}_s + F_e = 0 \tag{2.76}$$

with the desired inertia $\bar{M}$, damping $\bar{B}$ and stiffness $\bar{K}$ for each master robot and the environmental interaction force F_e. Via the definition of an extended error variable $\Omega(\mathbf{I}_e) \in \mathbb{R}^n$

$$\Omega = \int_0^t I_e(\tau) d\tau + K_i \int_0^t \int_0^\sigma sign(I_e(\tau)) d\tau d\sigma \tag{2.77}$$

with diagonal positive definite matrix $K_i \in \mathbb{R}^{n\times n}$ and the Lyapunov function $V = \frac{1}{2} I_e^T I_e$ the sliding condition was found. Note that in [148] the effect of time delay was not compensated by the sliding mode control.

2.3.8 Adaptive Fuzzy Control

Adaptive fuzzy control as a less common approach for teleoperation has been applied in [91] to a multilateral system. In fuzzy logic, fuzzy sets (also membership functions) are introduced that are a collection of related items which belong to the set to a certain degree. With the help of fuzzy sets and crisp boundaries, fuzzy rules can be declared that represent intuitively an expert's knowledge on the respective system behavior. In [91],

the robot parameters $(\mathbf{M}, \mathbf{C}, \mathbf{G}, \mathbf{D})$ are separated into a nominal part $(\mathbf{M}^0, \mathbf{C}^0, \mathbf{G}^0, \mathbf{D}^0)$ and uncertain parts $(\Delta\mathbf{M}, \Delta\mathbf{C}, \Delta\mathbf{G}, \Delta\mathbf{D})$ such that e.g.

$$\mathbf{M} = \mathbf{M}_0 + \Delta\mathbf{M}. \tag{2.78}$$

Then, model-based control was applied for the nominal system (X_1 subsystem) and another adaptive fuzzy control considered the uncertainties in the system (X_2 subsystem). The subsystems were transduced into the framework of a Markovian jump system in order to describe the delay by a stochastic model. Stochastic exponential mean square stability of X_2 subsystem has been proven with the help of the Lyapunov-Krasovskii functional and the application of a Markovian infinitesimal operator. Based on the proof in [92] the robust asymptotic stability of the X_1 subsystem was shown.

2.3.8.1 Transparency

The quality of transparency, i.e. the grade of immersion into the environment, that an operator perceives in a multilateral system is hard to evaluate since the master device displays not only information on one slave robot acting in its environment but also the interaction of one or more additional agents. The authors of [63, 67] proposed new methods to analyze the transparency in trilateral systems. With the metrics transmitted impedance and Z_{width} value, the impedance displayed to one operator and the bandwidth of achievable impedances can be evaluated. In addition, a bilateral distance transfer function was used to contrast the multilateral with the bilateral transmitted impedance. The transperancy optimized distance transfer function was proposed as a benchmark to compare different communication architectures.

2.4 Taxonomy of Multilateral Control Approaches

In literature, several stability approaches that have been introduced in the previous section have been applied to multilateral systems. Within the following taxonomy overview, different categories are identified that allow the classification of the approaches. Note that work that was developed in the course of this thesis has been included in the following overview in order to present a thorough literature review. For the sake of reading convenience and time-saving analysis, the survey is presented in a condensed form of tables. The references are ordered in the subcategories with respect to the publication date. The analysis of the taxonomy with respect to limitations and advantages of the different approaches is performed in the subsequent chapter.

The categorization with respect to different multilateral control structures and network typologies serves the rating of modularity and adaptability. Later on, the stability approaches are categorized concerning the implemented communication architecture and the necessity of system modeling.

In the following, the subindices of the literature references mark which stability criterion is applied in the respective paper. The meaning of the subindices can be looked up in Table 2.2. Furthermore, the literature considering time delay is marked with the indices $\mathfrak{T}, \mathfrak{W}, \mathfrak{B}, \mathfrak{R}, \mathfrak{L}, \mathfrak{H}$ and $\mathfrak{A}$, as noted in Table 2.3.

Table 2.2: Notification of Stability Approaches

Passivity	MPMT	A1
	Raisbeck	A2
	IPC	A3
	Passive Decomposition	A4
Absolute Stability	Llewellyn	B1
	Zeheb-Walach	B2
Lyapunov		C
$\mathcal{L}^p$ **Stability**	general	D1
	Consensus Algorithm	D2
$\mathcal{H}^\infty$ **Stability**		E

Table 2.3: Notification of Communication Delay Control Approaches

Time Domain Passivity Approach	$\mathfrak{T}$
Wave Variables	$\mathfrak{W}$
Wave-Based Time Domain Passivity Approach	$\mathfrak{B}$
Raisbeck	$\mathfrak{R}$
Lyapunov & $\mathcal{L}^p$ **stability**	$\mathfrak{L}$
$\mathcal{H}^\infty$	$\mathfrak{H}$
Adaptive Fuzzy Control	$\mathfrak{A}$

2.4.1 Application and Control Structures

The first set of categories summarizes which applications have been implemented in literature and in which setup they have been validated in the respective publication. Table 2.4 presents which applications have been evaluated by the respective authors with simulations or experiments. Furthermore, the number of degrees of freedom of the slave that was used in the particular experiments can be analyzed. Depending on the application, the master DoFs may differ from the slave DoFs. Still, to reduce complexity only the maneuverability of the slave is regarded as the best indicator for the level of complexity. The index $\natural$ denotes that the validation has been simulative.

The shared interaction as well as the term haptic augmentation refers to Dual-Master-Single-Slave setups. Shared interaction refers to training applications or asymmetric setups with different numbers of master and slave DoFs. The training scenario incorporates two human operators sharing the authority on one slave robot whereas haptic augmentation approaches often involve only one operator. In the latter setup an additional haptic channel can be provided to the operator via the second master device. For example, an additional interaction point other then the slave's TCP or the Nullspace of the slave robot can be controlled. In the Single-Master-Dual-Slave setups for coordinated motion, two slaves can be parallely controlled by one master device. The slaves can be moved synchronously or with a fix kinematic coupling such that a cooperatively grasped object can be manipulated. Thus, higher accuracy can be achieved in tasks that require a constant distance of the slave robots compared to the standard approach employing two separate teleoperators. Another application of multilateral teleoperation allows the

coupling of several operators in a virtual environment. This setup can be applied for operator training or even tele-rehabilitation.

Table 2.4: Application and Task Space DoFs

	1DoF	2DoF	3DoF	6DoF
Shared Interaction	[60],[63]$^{\natural}$,[64]$^{\natural}$, [122]$^{\mathfrak{T}}_{A1}$, [121]$^{\mathfrak{T}}_{A1}$, [86]$^{\natural}_{A2}$, [139]$^{\natural}_{B2}$, [105]$_{A2}$, [87]$_{B1}$, [89]$_{A2,B1}$, [32]$_{A3}$	[111]$^{\mathfrak{H}}_{E}$, [61], [41]$^{\mathfrak{L}}_{C}$, [88]$_{B1}$	[67], [68]$_{B1}$ [58]$^{\mathfrak{W}}$, [136]$^{\mathfrak{T}}$, [148]$^{\mathfrak{R}}$, [154] [167]$^{\mathfrak{B}}$	[35]
Haptic Augmentation			[97]$_{D1}$, [98]$_{D1}$, [99]$_{D1}$, [100]$_{D1}$	[127]$^{\mathfrak{T}}_{A1}$
Coordinated Motion	[178]$^{\natural}$		[69], [82]$^{\mathfrak{W}\natural}_{A4}$, [55], [96]$_{D1}$, [107]$^{\mathfrak{L}\natural}_{D1}$, [168]$^{\mathfrak{W}}_{C}$	[72]
Virtual Env. Interaction	[85]$^{\natural}_{A2}$			

Table 2.5: Multi-Robot Configuration

1:N	Kinematically Coupled Slaves	[72], [69], [82]$^{\mathfrak{W}}_{A4}$, [55], [96]$_{D1}$, [107]$^{\mathfrak{L}}_{D1}$
	Synchronous Slaves	[178],[168]$^{\mathfrak{W}}_{C}$
N:1	Asymmetric Systems	[61],[99]$_{D1}$,[101]$_{D1}$,[91]$^{\mathfrak{A}}_{C}$, [79]$^{\mathfrak{T}}$
	Additional Interaction Point	[97]$_{D1}$,[99]$_{D1}$, [100]$_{D1}$,[101]$_{D1}$,[127]$^{\mathfrak{T}}_{A1}$
	Projective Force Mappings	[98]$_{D1}$
	Dual Operator / Authority Sharing	[111]$^{\mathfrak{H}}_{E}$,[60],[63],[64],[66]$_{E}$,[67], [35],[153]$^{\mathfrak{R}}$,[178],[68]$_{B1}$,[122]$^{\mathfrak{T}}_{A1}$, [41]$^{\mathfrak{L}}_{C}$, [86]$_{A2,B1}$,[139]$_{B2}$,[170]$_{B1}$,[87]$_{B1}$,[89]$_{A2,B1}$,[32]$_{A3}$, [148]$^{\mathfrak{R}}_{C}$,[154],[124]$^{\mathfrak{T}}_{A1}$
	Virtual Env. Interaction	[85]$_{A2,B1}$
M:N	Theory	[172]$_{D2}$,[173]$_{D2}$,[174]$_{D2}$,[104]$_{A2,B1}$,[78]$^{\mathfrak{W}}_{D2}$, [58]$^{\mathfrak{W}}$, [136]$^{\mathfrak{T}}$, [105]$_{A2}$,[88]$_{B1}$
	Experimental Validation	[112]$^{\mathfrak{L}}_{D2}$, [167]$^{\mathfrak{B}}$
	Application	[121]$^{\mathfrak{T}}_{A1}$

Table 2.5 presents which multi-robot configurations are required for different applications. In contrast to Table 2.4, also publications without clear applications are considered. Therefore, the applications are split up in further subcategories. Single-Master-Multi-Slave setups are referred to as 1:N systems. One master device and thus only one operator is needed for the parallel control of n synchronously moving slaves or the control of kinematically coupled slave robots. The term N:1 system refers to Multi-Master-Single-Slave systems. Clearly, multi-operator scenarios as haptic training concepts or the virtual environment interaction of several operators belong to this subcategory. Other approaches in this category as the haptic augmentation approaches are 2:1 systems that involve only one operator with two master devices. In addition, there are 2:1 asymmetric systems that map the DoFs of two master devices to different

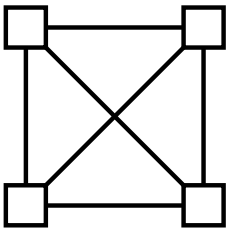

Figure 2.4.1: Fully Connected Topology

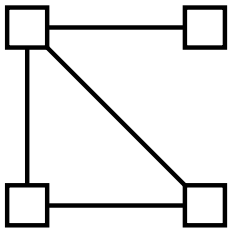

Figure 2.4.2: Arbitrary M:N Topology

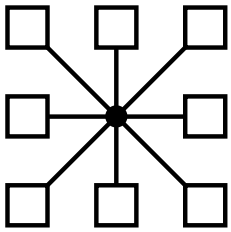

Figure 2.4.3: Star Topology

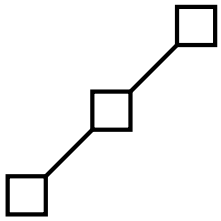

Figure 2.4.4: Line Topology

slave DoFs. Multi-Master-Multi-Slave setups as the most general multilateral setup are declared as M:N systems. Only one publication on M:N systems presents an application. The remaining literature is divided into pure theoretic work and publications with approaches validated in experiments.

The literature also differs with respect to the implemented network topology as visualized in Table 2.6. Each device is coupled electronically to each other device in a fully connected setup (see Fig. 2.4.1). The node in a star network does not represent a device but an interface that each device in the network is connected to (compare Fig. 2.4.3). A line network mostly consists of three devices (also pseudo-trilateral setup). As can be seen in Fig. 2.4.4, in such a pseudo-trilateral setup only the device in the center is coupled to the other two devices. Note that fully connected systems are the most general systems. Still, reasonable M:N applications might require networks in which some tracks are canceled (compare arbitrary topology in Fig. 2.4.2).

Table 2.6: Network Topology

Star	[69], $[82]^{\mathfrak{W}}_{A4}$, [55],$[112]^{\mathfrak{L}}_{D2}$,$[100]_{D1}$, $[58]^{\mathfrak{W}}$, $[85]_{A2,B1}$, $[168]^{\mathfrak{W}}_{C}$,$[107]^{\mathfrak{L}}_{D1}$
Fully Connected	$[111]^{\mathfrak{H}}_{E}$, [60], [61], [63], [64], $[172]_{D2}$,$[173]_{D2}$, $[66]_{E}$,$[174]_{D2}$, [67],[35], [178],$[153]^{\mathfrak{R}}$, $[104]_{A2,B1}$, $[78]^{\mathfrak{W}}$,$[68]_{B1}$, $[122]^{\mathfrak{T}}_{A1}$,$[41]^{\mathfrak{L}}_{C}$, $[86]_{A2,B1}$, $[136]^{\mathfrak{T}}$, $[170]_{B1}$, $[105]_{A2}$, $[139]_{B2}$, $[87]_{B1}$, $[88]_{B1}$, $[89]_{A2,B1}$, $[167]^{\mathfrak{B}}$, $[32]_{A3}$, $[148]^{\mathfrak{R}}_{C}$, $[127]^{\mathfrak{T}}_{A1}$, [154], $[124]^{\mathfrak{T}}_{A1}$
Line	[72], $[172]_{D2}$,$[79]^{\mathfrak{T}}$
Arbitrary	$[121]^{\mathfrak{T}}_{A1}$

2.4.2 Control Theory

Table 2.7 opposes the stability approach to the respective required modeling of the hardware, operator and environment (human operator H, master M, slave S, environment E). On the one hand approaches that consider models promise to be less conservative since for example the device damping is considered. On the other hand, models introduce uncertainties into the analysis and the approach is less modular since an element as a master device can not be extracted easily. The stability concepts have been introduced

in Section 2.2. Note that some literature does not provide a stability proof and that [104] is mentioned in Table 2.7 although the work lines out that one analyzed stability approach is not feasible.

Table 2.7: Stability Approach and Considered Models

		no models	M	M, S	H, M, S, E	M,S,E
Passivity	MPMT (A1)	$[122]^{\mathfrak{T}}_{A1}$, $[121]^{\mathfrak{T}}_{A1}$, $[127]^{\mathfrak{T}}_{A1}$, $[124]^{\mathfrak{T}}_{A1}$				
	Raisbeck (A2)			$[104]_{A2,B1}$,$[86]_{A2,B1}$, $[85]_{A2,B1}$,$[105]_{A2}$, $[89]_{A2,B1}$		
	IPC (A3)	$[32]_{A3}$				
	Passive Decomposition (A4)			$[82]^{\mathfrak{W}}_{A4}$		
Absolute Stability	Llewellyn (B1)			$[104]_{A2,B1}$, $[86]_{A2,B1}$, $[85]_{A2,B1}$, $[87]_{B1}$, $[88]_{B1}$, $[89]_{A2,B1}$	$[170]_{B1}$	$[68]_{B1}$
	Zeheb-Walach (B2)			$[139]_{B2}$		
Lyapunov	(C)			$[41]^{\mathfrak{L}}_{C}$, $[91]^{\mathfrak{A}}_{C}$, $[168]^{\mathfrak{W}}_{C}$, $[148]^{\mathfrak{R}}_{C}$		
$\mathcal{L}^p$ **Stability**	general (D1)			$[107]^{\mathfrak{L}}_{D1}$	$[97]_{D1}$, $[98]_{D1}$, $[100]_{D1}$, $[99]_{D1}$, $[96]_{D1}$, $[101]_{D1}$	
	Consensus Algorithm (D2)			$[172]_{D2}$, $[173]_{D2}$, $[174]_{D2}$, $[78]^{\mathfrak{W}}_{D2}$, $[112]^{\mathfrak{L}}_{D2}$		
$\mathcal{H}^{\infty}$ **Stability**	(E)		$[111]^{\mathfrak{H}}_{E}$		$[66]_{E}$	

Table 2.8: Stability Approach and Coupling Signals

		1Ch	2Ch	2Ch	2Ch	4Ch
		P^m	P^m,F^s_{comp}	P^m, P^s	P^m,F^s_{meas}	P^m,P^s,F^m_{meas}, ,F^s_{meas}
Passivity	MPMT (A1)		$[122]^{\mathfrak{T}}_{A1}$	$[121]^{\mathfrak{T}}_{A1}$, $[127]^{\mathfrak{T}}_{A1}$	$[124]^{\mathfrak{T}}_{A1}$	
	Raisbeck (A2)		$[105]_{A2}$	$[86]_{A2,B1}$, $[89]_{A2,B1}$	$[85]_{A2,B1}$	$[104]_{A2,B1}$
	IPC (A3)		$[32]_{A3}$			
	Passive Decomposition (A4)		$[82]^{\mathfrak{W}}_{A4}$			
Absolute	Llewellyn (B1)		$[170]_{B1}$	$[86]_{A2,B1}$, $[87]_{B1}$, $[88]_{B1}$, $[89]_{A2,B1}$	$[85]_{A2,B1}$	$[104]_{A2,B1}$, $[68]_{B1}$
Stability	Zeheb-Walach (B2)				$[139]_{B2}$	
Lyapunov	(C)		$[41]^{\mathfrak{L}}_{C}$, $[168]^{\mathfrak{W}}_{C}$		$[148]^{\mathfrak{R}}_{C}$	
$\mathcal{L}^p$ **Stability**	general (D1)			$[96]_{D1}$, $[107]^{\mathfrak{L}}_{D1}$		$[97]_{D1}$, $[98]_{D1}$, $[100]_{D1}$, $[99]_{D1}$, $[101]_{D1}$
	Consensus Algorithm (D2)		$[78]^{\mathfrak{W}}_{D2}$, $[112]^{\mathfrak{L}}_{D2}$			$[172]_{D2}$, $[173]_{D2}$, $[174]_{D2}$
$\mathcal{H}^\infty$ **Stability**	(E)	$[111]^{\mathfrak{H}}_{E}$		$[66]_{E}$		
None			[64], [55], $[153]^{\mathfrak{R}}$, $[58]^{\mathfrak{W}}$, $[136]^{\mathfrak{T}}$, [154]		[35], $[79]^{\mathfrak{T}}$	[60], [61], [63], [67], [178], $[167]^{\mathfrak{B}}$

The signals exchanged between two devices to realize the coupling are highly relevant as different qualities of transparency can be achieved and some applications require specific communication architectures. Table 2.8 presents the coupling signals implemented in combination with the respective stability approaches. The table is ordered with the increase of transparency achievable with the particular coupling signals. The publications without stability proof can be found in row declared with None. Note that there are cases for which the different devices are coupled with a different set of coupling signals. For those publications the coupling signals with highest achievable transparency are considered. In a 1-*Channel* ($1Ch$) architecture a position signal P^m is sent from master to slave whereas the human operator receives no force feedback but only visual information [111]. Es mentioned before, the 2-*Channel* setup ($2Ch$) can be realized by a position force architecture with computed (P^m,F^s_{comp}) or measured force feedback (P^m,F^s_{meas}) or alternatively by a position-position architecture (PP,P^m,P^s). The 3-*Channel* architecture mostly involves two force feedback signals ($3Ch$, P^m,F^s_{meas},F^s_{comp}). Still, in [171] it has been shown that the highest degree of transparency, theoretically even full transparency can be achieved with a 4-*Channel* setup ($4Ch$, P^m,P^s,F^m_{meas},F^s_{meas}).

2.4.3 Time Delay

The multilateral concept has to be applicable in scenarios involving time delay in the communication channel as for example in a space robotic setup. The various approaches guaranteeing stability despite time delay are listed in Table 2.9. If the multilateral system is designed based on the network representation and therefore relying on the passivity of the network subsystems, the communication channel with time delay can be modeled as a 2-port network. This network subsystem can be designed in a passive manner with the help of the TDPA or the wave variables approach. The authors of [153, 148] propose to consider time delay in a Raisbeck passivity analysis but do not provide an exemplary analysis. Based on the findings in [113], a combination of Lyapunov and $\mathcal{L}^p$ stability analysis can handle the effect of time delay. Furthermore, the time delay has been considered as an uncertainty in the $1Ch$ $\mathcal{H}^{\text{inf}}$ control framework of [111]. In the adaptive fuzzy logic control of [91], unsymmetrical delays have been assumed that have been modeled as a stochastic model governed by the Markov process

Table 2.9: Communication Delay Control Approach

Time Domain Passivity Approach	$[122]^{\mathfrak{T}}_{A1}$,$[79]^{\mathfrak{T}}$,$[136]^{\mathfrak{T}}$,$[121]^{\mathfrak{T}}_{A1}$,$[127]^{\mathfrak{T}}_{A1}$,$[124]^{\mathfrak{T}}_{A1}$
Wave Variables	$[82]^{\mathfrak{W}}_{A4}$, $[78]^{\mathfrak{W}}_{D2}$,$[58]^{\mathfrak{W}}$,$[168]^{\mathfrak{W}}_{C}$
Wave-Based Time Domain Passivity Approach	$[167]^{\mathfrak{B}}$
Raisbeck	$[153]^{\mathfrak{R}}$,$[148]^{\mathfrak{R}}_{C}$
Lyapunov & $\mathcal{L}^p$ stability	$[112]^{\mathfrak{L}}_{D2}$, $[41]^{\mathfrak{L}}_{C}$, $[107]^{\mathfrak{L}}_{D1}$
$\mathcal{H}^{\text{inf}}$	$[111]^{\mathfrak{H}}_{E}$
Adaptive Fuzzy Control	$[91]^{\mathfrak{A}}_{C}$

2.5 Conclusions from Background

Several stability approaches developed for bilateral teleoperation have been applied to multilateral control. Still, only few concepts have been presented for applications with

an arbitrary number of agents. The majority is focused on trilateral applications. The literature has been classified considering categories related to the stability analysis and the control framework. To find a control framework which is adequate for a large set of multilateral applications, as a next step, the requirements for these multilateral applications need to be identified. With respect to this, the capabilities of the approaches presented in literature have to be evaluated.

Chapter 3

The MPMT: A Methodology for Passivity-Based Multilateral Teleoperation

The main challenge in the control of multi-robot setups is the generalization of the stability proof independent of the number of robotic agents involved. Particularly in the presence of time delay in the communication channel, passivity control methods are widely used in bilateral as well as multilateral systems. As discussed before, the passivity principle can be applied in a highly modular manner. With the help of frameworks as the network representation, the passivity of the subsystems can be analyzed separately which renders a frequency-based analysis of the overall system unnecessary. The aim of this chapter is the establishment of a modular methodology that provides various modules applicable to a large set of multilateral scenarios. In the optimal case an additional robot can be added to the control structure without requiring a further extensive proof of stability. As a next step, the requirements on a generic system design and control framework will be formulated based on the results of the preceding literature review. Later, the main modules of the chosen framework are introduced and different types of multilateral couplings are tested experimentally.

3.1 A Suitable Control Approach

Based on the requirements drawn from aforementioned applications and the literature review of Section 2.4, the adaptability of different control approaches to different multilateral teleoperation applications will be analyzed in the following.

3.1.1 Objectives

Several scenarios of multilateral teleoperation have been described in the introduction and in the literature review section of this thesis. Considering these scenarios and the related functionalities, requirements on the control approach and the multilateral framework can be established.

The main requirements are:

I The stability approach has to be generic in that it is independent on the number and type of connected agents.

II The implementation and stability analysis of new applications should be straightforward.

III Communication architectures as PF_{meas}, 3-*Channel* and 4-*Channel* have to be feasible.

In a medical ultrasonics scenario, a haptic augmentation approach can be realized such that the human operator can precisely control one slave robot through two input devices. In order to train a novice operator, two more master devices need to be coupled into the system. If the control approach fulfills requirement I and requirement II, the required adaption of the control framework does not require high efforts. Therefore, a high modularity of the control concept is desired. Furthermore, if one device is removed from the setup, the reduced overall system damping changes. If the stability approach depends on the dynamic device properties as mass and damping, the stability proof holds only for a specific application.

For the sake of transparency, the impedance displayed at master and slave device should be as close to the real impedance of environment and human operator respectively. Therefore, it should be possible to integrate measured force feedback into the control loop.

The various types of multi-robot configuration (1:N,N:1,M:N), the applied hardware and the network topology lead to the following requirements:

IV Fully connected, multilateral M:N networks as well as e.g. star or pseudo-trilateral line networks should be feasible.

V It should be possible to weight or deactivate interconnections between agents.

VI Systems involving master and slave devices with different numbers of actuated or passive degrees of freedom have to be feasible.

Typical scenarios proposed in literature are the shared interaction of two operators or the coordinated control of kinematically coupled telemanipulators that are in general implemented as fully connected topologies. The interaction in virtual environments in contrast, can be designed with a star topology. If requirement IV is fulfilled, these applications can be realized through one common control principle or stability approach respectively. Especially for the sake of optimal position following, fully connected systems are preferred since a high coupling stiffness can be achieved.

For the implementation of a role distribution in a simple training scenario, the interconnection between the agents needs to be adaptive. With requirement V, a setup

can be designed in a fully connected topology, but later altered to vary the authority of specific agents within the setup. Thus, the system allows actors to intervene at different interaction levels via an authority or task allocation.

Simple applications can be realized with low-cost devices which are often underactuated. Thus, e.g. the rotational degrees of freedom might be passive and not provide torque feedback. Requirements V and VI are strongly connected since a passive DoF can be considered as an interconnection with deactivated feedback.

The functionalities drawn from the aforementioned multilateral scenarios lead to further requirements on the control approach:

VII The stability concept should consider a communication channel affected by time delay.

VIII The approach should be applicable to real and simulated slave robots.

IX Workspace scaling and indexing methods should be feasible.

X Virtual grasping points in the telemanipulator's environment should be practicable.

As analyzed before, the agents may be geographically distributed. Multilateral networks that are established through an internet or wireless link, may become unstable due to the effect of time delay. This issue is taken into account by requirement VII.

Especially in case of time delay, the feedback from the telemanipulator is not optimal. Still, the perception of the environment can be improved via model mediated teleoperation. Requirement VIII guarantees e.g. that in a multilateral system, the operator can receive merged force feedback from a local model and delayed feedback from the telemanipulator. Of course, real-time capabilities of the simulated models are premised.

In case of invasive telesurgery and of telemanipulation in industrial settings as atomic power plants, the feasibility of micro- or macroscale teleoperation respectively is mandatory. Since the manipulability or the workspace of the master device is insufficient for such applications, a workspace scaling or the indexing method is needed as indicated by requirement IX.

In order to implement haptic augmentation e.g. additional virtual interaction points in the slave environment need to be feasible (compare requirement X). This can be realized by spatial springs located apart from the devices' tool center points (TCP).

3.1.2 Analysis

In this section, the literature categorized in Section 2.4 will be discussed with respect to a set of the identified requirements. Note that the presented classification is limited to the available literature and does not refer to the respective stability condition in general. An unlimited insight into the stability methods would be required to extend the evaluation of the respective capabilities.

3.1.2.1 Consideration of Models

As mentioned above, the modeling of devices, environment and operator brings benefits as less conservatism but also limitations. Especially, approaches considering modeled

environments are exposed to high uncertainties and tendentially conservative as a thorough stability analysis requires the consideration of very stiff environments. Since the robots can in general be modeled as mass damper systems they are intrinsically passive. On one side, this simplifies a passivity proof of the overall system as the devices and even the terminations don't need to be considered in the stability proof. On the other side, control parameters with higher system performance can be achieved in the stability proof if the modeled, intrinsic hardware damping is considered. Still, a decisive factor for multilateral control is the adaptability of the control system to new scenarios that is clearly reduced if models have an influence on the choice of control parameters.

The following observations can be drawn from Table 2.7: In [121], a multilateral framework was proposed that is based on the network representation. The control parameters are purely dependent on the track design that is independent of the devices and the terminations human operator or environment. Also, the approach of [32] employing intrinsically passive springs, is based on a passive framework comparable to [121]. In contrast to these concepts, the Raisbeck and absolute stability criterion rely on the design of an impedance matrix $Z \in R^{nxn}$ with $n > 2$ presenting a non-modular approach. Depending on the chosen coupling signals the master and slave models need to be considered. In the open-loop control system of [111], only the master model is required.

Especially, stability concepts involving the terminations environment or human operator are difficult to adapt to other applications compared to concepts relying on the assumption of passive terminations.

3.1.2.2 Control Structures

As can be evaluated from Table 2.4 and Table 2.8, some scenarios have been solved with differing stability criteria. Although deep insight into the stability proofs is required for a thorough analysis, some limitations and advantages of particular approaches can be observed.

Coupling Signals Transparency is of extraordinary importance in bilateral as well as multilateral control. Though few effort has been put into the complex analytical transparency analysis in multilateral systems, the considered coupling signals allow a statement on the attainable grade of transparency.

So far, only 2-*Channel* architectures with computed and measured force feedback [124] but no 3-*Channel* or 4-*Channel* architecture have been presented for modular passivity-based concepts as the MPMT for multilateral systems. No 3-*Channel*, but a 4-*Channel* architecture [68] has been presented for the Llewellyn criterion in multilateral control. Although the authors of [104] analyzed the 4-*Channel* architecture under consideration of the Llewellyn and Raisbeck criteria, no guaranteed stable solution could be provided. In [68], a trilateral system with 4-*Channel* architecture was reduced to a 2-port and has been analyzed via the Llewellyn criterion. Still, the simplification renders the approach unsuitable to arbitrary setups. The authors of [139] showed absolute stability of a multilateral structure with 3-*Channel* architecture via the Zeheb-Wallach criterion. The literature on $\mathcal{H}^\infty$ control is limited to 1-*Channel* and 2-*Channel* approaches. For the 4-*Channel* architecture several stability concepts have been proposed that are not based on the analysis in the network representation or the impedance matrix

respectively. Note that some approaches consider disturbance observers instead of force sensors and that some literature (row 'None' in Table 2.8) provides no stability proofs.

System Asymmetry The possibility to scale the force feedback is of high importance for the authority sharing or the task allocation functionality.

This scaling results in an asymmetric system design for which the Raisbeck and Llewellyn criterion is limited because the stability requirements can only be fulfilled for equal authority of the operators. In [85], the symmetrization condition $Z_{13}Z_{21}Z_{32} = Z_{12}Z_{23}Z_{31}$ was formulated that can only be fulfilled if the authority factor $\alpha = 1/2$. In [139], the Zeheb-Wallach criterion was used to analyze absolute stability. In contrast to the literature applying the Llewellyn criterion, asymmetric systems with different authority scaling for the two operators could be achieved with the Zeheb-Wallach criterion. Furthermore, it was shown that the absolute stability region is maximal for symmetric systems ($\alpha = 0.5$) and decreases with increasing asymmetry. Also in the work applying $\mathcal{H}^\infty$ control and the MPMT approach, a scaling could be realized. Several other publications on authority scaling (compare Table 2.5) enable the scaling of the feedback signals for the sake of role distribution to the operators.

Network Structure Due to an easy adaption to new scenarios and multi-robot configurations an arbitrary network topology is favored. If the respective control approach allows the cancellation of particular interconnections, a fully connected topology can be transformed into arbitrary structures. The cancellation of particular interconnections can be achieved with stability criteria that enable a scaling of feedback signals. Via arbitrary concepts, any other topology can be achieved [121]. In trilateral line topologies the coupling of the involved devices is potentially loosened compared to the fully connected topology. In star topologies the interactions between two agents can not easily be further specified. This is sufficient for some scenarios but renders the topology inadequate for training or haptic augmentation approaches like the task allocation functionality. The adaptive control approach with Laplacian consensus algorithm of [112] is only applicable to communication graphs with star topology.

3.1.2.3 Time Delay

Several scenarios for multilateral teleoperation are meaningful in space or other sites of application as oil platforms that require a remotely controlling human operator. Therefore, the consideration of time delay is of high relevance. Still, time delay has been taken into account only in the minority of the literature (compare Table 2.9).

In [111], the time delay was considered in combination with $\mathcal{H}^\infty$ control though no force feedback to the master has been implemented. An exponential delay function of the Laplace domain was integrated in the impedance matrix in [148] but no stability analysis was presented. No other literature on the Raisbeck and also the Llewellyn criterion has focused multilateral systems with time delay. A Lyapunov-Krasovskii function in a Lyapunov consensus problem analysis was applied in [112] and [41] to consider time delay. The authors of [91] successfully handled the effect of time delay in an adaptive fuzzy control framework via the description of the delay by a stochastic model. The Time Domain Passivity Approach as well as the wave variables concept as the most

common methods to achieve stability in delayed teleoperation have been applied to a variety of setups.

3.1.3 Discussion

In the following, the decision on the MPMT as the focal development and tool of this thesis will be motivated based on the requirements of Section 3.1.1 and the analysis of the available literature in the preceding section.

In combination with the design tool network representation, the passivity criterion (compare Section 2.2) presents a highly modular stability concept, providing the desired universality (requirement I) and modularity (requirement II). Also, several network topologies can be designed in the network representation (compare requirement IV). The universality is further enhanced (but at the cost of increased conservatism) by the device, operator and environment model independence of network representation based approaches. In contrast, the majority of the stability approaches applied in multilateral control as H_∞, $\mathcal{L}^p$ and Lyapunov-based methods consider the models of master and slave or even of human and environment. As discussed above, thus, the universality of the concepts is reduced since the adaptability to new multilateral setups is hampered.

The time delay as another crucial requirement (VII) can be easily considered by the TDPA or the wave variables method within the network representation based framework of the MPMT. These commonly used concepts promise good performance despite delay [12]. Since the modular passivity framework is compatible with these both methods that have already been applied to multi-DoF systems and within 3-*Channel* and 4-*Channel* architectures [140, 7] it represents a promising concept for various multilateral setups and scenarios (compare requirement III). In contrast, other multilateral approaches as the Llewellyn and Raisbeck criterion do not consider time delay.

As discussed in detail in Section 3.3.3, the MPMT enables open-loop systems. Furthermore, an online adaption of control parameters can easily be integrated since the energy-based analysis can be performed in the time domain. Therefore, the MPMT promises to meet the requirements V and VI.

Since the stability analysis within the MPMT is independent of slave and environment models, the requirement VIII can be fulfilled. Applying simulated agents an excessive generation of artificial energy due to discretization effects or additional delays has to be avoided.

The workspace scaling and the indexing method (compare requirement IX) are applicable to the MPMT if they are designed in a passive manner.

The MPMTs adequacy for haptic augmentation approaches (see requirement X) as a main contribution of this thesis will be discussed in Chapter 5. Also, it has to be analyzed in the course of this thesis if all coupling architectures as PF_{meas}, 3-*Channel* and 4-*Channel* can be adapted to match the MPMT framework and if the independence from hardware models leads to too high conservatism.

3.2 Multilateral Passivity Principle

In the next step, the passivity condition in multilateral systems will be repeated based on the findings of [183]. As mentioned before, the proposed framework is based on the

design in the network representation that provides energy related ports at each network subsystem. Bilateral networks contain mainly 1-port and 2-port subsystems whereas multilateral setups require at least one three-port and even n-port networks.

The authors of [183] have shown that a n-port $\mathfrak{R}$ consisting of k interconnected passive n-ports $\mathfrak{R}_1, \cdots, \mathfrak{R}_k$ is passive. The following definitions, the theorem as well as the proof originate from [183].

Definition 3.2.1. ([183], Definition 1) The quintuplet of n-port properties (U,$\mathfrak{U}$,Σ,E,R) defines a state representation S of $\mathfrak{R}$, with

1. the set of admissible values $U \subset \mathbb{R}^n$.
2. the set of admissible input waveforms $\mathfrak{U}$ mapping $\mathbb{R}^+$ to U.
3. the state space $\Sigma \subset \mathbb{R}^m$.
4. the state equation E_1 with function $f(\cdot,\cdot)$ mapping $\Sigma \times U \to \mathbb{R}^m$

$$\dot{x} = f(x,u). \tag{3.1}$$

   and the output equation E_2 with function $g(\cdot,\cdot)$ mapping $\Sigma \times U \to \mathbb{R}^n$.

$$y = g(x,u). \tag{3.2}$$

5. the pair R of port voltage readout map $V : \Sigma \times U \to \mathbb{R}^n$ and port current readout map $I : \Sigma \times U \to \mathbb{R}^n$ that relate the voltages and port currents to the input and the state.

The interconnection of $\mathfrak{R}$ is called admissible if $\mathfrak{R}$ has a state representation as defined above and if its state space Σ is the Cartesian product of the individual state spaces $\Sigma = \Sigma_1 \times \cdots \Sigma_k$.

The following definition of passivity has been considered.

Definition 3.2.2. ([183], Passivity 3) Let x be the initial state of a n-port $\mathfrak{R}$ and E_A be the maximum energy that can be extracted from $\mathfrak{R}$. Then, if $E_A(x)$ is finite for each initial state x, the n-port $\mathfrak{R}$ is passive.

The power input $p : \Sigma \times U \to \mathbb{R}$ can be observed as follows:

$$p(x,u) \triangleq \langle V(x,u), I(x,u) \rangle . \tag{3.3}$$

In [183], the following assumptions have been made for the state representation S:

1. The continuousness of the functions $f(\cdot,\cdot)$, $g(\cdot,\cdot)$, $V(\cdot,\cdot)$ and $I(\cdot,\cdot)$ is assumed.
2. There is only one solution $x(\cdot) : \mathbb{R}^+ \to \Sigma$ of the differential equation $\dot{x} = f(x,u)$ for every $x_0 \in \Sigma$ and every $u(\cdot) \in \mathfrak{U}$ with $x_0 = x(0)$.
3. The port voltage and port current of $\mathfrak{R}$ are, $v(t) = V(x(t),u(t))$ and $i(t) = I(x(t),u(t))$, if assumption 2 holds for $\{u(\cdot), x(\cdot)\}$.
4. The function $t \to p(x(t),u(t))$ is locally integrable (locally L^1), i.e. its integral is finite, for every pair $\{u(\cdot), x(\cdot)\}$.

5. All sets of admissible input waveforms $\mathfrak{U}$ have to be measurable, translation invariant and closed under concatenation.

Please refer to [183] for the definition of translation invariancy and closure under concatenation.

Lemma 3.2.3. *([183], Lemma 2) "Let $\mathfrak{R}$ with state representation S be an admissible interconnection of $\mathfrak{R}_1, \cdots, \mathfrak{R}_k$ as defined above. Let $E_{A_j} : \Sigma_j \to \mathbb{R}^+$ be the available energy for $\mathfrak{R}_j$, $1 \leq j \leq k$, and $E_A : \Sigma = \Sigma_1 \times \cdots \times \Sigma_k \to \mathbb{R}^+$ be the available energy for $\mathfrak{R}$. Then if $x = (x_1, \cdots, x_k) \in \Sigma$, we have $E_A(x) \leq E_{A_1}(x_1) + \cdots + E_{A_k}(x_k)$."*

With the help of Tellegen's theorem it is clear that the sum of the output powers of $\mathfrak{R}_1, \cdots, \mathfrak{R}_k$ equals the power output of $\mathfrak{R}$ at any instant. The theorem formulated in [183] reads

Theorem 3.2.4. *([183], Theorem 4) If $\mathfrak{R}$ has a state representation S and if $\mathfrak{R}$ is an admissible interconnection of $\mathfrak{R}_1, \cdots, \mathfrak{R}_k$, then with the passivity of $\mathfrak{R}_1, \cdots, \mathfrak{R}_k$ the passivity of $\mathfrak{R}$ can be guaranteed.*

Proof. This conclusion can be drawn straight from Lemma 3.2.3.

With this proof, the passivity and therefore the unconditional stability [37] of all robotic networks that contain only passive subsystems with admissible interconnections is guaranteed. In the following, these subsystems need to be identified such that their energetic behavior can be analyzed.

3.3 The MPMT Framework

This section introduces the multilateral framework with modules that serve as a basic library for various multilateral setups. Also, the fundamental modules will be presented and analyzed with focus on their energetic behavior.

In the first step, the signal flow diagram of a trilateral teleoperator with PF_{comp} architecture as the simplest multilateral case is presented. The implementations of time delay, scaling et cetera will be discussed in the following chapters. In the trilateral system of Fig. 3.3.1, two master devices are coupled to each other and one slave device via PI-controllers. The position of each device is sent to two controllers such that it receives two computed force feedback signals. For instance, the slave is connected via PI2 to the Master 1 and via PI3 to Master 2. The feedback forces F_{PI2} and F_{PI3} as well as the environment interaction force F_e act on the slave. The communication channels (CC) are not depicted.

The corresponding network representation can be seen in Fig. 3.3.2. The sum of feedback forces sent to the respective device in the signal flow diagram results in a series connection in the electrical domain. The dashed boxes encapsulate elements that can be summarized to modules. As depicted in Fig. 3.3.3, the network representation can be drawn more abstractly with the help of these modules. The system is split up into agent subsystems, track subsystems and power control units (PCU).

Depending on the multilateral setup, the numbers of agents and tracks change and the interface of the PCU needs to be adapted. Still, the other modules can remain

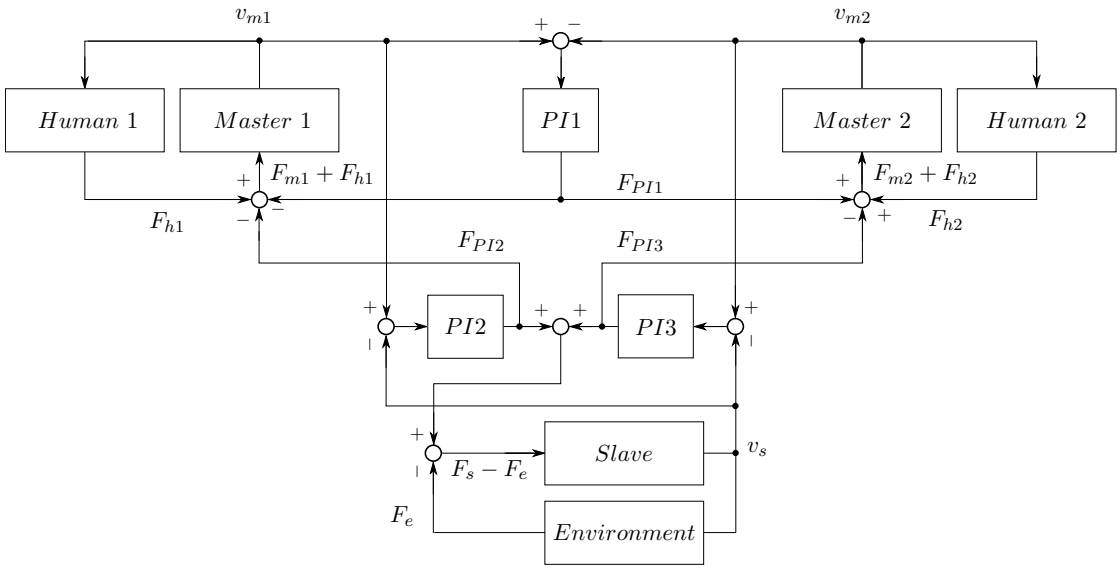

Figure 3.3.1: Signal Flow Diagram of a Trilateral PF_{comp} Architecture without Delay
In a trilateral architecture, three robotic agents can be coupled with three position controllers such that each controller assures the position tracking of two devices and each agent receives computed force feedback from each other agent.

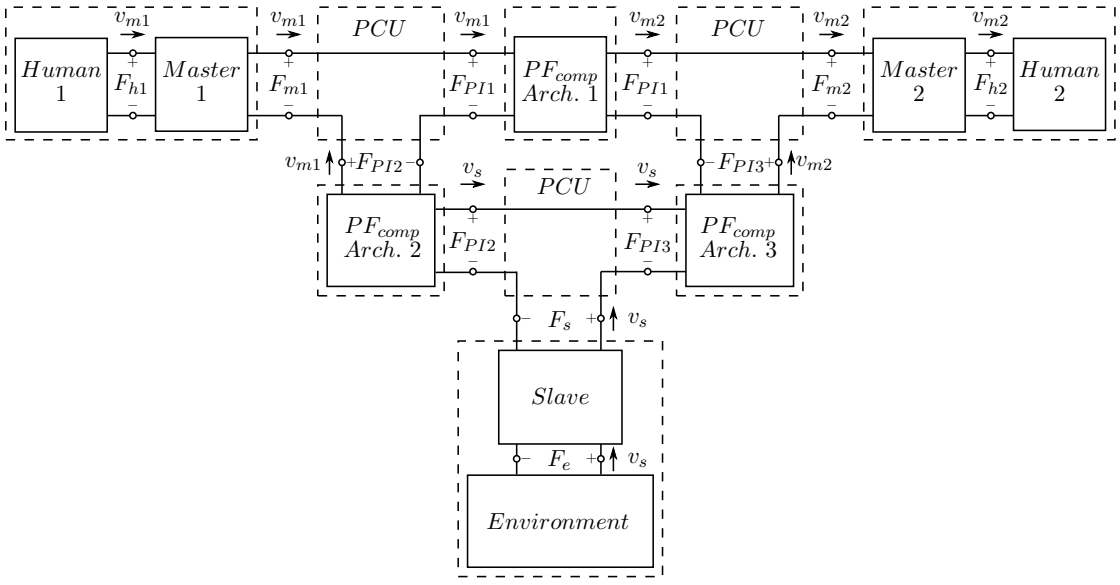

Figure 3.3.2: Network Representation of a Trilateral PF_{comp} Architecture without Delay
The sum of feedback force sent to one agent can be represented by a power control unit (PCU). These subsystems serve the power distribution between the respective agent and the tracks that it is connected to. Note that the PF_{comp} coupling has to be designed as described later in Fig. 3.3.7 to assure physically correct power ports.

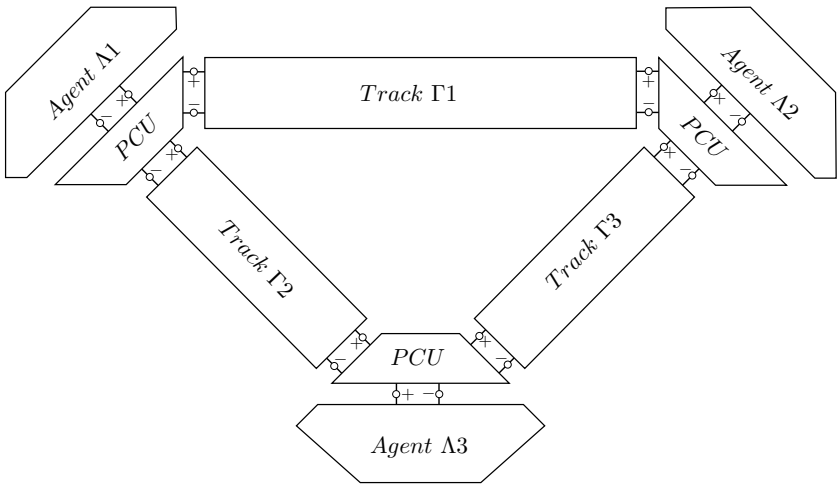

Figure 3.3.3: Generalized Modular Framework [127]
A multilateral network can be represented in a simplified modular way with the modules Agent, PCU and Track. The track contains the communication channels and the main coupling control structure.

unaltered. The tracks vary with respect to the implemented coupling signals (communication architecture) and haptic augmentation approaches. Note that not every agent is necessarily connected directly to each other via a track.

The three basic modules will be analyzed more closely in the following.

3.3.1 Power Control Unit

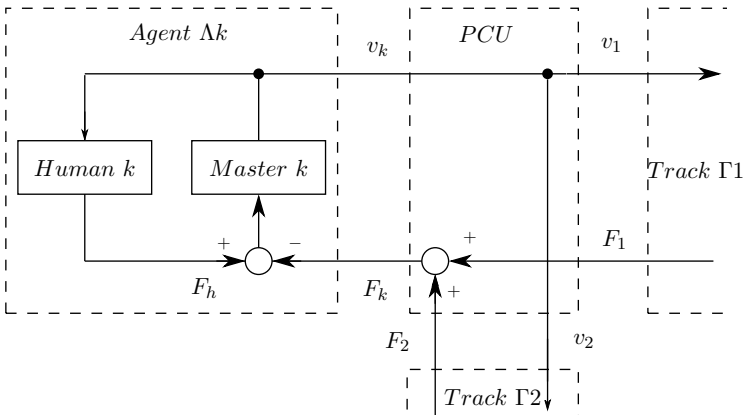

Figure 3.3.4: Signal Flow Diagram of a Power Control Unit
In the network representation, the PCU has to be designed analogous to the sum of feedback forces in the signal flow at the respective agent.

As mentioned before, the sum of feedback forces in the signal flow diagram are

represented by the power control unit in the network representation (compare Fig. 3.3.2):

$$F_{m1} = (-F_{PI1}) + (-F_{PI2}), \tag{3.4}$$
$$F_{m2} = F_{PI1} + (-F_{PI3}), \tag{3.5}$$
$$F_s = F_{PI2} + F_{PI3}. \tag{3.6}$$

The number of ports of this network module depends on the number n of tracks the respective agent is connected to. The PCU has at least two ports.

The passivity of the PCU can be proven analytically as follows. The force distribution of the PCU

$$F_k(t) = -\sum_{i=1}^{n} F_i(t) \tag{3.7}$$

gives a relationship between the force inputs F_i of the $n+1$ PCU ports. The force F_k is sent to the device k as depicted in Fig. 3.3.4. With the help of the network representation, it can be analyzed that the same velocity is flowing at each PCU port:

$$v_k(t) = v_i(t). \tag{3.8}$$

The following condition holds:

$$v_k(t)F_k(t) - \sum_{i=1}^{n} v_i(t)F_i(t) = 0$$

such that no energy is generated by the PCU:

$$P_k(t) + \sum_{i=1}^{n} F_i(t) = 0.$$

I.e., the PCU is a lossless subsystem

3.3.2 Agents

The agents are 1-port modules terminating the multilateral system. Agents can be e.g. human operators with their master device, slave robots in the environment, artificial objects in a virtual environment or artificial intelligent agents. The agents are networks with a 1-port interface connected to one power control unit. Exemplary, Fig. 3.3.5 depicts an agent subsystem with human operator and master device in a position control causality.

Since the human operators obviously introduce energy into the system, the energy exchange of the agent subsystems needs to be considered in the passivity analysis. It is a generally accepted assumption for bilateral systems that a human operator and the slave device in the environment behave passive in their interaction. That means that energy generated by the human operator is dissipated in the slave environment and vice versa. An alternative point of view to this assumption can be drawn from the observation that human operators are used to manipulate passive devices in active environments. This implies that the human operator should also be able to stabilize

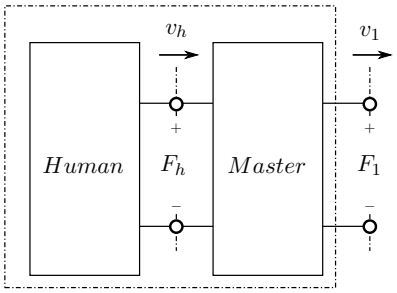

Figure 3.3.5: Master Agent for Teleoperation Setups with Position Control

a passive teleoperator as long as the visual and haptic feedback is of sufficient quality. Considering the passivity condition (2.43), the energy added/extracted by the agent modules (or human and environment subsystem more precisely) into/from the network subsystems connecting the agents is accounted by the supply rate $w(t)$. That means that the passivity condition allows that energy is added through the agent subsystems since the analyzed network itself does not generate the energy.

Several approaches rely on this assumption. Exemplary, the Raisbeck [137, 15] as well as the Llewellyn [94] criterion and the methods of passive decomposition [30] and μ-synthesis [156] require that the analyzed H-matrix has passive terminations. Strictly speaking, all control systems that rely on the passivity of its submodules as the wave variables method [5], the TDPA [144] or intrinsically passive controllers [166] rely on the assumption of passively interacting terminations (agents). Similar to this assumption, approaches applying the Lyapunov criterion assume a free system, i.e. that the input $u = 0$.

In position controlled teleoperation systems, the master and slave devices are generally considered as mass damper systems which evince a lossless or dissipative energy balance respectively. In contrast, in rate controlled teleoperation (e.g. of mobile robots) the physical interface of the master in the network representation is violated since a master position is translated into a desired velocity. I.e. though the human operator is not moving the master device, a power (resulting from desired velocity and force feedback) is sent to the slave robot. Still, the r-passivity concept of [81] guarantees the master's passivity in rate control systems. The authors applied a control variable $r_m = \dot{q}_1 + \lambda q_1$ with $\lambda \geq 0$ to a two-DoF master device controlling the velocity ($i = 1$) and the heading angle ($i = 2$) of a mobile slave robot. To preserve passivity, the master device has to be controlled locally with a spring damper system

$$\boldsymbol{M}\ddot{\boldsymbol{q}} + \begin{pmatrix} B_1\dot{q}_1 + K_1 q_1 \\ B_2\dot{q}_2 \end{pmatrix} = \begin{pmatrix} \bar{p}_1 + F_{h,1} \\ \bar{p}_2 + F_{h,2} \end{pmatrix}, \tag{3.9}$$

with damping B_i stiffness K_i, the human interaction force F_i and the slave's force feedback $\bar{p}$. The network representation of a rate control agent's (RCA) first DoF is depicted in Fig. 3.3.6. Since r_m is an artificial signal, a dependent flow source is necessary to define a physically valid port representing the user input in the slave side circuit. The source introduces energy resulting from the desired rate signals. The control loop to the master device is closed via the dependent effort source $\bar{p}$ that represents the force feedback to the master device.

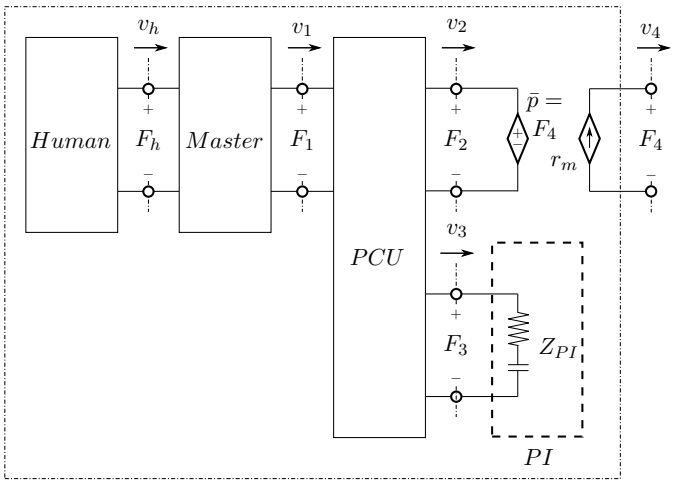

Figure 3.3.6: Master Agent Preserving Passivity in Teleoperation with Rate Control
Analogous to the r-passivity concept of [81], a master agent for rate control teleoperation requires a local PI controller to guarantee passivity. Also, additional flow and effort sources are necessary to transmit the control variable r_m with power consistent ports to the slave.

In [83], the r-passivity approach was applied to an interface of longitudinal velocity and yaw rate. If the master device can be assumed to be linear (constant mass matrix and zero coriolis and centrifugal effects), the parameters for both DoFs (i=1,2) need to be chosen according to

$$b_i \geq \lambda_i m_i \tag{3.10}$$

with $b_i, k_i \geq 0$.

In the context of the network representation and the passivity analysis, only the operational space of master and slave devices needs to be considered since the position, torque and impedance control framework of the devices can be designed in a passive manner [4]. The transformations between operational and joint space as forward kinematics as well as the velocity and force transformation in the operational space are assumed to exhibit an ideal, transparent behavior. Also, the Nullspace motion has by definition no effect on the motion and thus on the energy in the operational space independent of the numerical optimization algorithm of the Jacobian.

3.3.3 Tracks

The passivity condition is fulfilled for the PCU and the agents independent from the multilateral setup. In contrast, track networks are highly variable since they include the controller, the communication channels and software serving advanced functionalities as authority allocation or virtual grasping points.

The track of a generalized bilateral PF communication architecture is depicted in Fig. 3.3.7. The transmitted signals of the two communication channels without time delay are transmitted to slave and master respectively via dependent effort F_t and flow sources v_t [9]. The electrical circuit has been split into a left part connected to the left

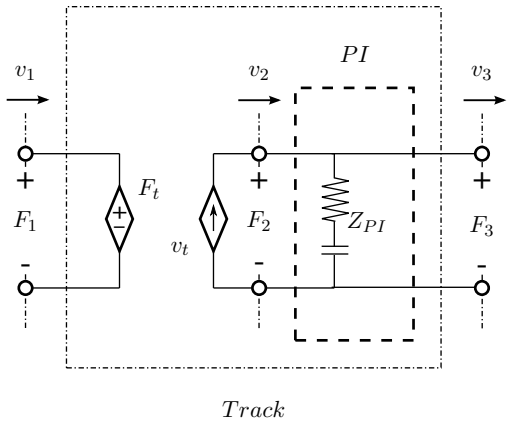

Figure 3.3.7: Network Representation of a Track with PF Architecture
A track contains the communication channel and the control structure of a bilateral link between two agents. The track is split up in two circuits with different energy flow direction The effort source F_t is general such that a measured force or a computed force can be fed back to the master side at port 1 in R2L direction. No delay is considered in the presented track. The flow source v_t generally transmits the velocity v_1 to the slave side in L2R direction.

agent via port 1 and a right part connected to the right agent via port 3. This design is necessary to introduce e.g. measured forces into the control loop with correct power-correlated ports as will be seen later (see Section 2.3.2.3). In the case of the PF_{comp} architecture the sources depend on F_2 and v_1:

$$F_t = F_2, \tag{3.11}$$

$$v_t = v_1. \tag{3.12}$$

In the left circuit, an amount of energy that is dependent on the effort source F_t flows from the right side to the left terminal (R2L). In the right circuit, the flow source v_t injects (in correspondence with the force F_2) energy in left to right (L2R) direction. It is important to note that the power flowing to the effort and flow source in the corresponding circuit is dissipated by the effort and flow sources. This is due to the fact that within this split circuit design not the power resulting from the force feedback at port 1, but the power injected into the PI controller at port 2 leads to the slave's motion. The energy that is introduced by the flow source represents the human operator command and can be accounted as a supply rate in the passivity condition therefore.

The basic track module contains only a PI controller (compare Fig. 3.3.7). The integral part has a spring like behavior as it acts on the position. The proportional part multiplied with a velocity leads to a damping. As the pair of damping and spring or resistor and capacity as the lumped electrical elements are dissipative or lossless respectively, the PI network has a passive behavior.

The PI with spring-like behavior can be regarded as an energy storage that is charged up from two sides (left and right agent). Energy plots of a PI controller are depicted in the plot Exp. 3.1. In this bilateral experiment with PF_{comp} architecture, *Agent* $\Lambda 1$ controls *Agent* $\Lambda 2$ in free motion until *Agent* $\Lambda 2$ touches a wall at about $t = 3.4s$. During free motion, *Agent* $\Lambda 1$ injects the energy ${}^{PI}E_2^{L2R}$ into the PI at port P2 on the master side which leaves the PI controller as ${}^{PI}E_3^{L2R}$ such that *Agent* $\Lambda 2$ is moved.

The nomenclature of the ports can be analyzed from Fig. 3.3.7. The storage of the PI controller is almost empty during free motion ($t = [0s, 3.4s]$). When *Agent* Λ2 touches the wall ($t = [3.4s, 5s]$), no energy can flow on the side of *Agent* Λ2 since its velocity is zero. With the penetration of *Agent* Λ1, the PI controller's energy storage E_{St} is filled up. When *Agent* Λ1 leaves out of the wall, the energy of the storage is released as ${}^{PI}E_2^{R2L}$, to press the *Agent* Λ1 out of the wall. The remaining energy E_{St} at $t = 6s$ has been dissipated by the damping part of the controller. As can be seen from the plots

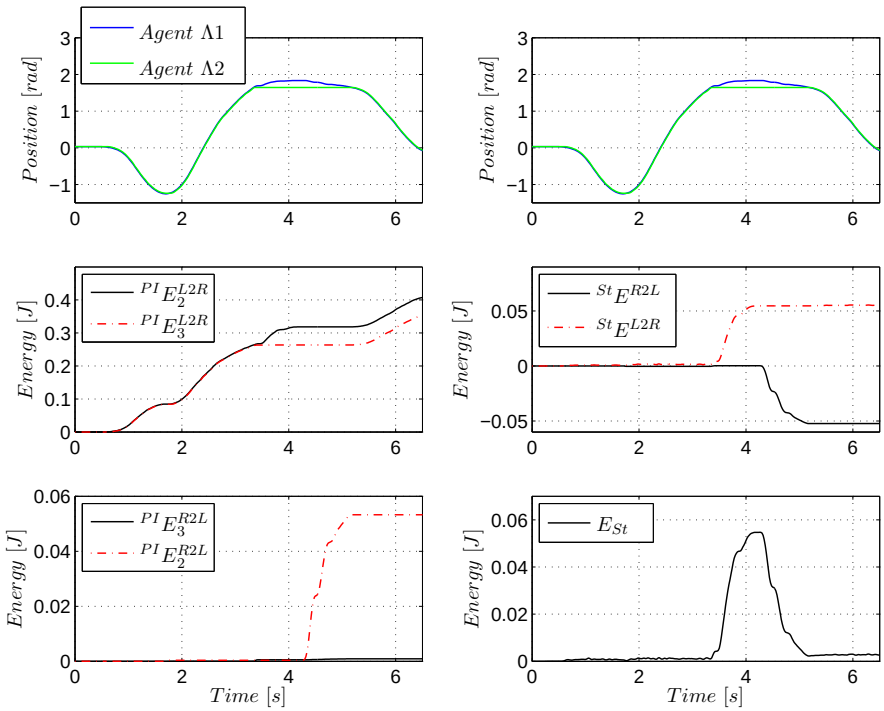

Experiment 3.1: Energy Behavior of a PI controller
Here, the position plot is presented in both columns for the sake of comprehensibility. The plot E_{St} depicts the potential energy storage of the PI controller. During the wall contact, the energy in the storage is charged up in L2R direction by ${}^{St}E^{L2R}$ and later released in R2L direction (compare ${}^{St}E^{R2L}$). With this passive spring-like behavior of the controller's I-part and the dissipating damping-like P-part of the controller, the PI controller is intrinsically passive.

${}^{St}E^{L2R}$ and ${}^{St}E^{R2L}$, it seems that energy is dissipated in L2R direction but generated in R2L direction if the energies are regarded in a direction dependent manner.

Since the PI controller is intrinsically passive, the whole track of the undelayed PF_{comp} architecture is passive. Therefore, a multilateral system with an arbitrary combination of such standard PF_{comp} tracks connecting a number n of agents is assured to be passive and thus $\mathcal{L}^2$-stable. Note that this analysis holds for continuous systems. Since the sampling in discrete systems can generate energy, the damping and the stiffness in the PI controller has to be chosen adequately to annihilate this effect and to stabilize the system.

The track representation of Fig. 3.3.7 also allows the analysis of open-loop teleoperation or zero force feedback which is fundamental for this work. In this case the effort

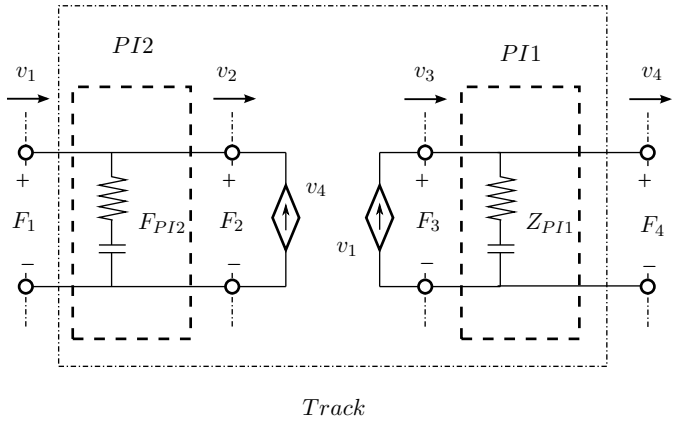

Figure 3.3.8: Network Representation of PP Architecture
In a PP architecture, each circuit of the track contains a PI controller. The velocity v_4 is transmitted via a dependent velocity source to the master side controller in R2L direction. Such as the velocity v_1 is transmitted to the slave side controller in R2L direction.

source injects no energy to the master side

$$F_t = 0. \tag{3.13}$$

This means that at port 1 zero power is measured in both directions of power flow. Still, the PI controller behavior leads to a slave motion. The energy required for this motion is injected into the right circuit by the flow source $v_t = v_1$. Applying an argumentation analogous to Section 3.3.2, the terminations of the right circuit of Fig. 3.3.7 (flow source v_t and right agent) can be assumed to behave passive in interaction since the flow source v_t represents the human operator. The visual feedback to the human operator that is not considered in the network representation is then sufficient to preserve a stable manipulation through the passive right circuit. This hypothesis is strengthened by the experience that well-tuned open-loop teleoperation systems are stable. Thus, it can be concluded that the track presented in Fig. 3.3.7 is passive for open-loop ($F_t = 0$) and PF_{comp} ($F_t = F_2$) teleoperation. Note that the track for measured force feedback ($F_t = F_e$) is analyzed in detail in Section 4.2.

Besides architectures incorporating measured force feedback, also the network representation of the position-position (PP) architecture relies on dependent sources. In contrast to the PF architecture, two flow sources are required since two position or velocity signals respectively are transmitted in the two communication channels. With the previous passivity discussion and two passive PI controllers, the track presented in Fig. 3.3.8 is passive, too. Note that differing parametrization of the two controllers in the PP architecture, have the same effect as the scaling of the force feedback signals such that a passive authority allocation (compare Section 5.2.1) can be achieved.

Note that the passivity proof of the PF_{meas}, 3-*Channel* and 4-*Channel* architecture are more complicated and will be presented in Chapter 4.

3.3.4 Multi-DoF Systems

For simplicity, the majority of the new concepts developed in this thesis are presented as 1-DoF systems. Still, a set of haptic augmentation approaches of Chapter 5 can only be applied in multi-DoF systems. Therefore, some relevant modules of the MPMT are presented in a multi-DoF version in the following.

The master device (m) and the slave robot (s) can be modeled as a multi-DoF system:

$$M_i(q_i)\ddot{q}_i + C_i(q_i, \dot{q}_i)\dot{q}_i + g_i(q_i) = \tau_i, \tag{3.14}$$

($i \in \{m, s\}$) with the joint acceleration $\ddot{q}_i$, velocity $\dot{q}_i$ and position q_i ($\ddot{q}_i, \dot{q}_i, q_i \in \mathbb{R}^n$). $M_i(q_i) \in \mathbb{R}^{(n\times n)}$ and $C_i(q_i, \dot{q}_i) \in \mathbb{R}^{(n\times n)}$ are the inertia and Coriolis/centrifugal effect matrix respectively. $g_i(q_i) \in \mathbb{R}^{(n)}$ is the gravitational force vector and $\tau_i \in \mathbb{R}^{(n)}$ is the vector of control torques.

The interaction force $F_j \in \mathbb{R}^n$ ($j \in \{h, e\}$) of the human operator (h) and the environment (e) or a manipulated object with the respective device is:

$$-F_j = M_j\ddot{x}_i + B_j\dot{x}_i + K_j\left[x_i - x_i^{\circ}\right] - f_j^*. \tag{3.15}$$

Where $\ddot{x}_i, \dot{x}_i, x_i \in \mathbb{R}^n$ are the Cartesian acceleration, velocity and position of the master or slave device respectively. The inertia matrix $M_j \in \mathbb{R}^{(n\times n)}$, the damping matrix $B_j \in \mathbb{R}^{(n\times n)}$ and the stiffness matrix $K_j \in \mathbb{R}^{(n\times n)}$ are positive definite. $f_j^* \in \mathbb{R}^{(n)}$ are the exogenous forces and $x_i^{\circ} \in \mathbb{R}^{(n)}$ describes the position of a fixed contact point.

Since the matrices are not diagonal, the human, the environment, the master and the slave modules lead to a coupling within the DoFs of the overall system. Still, other modules as the communication channel can be designed for each DoF separately. In multi-DoF systems, the PI controller can be implemented as a spatial spring according to [166] (see Section 2.3.2) which couples the degrees of freedom in multi-DoF systems.

As depicted in Fig. 3.3.9, each DoF can be considered as a separate port at the multi-DoF subsystems in the network representation [135].

The network representation diagrams of multilateral multi-DoF systems (in Chapter 5), the diagram of Fig. 3.3.9 can be simplified to Fig. 3.3.10. The n ports of each interconnection are replaced by one port with the velocity and force vectors $\boldsymbol{v}_i \in \mathbb{R}^{(n)}$ and $\boldsymbol{F}_i \in \mathbb{R}^{(n)}$.

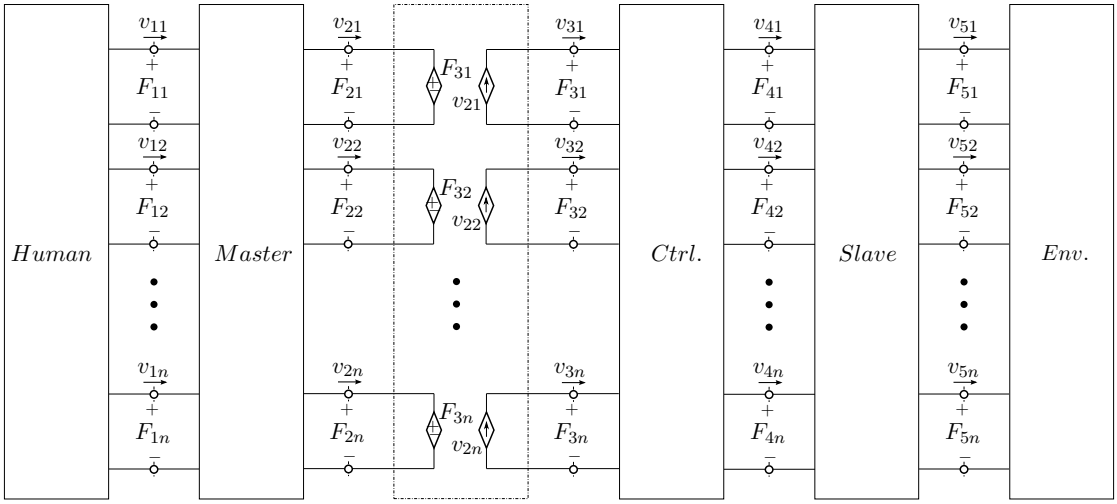

Figure 3.3.9: Network Representation of a Bilateral Multi-DoF Teleoperation System
In a n-DoF system, the network subsystems can be considered as 2n-ports or n-ports respectively. Although not visualized, the DoFs can be coupled inside the multi-port networks.

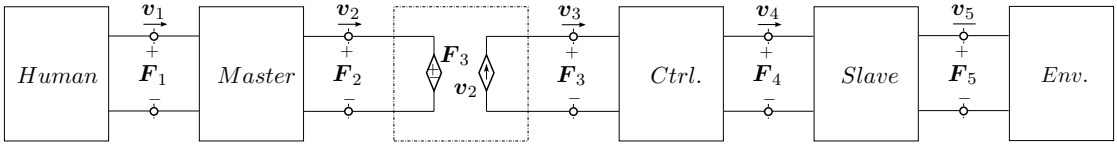

Figure 3.3.10: Simplified Network Representation of a Bilateral Multi-DoF Teleoperation System
The multi-DoF port interfaces of the networks can be visualized through bold effort and flow vectors.

3.4 Experimental Analysis of the Multilateral Coupling

As an introduction to multilateral control, this section provides a first analysis of the multilateral coupling. Therefore, the effect of a real and a pseudo trilateral setup on the coupling rigidity is regarded. Furthermore, the impact of varying communication architectures within the tracks is considered. The experiments were performed with the setup presented in Appendix A.1.

3.4.1 Network Topology

A simple coupling of agents can be achieved via different network topologies. A trilateral setup e.g. can be set up with a fully connected topology (compare Fig. 3.3.3) or a line topology as depicted in Fig. 3.4.1 that can be regarded as a pseudo trilateral system.

Since in the case of the line and the star topology, some agents are not coupled directly to each other, the coupling of these agents is less rigid. If for example *Agent* $\Lambda 1$ as a human operator resists the motion of *Agent* $\Lambda 2$ in the line topology of Fig. 3.4.1, the *Agent* $\Lambda 3$ is not affected by *Agent* $\Lambda 2$ at all. Even if *Agent* $\Lambda 1$ is not resisting, the coupling of *Agent* $\Lambda 2$ and *Agent* $\Lambda 3$ is reduced compared to the fully connected setup of Fig. 3.3.3 since the *Agent* $\Lambda 2$ hardware introduces inertia and damping into the connection of *Agent* $\Lambda 2$ and *Agent* $\Lambda 3$.

The position error of the three agents in a fully connected system (compare Fig. 3.3.3) can be analyzed in the experiment plot Exp. 3.2. All tracks were implemented as a PF_{comp} architecture. The human operator at *Agent* $\Lambda 2$ controls the slave (*Agent* $\Lambda 3$), while the human operator at *Agent* $\Lambda 1$ is not resisting.

In Exp. 3.3, the pseudo-trilateral setup of Fig. 3.4.1 with PF_{comp} architecture in both tracks can analyzed. The human operator at *Agent* $\Lambda 2$ controls the slave (*Agent* $\Lambda 3$) indirectly via *Track* $\Gamma 1$ and *Track* $\Gamma 2$. The human operator at *Agent* $\Lambda 1$ is neither resisting nor supporting the motion. The plots in Exp. 3.3 show that the position error of the devices during free motion is higher compared to the preceding experiment in the fully connected setup. Especially, the position error between *Agent* $\Lambda 2$ and *Agent* $\Lambda 3$ is high because of the missing *Track* $\Gamma 3$. Both, in the line topology as well es in the fully connected topology, during the wall contact, the forces sent to *Agent* $\Lambda 1$ almost cancel each other due to the PF_{comp} architecture.

For the sake of completeness, figure Exp. 3.4 presents an experiment in the line topology of Fig. 3.4.2 with PF_{comp} architecture. The human operator at *Agent* $\Lambda 2$ controls the slave (*Agent* $\Lambda 3$) directly via *Track* $\Gamma 3$. Since *Agent* $\Lambda 3$ is connected to *Agent* $\Lambda 1$, the position error is higher then in the fully connected system. Obviously, the human operator at *Agent* $\Lambda 1$ receives no information (zero force feedback) on the wall penetration of *Agent* $\Lambda 2$ ($t = [5.7s, 7.2s]$). In contrast, *Agent* $\Lambda 1$ would receive force feedback in this situation if *Track* $\Gamma 2$ would be designed in a PF_{meas} or 3-*Channel* architecture. The effect of the coupling signals is analyzed in detail in Section 3.4.2.

Still, the line topology of Fig. 3.4.1 is reasonable for scenarios in which a human operator (*Agent* $\Lambda 1$) controls two slave robots (*Agent* $\Lambda 2$ and *Agent* $\Lambda 3$) in parallel. Also, in a different scenario a human mentor (*Agent* $\Lambda 1$) is able to supervise the actions of a human trainee (*Agent* $\Lambda 2$) in the manipulation of a slave robot (*Agent* $\Lambda 3$). Though, as will be discussed later, higher performance can be achieved with a fully connected topology in combination with an authority allocation in this scenario.

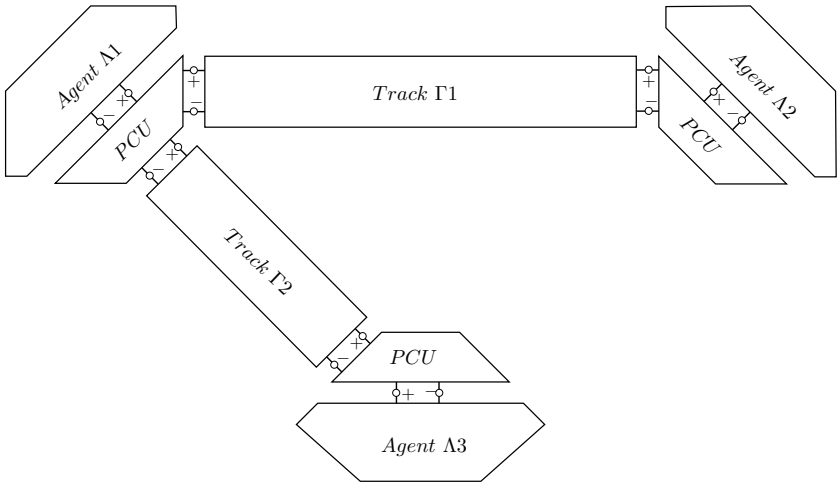

Figure 3.4.1: Network Representation of a Pseudo Trilateral Line Topology without *Track* Γ3

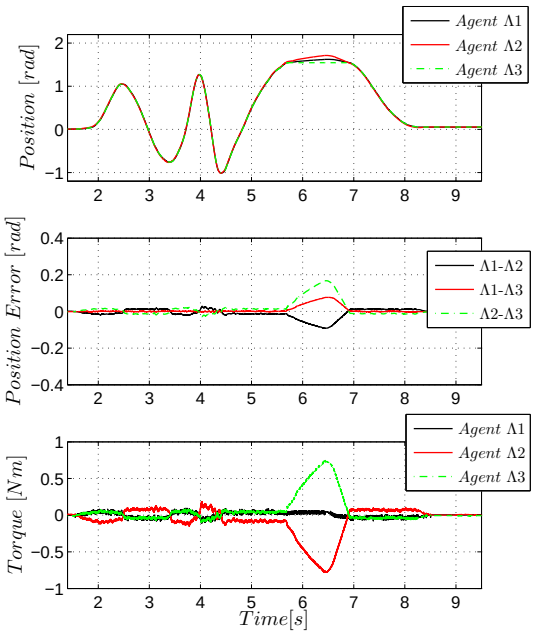

Experiment 3.2: Position Tracking in a Trilateral Setup with PF_{comp} Architecture with Tracks Γ1-Γ3
The human operator at Agent Λ2 controls Agent Λ3, while the human operator at Agent Λ1 is not resisting. A slow and fast sinusoidal motion and a wall contact is performed.

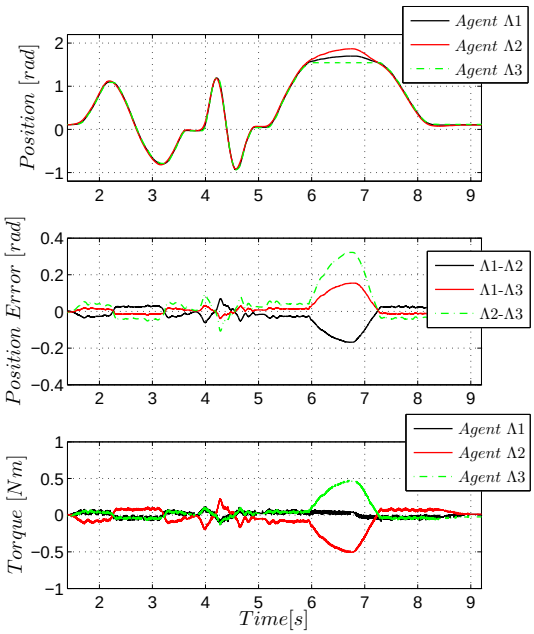

Experiment 3.3: Position Tracking in a Pseudo Trilateral Setup with PF_{comp} Architecture without *Track* Γ3
The human operator at Agent Λ2 controls the slave (Agent Λ3) indirectly via Track Γ1 and Track Γ2. The position error of the devices is higher compared to the fully connected setup.

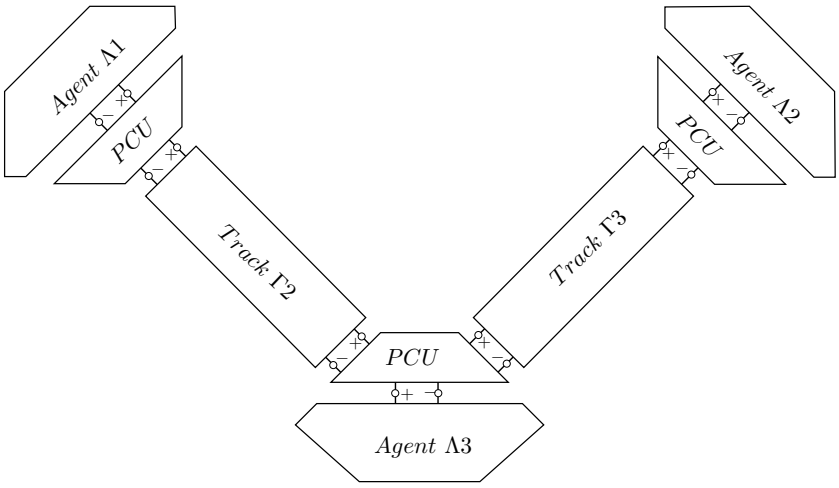

Figure 3.4.2: Network Representation of a Pseudo Trilateral Line Topology without *Track* Γ1

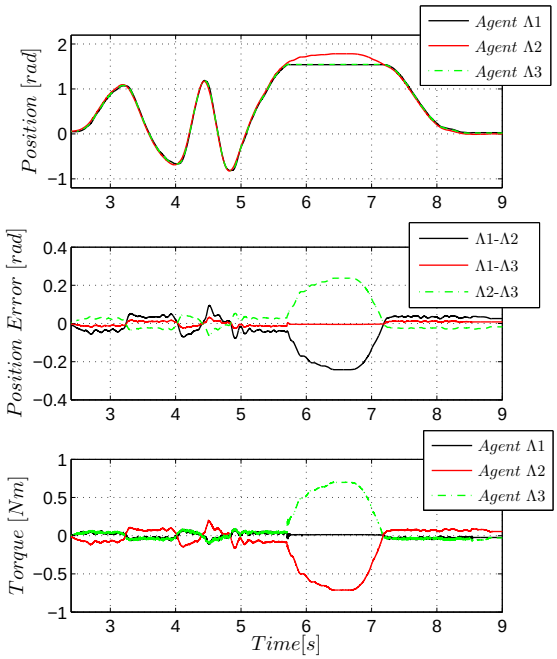

Experiment 3.4: Position Tracking in a Pseudo Trilateral Setup with PF_{comp} Architecture without *Track* Γ1

The human operator at *Agent* Λ2 controls the slave (*Agent* Λ3) directly via *Track* Γ3. The position error is higher then in the fully connected system. The human operator at *Agent* Λ1 receives no information on the wall penetration of *Agent* Λ2.

3.4.2 Track Communication Architecture

In contrast to bilateral teleoperation, the applied communication architecture inside the track is not only to be chosen with respect to the desired maximal transparency, but also to the respective scenario. Note that, to explain this more closely, tracks involving measured force feedback will be applied although their passivity will be proven later in Section 4.3.

In a mentor-trainee scenario different track types result in different perception of the operators. If no measured force feedback is considered, the operators perceive only position changes of the other two devices at their input device. Applying 3-*Channel* tracks that provide hybrid feedback of the computed and measured force feedback (compare Fig. 2.1.5), the operators receive information on the interaction of slave and environment in addition.

In experiment plot Exp. 3.5, the human operator at *Agent* $\Lambda 2$ moves the slave (*Agent* $\Lambda 3$) against a wall. The device of *Agent* $\Lambda 1$ follows this motion with minimum resistance in a fully connected trilateral system. The $Track$ $\Gamma 1$ connecting the master devices has a PF_{comp} architecture whereas $Track$ $\Gamma 2$ and $Track$ $\Gamma 3$ connecting the slave with the master devices have a 3-*Channel* architecture. When the human operator at *Agent* $\Lambda 2$ penetrates the wall at $t = 7s$, the measured force feedback from the slave (*Agent* $\Lambda 3$) in $Track$ $\Gamma 2$ received by *Agent* $\Lambda 1$ pushes *Agent* $\Lambda 1$ away from the wall. Still, the position controller in $Track$ $\Gamma 1$ resists this force such that the *Agent* $\Lambda 2$ position is maintained.

In contrast, in Exp. 3.6, the $Track$ $\Gamma 1$ is deactivated (compare Fig. 3.4.2) and the same procedure is performed. Since *Agent* $\Lambda 1$ receives only force feedback from the slave (*Agent* $\Lambda 3$), the device of *Agent* $\Lambda 1$ is pushed away from the wall when *Agent* $\Lambda 2$ penetrates the wall ($t = [5.5s, 9.5s]$, see Exp. 3.6). Note that this would not happen, if $Track$ $\Gamma 2$ had a PF_{comp} architecture. The position following in the experiment plot Exp. 3.4 in the same pseudo-trilateral system is better since both tracks provide full computed force feedback and thus higher stiffness.

Depending on the desired perception of the operators measured force feedback should be activated. If for example the interaction strength of the slave has higher importance to a trained person than the position following of the devices, the trainee should receive mainly measured force feedback.

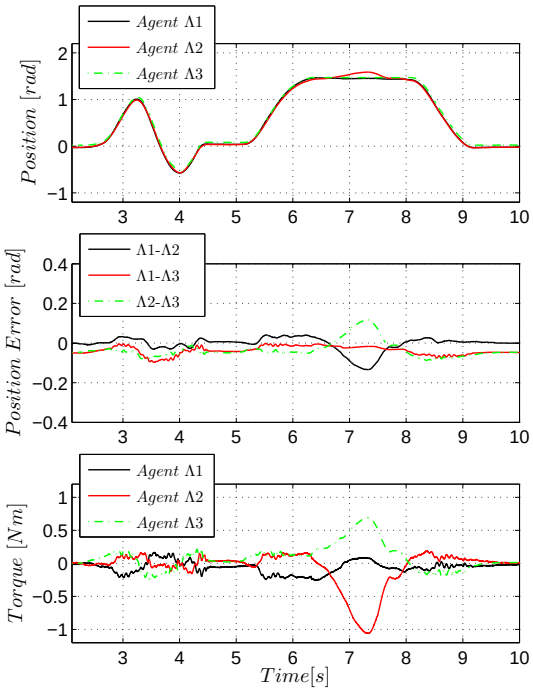

Experiment 3.5: Position Tracking in a Trilateral Setup with 3-*Channel* Architecture with Tracks Γ1-Γ3

The human operator at *Agent* Λ2 moves the slave (*Agent* Λ3) with a sinusoidal motion and against a wall. When the human operator at *Agent* Λ2 penetrates the wall, the measured force feedback from the slave in *Track* Γ2 received by *Agent* Λ1 pushes *Agent* Λ1 away from the wall. Still, the position controller in *Track* Γ1 resists this force such that the *Agent* Λ2 position is maintained.

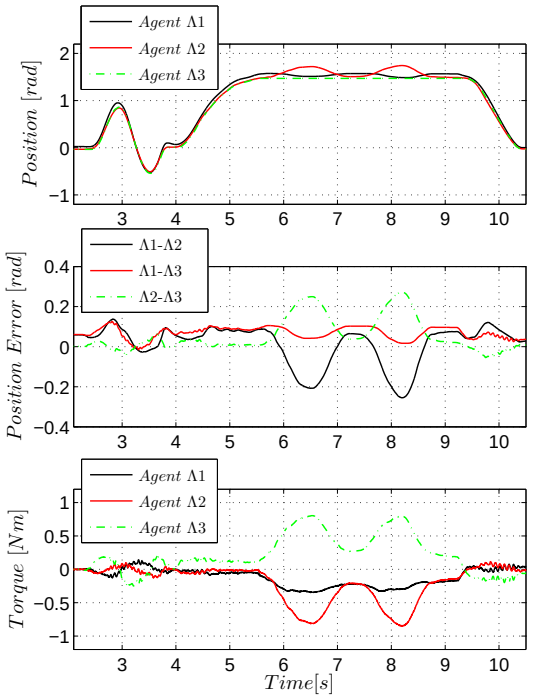

Experiment 3.6: Position Tracking in a Pseudo Trilateral Setup with 3-*Channel* Architecture without *Track* Γ1

A sinusoidal motion and a wall contact are presented. Since *Agent* Λ1 receives only force feedback from *Agent* Λ3, *Agent* Λ1 is pushed away from the wall when *Agent* Λ2 penetrates the wall.

3.5 Discussion on the MPMT Design

The modularity and adaptability to new scenarios are considered as crucial requirements of multilateral stability approaches. The analysis of the available literature on multilateral control approaches lined out that the passivity approach promises comparably high modularity in association with the network representation. Though passively designed systems might be conservative, the passivity approach leads to no restriction in the controller parametrization in the presented basic multilateral setup (PF_{comp} architecture). In the scope of this thesis, mainly time domain passivity control techniques are applied that can be less conservative than frequency-based passivity approaches since damping only occurs on demand and not constantly.

The following chapters will focus the design of new modules that extend the track functionalities. As will be shown later, the tracks of extended architectures involving three or four communication channels can be designed as 2-port subsystems. In contrast, concepts as haptic augmentation can require a double interconnection of agents via two separate tracks. In this case the port number of the PCU subsystems can be adapted without effect on its passive behavior.

Chapter 4

Passive Coupling Architectures for the MPMT

The main requirements for a general control framework suitable for multilateral teleoperation have been analyzed in Section 2.4. In this chapter, the Methodology for Passivity-Based Multilateral Teleoperation is extended with track modules for typical bilateral coupling architectures. Thanks to the modularity of the network representation, these tracks can be applied in the multilateral setups of the subsequent chapter.
The control architecture is characterized by the coupling signals that are exchanged in the communication channel and varies if the channel is affected by delay. Therefore, two novel passive track types that consider a time delay in the communication channel are presented. Furthermore, a method to guarantee passivity of a PF_{meas} architecture and building up on that a 3-*Channel* and 4-*Channel* track are developed. In addition to these position control architectures, a passive rate controlled wheeled mobile robot (WMR) with computed and measured force feedback is proposed. All approaches introduced in this chapter are based on the time domain passivity control. The developed concepts can be applied in bilateral as well as multilateral applications.

4.1 Time Delay

A communication channel affected by delay is an active network element. As presented in Exp. 4.1, a delayed coupled network system goes unstable if no passivity control is applied. This is due to the fact that the delay generates energy: The energy E_{in} entering the communication channel on one side is lower than the energy $E_{out}(t)$ leaving the communication channel in the same direction.

In Section 2.2, the conventional time delay control based on Time Delay Power Networks (TDPN, Approach 1) introduced by the authors of [9] was recapitulated. Here, two newly developed delay control schemes are presented that avoid the usage of admit-

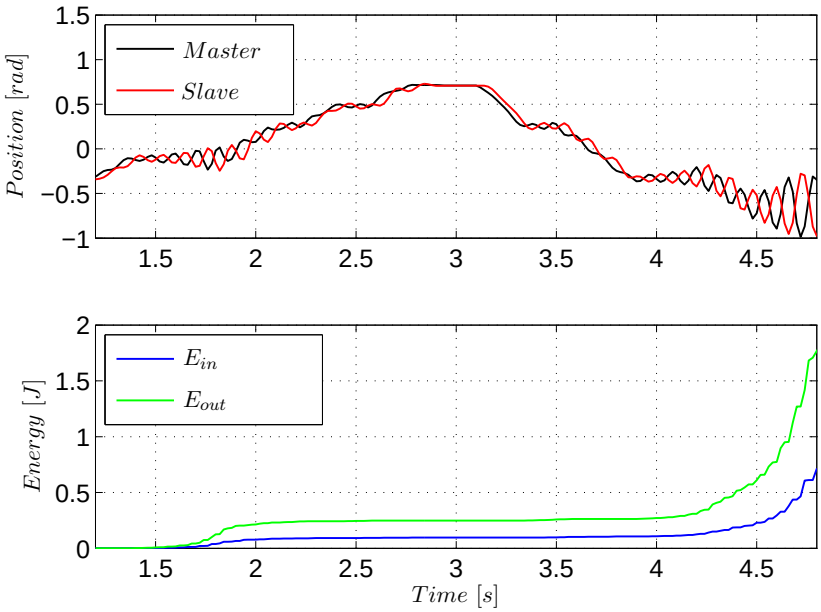

Experiment 4.1: Unstable Closed-Loop Teleoperation System with 30ms Roundtrip Delay
A coupled teleoperation network goes unstable at a roundtrip delay of 30ms without passivity control. The output energy E_{out} of the communication channel is higher than the input energy E_{in} since the delay leads to an energy generation.

tance type PCs. Especially in the fully connected coupling of multiple robots, a position drift is problematic since the differing drifts in the bilateral couplings can lead to contradictory spring tensions that disturb the coupling severely. In contrast to the TDPN approach, these concepts include besides the communication channel also the position controller in the passivity controlled subsystem (PCS). The motivation for this concept is a time domain passivity control without admittance type PC (compare Section 2.2). The main problem of this PC type is a position drift which needs to be compensated (see Section 2.3.2.3) and that the available compensation techniques can not reduce the drift completely.

Two methods (Approach 2 in Section 4.1.1 and Approach 3 in Section 4.1.2) are presented that account the energy behavior of the position controller in different ways. The drawbacks of the conventional TDPN approach (Approach 1) and Approach 2 are analyzed. Finally, the conventional TDPN approach (Approach 1) and the most promising Approach 3 are compared with respect to different transparency criteria.

Fig. 4.1.1 presents the energy flow, observation and control of the TDPN approach (Approach 1) of a 2-port network. The network includes the communication channel (delayed 2-port) and a storage element which represents the potential energy in the coupling position controller. Two PCs terminate the delayed 2-port (port A, B) which contains the communication channel (CC). The energy flow in the system is presented by thick arrows that are marked with orange (right to left: R2L) and blue color (left to right: L2R). The arrows inside the storage element show that a part of the power is transmitted through the storage element to the respective other sides whereas the other part is reflected back. In each direction of energy flow, an energy storage (battery-

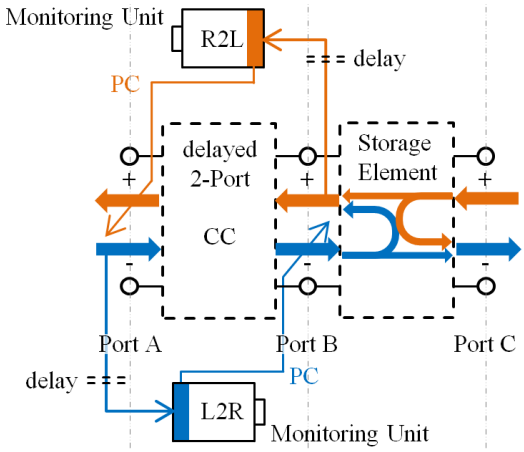

Figure 4.1.1: Energy Observation and Passivity Control of Approach 1 [8]
In Approach 1, two energy monitoring units are charged from port A and port B in L2R direction and R2L direction respectively. The PCs assure that not more energy then available in the energy monitoring unit leaves the delayed 2-port. The arrows in the storage element that represents the coupling controller indicate that energy is to some part transmitted through the network and to some part reflected by the network.

like shape) is calculated from the input power into the delayed 2-port (e.g. thin blue line at port A in L2R direction). On the output side (thin blue line at port B in L2R direction), a PC assures via energy dissipation that not more energy than available in the energy storage leaves the 2-port in the respective direction of power flow (port B in L2R direction). This figure is introduced to ease the comparison with Approach 2 and 3 presented in the following.

4.1.1 Direction Dependent Approach considering Controller Energy

This section presents the time delay control approach proposed in [121] that considers the energy behavior of PI and CC in the two directions of energy flow separately (similar to [145]). In contrast to Approach 1, the following approach considers collectively the energetic behavior of the communication channel (CC) and the coupling storage element (PI controller).

4.1.1.1 System Description

Figure 4.1.2 presents the energy observation and passivity control scheme of Approach 2. One impedance type PC is located on the left side of the CC (port A) and another impedance type PC is positioned on the right side of the storage element (port C). Also, on the right side, the power input to the storage element (port C) is observed instead of the right side input into the CC (port B). This setup considers the energy behavior of the storage element in a power flow direction dependent manner. This concept promises to reduce conservatism since energy generated by the time delayed communication might be partly dissipated by the damping of the position controller such that the passivity controller dissipate less. As mentioned before, another motivation is a time domain passivity control without admittance type PCs.

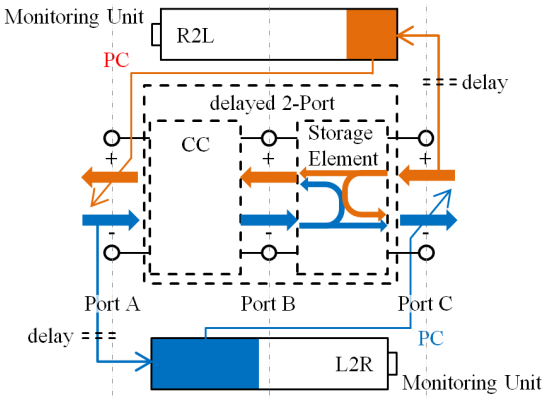

Figure 4.1.2: Energy Observation and Passivity Control of Approach 2 [145, 121]
In Approach 2, two energy monitoring units are charged from port A and port C in L2R direction and R2L direction respectively. Thus, the storage element is included in the network that is controlled by the PCs. The PCs assure that not more energy then available in the energy monitoring unit leaves the 2-port.

As depicted in the PP architecture track of Fig. 4.1.3, two impedance type PCs are located at the end of the track. This holds in PP as well as in PF architectures. $PC1$ dissipates energy that is overall generated in R2L direction by the combination of $PI1$ and $CC2$.

4.1.1.2 Passivity Control

For the sake of simplicity, only the energy flow from right to left (R2L) or from slave to master respectively is presented in the following for the case of a PP architecture. As this architecture is symmetric, the following equations hold for the opposite direction (L2R) in the same way. To analyze the behavior of the PI, the time delay in the $CC1$ is at first neglected. The energy behavior of the PI in direction R2L can be calculated analogous to the 2-port (equations (2.36) and (2.37)). The energy difference $E^{R2L,PI1}$ over the $PI1$ in direction R2L can thus be determined:

$$E^{R2L,PI1}(k) = T_s \sum_{n=0}^{k} P_{diff}^{R2L,PI1}(n) \quad \text{with} \tag{4.1}$$

$$P_{diff}^{R2L,PI1}(k) = P_{5a}^{R2L}(k) - P_{3}^{R2L}(k). \tag{4.2}$$

A part of the power that is flowing from Master to Slave is dissipated in the PI-controllers. This dissipation (positive $P_{diff}^{R2L,PI1}$) of the PI-controller results in a storage of positive energy. A small desired part of the storage is caused by the deflection of the spring in the PI controller.

Also in the conventional TDPN approach (Section 2.3.2.3), a small energy storage caused by short phases of dissipative behavior in the communication channel can appear. As the stored energy can be far higher in the case of Approach 2, the storage has to be limited such that no long phases of activity can appear. Generated energy is dissipated by the passivity controllers, only when this limited storage is discharged by a negative $P_{diff}^{R2L,PI1}$. The lower the energy limit is, the more conservative is the system.

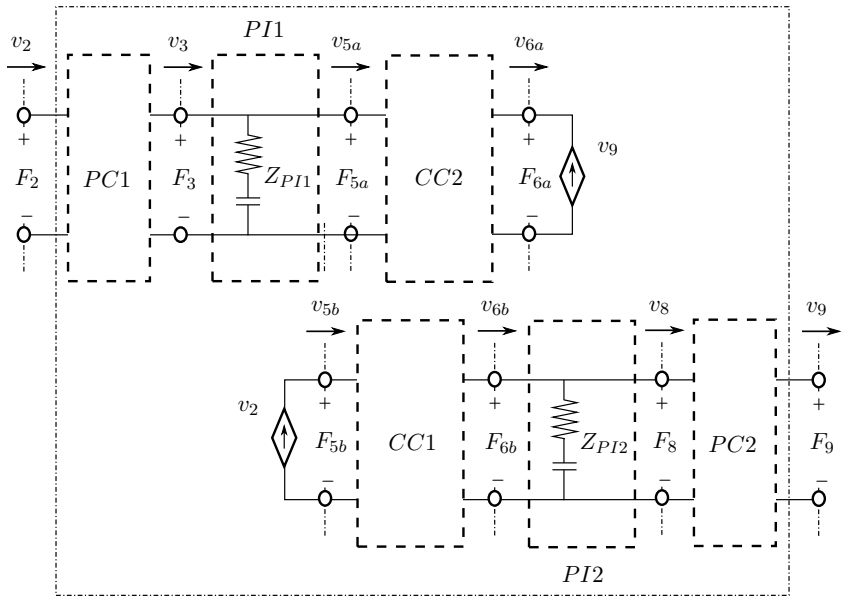

Figure 4.1.3: Network representation of a Track with PP Architecture with Time Delay Control Approach 2
PC1 assures that not more energy leaves at port 2 in R2L direction than has entered at port 6a. Analogously, PC2 acts in the L2R direction concerning the energy input at port 5b.

In [145], the limitation has been achieved by adjusting the output energy of the respected 2-port E_{5a}^{R2L} after a certain time period T_M of pure dissipation to the entering energy E_3^{R2L}. The time T_M can be chosen by the user. The presented alternative [122] introduces a limitation respecting an energy limit E_{lim} instead of a time criterion. Thus the energy $E_{obs}^{R2L,PC1}$ which has to be dissipated in time step k by PC1 can be calculated as follows:

$$
\begin{aligned}
&\{1\}: if(E^{R2L,PI1}(k) - E_{obs}^{R2L,PI1}(k-1) - E_{sto}^{R2L,PI1}(k-1) > E_{lim})\\
&\{2\}: \quad E_{sto}^{R2L,PI1}(k) = E_{sto}^{R2L,PI1}(k-1) + (E^{R2L,PI1}(k) -\\
&\qquad\qquad E_{obs}^{R2L,PI1}(k-1) - E_{sto}^{R2L,PI1}(k-1) - E_{lim})\\
&\{3\}: if(E^{R2L,PI1}(k) - E_{obs}^{R2L,PI1}(k-1) - E_{sto}^{R2L,PI1}(k) < 0)\\
&\{4\}: \quad \Delta E_{obs}^{R2L,PI1}(k) = (E^{R2L,PI1}(k) - E_{obs}^{R2L,PI1}(k-1)\\
&\qquad\qquad - E_{sto}^{R2L,PI1}(k))\\
&\{5\}: \quad E_{obs}^{R2L,PI1}(k) = E_{obs}^{R2L,PI1}(k-1) + \Delta E_{obs}^{R2L,PI1}(k).
\end{aligned}
$$

The variable $E_{sto}^{R2L,PI1}$ stores the amount of energy that has not been considered because of limit violations. Line $\{1\}$ observes the violation of the limitation. In the case of a violation, the storage is adapted through line $\{2\}$. As soon as the small energy storage of E_{lim} is deleted by active behavior, the if enquiry in line $\{3\}$ is true and the PC is activated. Therefore the current energy difference $\Delta E_{obs}^{R2L,PI1}$ which currently has to be dissipated by the PC is calculated (line $\{4\}$) and the amount of energy $E_{obs}^{R2L,PI1}$ dissipated by the PC so far, is updated (line $\{5\}$). The effect of the limitation in a system with $E_{lim} = 5mJ$ is depicted in experiment plot Exp. 4.2.

The passivation of the PI through this Approach 2 allows a stability independent choice of PI-parameters. Of course, the parameters have to be selected corresponding to the optimal transparency of the system.

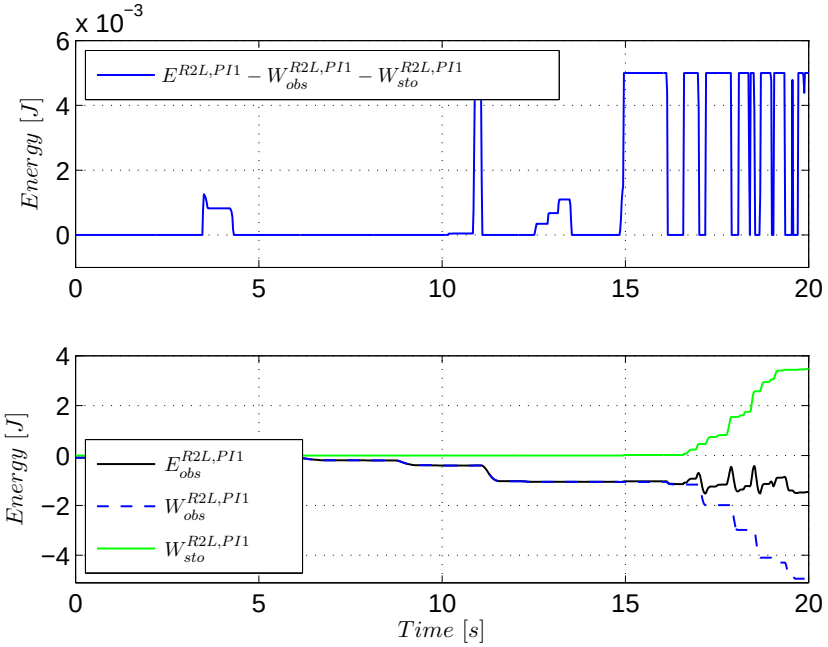

Experiment 4.2: Limitation of $W_{obs}^{R2L,PI1}$
Here, the energy limit was set to 5mJ. The energy leaving the PC in R2L direction needs to be lower than $W_{sto}^{R2L,PI1}(n)$ to assure passivity.

In the presence of time delay in the $CC2$, the observed energy $E_{obs}^{R2L,CC2}(k)$ of $CC2$ can be calculated as follows.

$$E_{obs}^{R2L,CC2}(k) = \sum_{n=0}^{k} (P_{6a}^{R2L}(n - T_2) - P_{5a}^{R2L}(n))T_s \tag{4.3}$$

In summary, the energy $E^{PC1}(k)$ for the PC-controlled R2L part of the track from slave to master including PI1 and CC2 can be calculated:

$$E_{obs}^{PC1}(k) = E_{obs}^{R2L,CC2}(k) + E_{obs}^{R2L,PI1}(k). \tag{4.4}$$

The limitation algorithm stays as described above. The energy that has to be dissipated has to be calculated analogous to equations (2.50) and (2.51). The functionality of the impedance PCs is described in Section 2.3.2.3.

4.1.1.3 Experiments

In this section, the first three experiments for the proposed passivity control scheme are presented within a bilateral PP architecture with time delay. The 1-DoF setup presented in appendix A.1 was applied. For the experiments, the communication channels have been restrained by one unique time delay ($T_1 = T_2$). The system has been tuned at the

verge of stability with $T_i = 10ms$ ($i \in \{1, 2\}$) round trip delay (PI parameters: damping $B_{PI} = 0\frac{Nms}{rad}$, stiffness $K_{PI} = 2\frac{Nm}{rad}$, local damping of master $B_{local}^{master} = 10\frac{Nms}{rad}$ and Slave $B_{local}^{slave} = 20\frac{Nms}{rad}$). The energy limit E_{lim} has been set to $5mJ$ for all experiments.

An experiment at 30ms roundtrip delay with passivity control is depicted in Exp. 4.3. Exp. 4.3b depicts the energy behavior of the subsystems CC2 and PI1 and the behavior of the whole track including the PCs are presented respectively. A comparison of the two figures makes clear that the PC reduces the energy $E_3^{R2L}(k)$ to $E_2^{R2L}(k)$. Under passivity-control $E_2^{R2L}(k)$ is always lower than $E_{6a}^{R2L}(k - T_2)$ and so, the track in direction R2L is passive. The position tracking such as the wall contact of the slave is comparable with a system without delay.

A negative effect of this Approach 2 with direction dependent controller energy consideration can be seen at $t = 2.6s$ and $t = 7.2s$. The PC dissipates energy when the master is reducing the wall penetration. This is due to the fact that the POs analyze that energy is introduced in R2L direction. Since the slave is not moving, no power is sent from slave to master. Still, the spring in the coupling controller is unloaded by the backwards moving master which is interpreted as energy generation by the approach although it is a passive action (compare Section 3.3.3). This negative effect is resolved by Approach 3 through a direction independent energy consideration, presented in Section 4.1.2.

The position tracking in a system with roundtrip delay of 200ms (see plot Exp. 4.4a of experiment Exp. 4.4) is as well satisfactory. The step-wise motion is a negative effect of the two PI controllers that are located remotely from each other in the PP architecture. This can be avoided through a PF_{comp} architecture. Analyzing the energy difference in plot Exp. 4.4b, one can see that the PI and the CC in combination produce a high amount of energy. The activity of the subsystems surrounded by the PCs has increased gravely compared to the system with 30ms roundtrip delay (compare plot Exp. 4.3b), although the devices' motion in the two experiments are similar. This high activity difference is caused by the increase of time delay which leads to high energy generation in the CC.

To analyze the adequacy of Approach 2 for the multilateral case, a simulation (Exp. 4.5) of the system depicted in Fig. 4.1.4 is presented in the following.

All master and slave devices have been modeled as mass-damper systems with unitary parameters ($M_i = 0.1kg$, $B_i = 0.3Ns/m$, $i \in \{m, s\}$). Also all PI-controllers equal each other. The Mentor (*Agent* $\Lambda 1$) is virtually located distant from the trainee in *Agent* $\Lambda 3$ and from the slave in *Agent* $\Lambda 2$ (100ms roundtrip delay in $Tracks$ $\Gamma 1$ and $\Gamma 2$). There is a roundtrip delay of 30ms in $Track$ $\Gamma 4$ between *Agent* $\Lambda 2$ and $\Lambda 3$. *Agent* $\Lambda 4$ is a local simulation of *Agent* $\Lambda 3$ (no delay in $Track$ $\Gamma 3$). Each track is of PP architecture type. The simulation was tuned to go unstable without passivity control at 10ms roundtrip-delay in $Tracks$ $\Gamma 1$, $\Gamma 2$ and $\Gamma 4$. The position tracking of the four devices can be seen in plot Exp. 4.5. The mentor is leading the other devices and the trainee grips his device strongly. The positions of *Agent* $\Lambda 1$ and $\Lambda 2$ match very well as there is no delay between these two devices and as a high stiffness has been chosen for the PI-controllers. The mentor and trainee motions have the same authority on the slave motion. Thus, *Agent* $\Lambda 3$ is located between *Agent* $\Lambda 1$ and $\Lambda 2$. Plot Exp. 4.5 shows two passivity proofs of two different tracks ($\Gamma 1$ and $\Gamma 3$) in one direction each. As both energies $E^{L2R,\Gamma 1}$ and $E^{L2R,\Gamma 3}$ are always higher than the storage limitation ($E^{L2R,\Gamma i} > W_{sto}^{L2R,\Gamma i}$) and since $W_{sto}^{L2R,\Gamma i} > 0$, these tracks are passive in direction L2R. The energy difference of $Track$

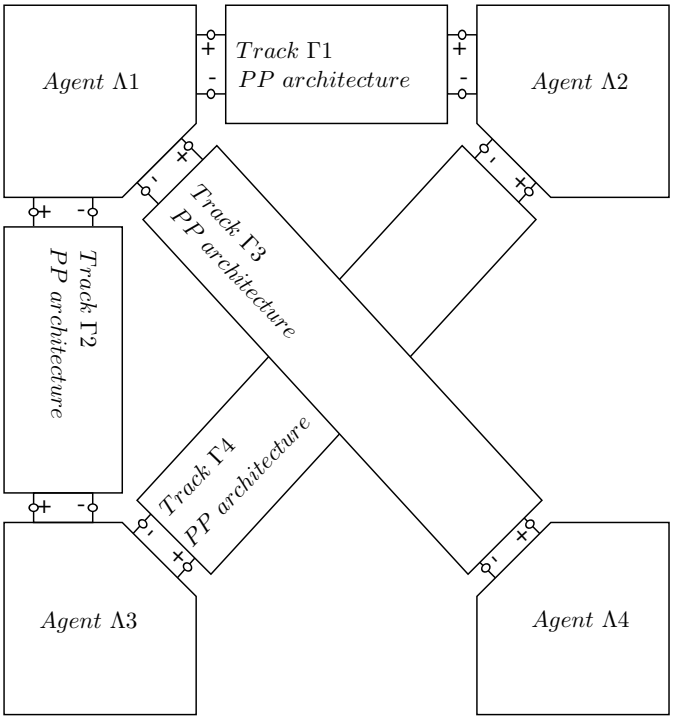

Figure 4.1.4: Assembly of Tracks to a Multilateral System

Γ1 reaches far higher values than in *Track* Γ3 due to the differing time delays.

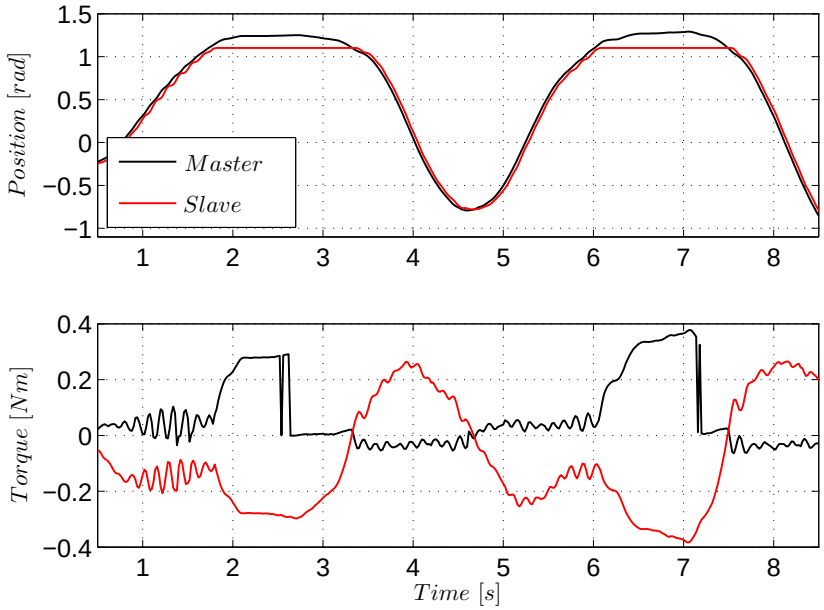

(a) Position and Force of Devices

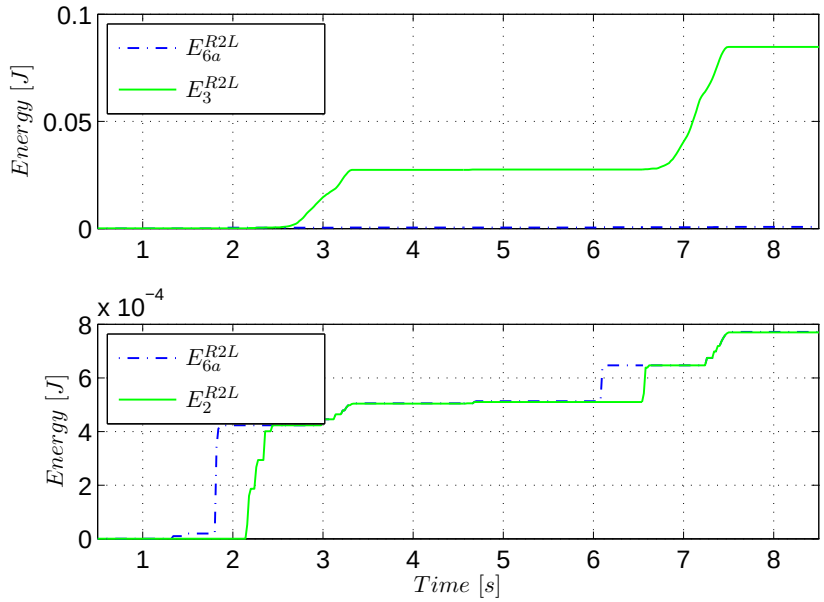

(b) Passivity Proof

Experiment 4.3: 30ms Roundtrip Delay with Passivity Control
Two wall contacts are preformed in this experiment. The PC reduces the energy E_3^{R2L} to E_2^{R2L} such that the passivity controlled track is passive ($E_2^{R2L}(k) < E_{6a}^{R2L}(k-T_2)$). Due to the direction dependent energy monitoring of Approach 2, the feedback forces to the master are heavily varied by the PC.

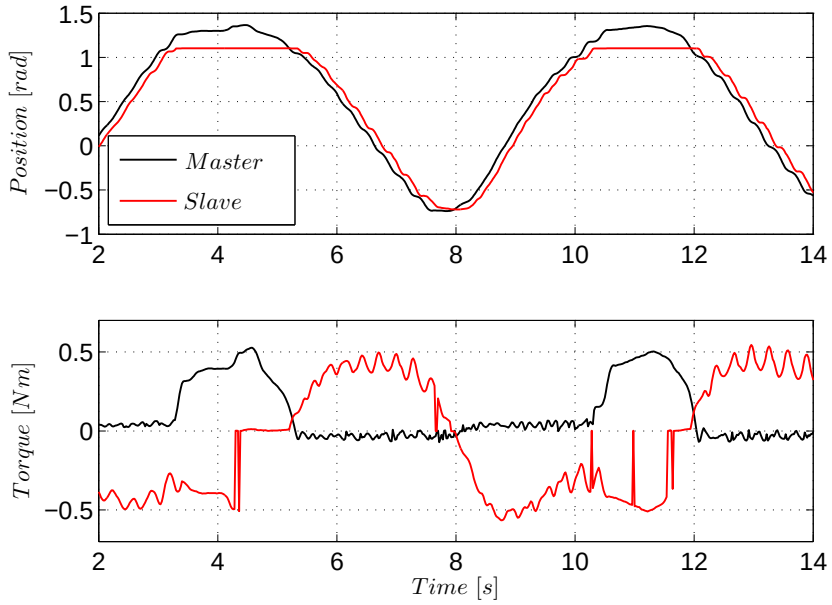

(a) Position and Force of Devices

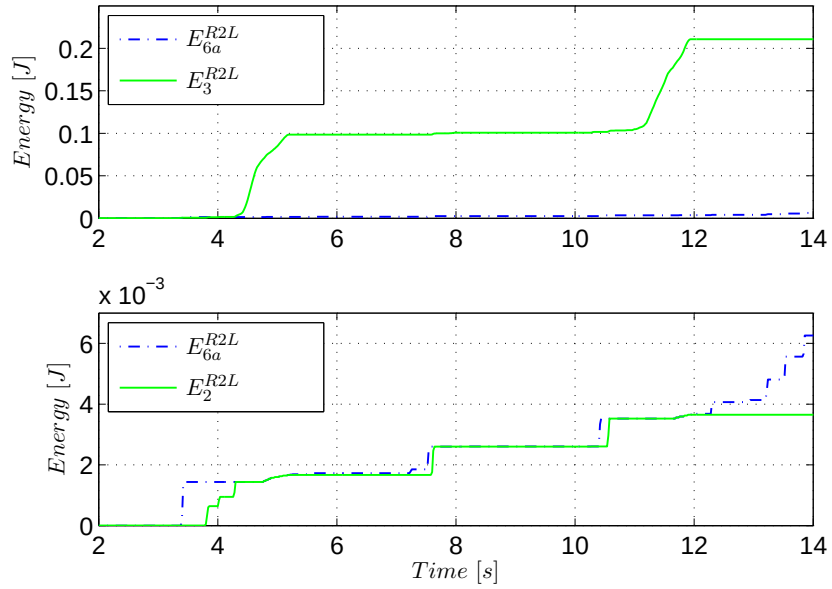

(b) Passivity Proof

Experiment 4.4: 200ms Roundtrip Delay with Passivity Control
The passivity control assures the stability of the system at 200ms roundtrip delay. The step-wise motion of the devices at $t = [5.4s, 8s]$ results from the large delay and the PP architecture.

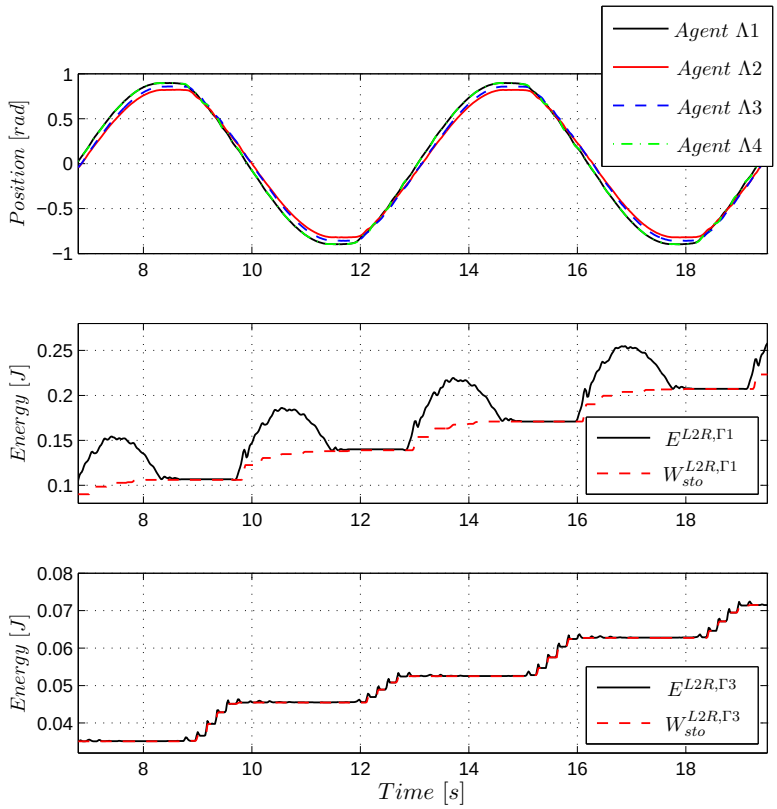

Experiment 4.5: Simulation of Multilateral Teleoperation
Four Agents are coupled at different roundtrip-delays (100ms in Track Γ1 and Γ2, 30ms in Track Γ4) in this simulation according to Fig. 4.1.4. The passivity proof of Track Γ1 and Γ3 in L2R direction are presented representatively.

4.1.2 Approach considering Stored Controller Energy and Energy Reflection

The following time delay control approach (Approach 3) circumvents the excessive dissipation of Approach 2 described in Section 4.1.1.3 since, in contrast to Approach 2, the energetic behavior of the PI controller is not considered in a direction dependent manner.

Regarding the energy behavior of the PI controller (Section 3.3.3), it can be interpreted that the time delay control approaches of [145, 121] (Approach 2) wrongly assumed that the energy is leaving the PI in the same direction as it has entered. Approach 3 considers that energy is reflected by the PI controller which is regarded as a storage of potential energy.

Fig. 4.1.5 presents the application of the proposed approach to a delayed 2-port including storage element. Similar to Approach 2, the passivity controllers are located at port A and port C such that the storage element is located inside the passivity controlled delayed 2-port. In contrast to Approach 1 and 2, one unique monitoring unit is considered that contains the energy that may leave the delayed 2-port in both directions. The virtual storage is charged up by the blue (port A) and orange arrow (port C) representing the power input in L2R and R2L direction respectively. The green arrows indicate where the passivity controllers dissipate the excessive amount of energy considering the common storage in the energy monitoring unit. Since a unique storage is regarded, the energy distribution in a power flow direction independent manner is possible and reflections of the storage element are respected.

4.1.2.1 System Description

As can be seen in Fig 4.1.6, one impedance type passivity controller is located left from the communication channel and another on the right of the PI controller in a PF_{comp} architecture. In the following, we assume that a human operator with master terminates the track on the left and a slave with environment terminates the track on the right side.

The desired energies E_6^{R2L} and E_2^{L2R} build up a storage of potential energy in the PI controller. From the power P_6^{R2L} at port 6 the energy entering the PI from the right side can be determined. The undelayed power P_2^{L2R} at port 2 sent from master to slave can be regarded as the desired input to the PI controller from the left side. Note that the real input to the PI from the left side is the power P_{4b}^{L2R}. The resulting energy content of the storage element (ideal storage) is not equal to the real potential energy of the controller, since that is affected by energy generation in the CC (P_{4b}^{L2R}).

Fig. 4.1.7 explains the difference between the ideal and real potential energy storage in more detail. Since the active element CC adds energy in L2R direction, the real storage which is filled up with the energies at Port 2 and Port 3 is equal to or higher than the ideal storage. The ideal storage collects the energy that is introduced from the agents into the 2-port between port 1 and 5 such that the ideal storage can be regarded as the desired energy content of the controller. The energy stored in the ideal storage may leave the storage element to both sides. Considering the intrinsically passive behavior of the PI controller, it is clear that not more power than this ideal storage allows, may leave the PI controller to left and right side. The by this means limited power $P^{L2R,des}$ may leave to the slave at port 6. In the same way, the limited power $P^{R2L,des}$ sent to

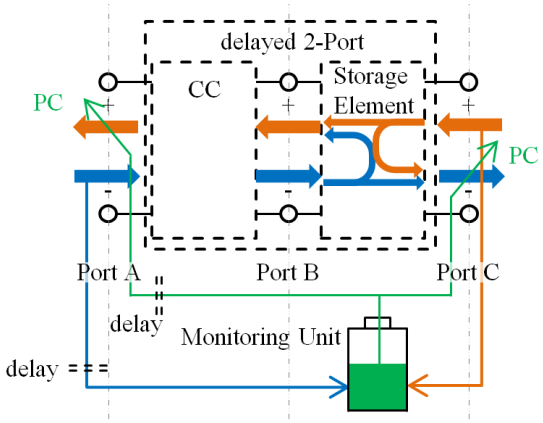

Figure 4.1.5: Energy Observation and Passivity Control Considering Energy Reflection (Approach 3)
In Approach 3, only one energy monitoring unit is charged from port A and port C in L2R direction and R2L direction respectively. The PCs assure that not more energy then available in the energy monitoring unit leaves the 2-port at port A and port C.

the master may exit at port 2 on the master side of the communication channel. That means that $P^{R2L,des}$ is the reference power that determines the dissipation of the master side $PC1$ and $P^{L2R,des}$ is the reference power that determines the dissipation of the slave side $PC2$.

4.1.2.2 Passivity Control

For the sake of simplicity, at first a controller with potential storage element (e.g. stiffness) only is regarded. Since in teleoperation control loops often not only local damping at the robots but also a damping element in the coupling controller is applied, a method to consider such a damping element in the proposed structure is introduced later. The energy input that is accounted in the energy storage $E_{St}(k)$ can be determined:

$$E_{St}(k) = E_{St}(k-1) + P_2^{L2R}(k-T_1)T_s + P_6^{R2L}(k)T_s. \tag{4.5}$$

It is important to note that not the energy $P_{4b}^{L2R}(k)$ measured at port 4b is considered as an input, since it is affected by delay. The actual output $P_{out}^{act}(k)$ in both direction of energy flow has to be calculated:

$$P_{out}^{act}(k) = P_{4b}^{R2L}(k) + P_5^{L2R}(k). \tag{4.6}$$

If this power is smaller than or equal to the energy content of the controller ($P_{out}^{act}(k)T_s \leq E_{St}(k)$), this power may leave at the respective ports. Just if more power than available is exiting at port 4b or 5, the power output has to be limited. The excessive power P_{exc} can be calculated as

$$P_{exc}^{R2L}(k) = \begin{cases} P_{diss}(k)\frac{P_{4b}^{R2L}(k)}{P_{out}^{act}(k)}, & \text{if } E_{St}(k) < P_{out}^{act}(k)T_s \\ 0, & \text{if } E_{St}(k) > P_{out}^{act}(k)T_s \end{cases}, \tag{4.7}$$

$$P_{exc}^{L2R}(k) = \begin{cases} P_{diss}(k)\frac{P_{5}^{L2R}(k)}{P_{out}^{act}(k)}, & \text{if } E_{St}(k) < P_{out}^{act}(k)T_s \\ 0, & \text{if } E_{St}(k) > P_{out}^{act}(k)T_s \end{cases}, \tag{4.8}$$

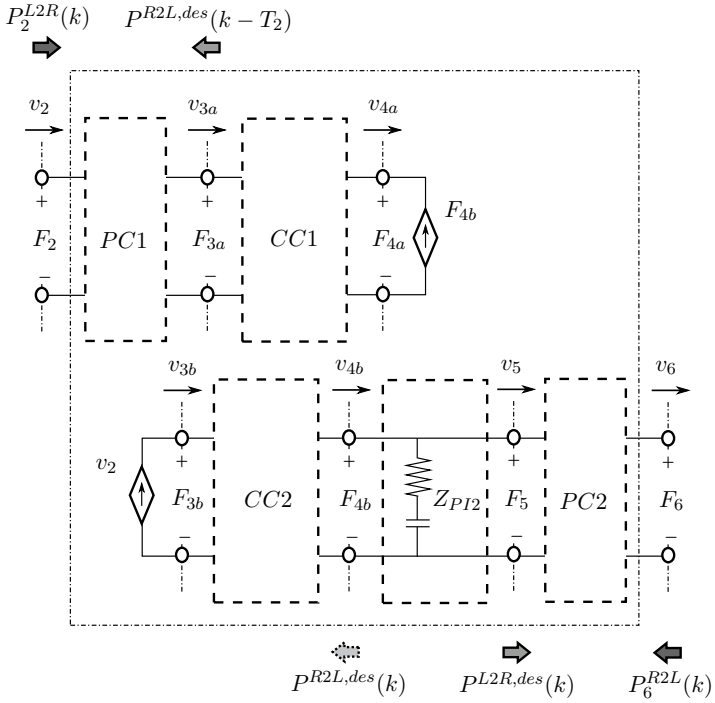

Figure 4.1.6: Time Delay Control Approach 3 for a PF_{comp} Architecture
Analogous to Approach 2, the PC2 is located on the right side of the PI controller (storage element). For the sake of passivity, the power output of the 2-port needs to be limited by the PCs to $P^{L2R,des}(k)$ and $P^{R2L,des}(k-T_2)$ in L2R and R2L direction respectively.

with the power $P_{diss}(k)$ that has to be dissipated in the current time step:

$$P_{diss}(k) = E_{St}(k)/T_s - P_{out}^{act}(k). \tag{4.9}$$

The excessive power $P_{exc}^{L2R}(k)$ can be directly dissipated from the power $P_5^{L2R}(k)$ by the right hand side $PC2$

$$P^{L2R,des}(k) = P_5^{L2R}(k) + P_{exc}^{L2R}(k), \tag{4.10}$$

$$E_{obs}^{PC2}(k) = T_s \sum_{i=0}^{k} (P^{L2R,des}(i) - P_5^{L2R}(i)). \tag{4.11}$$

With $P_{exc}^{R2L}(k)$, the desired power output $P^{R2L,des}(k)$ on the left side of the communication channel can be determined:

$$P^{R2L,des}(k) = P_{4b}^{R2L}(k) + P_{exc}^{R2L}(k), \tag{4.12}$$

$$E_{obs}^{PC1}(k) = T_s \sum_{i=0}^{k-T_2} P^{R2L,des}(i) - T_s \sum_{i=0}^{k} P_{3a}^{R2L}(i). \tag{4.13}$$

The energy that has to be dissipated has to be calculated analogous to equations (2.50) and (2.51). The functionality of the impedance PCs is described in Section 2.3.2.3.

For the next time step, the energy content E_{St} has to be updated, as the power $P_{4b}^{R2L}(k)$ and $P_5^{L2R}(k)$ exited at the respective ports:

$$E_{St}(k) = E_{St}(k-1) + (P_2^{L2R}(k-T_1) + P_6^{R2L}(k) - P_{4b}^{R2L}(k) - P_5^{L2R}(k))T_s. \tag{4.14}$$

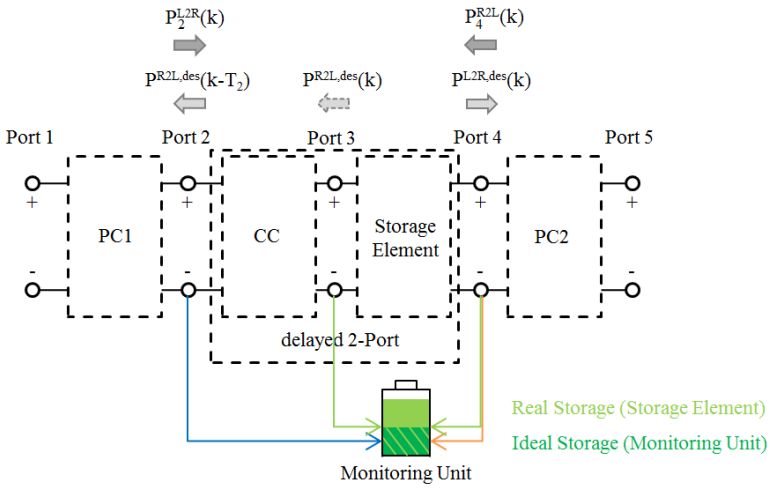

Figure 4.1.7: Comparison of Real and Ideal Potential Energy Storages
The energy monitoring unit is charged by the energy input from port 2 and port 4 that represents the intended energy input by the agents that are coupled by the 2-port. This ideal storage differs from the real energy storage of the storage element which is charged up from port 3 and port 4. The energy flowing at port 3 in L2R direction contains the energy that is generated by the delay and that may lead to instability.

Note that $P_{4b}^{R2L}(k)$ needs to be considered instead of $P_2^{R2L}(k - T_2)$ due to the delay.

4.1.2.3 Experiments

The following experiments have been performed in the bilateral 1-DoF setup presented in appendix A.1. The first experiment Exp. 4.6 presents the performance of the system at 30ms roundtrip delay. The energy plot E_{PP} serves the passivity proof of the PC controlled two port

$$E_{PP}(k) = E_1^{L2R}(k) + E_5^{R2L}(k) - E_1^{R2L}(k) - E_5^{L2R}(k). \tag{4.15}$$

The charging and releasing of the spring during the two wall contacts ($t = [9.2s, 10.5s]$ and $t = [12.7s, 13.2s]$) is clearly visible in the energy plot. Only in short phases during the contact, the passivity controllers are active. The position following of the two devices is very good.

The second experiment Exp. 4.7 presents a wall contact at 400 ms roundtrip delay. The position following is clearly affected by the high delay. The energy plot E_{PP} is always positive and thus confirms the passivity of the PC controlled two port. The passivity controllers are mainly active during the wall contact but not in free motion.

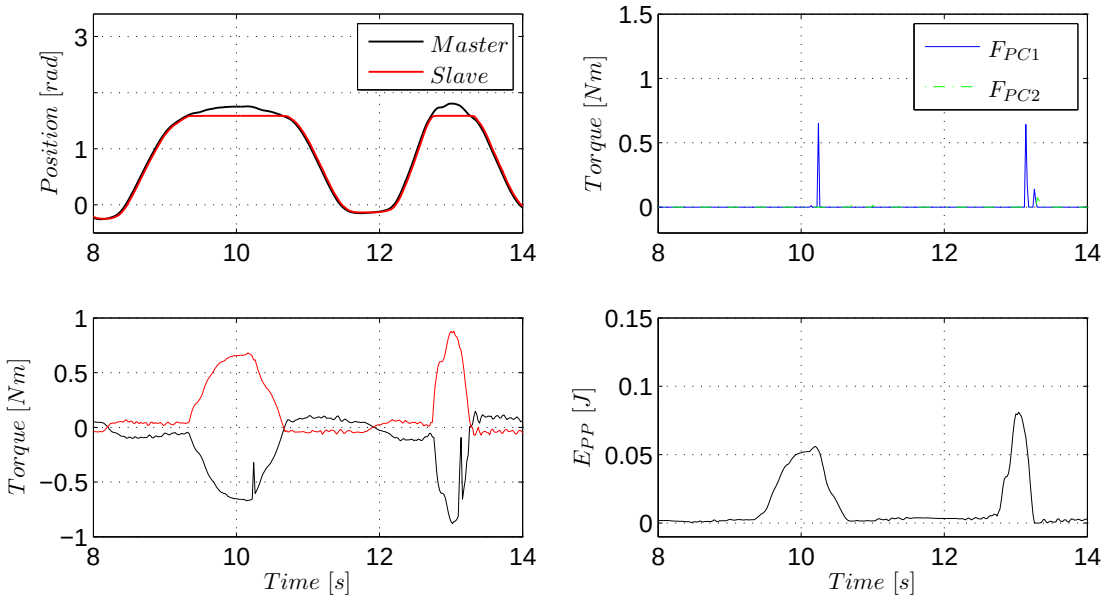

Experiment 4.6: Wall Contact with 30ms roundtrip delay in Approach 3
A slow and a fast wall contact are performed in this experiment. The passivity proof plot E_{PP} clearly depicts the potential energy storage during the wall contacts. Only little energy has to be dissipated by the PCs. Obviously, only the PC1 on the master side needs to inject a damping.

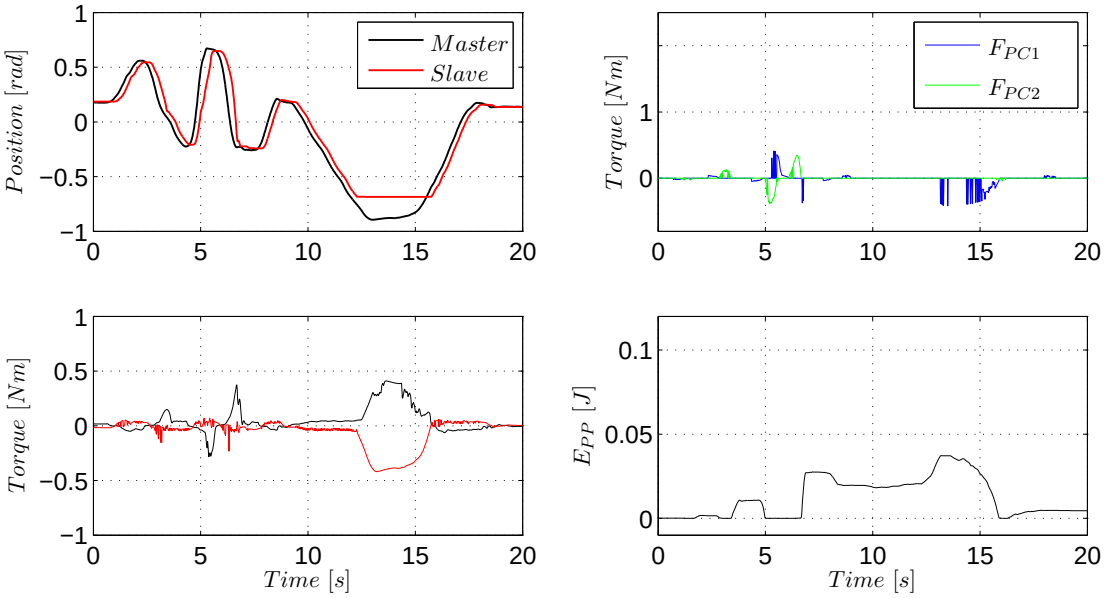

Experiment 4.7: Wall Contact with 400ms roundtrip delay in Approach 3
This experiments presents one wall contact and free motion. Despite the large delay, the position tracking of master and slave device is satisfactory. Mainly PC1 has to dissipate energy since the largest part of the energy is reflected back to the master by the PI controller representing the energy storage element.

4.1.3 Comparison of Time Domain Passivity Approaches

This section recapitulates the drawbacks and advantages of the three discussed approaches. Furthermore, the time delay control methods of Approach 1 (Section 2.3.2.3) and Approach 3 (Section 4.1.2) are compared with respect to different transparency measures at varying delays.

Energy Reflection The main drawback of the direction dependent Approaches 1 and 2 can be analyzed from the energy behavior of a controller with storage element presented in Exp. 4.8. A free motion and a wall contact and the respective observed energies are presented. The port nomenclature of Fig. 4.1.5 is applied. The delay was set to zero in this experiment. The controller's potential energy storage can be charged up from both sides (*Agent* $\Lambda 1$ and *Agent* $\Lambda 2$). In this bilateral experiment with PF_{comp} architecture, *Agent* $\Lambda 1$ controls *Agent* $\Lambda 2$ in free motion until *Agent* $\Lambda 2$ touches a rigid wall ($K_e \approx \infty$, $B_e \approx 0$) at about $t = 3.4s$. During free motion ($K_e = 0$, $B_e \approx 0$), *Agent* $\Lambda 1$ injects the energy E_B^{L2R} into the controller (storage element) at port B in L2R direction which leaves this storage element mainly as E_C^{L2R} such that *Agent* $\Lambda 2$ is moved. Therefore, the energy storage of the controller E_{St} is almost empty during free motion ($t = [0s, 3.4s]$).

When *Agent* $\Lambda 2$ touches the wall ($t = [3.4s, 5s]$), no energy can flow on the side of *Agent* $\Lambda 2$ since its velocity is zero (constant E_C^{L2R} and E_C^{R2L}). With the wall penetration of *Agent* $\Lambda 1$, the energy storage E_{St} is filled up by energy E_B^{L2R}. When *Agent* $\Lambda 1$ moves out of the contact, the energy of the storage is released as E_B^{R2L} in R2L direction to press the *Agent* $\Lambda 1$ out of the wall (energy reflection).

Mainly during wall contacts, or in general when the motion of one robot is hindered e.g. by obstacles, workspace limitations or high damping, energy might be reflected by the network element storing potential energy. Respecting the energetic behavior of the storage element, Approach 1 and 2 have the following conservatism:

- In Approach 1, the passivity controller at port B preserving passivity of the delayed 2-port in L2R direction may dissipate energy that would later have been reflected back in R2L direction by the storage element. This can lead to over-conservative energy dissipation. Also, for example the position that is sent to the storage element from *Agent* $\Lambda 1$ is varied by the PC at port B. Thus, the charging of the potential storage is lower than intended by *Agent* $\Lambda 1$ which can change the coupling behavior drastically, as among others, position drift can appear. The effect of the port B PC on the conservatism of Approach 1 will be further analyzed later.

- The energy plots ${}^{St}E^{R2L}$ and ${}^{St}E^{L2R}$ in Fig. 4.8 serve the analysis of the conservatism of Approach 2. The charging of the spring by E_B^{L2R} is considered as an energy dissipation ${}^{St}E^{L2R}$ in Approach 2 since no power leaves the storage element during the wall contact at port C (E_C^{L2R}). In contrast, the release of energy in R2L direction is observed as an energy generation since no power enters at port C (E_C^{R2L}) during the wall contact. Thus, the power flow direction dependent analysis of Approach 2 results in high dissipation and high conservatism.

Approach 3 promises to be less conservative than Approach 1 since energy can pass at port B to the storage element (L2R) without being affected by a PC which prevents

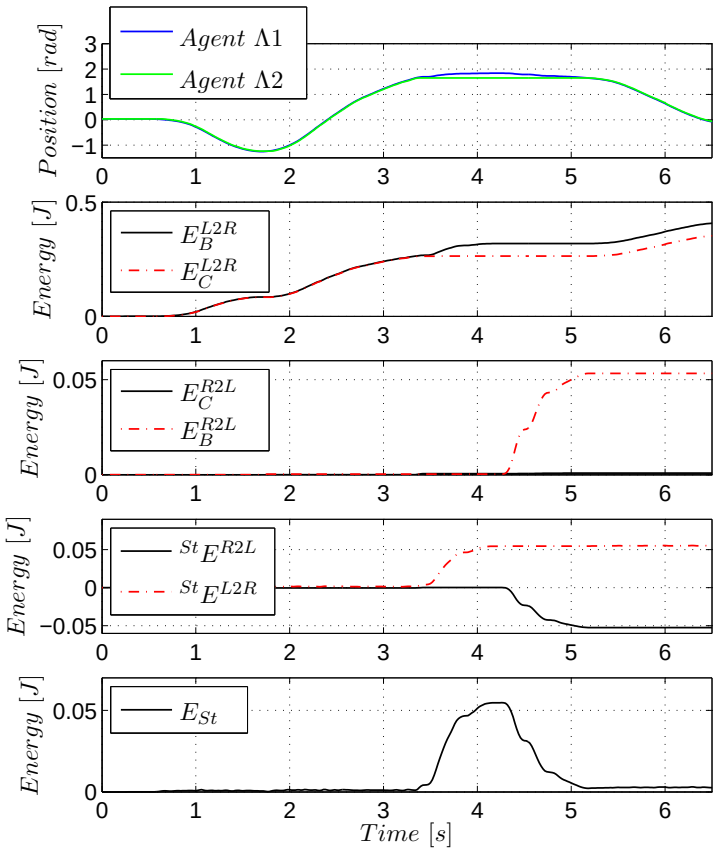

Experiment 4.8: Energy Behavior of a Controller with Energy Storage Element
This experiment presents a free motion and a wall contact in a teleoperation setup without communication delay. The plot E_{St} depicts the potential energy storage of the PI controller. During the wall contact, the energy in the storage is charged up in L2R direction by $^{St}E^{L2R}$ and later released in R2L direction (compare $^{St}E^{R2L}$).

position drift and leads to the intended charging of the coupling controller as the energy storage element. Similarly to Approach 2, the energy that is generated by the CC in L2R direction and crosses the storage element can be limited on the right side of the storage element (port C). In contrast, energy that crosses the CC in L2R direction and that is reflected by the storage element back in R2L direction is, in Approach 3, only affected by passivity control when it leaves the delayed 2-port on the left side.

Position Drift The following experiments that have been performed with the bilateral rotatory 1-DoF setup described in appendix A.1 line out another critical drawback of the TDPN approach. The first experiment Exp. 4.9 considers a symmetric roundtrip delay of 30ms in a PF_{comp} architecture (compare Fig. 2.3.5). A free motion with low ($t = [0.2s, 3s]$) and high velocities ($t = [3s, 5s]$) as well as a wall contact of the slave device ($t = [5.7s, 7.3s]$) are presented. Already at low velocity, a position drift results from the dissipation of the admittance type PC although with position drift compensation [8] has been implemented. The position drift compensation acts at $t = 3.2s$ such that the slave is matched to the delayed master position. Although the human operator initiates the motion, overall, more energy is flowing from slave to master (compare E_3^{R2L} and E_4^{L2R}). Especially during the wall contact, energy is transmitted in this direction. Since the energies leaving the PC in the relevant direction (E_6^{L2R}, E_1^{R2L}) are always lower than the energies entering the communication channels (E_4^{L2R}, E_3^{R2L}), the set of TDPNs and PCs is passive.

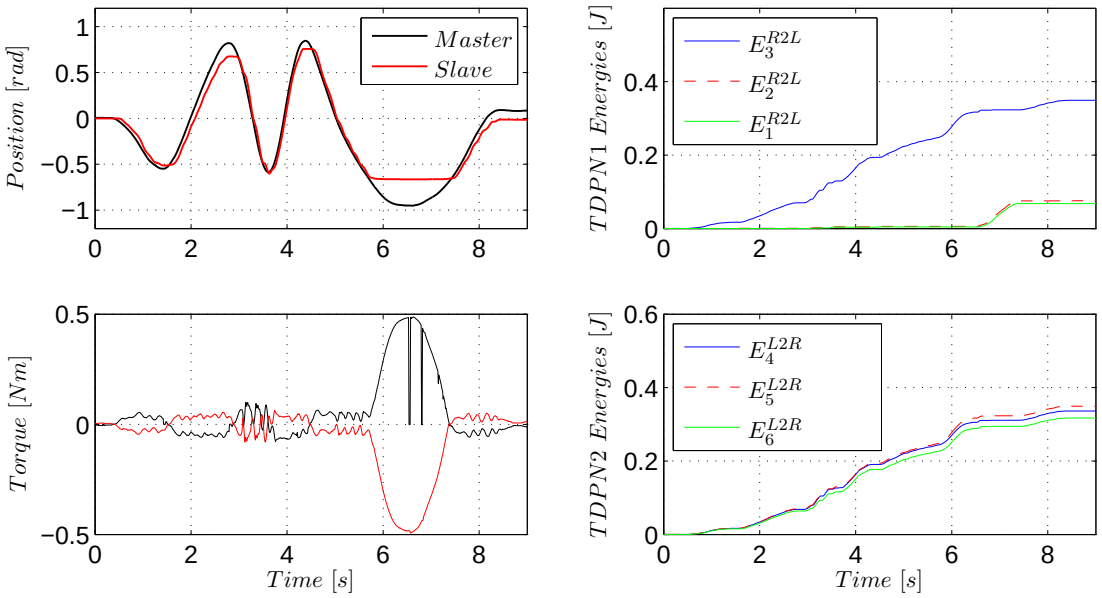

Experiment 4.9: Free Motion and Wall Contact with 30ms roundtrip delay in Approach 1
This experiment presents a slow and fast sinusoidal free motion and a wall contact. The admittance type PC leads to a position drift due to which the maximum deflection of the master device is not reached by the slave device ($t = 3s$, $t = 4.2s$). Also, after the wall contact, a position offset can be analyzed although the coupling torque is zero. The position drift compensation acts at $t = 3.2s$ such that the slave is matched to the delayed master position.

In the second experiment Exp. 4.10, the approach is applied at a roundtrip delay

of 200ms. A wall contact ($t = [2s, 4.3s]$) and a slow and fast free motion situation ($t = [4.3s, 10s]$) is depicted in plot Exp. 4.10. Despite the slow master motion, the position tracking of the slave device is week due to the dissipation of the admittance PC. Since there are few phases of energy dissipation in the communication channel, the position drift can not be fully compensated. During the wall contact, the impedance type PC dissipates energy generated in TDPN1. The energies leaving the PCs are always lower then the energies entering the respective TDPN. That confirms that the PCs guarantee a passive communication. Since Approach 3 applies only impedance type

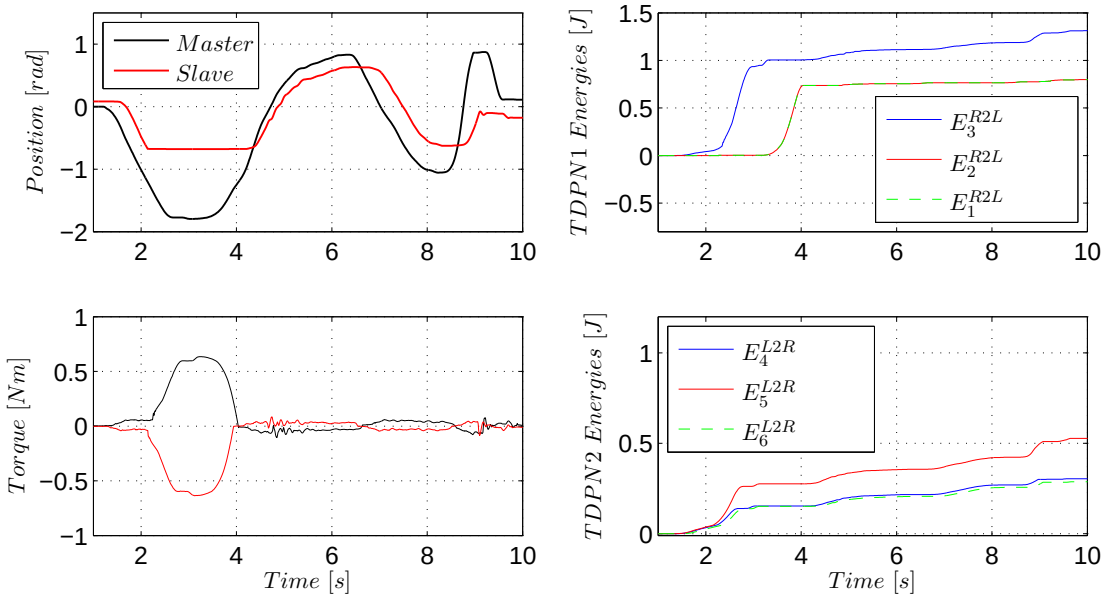

Experiment 4.10: Free Motion and Wall Contact with 200ms roundtrip delay in Approach 1 This experiment presents a wall contact and a slow and fast sinusoidal free motion. Despite the slow master motion, the position tracking of the slave device is week due to the dissipation of the admittance PC. Since there are few phases of energy dissipation in the communication channel, the position drift can be only once ($t = 4.2s$) well compensated.

passivity controllers position drift can be avoided. This renders Approach 3 especially favourable for the coupling of autonomous robotic systems since there, in contrast to teleoperation, no human operator can compensate for the position mismatch.

Since Approach 3 seems to be superior to Approach 2 which dissipates too much energy due to flow direction dependency, Approach 1 and Approach 3 are contrasted in a comparative study in the following.

4.1.3.1 Technical Setup

The 1-DoF hardware described in appendix A.1 has been applied due to its low mass and low damping. To assure the reproducibility of the results and consistent system inputs, a human operator has been simulated with an additional 1-DoF system connected with the master device through a rigid bar as presented in Fig. 4.1.8. In both approaches, a PF_{comp} architecture and for Approach 1 a position drift compensation has been implemented.

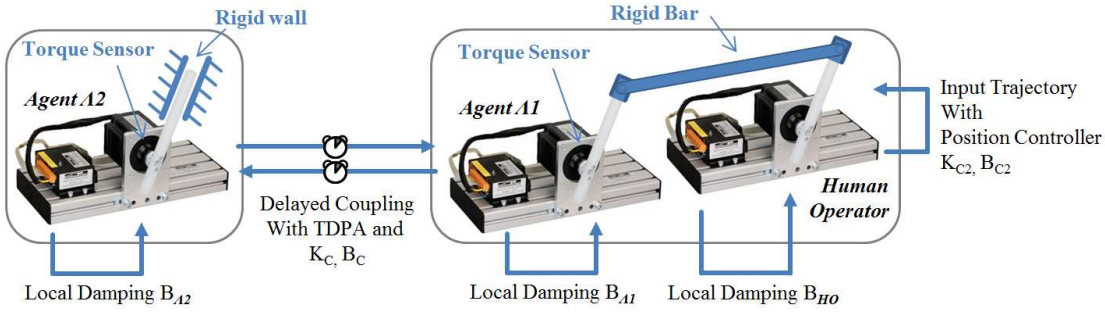

Figure 4.1.8: Technical Setup of Comparative Study
A human operator has been simulated with an additional 1-DoF system connected with the master device through a rigid bar. A rigid wall could be applied at the slave device.

4.1.3.2 Method

A position controller acted on the human operator device aiming a sinusoidal motion with increasing frequency $f \in [0.2, 1.2]$. The approaches were analyzed respecting different roundtrip-delays ($T_i \in \{30ms, 100ms, 200ms, 400ms\}$, $i \in \{1, 2\}$). The stiffness K_{PI} of the position controller connecting master and slave device was set to $K_{PI} = 2\frac{Nm}{rad}$ in both approaches. Individual position controller damping B_{PI} and local damping gains of the devices were set for each roundtrip-delay, to achieve (subjectively rated) the best performance regarding the specific roundtrip-delay. To consider different environmental impedances Z_e, the approaches were evaluated in a free motion ($Z_e = 0$) and a wall contact situation with fixed slave device ($Z_e \approx \infty$).

The metrics included the

- mean effective impedance $MV(K_{eff})$ of evaluated frequencies $f \in [0Hz, 1.4Hz]$ [12],
- the path error $Path_{error}$ between the path length of the human operator motion and the motion of the slave device,
- the path $Path_m$ of the master device,
- the mean position error $MV(|P_{error}|)$ between the slave device and the delayed master device position,
- the mean value of the absolute slave interaction torques $MV(|T_s|)$,
- the sum of energy E_{diss} dissipated by the two passivity controllers,
- the mean value of the division $PCT_T = (T_m + T_s)/(2T^K)$ of actual torque T_i $i \in \{m, s\}$ at master (m) and slave device (s) and expected computed torque $T^K = (x_s(k) - x_m(k))K_C$ and
- the division $PCT_E = (E_m + E_s)/(E_m^K + E_s^K)$ of actual $E_i(k) = \sum_{n=0}^{k}(v_i(n)F_i(n))$ and expected energy flow $E_i^K = \sum_{n=0}^{k}(v_i(n)(x_s(n) - x_m(n))K_C)$.

In the wall contact experiments, high effective stiffness values $MV(K_{eff})$ are desired. In contrast, in free motion without environment contact, $MV(K_{eff})$ should be zero. The position and path error should be low in both situations. The percentage of transmitted energy (PCT_E) and the percentage of torques (PCT_T) should be close to one. In the wall contact scenario, the slave is not able to move such that $Path_m$ and PCT_T are considered instead of position error and PCT_E. The metric $Path_m$ should have low values. The dissipated energy E_{diss} should be low and the interaction torque T_{Sl} contains information on the desired motion on the slave side.

4.1.3.3 Results

The experiment plots Exp. 4.11a to Exp. 4.12b depict the results for different environmental impedances and roundtrip-delays. Since, in general, the system performance at high delays is better at low frequency motions, the results of different frequency bandwidths are depicted.

In experiment Exp. 4.11a, the free motion scenario at low input frequencies is depicted. At a roundtrip delay of 30ms, the dissipated energy and the position and path errors are lower for Approach 3. With increasing delay, the position and path errors increase intensively in Approach 1 despite the slow motion. The dissipated energy E_{diss} is higher for Approach 3 for most situations. PCT_E has better values for Approach 3 at all delays. Aside from the 200ms condition, the effective stiffness is low in both approaches. The high $MV(K_{eff})$ of Approach 3 can be avoided in a real scenario by the human operator that can react on a perceived resistance.

In the wall contact situation, at slow motion (see Exp. 4.11b), the $MV(K_{eff})$ is higher for Approach 3. The large path error of Approach 1 results from position drift. PCT_T has better values for Approach 3 at all delays. Also, the metric $MV(|T_s|)$ indicates that the desired slave motion results in higher slave torques in Approach 3. This is a result of the position drift of the admittance type in Approach 1 that leads to a lower wall penetration of the master although the path of the master device equals in both approaches.

The results at a bigger range of input frequencies in Exp. 4.12 are similar but less pronounced. This is due to the fact that the automated high frequency inputs do not react on the system behavior in contrast to a human operator. Furthermore, the position and path errors are increased for both approaches due to faster motions. To avoid large position drift in Approach 1 and to avoid high resistive torques due to position deviations in Approach 3, with increasing delays, slower motions are required. Note that the path of the master in the wall contact situation reduces with the delay since the maximum frequency was set to $1.2Hz$ for $100ms$ roundtrip delay and to $1Hz$ for $200ms$ and $400ms$ roundtrip delay.

4.1.3.4 Discussion of Experimental Comparison

In free motion, the position following is the most relevant criterion. The large path and position error of Approach 1 reduces transparency strongly. The effective stiffness criterion provides low accuracy in the free motion situation (compare Exp. 4.11a and Exp. 4.12a). The dissipated energy is no suitable criterion since the energy amount of the system depends on the system behavior which differs strongly for the two approaches.

Due to the position drift in Approach 1, the torques and also the power flow are lower. Thus, also the relative dissipation of energy is not a reliable criterion. In contrast, the percentage of transmitted energy which refers to the expected power flow resulting from the reference position and the controller constant K_C is more reasonable. Overall, considering free motion, Approach 3 with lower position and path errors and higher PCT_E promises higher transparency.

Also during wall contacts, Approach 3 provides better performance. This fact can be drawn from the higher effective stiffness and higher slave interaction torques (compare PCT_T and $MV(|T_s|)$) throughout all experiments.

4.1.4 Discussion on Time Delay Control Approaches

Two time delay control approaches that can be applied in a modular way to multilateral control have been presented in this section. Approach 2 and Approach 3 do not require admittance type PCs that lead to position drift but only impedance type PCs since besides the communication channel also the energy behavior of the PI controller is considered. Approach 3 does not require conservative energy limitations in contrast to Approach 2. Also, the force feedback quality during wall contact is improved by Approach 3. The comparative study of Section 4.1.3 showed that compared to Approach 1, Approach 3 leads to higher performance in free motion and wall contact scenario for all delays.

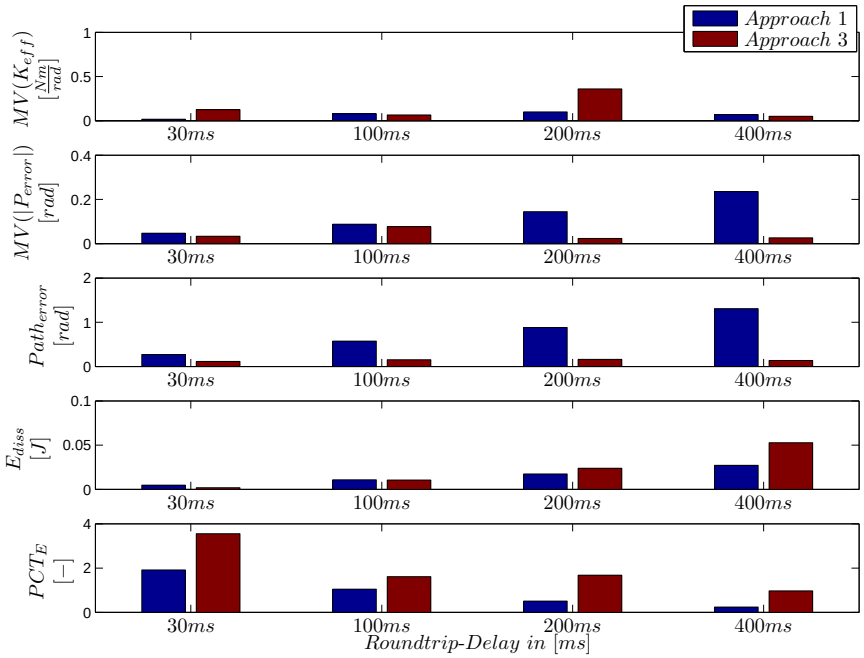

(a) Free Motion

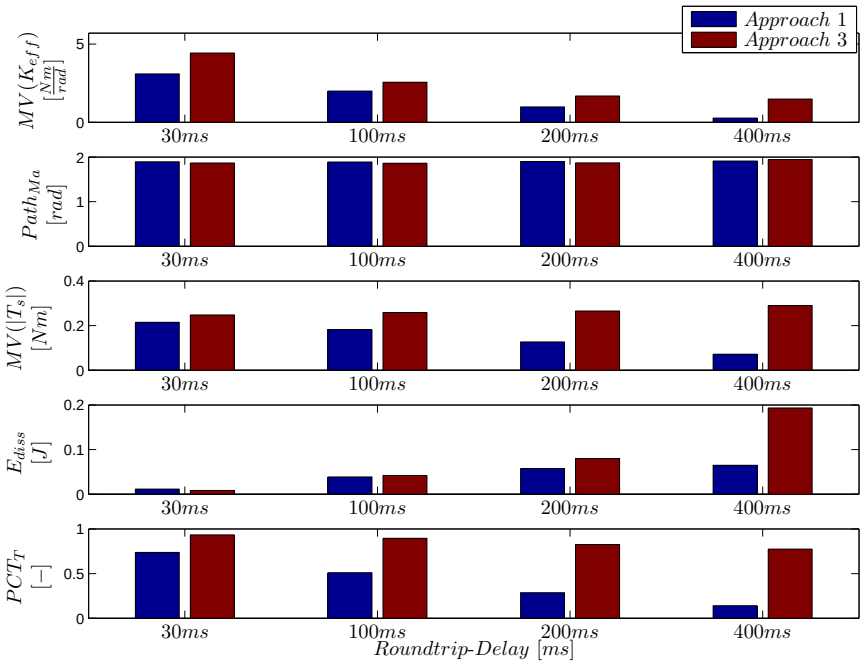

(b) Wall Contact

Experiment 4.11: System Comparison at $f \in [0.2Hz]$
The large path error of Approach 1 during free motion results from position drift and reduces transparency strongly. In the wall contact situation, the $MV(K_{eff})$ metric with higher values for Approach 3 promises higher transparency in terms of transmitted impedances for Approach 3. At higher delays, more energy is dissipated in Approach 3. This is due to the fact that the position drift leads to lower coupling torques and therefore to lower power flow in Approach 1. PCT_E and PCT_F have better values for Approach 3 at all delays.

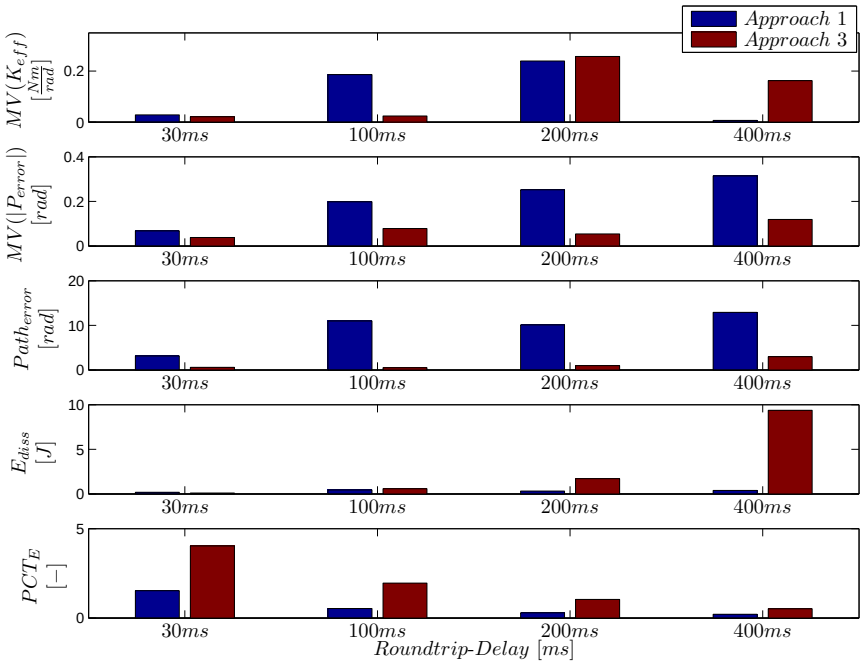

(a) Free Motion

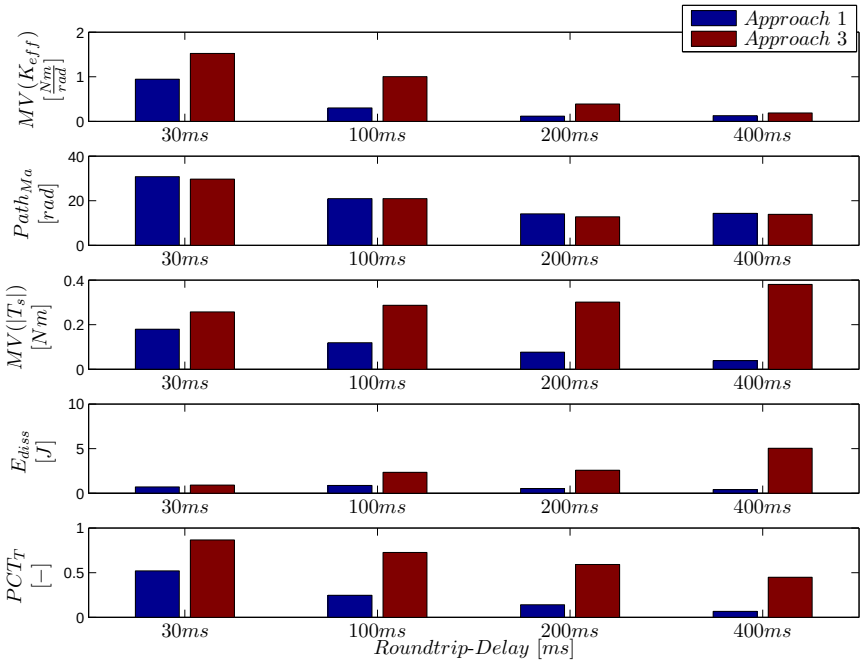

(b) Wall Contact

Experiment 4.12: System Comparison at $f \in [0.2Hz - 1.4Hz]$
The differences of Approach 1 and 3 at a bigger range of input frequencies are less pronounced. This is due to the fact that the automated high frequency inputs do not react on the system behavior. To avoid large position drift in Approach 1 and to avoid high resistive torques due to position deviations in Approach 3, with increasing delays, the human operator has to adapt his/her inputs to the system behavior. PCT_E and PCT_F have better values for Approach 3 at all delays.

4.2 Measured Force Feedback

The performance of a telepresence system in terms of transparency can be enhanced if the slave robot is equipped with a force sensor that measures the interaction force between slave and environment. This is due to the fact that such measured forces have a higher frequency bandwidth and thus present contacts more accurately than the computed force of a PI controller. Furthermore, the dynamics of the slave robot are masked more effectively if the force sensor is positioned close to the slave's tool tip. I.e. in free motion and during acceleration no force feedback is generated.

In this section, it will first be shown that the only available approach for passivity control of systems with measured force feedback [180] is not applicable to multilateral systems. Furthermore, a concept based on passivity control in the time domain [124] is introduced that promises to be less conservative in comparison to other time invariant or model based approaches. This holds for multilateral as well as for bilateral systems.

4.2.1 System Description

Figure 2.1.3 in Section 2.1 depicts a 1-DoF PF_{meas} architecture [44, 77, 24]. A position or velocity respectively is sent from master to the PI controller on the slave side. The measured interaction force between slave and environment F_e is fed back to the master through the communication channel. The communication channel is represented by the Laplace transformation of a pure constant delay $e^{-T_1 s}$ and $e^{-T_2 s}$.

The network representation of a PF_{meas} architecture without time delay is depicted in Fig. 4.2.1. In this architecture, the dependent effort source injects the measured force $F_t = F_e$ into the circuit of the master side.

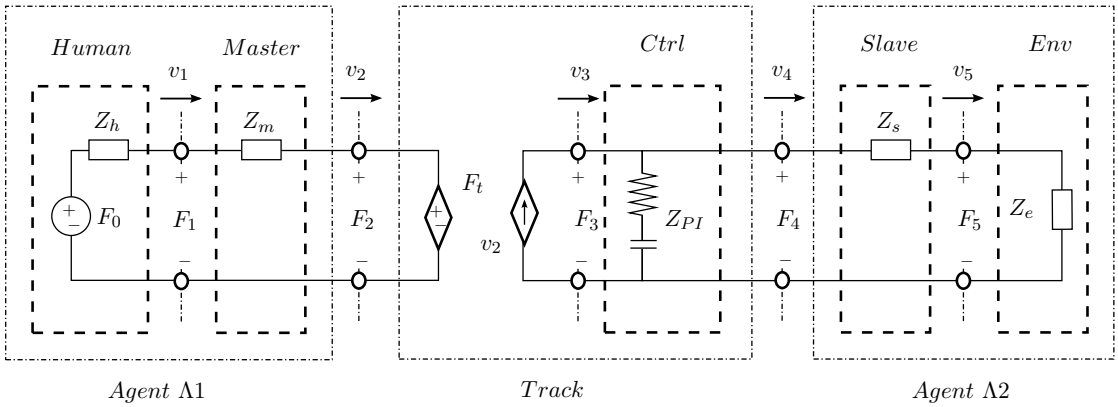

Figure 4.2.1: Network Representation of a PF architecture without Time Delay
The track is split up in two circuits with different energy flow direction. The effort source F_t is generalized such that a measured force or a computed force can be fed back to the master side at port 1 in R2L direction. No delay is considered in the presented track. The flow source transmits the master velocity v_m to the slave side in L2R direction.

The approach allowing measured force feedback in passive bilateral teleoperators proposed in [180] relies on a different network scheme. Fig. 4.2.2 shows the 1-port teleoperator considered in the respective passivity analysis. The authors of [180] showed that this 1-port teleoperator is a correct, power correlated network representation of the

PF_{meas} architecture. They analyzed that passivity can only be achieved if all models in the 1-port teleoperator (master, slave, environment) are considered which results in a controller parametrization providing low performance. Furthermore, a maximal environment impedance has to be assumed, such that the force feedback and thus the system's transparency does not need to be further reduced. Analyzing Fig. 4.2.2, it becomes obvious that it is impossible to consider a communication channel 2-port in a system with 1-port teleoperator since the communication channel lies inside the 1-port teleoperator. Therefore, the approach is incompatible to delayed teleoperation systems. Also, no 1-port teleoperator can be designed for multilateral setups since the extraction of a track subsystem is not possible. Thus, the method of [180] is not employable in multilateral control.

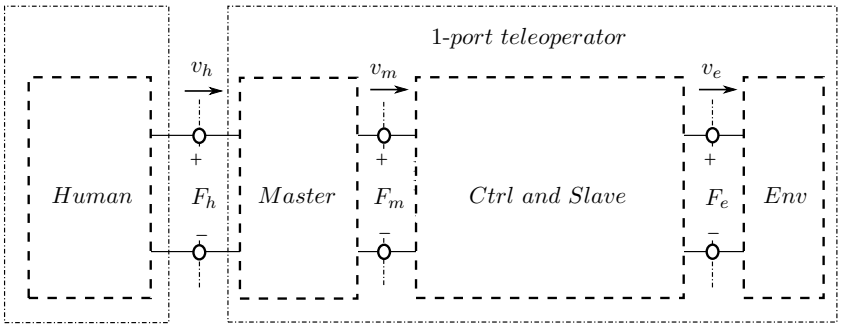

Figure 4.2.2: Network Representation of the 1-port Teleoperator Proposed in [180]
The 1-port teleoperator considered in the passivity analysis of [180] includes Master, Controller, Slave and Environment.

The authors of [180] showed that the 1-port teleoperator presented in Fig. 4.2.2 is a correct, power correlated network representation of the PF_{meas} architecture. They analyzed that passivity can only be achieved if all models in the 1-port teleoperator (master, slave, environment) are considered which results in a controller parametrization providing low performance. Furthermore, a maximal environment impedance has to be assumed, such that the force feedback and thus the system's transparency does not need to be further reduced. Still, several control methods require the passivity of the whole system since a passive subsystem only guarantees stability if all other subsystems are passive. On the other hand, analyzing Fig. 4.2.2 it becomes obvious that it is impossible to integrate a communication channel 2-port into a system with 1-port teleoperator since the communication channel lies inside the 1-port teleoperator. Therefore, the approach is incompatible to delayed teleoperation systems. Also, no 1-port teleoperator can be designed for multilateral setups since the extraction of a track subsystem is not possible. Thus, the method of [180] is not employable in multilateral control.

4.2.2 Passivity Control

The proposed concept is based on the time domain passivity control. It is applicable in bilateral as well as multilateral systems, does not rely on imprecise model parameters and guarantees passivity of a track module via an adaptive and thus non-conservative control method.

Through the dependent effort source F_t a correct, power correlated network representation can be found for measured force feedback. Based on the generalized PF architecture in Fig. 4.2.1, the passivity of an open-loop teleoperator system has been discussed in Section 3.3.3. This evaluation is fundamental for the proposed control approach for measured force feedback. Considering the network representation of Fig. 4.2.1, the energy that leads to the slave motion E_4^{L2R}, depends on the energy input to the coupling controller E_4^{R2L} and E_3^{L2R} but not on the energy E_2^{L2R} of the master side circuit. The energy that leaves to the master in a PF_{comp} architecture at port 2 E_2^{R2L} equals E_3^{R2L}. Since the PF_{comp} architecture can be considered as a passive reference, any force feedback F_t that guarantees that $E_2^{R2L} < E_3^{R2L}$ results in a passive system. Therefore, the power in R2L direction at port 2 can be reduced or even canceled (as for open-loop systems) without disturbance of the system's passivity. This is a fundamental insight for the comprehension of the presented passivity control concept.

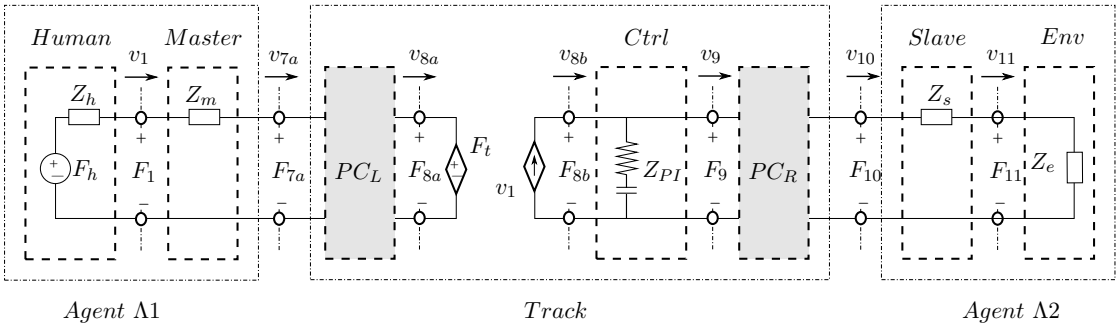

Figure 4.2.3: Network Representation of a Passive PF_{meas} Architecture without Time Delay
The passivity controllers PC_L and PC_R are located on the left and right end of the track. Therefore, the PI controller is considered in the passivity controlled subsystem. PC_L controls the R2L and PC_R controls the L2R direction of energy flow.

Fig. 4.2.3 presents a more detailed network representation with passivity controllers PC_L and PC_R that can be neglected in the beginning. The power at the ports in different direction of flow can be distinguished with respect to the sign according to Section 2.1.3.3.

The proposed passivity control (compare Fig. 4.2.3) is based on the following observations:

- In a PF_{comp} architecture, the effort source injects the force $F_t = F_{8b}$. This system is passive as the PI controller has a passive behavior (compare analysis of PI energy behavior in Section 4.1.2):

$$\sum_{n=0}^{k}(P_{8b}^{L2R}(n)+P_9^{R2L}(n)) \geq \sum_{n=0}^{k}(P_{8b}^{R2L}(n) + P_9^{L2R}(n)). \tag{4.16}$$

  The power flowing at port 8b and 8a equal in the PF_{comp} architecture.

- The overall system remains passive if the computed force feedback is reduced or canceled, as discussed in Section 3.3.3.

- I.e. as long as the effort source ($F_t = F_{11}$) does not inject more energy in R2L direction compared to the computed force feedback ($F_t = F_{8b}$), the control architecture remains passive. The L2R part of the track is not directly influenced by the measured force feedback.
- The PI controller represents an energy storage. The release of the stored energy is not an energy generation but preserves passivity.

The implementation of the proposed time domain passivity control concept is based on two principles:

- In order to calculate the energy E_{St} injected into the PI controller, the energies flowing at port 8b in L2R and at port 9 in R2L direction have to be observed.
- With respect to the energy storage in the PI controller, the power exiting at port 9 in L2R and at port 8a in R2L direction have to be limited by a passivity controller.

This limitation can be realized by dissipative impedance type PCs as depicted in Fig. 4.2.3. Only if enough energy has entered the controller beforehand a certain power may leave at port 8a or 9 (P_{8a}^{R2L} or P_{9}^{L2R}).

In each time step the energy content E_{St} of the controller has to be updated:

$$E_{St}(k) = E_{St}(k-1) + (P_{8b}^{L2R}(k) + P_{9}^{R2L}(k))T_s. \tag{4.17}$$

The desired output P_{out}^{des} in both direction of energy flow has to be calculated first:

$$P_{out}^{des}(k) = P_{8a}^{R2L}(k) + P_{9}^{L2R}(k). \tag{4.18}$$

If this power is smaller than or equal to the energy content of the controller ($P_{out}^{des} \leq E_{St}$), this power may leave at the respective ports. Just if more power than available is exiting at port 8a or 9, the passivity controllers need to dissipate the excess power:

$$P_{obs}^{PC_L}(k) = \begin{cases} P_{obs}(k)\frac{P_{8a}^{R2L}(k)}{P_{out}^{des}(k)}, & \text{if } E_{St}(k) < P_{out}^{des}(k)T_s \\ 0, & \text{if } E_{St}(k) \geq P_{out}^{des}(k)T_s \end{cases},$$

$$P_{obs}^{PC_R}(k) = \begin{cases} P_{obs}(k)\frac{P_{9}^{L2R}(k)}{P_{out}^{des}(k)}, & \text{if } E_{St}(k) < P_{out}^{des}(k)T_s \\ 0, & \text{if } E_{St}(k) \geq P_{out}^{des}(k)T_s \end{cases}.$$

T_s is the system sampling time and P_{obs} is the observed power

$$P_{obs}(k) = E_{St}(k)/T_s - P_{out}^{des}(k). \tag{4.19}$$

Thus, $E_{obs}(k)$ results in

$$E_{obs}^{PC_i}(k) = T_s \sum_{n=0}^{k} P_{obs}^{PC_i}(k), \tag{4.20}$$

with $i \in \{L, R\}$. The energy that has to be dissipated has to be calculated analogous to equations (2.50) and (2.51). The functionality of impedance type PCs is explained in

Section 2.2. The passivity of the track in Fig. 4.2.3 can be guaranteed, if the 4-port of PC_L, PI and PC_R is passive:

$$E_{PP}(k) = T_s \sum_{n=0}^{k} (P_{8b}^{L2R}(n) + P_9^{R2L}(n) - P_{7a}^{R2L}(n) - P_{10}^{L2R}(n)) \geq 0. \tag{4.21}$$

Equ. (4.21) is fulfilled since the passivity controllers assure that the output energy at those 4 ports is lower or equal to the input energy and the power is monotonously increasing:

$$\sum_{n=0}^{k} (P_{8b}^{L2R}(n) + P_9^{R2L}(n))T_s \geq \sum_{n=0}^{k} (P_{8b}^{R2L}(n) + P_9^{L2R}(n))T_s, \tag{4.22}$$

$$P_{7a}^{R2L}(k) \leq P_{8a}^{R2L}(k) \quad \text{and} \quad P_{10}^{L2R}(k) \leq P_9^{L2R}(k). \tag{4.23}$$

For the next time step, the energy content E_{St} has to be updated, as the power P_{7a}^{R2L} and P_{10}^{L2R} exited at the respective ports:

$$E_{St}(k) = E_{St}(k-1) + P_{8b}^{L2R}(k) + P_9^{R2L}(k) - P_{7a}^{R2L}(k) - P_{10}^{R2L}(k). \tag{4.24}$$

During free motion of the slave, this time domain passivity control concept maintains passivity without dissipation. When the slave goes into a sudden wall contact due to the commands of the master device, energy is flowing from master to slave. Therefore, the PC_L does not need to dissipate energy such that the measured force feedback with peak forces is provided to the operator and the impact dynamics can be well perceived. The PC_L only needs to dissipate energy when energy is injected from the slave side, e.g. if an external force acts on the slave and if the required additional amount of energy is not stored in E_{St}. Still, in these situations the PC only filters out high frequency forces such that approximately the force produced by the PI controller will be displayed at the master device.

In order to stabilize the system despite time delay, this approach can be merged with the TDPA proposed in [9] (Section 2.3.2.3). The delayed communication channel is then represented by two Time Domain Power Networks (TDPN, Fig. 4.2.4) and two PCs (PC_1, PC_2) are introduced aside these TDPNs. Analogously to Section 2.3.2.3, the energy behavior of the $TDPN1$ can be observed at port 7a and 5a. The energy generated in R2L direction by the time delay in $TDPN1$ is dissipated by the impedance type PC_1. This holds for the $TDPN2$ and admittance type PC_2 in the same way. Thus, the passivity of the track can be preserved despite time delay. The resulting track module for the PF_{meas} architecture can be applied directly in multilateral systems.

4.2.3 Experiments

The experiments on the PF_{meas} approach have been performed with the 1-DoF setup presented in detail in Appendix A.1.

In the first experiments Exp. 4.13 and Exp. 4.14, the performance of bilateral measured and computed force feedback are compared in free motion and during a wall contact. Since the devices have a very low mass and friction, a local damping was applied to each device. Still, zero damping was chosen in the PI controller parameters

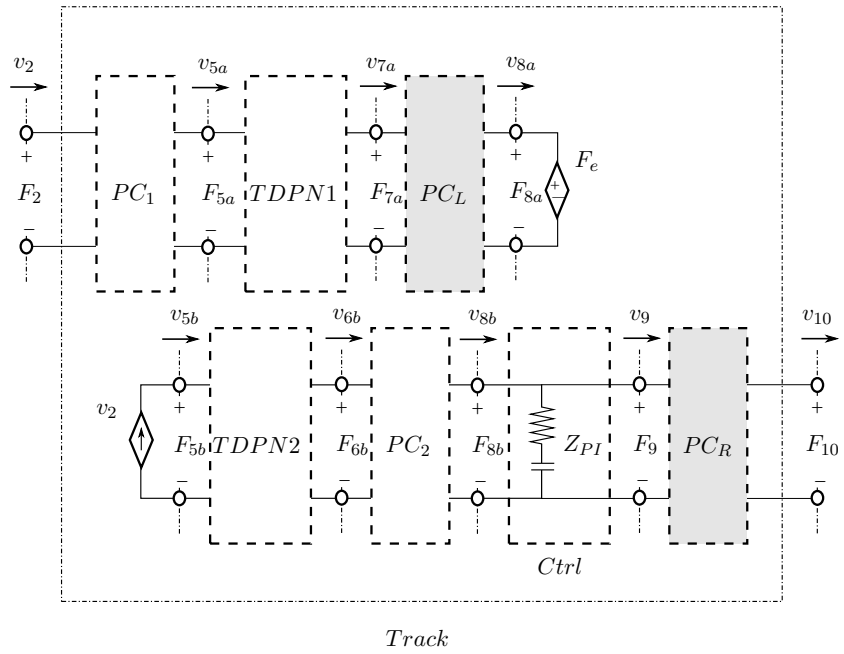

Figure 4.2.4: Network Representation of passive PF_{meas} Architecture with Time Delay
In case of delay in the communication channel, two sets of TDPN and PC subsystems need to be considered in the track. PC_L as well as PC_R are implemented on the right side of the communication channel.

in order to test the most critical case for the proposed passivity control for the PF_{meas} architecture. The performance of computed force feedback is displayed in plot Exp. 4.13 and of measured force feedback in plot Exp. 4.14. The plot of P_9^{L2R} in Exp. 4.13 shows that in free motion and during the entering phase of the wall penetration, energy is mainly generated at the master device. At low speeds the master obviously perceives higher resistance in the PF_{comp} architecture as can be analyzed in Exp. 4.13 ($t = [2.5s, 4s]$) and Exp. 4.14 ($t = [4.2s, 5.6s]$). Since the torque sensor is not positioned at the tool tip, the grip mass leads to a measured feedback force due to high acceleration during faster motions (plot Exp. 4.13: $t = [1.5s, 2.5s]$; plot Exp. 4.14: $t = [3s, 4s]$). When the master moves out of the penetrated wall ($t = [4.8s, 5s]$ in plot Exp. 4.13) energy is flowing into direction to the master. This energy exiting the PI controller has been introduced before when the master moved into the wall. During the wall contact, no power is flowing to the slave since its velocity is zero. The impact into the wall causes a peak in the measured force ($t = 6.4s$ in plot Exp. 4.14). In contrast to the PF_{comp} architecture, in the PF_{meas} version this impact can be well perceived by the operator. Although the dissipative damping of the controller was zero, the passivity controllers PC_L and PC_R do not need to dissipate energy (see F_{PC} in plot Exp. 4.14). The passivity of the subsystem consisting of PI, PC_L and PC_R is guaranteed as the sum of input and output energy E_{PP} measured at port $7a$ and port 10 (compare equation (4.21)) is never negative. Since alternative approaches require a constant high down-scaling of the measured feedback force, the time domain control obviously provides higher transparency.

The second experiment Exp. 4.15 considers a delayed communication channel with

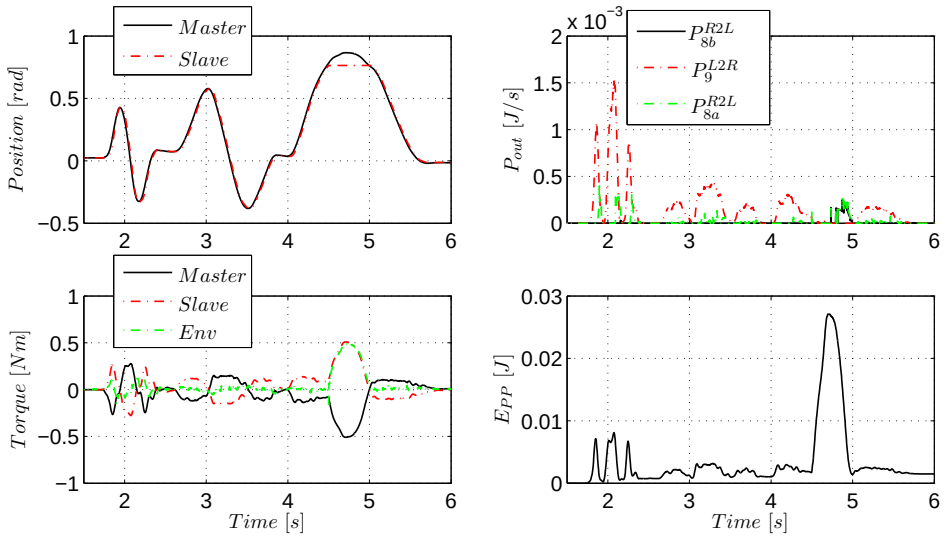

Experiment 4.13: Free Motion and Wall Contact with Computed Force Feedback
A slow and fast sinusoidal motion and a wall contact is performed. In the instant when the slave gets in contact with the wall, the master doesn't receive a high feedback force. The impact is measured by the force sensor, but the computed controller force feedback is smooth in contrast. The passivity proof plot shows that the energy storage is filled up but never emptied such that the passivity controllers PC_L and PC_R do not need to dissipate energy.

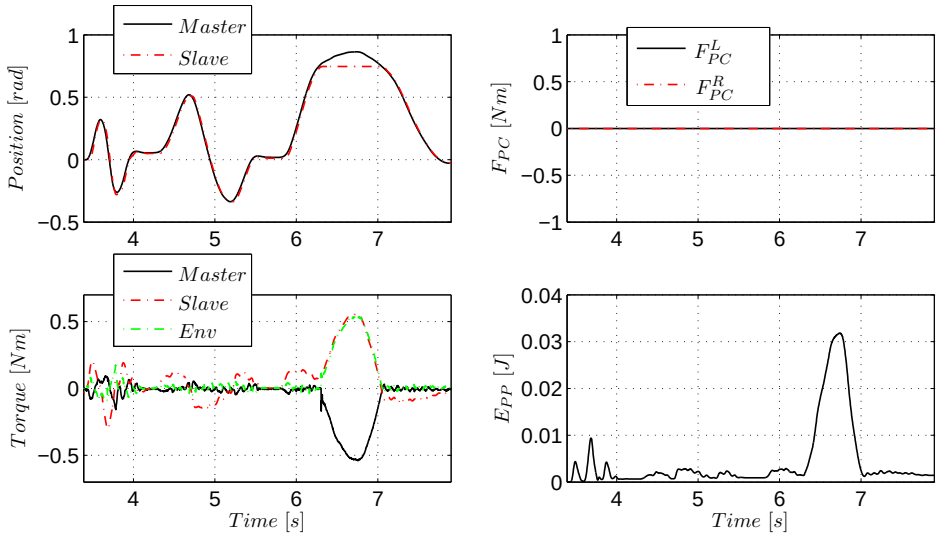

Experiment 4.14: Free Motion and Wall Contact with Measured Force Feedback
A slow and fast sinusoidal motion and a wall contact is performed. In the instant when the slave gets in contact with the wall, the master receives a high feedback force that is measured by the force sensor. The plot of E_{PP} serving the passivity proof shows that the energy storage is filled up but never emptied such that the passivity controllers PC_L and PC_R do not need to dissipate energy.

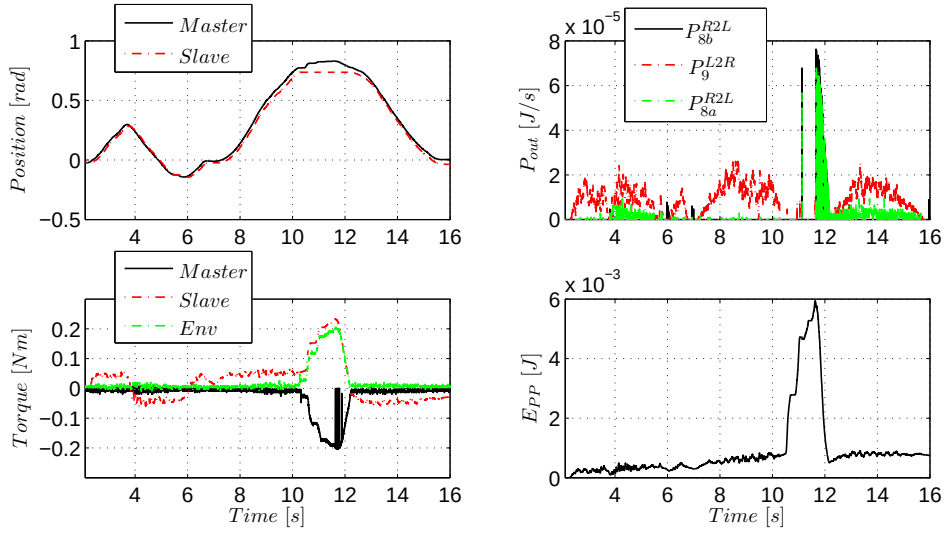

Experiment 4.15: Wall Contact with Measured Force Feedback at 100ms Roundtrip Delay
The delay reduces the position tracking quality when compared to the undelayed case. The strictly positive energy sum E_{PP} confirms that the passivity of the subsystem consisting of PI, PC_L and PC_R is still guaranteed. The PC_L and PC_R does not need to dissipate energy.

100ms roundtrip delay. The same motion sequence as above is performed. Of course, the delay reduces the position following quality in contrast to the undelayed case of Exp. 4.14. The strictly positive energy sum E_{PP} confirms that the passivity of the subsystem consisting of PI, PC_L and PC_R is still guaranteed.

The PF_{meas} architecture has been applied to a trilateral fully connected system (compare Fig. 3.3.3) in experiment Exp. 4.16. *Agent* $\Lambda 1$ and *Agent* $\Lambda 2$ are human operators with the respective master devices that are coupled to the slave *Agent* $\Lambda 3$ with a PF_{meas} track each. The *Agent* $\Lambda 1$ and *Agent* $\Lambda 2$ in contrast, receive computed force feedback from each other. For the sake of clarity, only the signals of *Track* $\Gamma 2$ connecting *Agent* $\Lambda 1$ and *Agent* $\Lambda 3$ are presented in plot Exp. 4.16. The slave is moved by *Agent* $\Lambda 1$ against the wall. Also, the trilateral setup provides satisfactory position tracking and the energy plot confirms the passivity of the approach. Note that in the analysis of multilateral couplings in Section 3.4, the adequacy of measured force feedback for multilateral scenarios has been discussed.

4.2.4 Discussion on PF_{meas} Architecture

A passive module for PF_{meas} architecture based on the TDPA has been designed for multilateral architectures in this section. As other approaches aiming at absolute stability or passivity of measured force feedback systems consider physical model parameters and therefore limit the force feedback more gravely and as the PCs dissipate rarely, the proposed approach designed in the time domain can be assumed to provide better performance. This holds for multilateral as well as general bilateral systems in the same way. Experiments with time delay proved the system's adequacy for the classical teleopera-

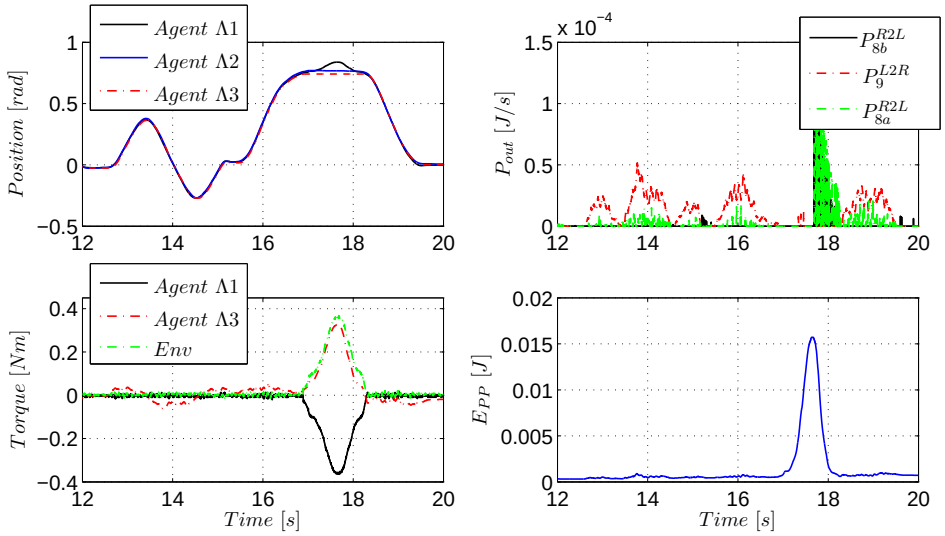

Experiment 4.16: Position Tracking in a Multilateral Setup (Forces and Energy Behavior of *Track* Γ2)
The human operators *Agent* Λ1 and *Agent* Λ2 are coupled with a PF_{comp} track, whereas *Agent* Λ1 and *Agent* Λ2 are coupled to the slave *Agent* Λ3 with a PF_{meas} track each. The trilateral setup provides satisfactory position tracking and the energy plot E_{PP} confirms the passivity of *Track* Γ2 representatively.

tion scenarios. Subjectively rated, the performance with respect to transparency could be improved substantially in free motion and at fast collisions compared to a PF_{comp} architecture.

4.3 3-Channel Architecture

As analyzed in [155, 46], the hybrid feedback of computed and measured force in a 3-*Channel* architecture leads to higher fidelity compared to systems with pure computed or measured force feedback. Literature on passive control of delayed bilateral teleoperation considers in general that the 3-*Channel* approach can be parametrized in a passive manner without further proof. But, to the best of the author's knowledge it has so far not been shown how the passivity of a 3-*Channel* coupling can be guaranteed.

In order to design a track module for this communication architecture, the control approach [124] presented in Section 4.2 is extended in the following. The developed time domain passivity control approach does not require models or conservative constant controller parameters and can be applied with benefit to both multilateral and bilateral 3-*Channel* teleoperation.

4.3.1 System Description

In Section 2.1, the signal flow diagram of a 3-*Channel* architecture has already been introduced with Fig. 2.1.5. Compared to the PF_{comp} architecture with two channels the force measured at the slave environment interaction is sent to the master side in addition to the computed force feedback. The computed force feedback F_c^{del} to the

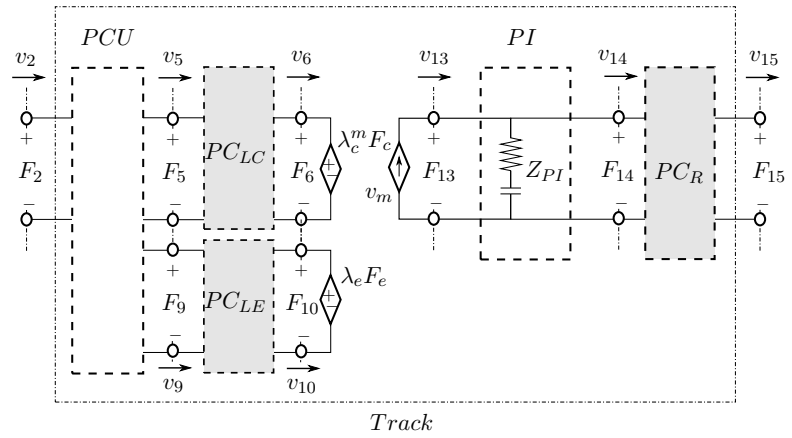

Figure 4.3.1: Network Representation of a 3-*Channel* Architecture with Passivity Control
Three PCs assure the passivity of the 3-*Channel* track. PC_R dissipates excessive energy in L2R direction. In R2L direction, PC_{LC} assures the passivity in the computed channel and PC_{LE} in the measured channel. The computed and measured force feedback is scaled by λ_c and λ_e respectively.

master is scaled by the parameter λ_c^m and the measured force feedback F_e^{del} by λ_e. The parameter have to be designed as follows:

$$\lambda_c^m, \lambda_e \in \mathbb{R}_0^+, \tag{4.25}$$

$$\lambda_c^m + \lambda_e = 1. \tag{4.26}$$

The coupling signals can be delayed by a time delay (T_1, T_2) in the communication channel.

In the network representation of a 3-*Channel* track in Fig. 4.3.1, delay is not considered in the first step. The network structure is split up into two circuits. In the case of the 3-*Channel* architecture, the communication channel is represented by the velocity source v_m and the force sources $\lambda_c^m F_c$ and $\lambda_e F_e$. The velocity source injects the energy from the master side (that leads to the motion of the slave) into the slave side circuit. The force sources inject the energy from the slave side into the circuit of the master. Note that energy flowing in direction from master to slave in the master's circuit is dissipated by the force sources. This is due to the fact that not the power resulting from the force feedback at port 2, but the power injected into the PI controller at port 13 leads to the slave's motion. The passive power control unit (PCU) represents the sum of feedback forces in the signal flow diagram.

4.3.2 Passivity Control

As mentioned before, the approach presented in [124] (Section 4.2) needs to be extended in the following. In analogy to this work, the hybrid force feedback and thus the two feedback channels are controlled with PCs as can be seen in Fig. 4.3.1.

As discussed in detail in [124], the PI position controller and thus the PF_{comp} architecture is passive such that its energy behavior (see Section 4.1.2) can be considered as a reference to the 3-*Channel* control structure. I.e. as long as not more energy is

flowing from slave to master at port 2 than in the case of the PF_{comp} architecture, the passivity of the control structure is maintained. This can be achieved via two methods:

- One passivity controller assures that the power flowing from slave to master at port 2 is always lower than the one flowing in the same direction at port 13 which represents the feedback that would result in case of the passive PF_{comp} architecture.
- The energy storage in the PI controller can be considered as a energy reference of a passive system. Energy that has entered the PI controller at port 13 and 14 may leave in direction to slave at port 15 and to the master at port 5 and port 9. This can be guaranteed by three passivity controllers.

The latter method is presented in the following as it promises the lowest conservatism.

The PI controller energy storage is charged up via the power entering the PI subsystem from port 13 and 14. The energy output of the controller at port 6, 10 and 14 may not exceed the current energy content of the PI controller. Therefore, the PC_{LC} dissipates excessive power in the computed force feedback channel, the PC_{LE} in the measured force feedback channel and PC_R can dissipate excessive energy in direction to the slave respectively.

The energy storage E_{St} of the PI controller can be calculated in each time step as follows:

$$E_{St}(k) = E_{St}(k-1) + (P_{13}^{L2R}(k) + P_{14}^{R2L}(k))T_s. \tag{4.27}$$

As analyzed in Section 3.3.3, the PI has a passive behavior:

$$\sum_{n=0}^{k}(P_{13}^{L2R}(n) + P_{14}^{R2L}(n))T_s \geq \sum_{n=0}^{k}(P_{13}^{R2L}(n) + P_{14}^{L2R}(n))T_s. \tag{4.28}$$

Therefore, to preserve passivity in the 3-*Channel* architecture, the power exiting at port 5,9 and 15 may not exceed the current energy content E_{St}. The PC_{LC}, PC_{LE} and PC_R dissipate excessive power exiting at port 6,10 and 14 respectively. The desired output power $P_{out}^{des}(k)$ at those ports is

$$P_{out}^{des}(k) = P_6^{R2L}(k) + P_{10}^{R2L}(k) + P_{14}^{L2R}(k). \tag{4.29}$$

If $P_{out}^{des}(k)$ does not exceed E_{St} no energy has to be dissipated. Otherwise, the PC can act as follows:

$$P_{obs}^{PC_{LC}}(k) = \begin{cases} P_{obs}(k)\frac{P_6^{R2L}(k)}{P_{out}^{des}(k)}, & \text{if } E_{St}(k) \leq P_{out}^{des}(k)T_s \\ 0, & \text{if } E_{St}(k) > P_{out}^{des}(k)T_s, \end{cases} \tag{4.30}$$

$$P_{obs}^{PC_{LE}}(k) = \begin{cases} P_{obs}(k)\frac{P_{10}^{R2L}(k)}{P_{out}^{des}(k)}, & \text{if } E_{St}(k) \leq P_{out}^{des}(k)T_s \\ 0, & \text{if } E_{St}(k) > P_{out}^{des}(k)T_s, \end{cases} \tag{4.31}$$

$$P_{obs}^{PC_R}(k) = \begin{cases} P_{obs}(k)\frac{P_{14}^{L2R}(k)}{P_{out}^{des}(k)}, & \text{if } E_{St}(k) \leq P_{out}^{des}(k)T_s \\ 0, & \text{if } \Delta E_{St}(k) > P_{out}^{des}(k)T_s, \end{cases} \tag{4.32}$$

with the observed power P_{obs} in the current time step:

$$P_{obs}(k) = E_{St}(k)/T_s - P_{out}^{des}(k). \tag{4.33}$$

Thus, $E_{obs}(k)$ results in

$$E_{obs}^{PC_j}(k) = T_s \sum_{n=0}^{k} P_{obs}^{PC_j}(k), \tag{4.34}$$

with $j \in \{LE, LC, R\}$. The energy that has to be dissipated has to be calculated analogous to equations (2.50) and (2.51). The functionality of impedance type PCs is explained in Section 2.2. Afterward, the available power E_{St} has to be updated, as the power P_5^{R2L},P_9^{R2L} and P_{15}^{L2R} left the track:

$$\begin{aligned} E_{St}(k) =& E_{St}(k-1) + (P_{13}^{L2R}(k) + P_{14}^{R2L}(k) - P_5^{R2L}(k) \\ & - P_9^{R2L}(k) - P_{15}^{L2R}(k))T_s. \end{aligned} \tag{4.35}$$

As the PCU can be analytically proven to be passive [121], the whole track in Fig. 4.3.1 is passive, if the combination of time domain passivity controlled subsystems PC_{LE}, PC_{LC}, PC_R and PI is passive:

$$E_{PP}(k) = \sum_{n=0}^{k} (P_{13}^{L2R}(n) + P_{14}^{R2L}(n) - P_5^{R2L}(n) - P_9^{R2L}(n) - P_{15}^{L2R}(n))T_s \geq 0. \tag{4.36}$$

This holds, since the energies are monotonously increasing and the passivity controllers assure that the output energy is lower or equal to the input energy in the relevant direction of power flow.

A 3-*Channel* track with delayed communication is shown in Fig. 4.3.2. The power consistency of the communication channels is assured via three TDPNs [10]. Three passivity controllers PC_1, PC_2 and PC_3 dissipate the energy generated by the time delays. The resulting track can be applied in multilateral systems in a modular way.

4.3.3 Experiments

In this section, the performance of the proposed passivity control for the 3-*Channel* architecture is evaluated. The applied 1-DoF setup is presented in detail in Appendix A.1.

The first experiment Exp. 4.17 presents a bilateral hybrid teleoperation setup ($\lambda_c^m = 0.5$, $\lambda_e = 0.5$). Analogously to the measured force feedback experiment ($\lambda_c^m = 0$, $\lambda_e = 1$, Exp. 4.14) in Section 4.2, free motions at different velocities and a wall contact of the slave are performed. In contrast to the pure measured force feedback setup in Exp. 4.14, the operator receives reduced haptic feedback on the dynamics of the slave during free motions at high acceleration as can be analyzed in Exp. 4.17. The peak force resulting from the impact into the wall is reduced ($\lambda_e = 0.5$) compared to pure measured force feedback. The plot of the strictly positive energy E_{PP} of the passivity controlled subsystems confirms the passivity of the track. The PCs do not need to dissipate energy.

Experiment Exp. 4.18 considers a 3-*Channel* architecture with 30ms roundtrip delay. The TDPA track as proposed in Fig. 4.3.2 is applied to preserve stability. As can be analyzed in plot Exp. 4.18 the position of the slave is delayed with respect to the master position. The 3-*Channel* architecture is proven to be passive since energy E_{PP} is positive.

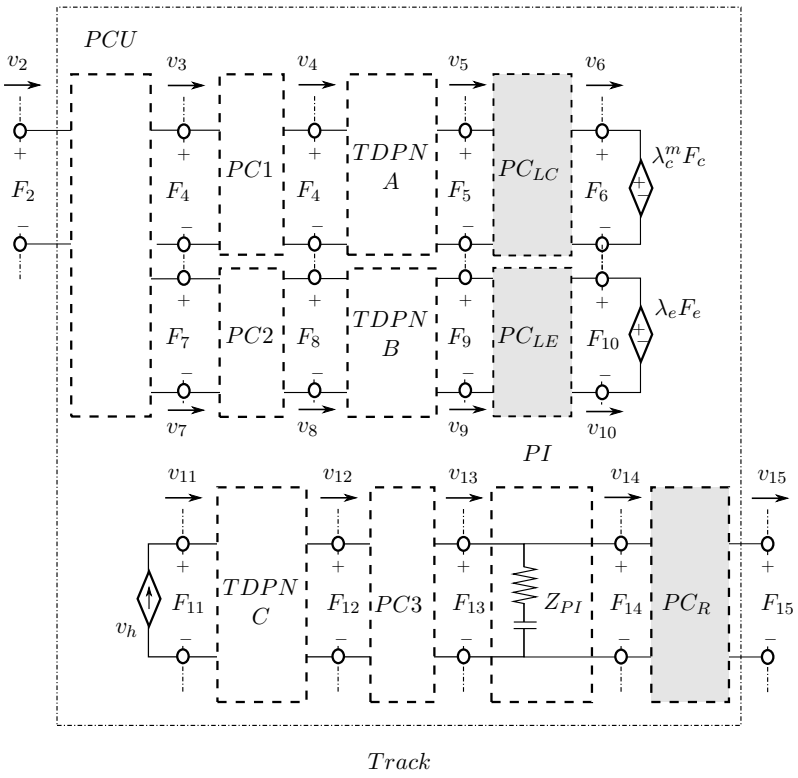

Figure 4.3.2: Passive 3-*Channel* Architecture with Time Delay
To consider a delay in the communication channels, three sets of TDPN and PC have to be introduced. The PCs PC_{LC}, PC_{LE} and PC_R are located on the right side of the communication channel.

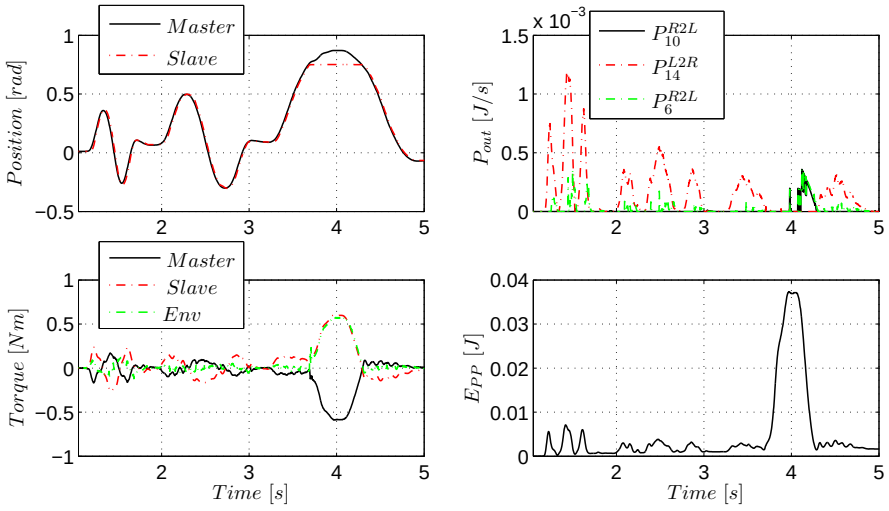

Experiment 4.17: Free Motion and Wall Contact with Hybrid Force Feedback in a 3-*Channel* Architecture
Free motion at different velocities and a wall contact of the slave are performed. The peak force resulting from the impact into the wall is reduced ($\lambda_e = 0.5$) compared to pure measured force feedback. The strictly positive plot of E_{PP} confirms the passivity of the track. The passivity controllers don't have to dissipate energy.

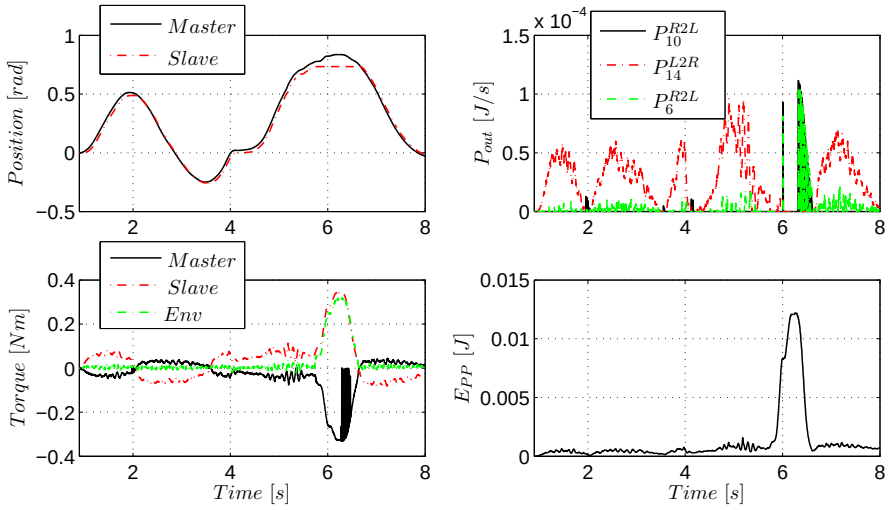

Experiment 4.18: Free Motion and Wall Contact with Hybrid Force Feedback in a 3-*Channel* Architecture at 30ms roundtrip delay
The position tracking of master and slave is satisfactory despite the delay. Since E_{PP} is positive, the passivity controllers don't have to dissipate energy.

In the trilateral experiment Exp. 4.19, *Track* Γ1 connects the master devices (*Agent* Λ1, *Agent* Λ2) and *Track* Γ2 and *Track* Γ3 link the slave with *Agent* Λ1 and *Agent* Λ2 respectively. In *Track* Γ1, the measured force feedback is deactivated ($\lambda_c^m = 1$, $\lambda_e = 0$). *Track* Γ2 and *Track* Γ3 have equal feedback scaling such that $\lambda_c^m = \lambda_e = 0.5$. The respective plots in Exp. 4.19 present only the signals of *Track* Γ2 for the sake of clarity. Between $t = [5s, 9s]$, the operator of *Agent* Λ2 moves the slave against a wall. The other operator (*Agent* Λ1) can perceive this procedure via the force feedback from the environment of the slave in *Track* Γ2. Still, the perception of the force is reduced since the computed force feedback from *Agent* Λ2 acts in opposite direction.

The analogous experiment with delay is presented in plot Exp. 4.20. The plot of E_{PP} confirms the passivity of the 3-*Channel* architecture.

4.3.4 Discussion on 3-Channel Architecture

The 3-*Channel* architecture increases the performance potential compared to PF_{comp} and PF_{meas} architectures. Although often neglected, the 3-*Channel* control has to preserve passivity of the overall system if the stability proof of one module of the control loop as the communication channel is based on the passivity concept. The passivity and thus the $\mathcal{L}2$-stability of the proposed control concept for the bilateral and multilateral case has been proven in this section. Bilateral and multilateral experiments showed promising results even at high time delay. The preceding experiments in Section 3.4.2 showed that depending on the multilateral scenario different coupling signals and network topologies are reasonable.

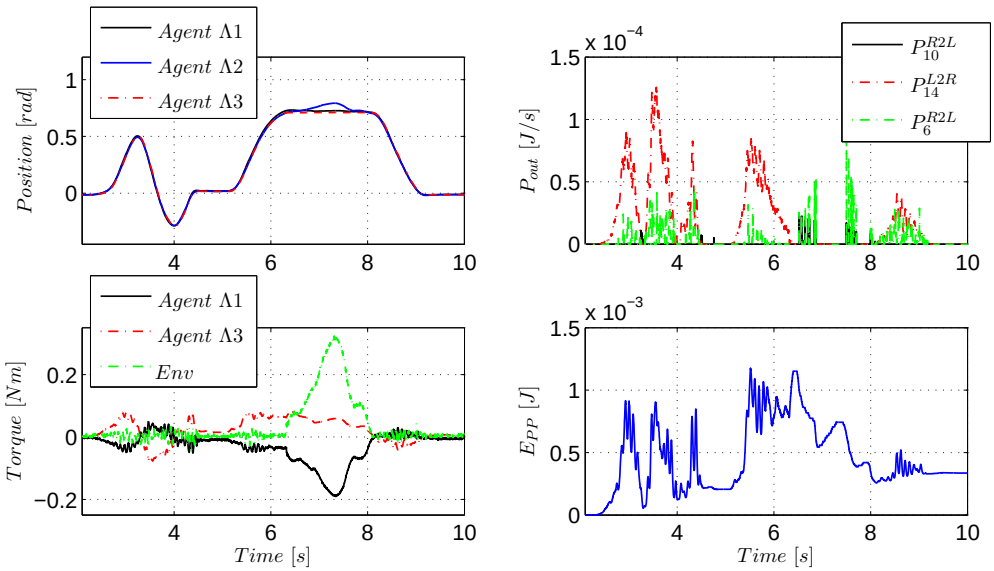

Experiment 4.19: Position Tracking in a Trilateral Setup with Hybrid Force Feedback
The multilateral coupling leads to a satisfactory position tracking. Since E_{PP} is positive in *Track* Γ2, the *PC*s PC_{LC}, PC_{LE} and PC_R of *Track* Γ2 don't have to dissipate energy.

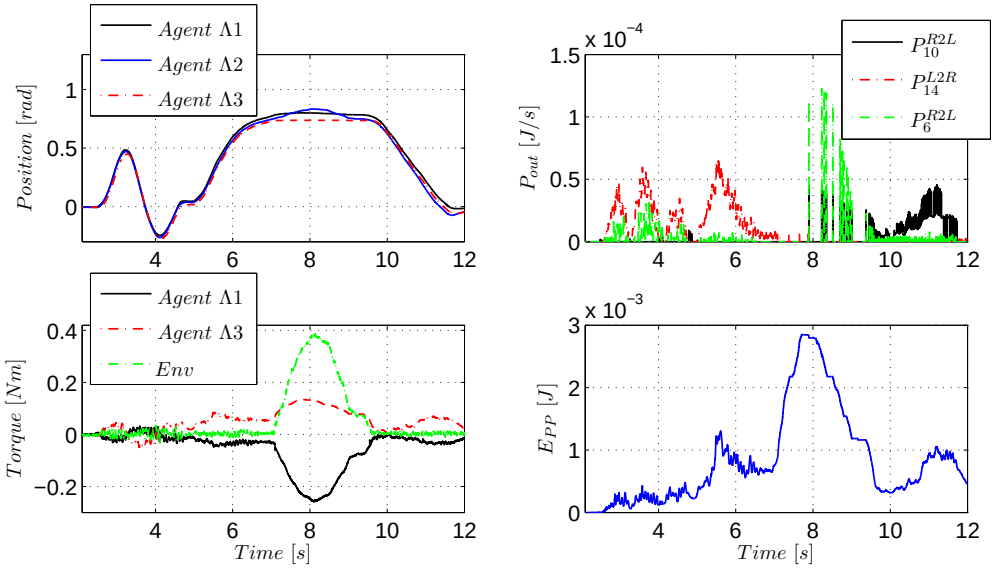

Experiment 4.20: Position Tracking in a Trilateral Setup with Hybrid Force Feedback at 30ms Roundtrip Delay
The delayed multilateral coupling leads to a satisfactory position tracking of the three agents. Since E_{PP} is positive in *Track* Γ2, the *PC*s PC_{LC}, PC_{LE} and PC_R of *Track* Γ2 don't have to dissipate energy.

4.4 4-Channel Architecture

In teleoperation setups that provide a force sensor at the master and the slave device, a 4-*Channel* architecture can be implemented. According to [171], the 4-*Channel* architecture can provide perfect transparency in a bilateral teleoperation system.

In this section, the 4-*Channel* architecture will be first compared to the real scenario of free motion and object interaction without teleoperator. Based on that analysis, a passivity control approach is presented.

4.4.1 System Description

As presented in Fig. 2.1.6 of Section 2.1, the interaction force measured at the master and the master position is sent to the slave robot in the 4-*Channel* architecture. The computed controller force as well as the interaction force measured at the slave are fed back to the master side.

This architecture is, considering the control structures mentioned in Section 2.1, the one that is most similar to the real physical interaction e.g. of a human's finger and an object. In case of no contact, the free motion control of the finger is realized via a kind of position controller with visual feedback (compare Fig. 4.4.1a). In the case of a teleoperation system, the position controller aims the position tracking of master and slave devices (see Fig. 4.4.1b). The feed forward of the human interaction force can be regarded as an assistive force to the position controller representing the intention of the human operator. In free motion, the operator aims to accelerate and decelerate the slave robot with this force.

In real physical interactions, the human generates a specific force F_h with which he or she wants to manipulate an object as depicted in Fig. 4.4.2a. In a teleoperation system, the feed forward of the interaction force of the master device to the slave resembles this desired interaction force (compare Fig. 4.4.2b). The operator exerts this force to accelerate and decelerate the slave and the object. The force F_e, felt in the real interaction scenario, equals the measured force feedback in the teleoperation setup. During interaction, the position controller presents a behavior that has no direct analog in the teleoperator-free scenario.

In free motion, the 4-*Channel* controller represents well the situation without teleoperator. In contact, the feed forward of the interaction force is very natural.

Only a 2-*Channel* architecture without position controller, in which the coupling is established by the exchange of measured forces of the master and slave device represents the real physical interaction better since no position controller is applied. Still, this structure is mainly useful in constant contact of the slave and the object since the control of the slave robot in free motion with pure force control is challenging.

4.4.2 Passivity Control

The network representation is fundamental for the passivity analysis of the 4-*Channel* architecture. In the 4-*Channel* architecture, the forces F_h, F_e and F_c have to be scaled down to achieve a natural tracking behavior of finger and slave ($\lambda_c^m \neq 0$, $\lambda_c^s \neq 0$ compare

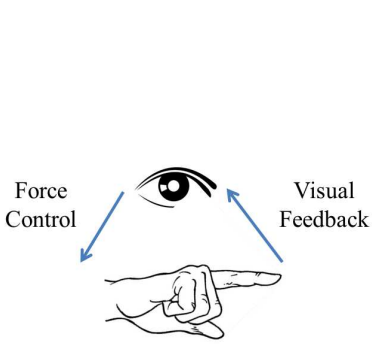

(a) Free Motion without Teleoperation System
In the real situation without teleoperation system, the human controls the finger motion with a desired force and with visual feedback. Thus, the free motion control of the finger is realized similar to a position controller with visual feedback.

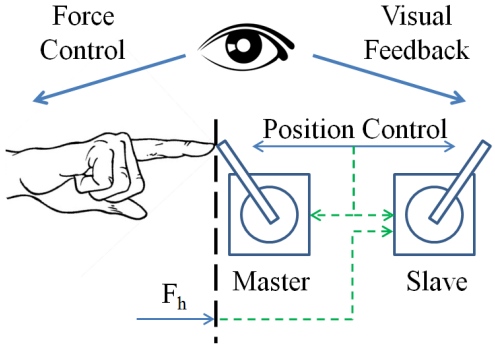

(b) Free Motion with Teleoperation System
In the case of a teleoperation system, the position controller aims the position tracking of master and slave devices. The feed forward of the human interaction force can be regarded as an assistive force to the position controller representing the intention of the human operator.

Figure 4.4.1: Free Motion

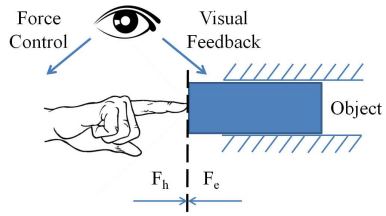

(a) Contact without Teleoperation System
In real physical interactions, the human generates a specific force F_h with which he or she wants to manipulate an object.

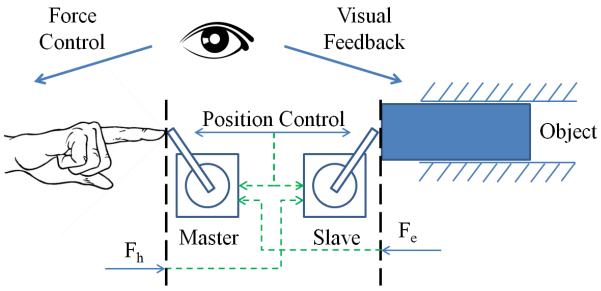

(b) Contact with Teleoperation System
In a teleoperation system, the feed forward of the interaction force of the master device to the slave resembles this desired interaction force. The force F_e, felt in the real interaction scenario, equals the measured force feedback in the teleoperation setup. During interaction, the position controller presents a behavior that has no direct analog in the teleoperator-free scenario.

Figure 4.4.2: Contact

Fig. 4.4.1a and Fig. 4.4.1b):

$$\lambda_c^m, \lambda_c^s, \lambda_e, \lambda_h \in \mathbb{R}_0^+, \tag{4.37}$$

$$\lambda_c^m + \lambda_e = 1, \tag{4.38}$$

$$\lambda_c^s + \lambda_h = 1. \tag{4.39}$$

Therefore, the network representation of the 4-*Channel* architecture depicted in Fig. 4.4.3 contains the four dependent sources $\lambda_c^m F_c$, $\lambda_c^s F_c$, $\lambda_e F_e$ and $\lambda_h F_h$. Since the controller force is scaled down in both directions of energy flow, the PI is designed in a separate circuit.

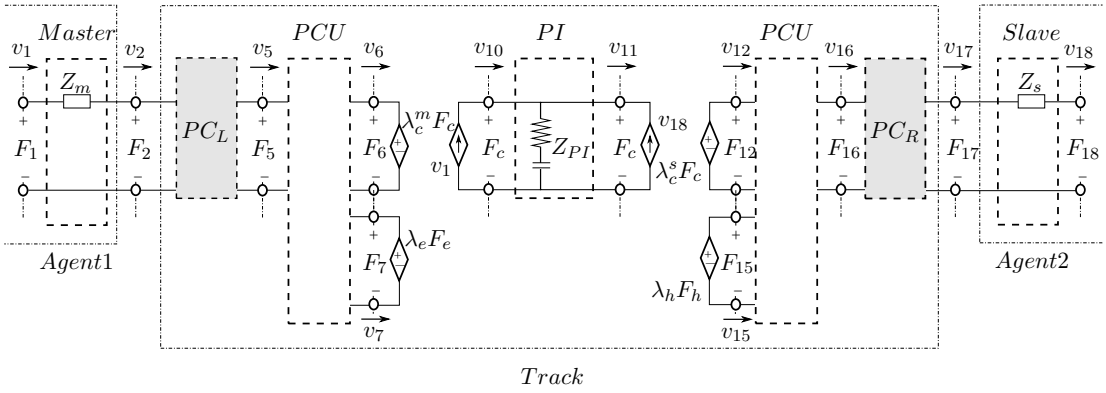

Figure 4.4.3: Network Representation of a 4-*Channel* Architecture with Passivity Control
Two PCs PC_L and PC_R are located on the left and right side of the 4-*Channel* track. The power input at port 1 and port 18 into the track in L2R and R2L direction respectively can be regarded as the intended energy input into the teleoperator. If the energy output at port 2 and port 17 in R2L and L2R direction respectively is lower than this energy input, the 4-*Channel* architecture is passive. This can be assured by the two passivity controllers. The computed force and the human interaction force, commanded to *Agent* $\Lambda 2$ is scaled by λ_c^s and λ_h respectively. The computed force and the environment interaction force, commanded to *Agent* $\Lambda 1$ is scaled by λ_c^m and λ_e respectively.

Two methods can be applied for the time domain passivity control of a 4-*Channel* architecture:

- Analogously to the control in the PF_{meas} and 3-*Channel* architecture, the PI controller energy can be considered as an energy storage E_{St}, limiting the power output to the left and right agent:

$$E_{St}(k) = E_{St}(k-1) + (P_{10}^{L2R}(k) + P_{11}^{R2L}(k))T_s. \tag{4.40}$$

  Therefore, to preserve passivity in the 4-*Channel* architecture, the power exiting from the dependent flow and effort sources may not exceed the current energy content E_{St}. Four PC controllers PC_{LC}, PC_{LE}, PC_{RC} and PC_{RE} can dissipate the excessive power exiting at these ports. Analogously to the preceding sections, the overall desired output power $P_{out}^{des}(k)$ at these ports has to be calculated. If $P_{out}^{des}(k)$ does not exceed E_{St}, no energy has to be dissipated. Otherwise, the PCs have to dissipate the power P_{diss} in the current time step

$$P_{diss}(k) = E_{St}(k)/T_s - P_{out}^{des}(k) \tag{4.41}$$

in a distributed manner equivalently to equations (4.30)-(4.32).

- In the real scenario of interaction depicted in Fig. 4.4.2a, the human operator and the environment interact with the forces F_h and F_e. In this interaction the human and the environment behave passively. Analogously, the human operator should be able to manipulate an object with the feed forward of the master interaction force F_h and feedback of the slave interaction force F_e as depicted in Fig. 4.4.4. The power input form the master port $\langle v_h, F_h \rangle$ as well as the power input from the environment $\langle v_e, F_e \rangle$ reflects the power flow in the real scenario of Fig. 4.4.2a. Since a 2-*Channel* teleoperation setup, applying the measured forces as coupling signals (see Fig. 4.4.4), is designed analogous to the real scenario, it can be regarded as a reference for a passivity preserving 4-*Channel* architecture.

  In contrast to the 2-*Channel* architecture, the power correlation of the real scenario and the 4-*Channel* architecture differs due to the PI controller. A freely moving finger produces a non-zero force F_h whereas a slave moving without contact to the environment requires a force F_h. For that reason, a reference energy storage similar to the control approach of the 3-*Channel* architecture in Section 4.3 can be calculated with respect to which the power output from the track to master and slave can be limited. The energy storage can be calculated from the power input to the track at port 1 ($P_1^{L2R} \langle v_h, F_h \rangle$) and port 18 ($P_{18}^{R2L} \langle v_e, F_e \rangle$). The power output at port 2 (P_2^{R2L}) and at port 17 (P_{17}^{L2R}) can be limited by the impedance type passivity controllers PC_L and PC_R. The ports at which the input and output power is calculated may differ since the master and slave subsystems have a passive energy behavior and thus dissipate energy in the output flow direction.

The first method is a direct extension of the approaches of Section 4.2 and 4.3. As, the latter approach is mainly relevant for 4-*Channel* architectures (force sensor at master and slave device required), it is explained in detail in the following.

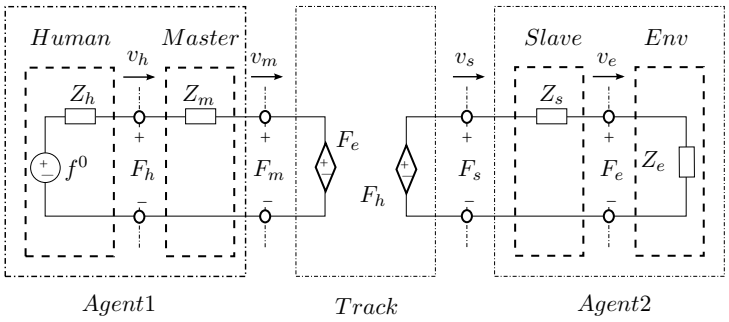

Figure 4.4.4: Network Representation of a 2-*Channel* Architecture
The 2-*Channel* architecture with exchange of master F_h and slave interaction force F_e can be regarded as a reference for a passivity preserving 4-*Channel* architecture.

4.4.3 Bilateral Setup

The energy storage E_{St} can be calculated in each time step as follows:

$$E_{St}(k) = E_{St}(k-1) + (P_1^{L2R}(k) + P_{18}^{R2L}(k))T_s. \tag{4.42}$$

To preserve passivity in the 4-*Channel* architecture, the power exiting at port 2 and 17 may not exceed the current energy storage E_{St}. Therefore, PC_L and PC_R dissipate excessive power exiting at port 5 and 16 respectively. The desired output power $P_{out}^{des}(k)$ at those ports is

$$P_{out}^{des}(k) = P_5^{R2L}(k) + P_{16}^{L2R}(k) \tag{4.43}$$

If $P_{out}^{des}(k)$ does not exceed E_{St}, no energy has to be dissipated. Otherwise, the PC has to act as follows:

$$P_{obs}^{PC_L}(k) = \begin{cases} P_{obs}(k)\frac{P_5^{R2L}(k)}{P_{out}^{des}(k)}, & \text{if } E_{St}(k) \leq P_{out}^{des}(k)T_s \\ 0, & \text{if } E_{St}(k) > P_{out}^{des}(k)T_s, \end{cases} \tag{4.44}$$

$$P_{obs}^{PC_R}(k) = \begin{cases} P_{obs}(k)\frac{P_{16}^{L2R}(k)}{P_{out}^{des}(k)}, & \text{if } E_{St}(k) \leq P_{out}^{des}(k)T_s \\ 0, & \text{if } E_{St}(k) > P_{out}^{des}(k)T_s, \end{cases} \tag{4.45}$$

P_{obs} is the power that has to be dissipated in the current time step:

$$P_{obs}(k) = E_{St}(k)/T_s - P_{out}^{des}(k). \tag{4.46}$$

Thus, $E_{obs}(k)$ results in

$$E_{obs}^{PC_i}(k) = T_s \sum_{n=0}^{k} P_{obs}^{PC_i}(k), \tag{4.47}$$

with $i \in \{L, R\}$. The energy that has to be dissipated has to be calculated analogous to equations (2.50) and (2.51). The functionality of impedance type PCs is explained in Section 2.2. Afterwards, the available power E_{St} has to be updated, as the power P_5^{R2L} and P_{16}^{L2R} left the track:

$$E_{St}(k) = E_{St}(k-1) + (P_1^{L2R}(k) + P_{18}^{R2L}(k) - P_5^{R2L}(k) - P_{16}^{L2R}(k))T_s. \tag{4.48}$$

4.4.4 Multilateral Setup

In the multilateral setup, the input power needs to be calculated with respect to all tracks that are connected to the PCU of the respective device. Assume that the device of *Agent* $\Lambda 1$ is connected to n tracks. The force applied at the master devices is a result of the feedback force of all n tracks. Since only a part of the power introduced by the human at the master device is sent in one specific track, the power has to be split up under consideration of the direction of power flow in each track. The power $P_j^{\Lambda 1,\Gamma i}$ ($i \in \{L2R, R2L\}$) in each *Track* Γi (here L2R denotes the power flowing into the track and R2L denotes the power flowing out of the track) can be calculated via the respective force feedback $F^{\Gamma i}$ and the velocity of the master $v_{\Lambda 1}$. The sum of the absolute values of the forces $F_{fb,abs}^{\Lambda 1}$ is

$$F_{abs}^{\Lambda 1}(k) = \sum_{i=1}^{n} |F^{\Gamma i}(k)|. \tag{4.49}$$

The proportional part $p^{\Gamma i}$ of $Track\ \Gamma i$ can be calculated as

$$p^{\Gamma i}(k) = \frac{|F^{\Gamma i}(k)|}{F^{\Lambda 1}_{abs}(k)}. \tag{4.50}$$

The absolute value of the measured force feedback $F^{\Lambda 1}_{m,abs}$ can be estimated from the proportional parts, the direction of power flow and the measured force $F^{\Lambda 1}_{m}$ at master $\Lambda 1$

$$F^{\Lambda 1}_{m,abs}(k) = \frac{|F^{\Lambda 1}_{m}(k)|}{\sum_{i=1}^{n} p^{\Gamma i}_{\pm}(k)}, \tag{4.51}$$

where

$$p^{\Gamma i}_{\pm} = \begin{cases} p^{\Gamma i} & \text{if } P^{\Lambda 1,\Gamma i}_{L2R} > 0, \\ -p^{\Gamma i} & \text{if } P^{\Lambda 1,\Gamma i}_{R2L} \geq 0. \end{cases} \tag{4.52}$$

If power is flowing into $Track\ \Gamma i$ ($P^{\Lambda 1,\Gamma i}_{L2R} > 0$), the input power resulting from the measured force feedback can be calculated as

$$P^{\Gamma i}_{m,L2R}(k) = p^{\Gamma i}(k) F^{\Lambda 1}_{m,abs}(k) |v_{\Lambda 1}(k)|. \tag{4.53}$$

This power $P^{\Gamma i}_{m,L2R}$ is then used as the measured input power $P^{L2R}_{1}(k)$ in $Track\ \Gamma i$ in equation Equ. 4.42 and Equ. 4.48. Analogously, the power inputs can be calculated for every track at each device.

4.4.5 Time Delay

In presence of time delay, the network presentation of a 4-*Channel* track changes as presented in Fig. 4.4.5. The power consistency of the communication channels is assured via four TDPNs [10]. Three passivity controllers PC_1, PC_2 and PC_3 dissipate the energy generated by the time delay. The energy storage calculation changes slightly:

$$E_{St}(k) = E_{St}(k-1) + (P^{L2R,del}_{1}(k) + P^{R2L}_{18}(k)) T_s, \tag{4.54}$$

where $P^{L2R,del}_{1}(k)$ equals the power $P^{L2R}_{1}(k)$ delayed by T_1 of $TDPN\ A$. Finally, the available power E_{St} has to be updated. The power P^{R2L}_{5} and P^{L2R}_{16} are considered to exit, although the delay may lead to a lower exit power at port 2:

$$E_{St}(k) = E_{St}(k-1) + (P^{L2R,del}_{1}(k) + P^{R2L}_{18}(k) - P^{R2L}_{5}(k) - P^{L2R}_{16}(k)) T_s \tag{4.55}$$

The resulting passivity controlled track can be applied in multilateral systems in a modular way. Analogously to the preceding section, in the multilateral case, only the proportional part of the overall energy flow may be considered. Then, $P^{L2R,del}_{1}$ equals then the power $P^{\Gamma i}_{m,L2R}$ of equation (4.53), delayed by T_1 of $TDPN\ A$.

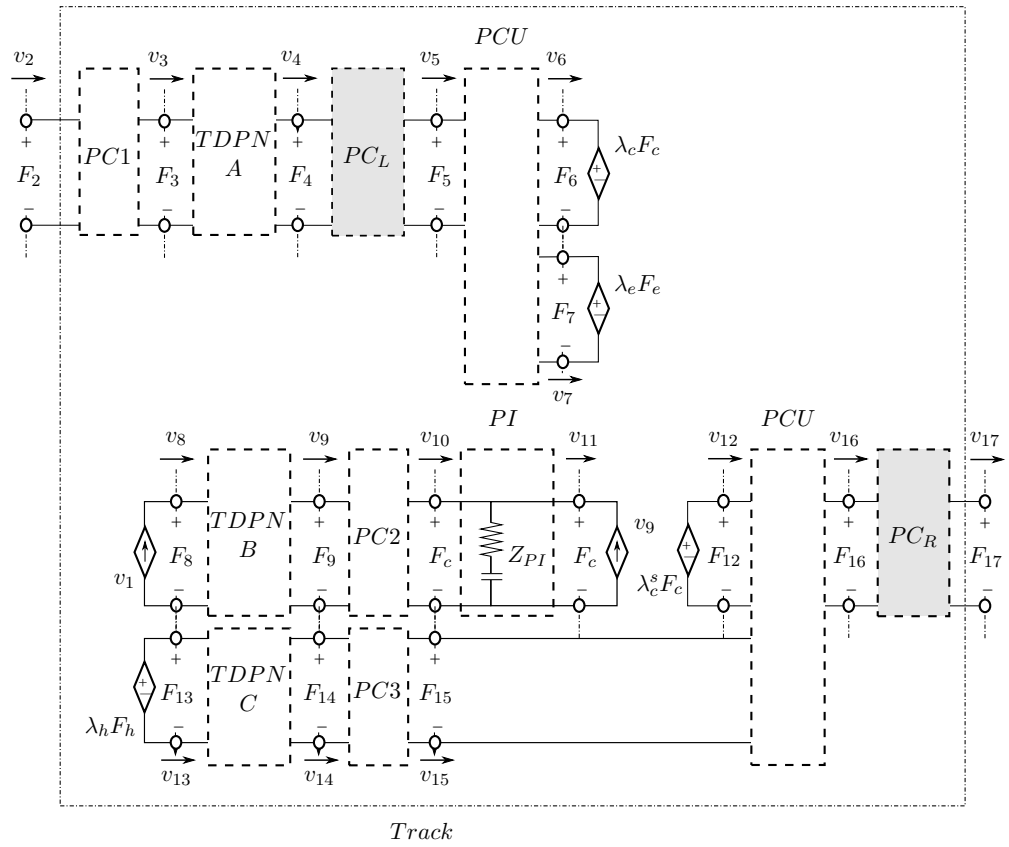

Figure 4.4.5: Passive 4-*Channel* Architecture with Time Delay
To consider a delay in the communication channels, three sets of TDPNs and PCs have to be integrated. The PCs PC_L and PC_R are located on the right side of the communication channels.

4.4.6 Experiments

The following experiments serve the evaluation of the proposed passive 4-*Channel* track. The 1-DoF setup presented in detail in Appendix A.1 has been applied. The force scalings λ_c^m, λ_c^s, λ_e and λ_h have been set to 0.5 each.

The first experiment presented in plot Exp. 4.21 considers a bilateral setup with 4-*Channel* architecture. The human operator at *Agent* $\Lambda 1$ controls the slave *Agent* $\Lambda 2$ in slow ($t = [0.9s, 2.3s]$) and fast motion ($t = [2.6s, 3.5s]$). Also, a wall contact is performed ($t = [4.2s - 5.5s]$). Since the reference energy E_{St} is positive, the passivity controllers PC_L and PC_R do not need to be activated. Although it is mathematically correct to store the dissipation of the system in E_{St}, E_{St} should be limited similar to the limitation algorithm in Section 4.1.1.

The same sequence is performed in experiment Exp. 4.22 at 100ms roundtrip delay. The TDPN approach of Section 2.3.2.3 has been applied to guarantee stability despite time delay. Since the reference energy E_{St} is positive, the passivity controllers PC_L and PC_R do not need to dissipate energy.

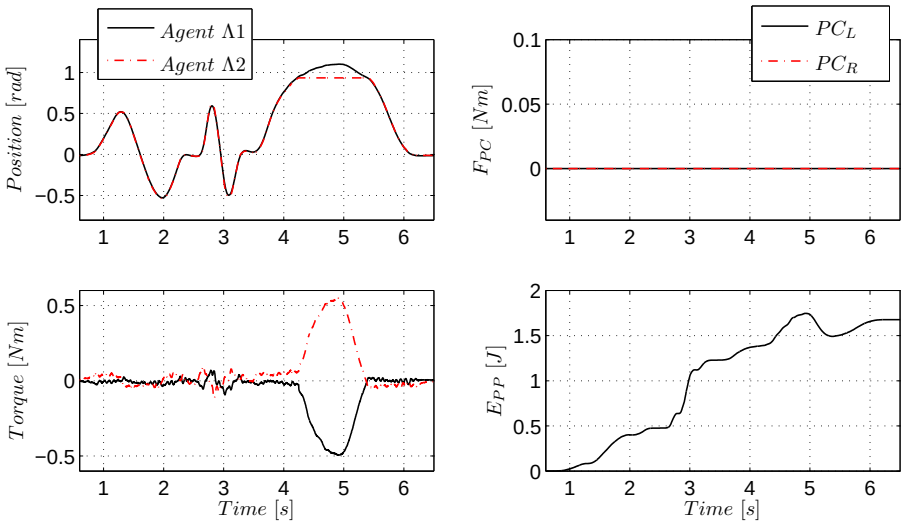

Experiment 4.21: Free Motion and Wall Contact of a Bilateral Teleoperator with 4-*Channel* Architecture
A slow and fast sinusoidal motion and a wall contact is presented. Since the reference energy E_{PP} is positive, the passivity controllers PC_L and PC_R do not need to dissipate energy.

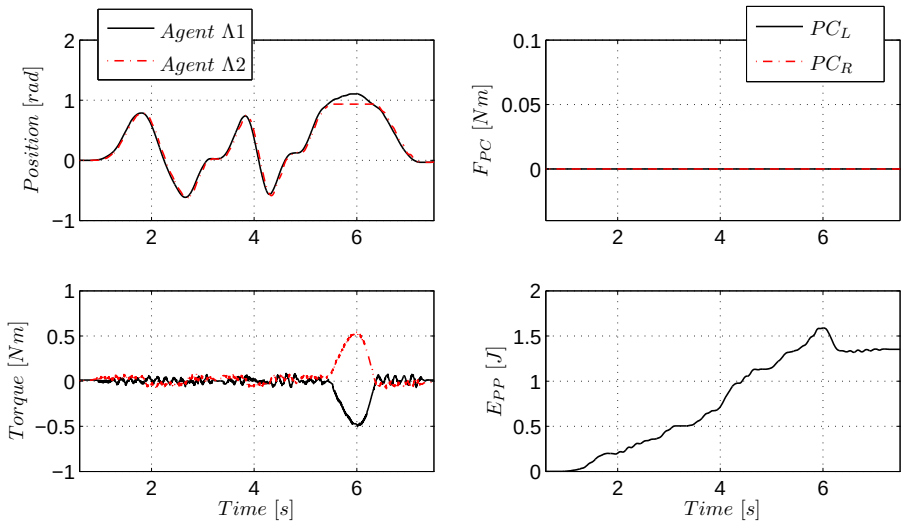

Experiment 4.22: Free Motion and Wall Contact of a Bilateral Teleoperator with 4-*Channel* Architecture at 100ms Roundtrip Delay
The position tracking of the devices is satisfactory despite the high roundtrip delay. Since the reference energy E_{PP} is positive, the passivity controllers PC_L and PC_R do not need to dissipate energy.

4.4.7 Discussion on 4-Channel Architecture

With a 4-*Channel* architecture a higher performance and a higher degree of transparency can be achieved compared to 2-*Channel* and 3-*Channel* architectures. In this section, two time domain control methods have been proposed. One method is analogous to the 3-*Channel* approach of the preceding section. The second method considers the energy exchange in a real scenario without teleoperation system as a reference. The bilateral experiments showed promising results even at high time delay.

4.5 Model-Mediated Teleoperation for Rate Control Setups

This section examines the adequacy of the MPMT to the concept of model-mediated teleoperation and rate control systems. In order to compensate for delay effects to some extent, model-mediated teleoperation has been proposed [106], where a local virtual model of the slave robot and/or its environment can provide instantaneous force feedback to the operator's commands. The remote slave is controlled by the delayed user inputs and the virtual model of slave and environment on the master side is updated by the states and the sensor information of the remote slave robot. The teleoperation of stationary robot manipulators differs to the remote control of mobile robots [95] especially with respect to the coupling signals. Since mobile robots have by far larger workspaces than the respective human machine interface (HMI), generally at least one DoF of the slave robot is rate controlled. Typical applications of mobile robots are the cleaning of nuclear plants [70], the clearing of mines [163] or the inspection of underwater structures [93]. Several applications of wheeled mobile robots (WMR) require a human operator in the control loop since the autonomous task execution is often limited. This is due to the fact that for example the scene analysis of rough terrain might be incomplete as a result of occlusions, or the safety margins may hinder the autonomous system in passing through a narrow canyon-like structure.

In literature, a variety of control paradigms and HMIs [142] have been proposed. The longitudinal DoF is mainly controlled by a velocity v_x. Only in small workspace a position control is reasonable. In contrast, in the lateral DoF, for example the lateral velocity v_y, the yaw rate $\dot{\psi}$ or the curvature κ can be commanded. Through the yaw rate $\dot{\psi}$ and the curvature κ, the longitudinal and lateral DoFs are coupled.

As discussed in Section 3.3.2, rate control violates the physical interface of the master in the network representation since the master position is translated into a desired velocity. The authors of [81, 83] proposed the concept of r-passivity that allows the design of a passive master providing a physically sound interface in the rate control structure. In [81], the velocity and the respective heading angle of a WMR are controlled whereas a more car-driving like tele-driving mode with velocity and yaw-rate interface was considered in [83]. The network representations of different rate control approaches have been presented in [177]. Still, the focus lied on the passivity of the communication affected by time delay. The passivity of the overall system has not been proven.

Analogous to the control of stationary manipulators, a force feedback can be generated from the controller of the respective actuators (steering, traction), from sensors at the slave or from a virtual environment (VE). The controller torque of the traction

motors and the torque input to the steering actuators can be fed back to the input device in the longitudinal and lateral degree of freedom respectively. Alternatively or additionally, the interaction force measured by a force torque sensor or a fictitious force calculated in a virtual model of the save's environment can be displayed at the master device. In [81], the computed linear velocity and heading angle errors were fed back at the master device. In contrast to the measured feedback in the control of a stationary robotic manipulator, the force calculated e.g. from a potential field of obstacles in a modeled environment have no physical relation to the control forces of the actuator. Although the mobile robot is moving in a plane area requiring low traction and steering torques, the potential field of a close object as a hill may produce a repelling force.

The fictitious force calculated from a potential field in [160] has been applied in a local slave control loop but the computed linear velocity and yaw rate errors are fed back to the master device. In [161], the fictitious force feedback of a virtual potential field has been applied as a feedback force. The system stability was proven via the Lyapunov approach however the feedback loop to the human operator was neglected. In contrast, the Routh-Hurwitz criterion was applied in [31] to analyze the stability of the whole control loop. An environment model provided a repelling force feedback in [162]. The paper provides no stability proof but an evaluation of the teleoperator's transparency according to different control structures and autonomy levels. Network representations and TDPN approaches for different computed and measured force feedback strategies have been presented in [177]. It was mentioned that no physical interface could be found for the fictitious force feedback in the network such that no stability proof and no experiments could be presented. Analogous to stationary robot teleoperation (compare Section 4.2), this is the general challenge in control loops involving measured or fictitious forces. The TDPA has been applied in combination with the Llewellyn criterion and the r-passivity method to a undelayed rate controlled teleoperator in [90]. The authors showed the non-passivity of the environment in slippage conditions and applied the TDPA to the environment 1-port to maintain the system's passivity.

The time delay plays a crucial role in mobile robot teleoperation. The stability of the remote control of a formation of nonholonomic WMRs was assured with the Lyapunov-Krasovskii functional in [120]. Also in [162], the Lyapunov-Krasovskii functional was used to consider the time delay. In [177], the TDPN or TDPA approach respectively has been applied to the communication in different control structures. The passive set-position modulation PSPM framework (a time tomain control concept) was extended in [188] to match the tele-driving of WMRs.

In this section, the focus lies on a teleoperation system involving a 2-DoF Joystick master device and a nonholonomic WMR with adjustable control interface [123]. The system design will consider a time delay in the communication channel and different force feedback strategies and coupling signals. In the following, the longitudinal DoF of the joystick controls the linear velocity v of the WMR. Via the lateral DoF either the yaw rate $\dot{\Psi}$ (mode I) or the curvature κ (mode II) of the WMR can be commanded such that the two DoFs are coupled. An interface of longitudinal v_x and lateral velocity v_y is not considered since using a 2-DoF master, the rotation would need to be commanded in an additional control mode. This would lead to an interruptive, non-continuous motion in curvy trajectories. Note that the two lateral control modes I,II have different properties respecting velocity variation. In contrast to the curvature command of mode II, the

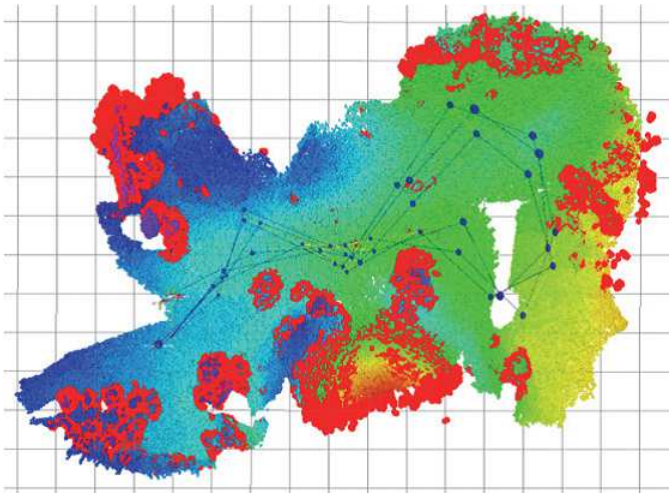

Figure 4.5.1: Exemplary Height Map
The height map of the environment of a robot can be generated via stereo vision. Based on the height map, a danger map can be calculated.

variation of the linear velocity command leads in mode I to a variation of the desired curvature despite a constant yaw-rate command since

$$\frac{1}{\kappa} = \frac{v}{\dot{\Psi}}. \tag{4.56}$$

4.5.1 Fictitious Force Feedback

This work considers WMRs as the Lightweight Robot Unit (LRU, see Appendix A.6) that are equipped with stereo vision [123]. Via this sensor, a grid map of the WMR surroundings (compare Fig. 4.5.1) can be generated. The height of the grid cells in a specific area of the map can be used to determine a repulsive force feedback. The force can be calculated from a triangular area in the vehicle motion vector if the control input is based on velocities (v_x,v_y). Since here, the lateral master DoF commands a curvature or a yaw-rate, the evaluated area of the map needs to consider the desired curvature.

4.5.1.1 Polygon Calculation

The relevant area of the map can be designed with polygons. An exemplary set of curvature polygons can be found in Fig. 4.5.2. The polygon corners are located on the middle desired R^{des}, inner R^i and outer radius R^o. Π_L is the left set of polygons (1-4) and Π_R the right set of polygons (5-8). To find the corners c_l^k of the polygons ($k = [m, i, o]$), a maximum path length $L_{max}(T_d, v^{des})$ on the middle circuit which can depend on delay T_d and desired velocity v^{des} has to be defined. Then the maximal path length can be divided into a number of parts m ($m = 4$ in Fig. 4.5.2) that provide a sufficient resolution for the definition of Π_L and Π_R:

$$\Delta L = \frac{L_{max}(T_d, v)}{m}. \tag{4.57}$$

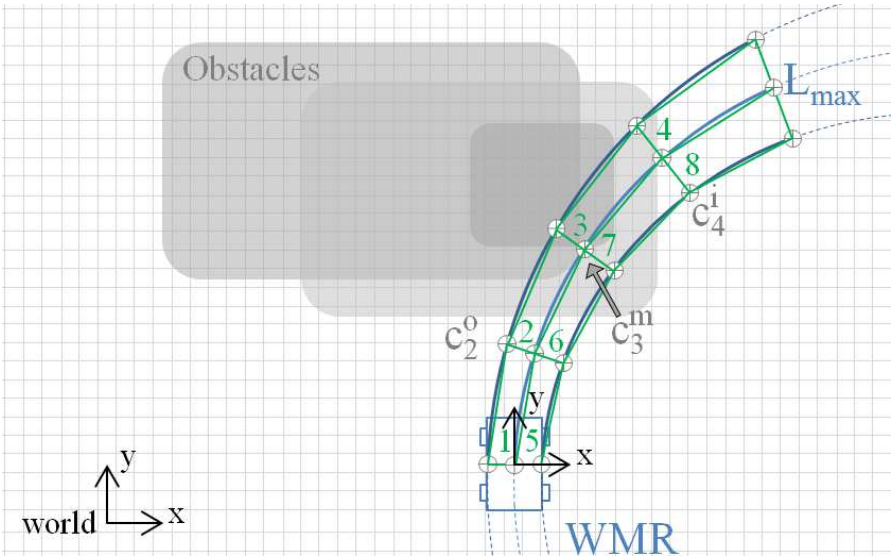

Figure 4.5.2: Grid Map with Curvature Polygon
A polygon can be determined from the curvature command to the wheeled mobile robot. Depending on the overlap of this polygon and the obstacles in the grid map (or danger map), a fictitious force feedback can be calculated.

The length of the n'th polygon can then be calculated as

$$L_n = \sum_{j=1}^{n} \Delta L. \tag{4.58}$$

The positions of the polygon corners on the circles can be calculated through the angle α with respect to the distance L_n:

$$\alpha_n(k) = L_n / R^{des}(k). \tag{4.59}$$

The inner $R^i(k)$ and outer circles $R^o(k)$ can be calculated from the desired radius $R^{des}(k) = \frac{1}{|\kappa^{des}(k)|}$:

$$R^i(k) = |R^{des}(k)|(1-c) \tag{4.60}$$
$$R^o(k) = |R^{des}(k)|(1+c) \tag{4.61}$$

with the radius divergence factor c and the switch radius $R_{swi} = 40m$

$$c = \begin{cases} 0.2R^{eval}(k) & \text{,if } |R^{des}(k)| \leq R_{swi}, \\ 0.2R_{swi}\frac{R_{max}-R^{eval}(k)}{R_{max}-R_{swi}} + \frac{b}{2}(1 - \frac{R_{max}-R^{eval}(k)}{R_{max}-R_{swi}}) & \text{,if } |R^{des}(k)| > R_{swi}, \end{cases} \tag{4.62}$$

where $R^{eval}(k) = max(min(|R^{des}(k)|, R_{max}), R_{min})$, $R_{max} = 200m$, $R_{min} = \frac{b}{2}$. b is the width of the WMR. Note that also this divergence factor can be designed in a velocity dependent manner. Since the instantaneous center of rotation of the WMR lies on the center axis, the following calculations refer to the center frame of the WMR. The center

point of the circles (p^i,p^o) can be calculated from the center point of the desired radius R^{des}:

$$x^{des}(k) = |R^{des}(k)|, \tag{4.63}$$

$$x^i(k) = x^{des}(k) + (R^i(k) - |R^{des}(k)|) + \frac{b}{2}, \tag{4.64}$$

$$x^o(k) = x^{des}(k) + (R^o(k) - |R^{des}(k)|) - \frac{b}{2}, \tag{4.65}$$

$$y^i(k) = y^o(k) = y^{des}(k) = 0. \tag{4.66}$$

Thus, the corner locations c^j ($j \in \{i, m, o\}$) on the inner (i), middle (m) and outer (o) circle can be determined:

$$c^j_{x,n}(k) = max(0, x^j(k) + R^j(k)cos(\pi - \alpha_n(k))), \tag{4.67}$$

$$c^j_{y,n}(k) = max(-\frac{b}{2}, y^j(k) + R^j(k)sin(\pi - \alpha_n(k))). \tag{4.68}$$

The corner position is restricted to the first quadrant of the plane.

The corner points have to be flipped on the WMR's longitudinal y-axis if $sign(R^{des}(k)) < 0$. Finally, the corner points need to be translated into the position of the WMR in the map's world frame and rotated around heading angle ψ of the WMR with respect to the map's world frame.

For backward driving, the polygon can be flipped along the WMR's x-axis.

4.5.1.2 Force Feedback Calculation

For the force feedback calculation, the height h_d of the polygon cells can be considered. Therefore, a maximal height h_{max} can be used to limit the resulting force feedback F_f. Note that the height values h_d of unknown cells are set to the maximal height h_{max}. Also, the absolute value of the height is regarded such that a negative height with respect to the WMR is considered as a positive height.

Step 1 The fictitious force F_f can be calculated with

$$F_f(k) = \sum_{d=1}^{n} (min(h_d, h_{max})q) f(\tilde{s}_d), \tag{4.69}$$

with the force gain q and the number of cells n in the respective polygon. The function $f(\tilde{s}_d)$ serves the weighting of the cell influence depending on the distance $\tilde{s}_d$ of the respective cell to the WMR center. The distance $\tilde{s}$ is the value of distance s normed with respect to the maximal considered path length L_{max}.

$$f(\tilde{s}_d) = a(k) - \frac{g(k)(arctan(r(k)\tilde{s}_d - d(k)) + arctan(d(k)))}{arctan(r(k) - d(k)) + arctan(d(k))}, \tag{4.70}$$

with

$$a(k) = \begin{cases} 1 + g(k) & \text{,if } sign(g) \leq 0 \\ g(k) & \text{,if } sign(g) > 0. \end{cases} \tag{4.71}$$

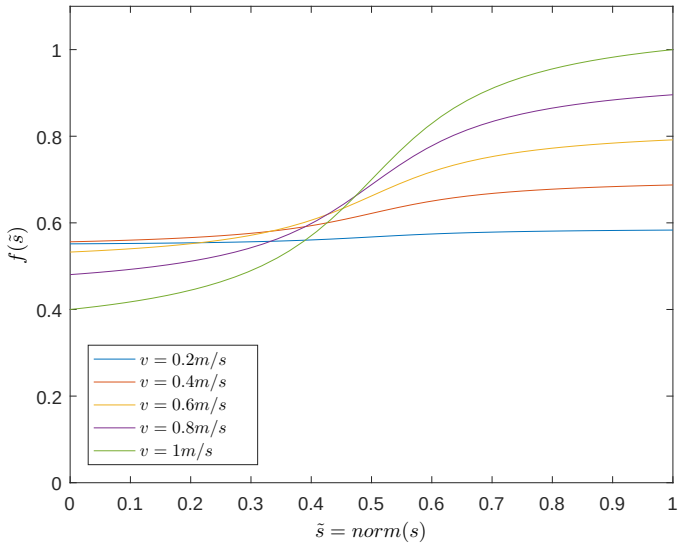

Figure 4.5.3: Curves of Weighting Functions at Different Velocities
The polygon weights can be designed depending e.g. on the longitudinal velocity of the WMR or the delay in the communication channel.

A set of such curves for different velocities is presented in Fig. 4.5.3. The constant d and r shift and stretch respectively the curve sidewards. The velocity dependency of the function $f(\tilde{s}_d)$ can be achieved via a linear scaling w

$$v^{des,*}(k) = min(max(v^{des}(k), v_{min}), v_{max}) \tag{4.72}$$

$$w(k) = \frac{v_{max} - v^{des,*}(k)}{v_{max} - v_{min}} \tag{4.73}$$

$$d(k) = d_e + w(k)(d_s - d_e) \tag{4.74}$$

$$r(k) = r_e + w(k)(r_s - r_e) \tag{4.75}$$

$$g(k) = g_e + w(k)(g_s - g_e) \tag{4.76}$$

with the constants $d_s = 4$, $r_s = 8$, $g_s = 0.8$, $d_e = 3$, $r_e = 6$, $g_e = -0.8$, $v_{max} = 3m/s$ and $v_{min} = 2m/s$. Analogously, a delay dependency can be implemented.

Step 2 Furthermore, the maximal height of the polygon areas needs to be respected. In the situation depicted in Fig. 4.5.2, the polygon 4 has a lower force value than polygon 3. This results in a lower feedback force than desired, since polygon 4 can not be reached on the chosen trajectory. Therefore, the force $F_{f,4}$ of polygon 4 should be overwritten with the force $F_{f,3}$ of polygon 3. Depending on the maximum speed and the topology, a reasonable polygon set resolution needs to be defined by the number of polygons m. If the lateral resolution is insufficient, the polygon sets Π_L and Π_R can be split laterally into polygon subsets.

Step 3 Depending on the applied WMR, also the slope of the topologies may play a crucial role. If the resolution of the polygon set is well tuned, the aforementioned

approach of step 3 takes the topology slope into account. Alternatively, the standard deviation σ_h of the height values can be regarded to consider the slope of the objects:

$$\sigma_h = \sqrt{\frac{\sum_{j=1}^{n}(h_j - H)^2)}{n-1}}, \tag{4.77}$$

$$F_f^*(k) = min(max(\sigma_{min}, \sigma_h), \sigma_{max})F_f(k), \tag{4.78}$$

for height values h of the n cells of the polygon Π and their mean value H. σ_{min} and σ_{max} have to be chosen according to the minimally and maximally considered slope respectively.

Step 4 The left set of polygons Π_L should produce a force pushing the joystick to the right and vice versa. Still, the sum of forces calculated by both sets of polygons Π_L and Π_R should result in a force that acts against the driving command. Thus, no favorite steering direction can be displayed in case the forces of left and right polygon equal, but the feedback force leads to a deceleration of the WMR.

4.5.2 System Design

As mentioned before, control structures with different coupling signals are regarded in the following. First a system with computed (Section 4.5.2.1) and second with measured force feedback (Section 4.5.2.2) is presented. Depending on the following equations referring to Fig. 4.5.4 and Fig. 4.5.6, a rate or position control can be realized in the lateral DoF. Note that the longitudinal DoF of the master controls consistently the linear velocity (rate) of the WMR.

The equation of the local master controller $PI1$ is

$$\boldsymbol{F}_{PI1}(k) = \begin{bmatrix} K_1 \\ K_2 \end{bmatrix} (\boldsymbol{\delta}_m(k) - \boldsymbol{\delta}_m^0) + \begin{bmatrix} B_1 \\ B_2 \end{bmatrix} \dot{\boldsymbol{\delta}}_m(k) \tag{4.79}$$

with stiffness K, damping B, deflection δ and the stiffness reference deflection δ_m^0. The value r_m commanded by the human operator is defined as

$$\boldsymbol{r}_m(k) = \begin{bmatrix} \mu_1 \dot{\delta}_{m,1}(k) + \lambda_1 \delta_{m,1}(k) \\ \mu_2 \dot{\delta}_{m,2}(k) + \lambda_2 \delta_{m,2}(k) \end{bmatrix}. \tag{4.80}$$

In case of mode I (yaw-rate $\dot{\psi}$) the slave state vector $\boldsymbol{r}_s$ is

$$\boldsymbol{r}_s(k) = \begin{bmatrix} v_s(k) \\ \dot{\psi}(k) \end{bmatrix} \tag{4.81}$$

and $\mu_j = 1$ ($j \in \{1, 2\}$). Whereas in mode II (curvature κ) $\boldsymbol{r}_s$ is

$$\boldsymbol{r}_s(k) = \begin{bmatrix} v_s(k) \\ \kappa(k) \end{bmatrix} \tag{4.82}$$

and the controller parameters K_2 and B_2 can be set to zero (compare [81, 83]). Furthermore, $\mu_1 = 1$, $\mu_2 = 0$ and $\lambda_2 = 1$. The λ_1 value have to be determined via the r-passivity approach in order to achieve a passive master subsystem.

Thus, in mode I two velocities (v, $\dot{\psi}$) and in mode II one velocity (v) and one position (κ) are sent through the communication channel.

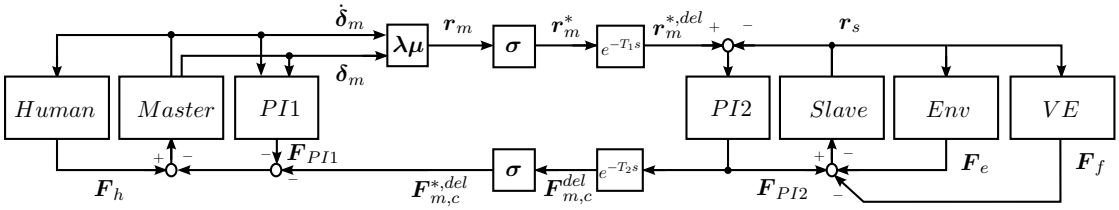

Figure 4.5.4: Signal Flow Diagram of a WMR Teleoperator with Computed Force Feedback
The fictitious force F_f can be commanded directly to the slave. According to the r-passivity approach, the signal $\boldsymbol{r}_m$ is sent to the slave side controller and a local PI controller is implemented at the master side. The command $\boldsymbol{r}_m$ is scaled with $\boldsymbol{\sigma}$ to adapt the workspace of the hardware. The feedback force also has to be scaled with $\boldsymbol{\sigma}$ for the sake of passivity.

4.5.2.1 Computed Force Feedback

Fig. 4.5.4 depicts the signal flow diagram of a computed force feedback architecture with communication channel. The master has a local controller $PI1$ and sends the signal $\boldsymbol{r}_m$ to the slave which is a combination of master positions and velocities (compare Equ. 4.80). For the sake of passivity, the signal $\boldsymbol{r}_m$ and the force feedback $\boldsymbol{F}_{m,c}^{del}$ are scaled with the same factor $\boldsymbol{\sigma}$. The interaction force with the real environment as well as the fictitious force calculated in the virtual environment (VE) act on the WMR slave robot. This local interaction of slave and virtual environment promises good performance in delayed systems. In this architecture, the human operator does not receive the fictitious force F_f directly. Still, through the computed force $\boldsymbol{F}_{m,c}^{del}$ he has vanished information on the fictitious force F_f since the controller $PI2$ has to act against F_f. This setup probably provides less performance compared to direct fictitious force feedback.

Fig. 4.5.5 depicts the network representation of this computed force feedback architecture. The master subsystem in this network representation equals the one of the agent presented in Fig. 3.3.6 of Section 3.3.2. A time delay is considered via TDPA Approach 1 (presented in Section 2.3.2.3). The scaling $\boldsymbol{\sigma}$ as an intrinsically passive functionality is represented by an additional subsystem in the track. A PCU allows the coupling of real and virtual environment to the slave. The PC_{VE} will be presented in Section 4.5.3.

4.5.2.2 Fictitious Force Feedback

Figure 4.5.6 depicts the signal flow diagram of a fictitious force feedback architecture with communication channel. The master has a local controller $PI1$ and sends the signal $\boldsymbol{r}_m$ to the slave which is a combination of master positions and velocities (compare Equ. 4.80). For the sake of passivity, the signal $\boldsymbol{r}_m$ and the force feedback $\boldsymbol{F}_{m,f}^{del}$ are scaled with the same factor $\boldsymbol{\sigma}$. In this architecture, the human operator receives the fictitious force F_f directly through $\boldsymbol{F}_{m,f}^{*,del}$. Note that also in this architecture, additionally, the fictitious force calculated in the virtual environment can act on the WMR slave robot as in Fig. 4.5.4.

Figure 4.5.7 depicts the network representation of this measured force feedback architecture. The master subsystem in this network representation equals the one of the agent presented in Fig. 3.3.6 of Section 3.3.2. A time delay is considered via TDPA Approach 1 (presented in Section 2.3.2.3). The scaling $\boldsymbol{\sigma}$ as an intrinsically passive functionality is represented by an additional subsystem in the track. The PC_{VE} will be

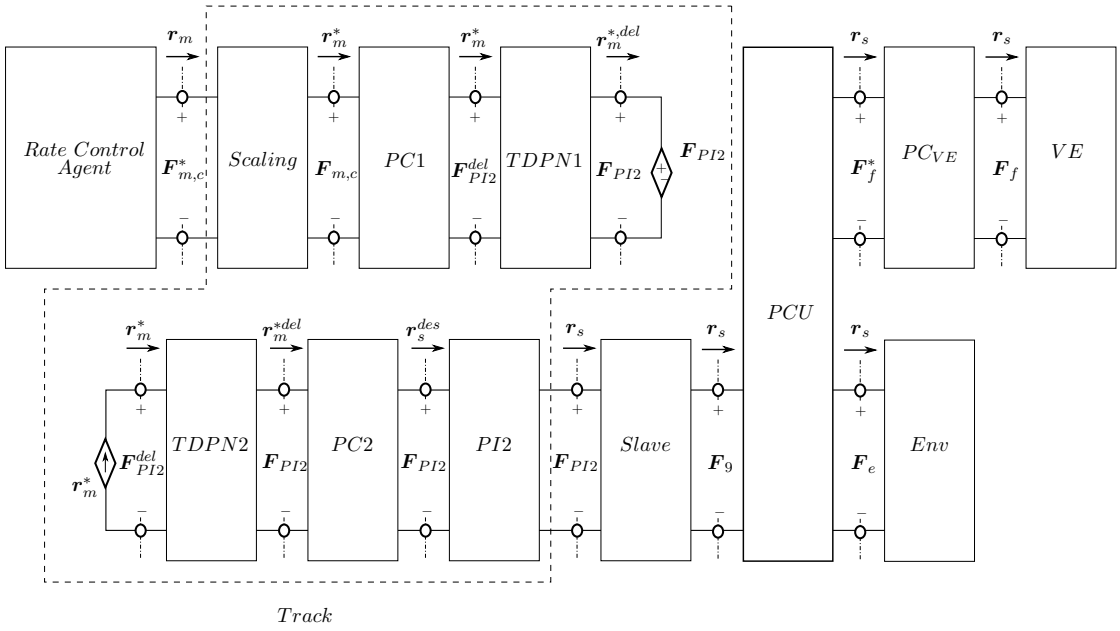

Figure 4.5.5: Network Representation of a WMR Teleoperator with Computed Force Feedback and Time Delay
The delay is considered via two sets of TDPNs and PCs. The forces of real and virtual environments acting on the slave are fused by a PCU. The 1-port of the virtual environment VE is passivity controlled by PC_{VE}.

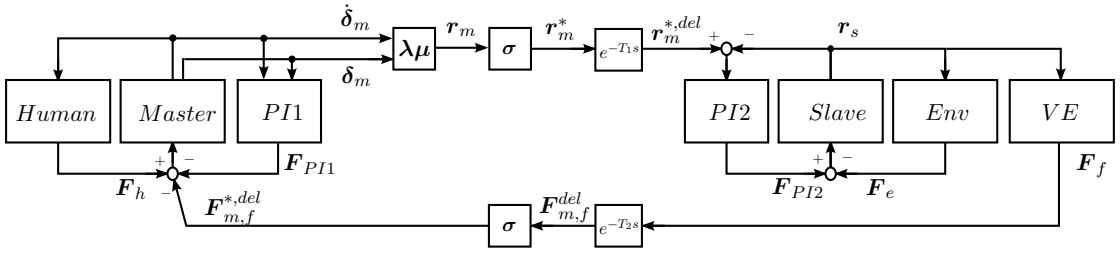

Figure 4.5.6: Signal Flow Diagram of a WMR Teleoperator with Fictitious Force Feedback
Here, the fictitious force F_f does not act on the slave but is scaled and sent through the communication channel to the rate control agent.

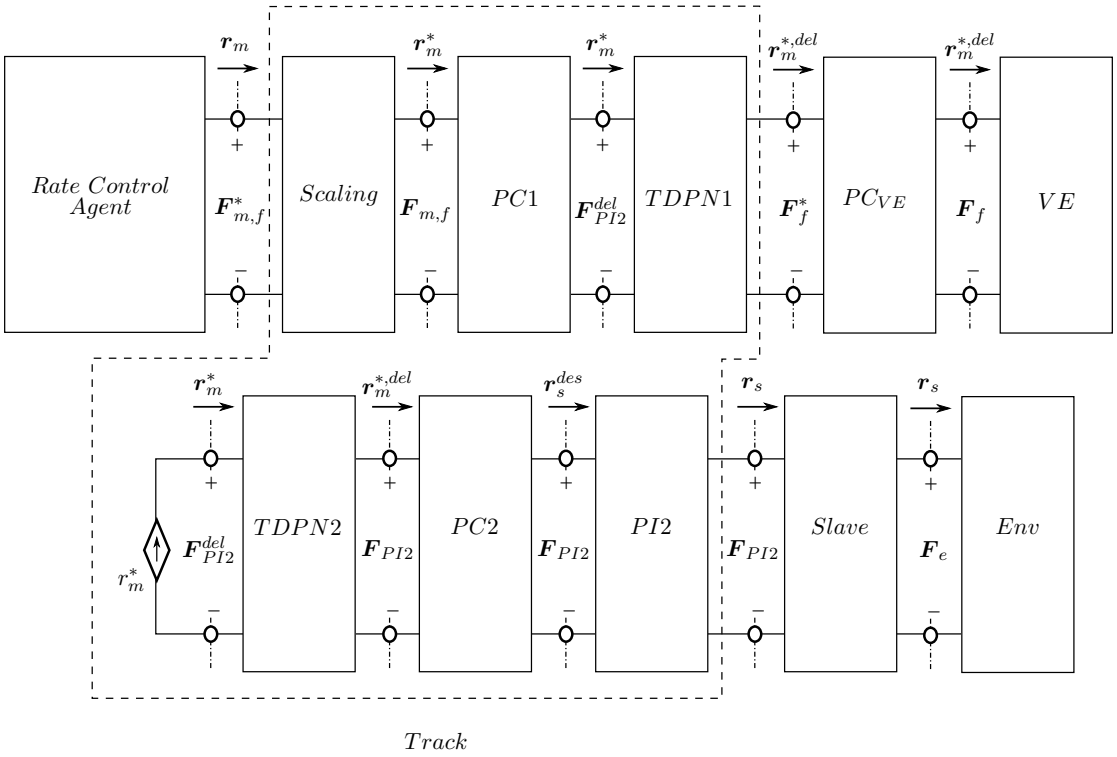

Figure 4.5.7: Network Representation of a WMR Teleoperator with Measured Force Feedback and Time Delay
The delay is considered via two sets of TDPNs and PCs. The 1-port of the virtual environment VE is passivity controlled by PC_{VE}.

presented in Section 4.5.3.

4.5.2.3 Multilateral Coupling

The cooperative teleoperation of a group of robots is not always reasonable since each robot might require a different trajectory. Due to this fact a high level of autonomy is required in such setups. The authors of [120] analyzed that in logistic operations several small robots might carry out a task in a more convenient and cheaper manner than one single bigger robot. The application of such cooperative swarms can be found in exploration, construction, as well as in recovery and rescue scenarios. The teleoperation of a formation of nonholonomic WMRs with constant time delay has been presented in [120]. Here, the coupling is multilateral in that the human operator is connected to the remote slave and the local model.

Extended Model Mediated Teleoperation A model mediated teleoperation framework provides a haptic loop between a human operator and a local model of a remote environment. The remote WMR is controlled by the inputs of the master device and the virtual model is updated by the states and the sensor information of the remote slave robot. The local model depends on the delayed state of the remote WMR (pose $\boldsymbol{x}_s^{del}$ of the WMR), but the force feedback may result from the local desired curvature and

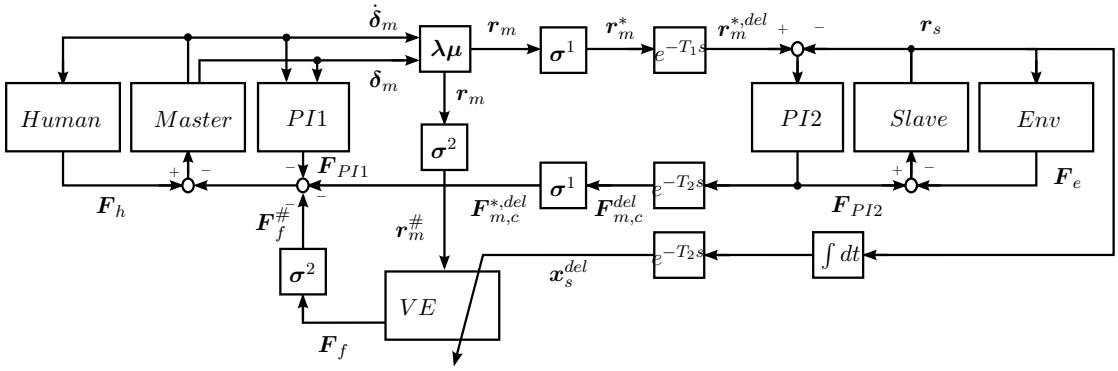

Figure 4.5.8: Signal Flow Diagram of an Extended Model Mediated Teleoperation Architecture for WMRs
The rate control agent receives hybrid force feedback. The computed controller force of $PI2$ is sent through the communication channel. Additionally, a local virtual environment, that is updated by the delayed slave state, provides the master device with a fictitious feedback force.

longitudinal velocity. Thus, instantaneous force feedback on the operator's input can be provided. This model mediated concept is here extended in a multilateral manner by additional computed force feedback from the slave to the master device. The respective signal flow diagram is depicted in Fig. 4.5.8. An additional scaling $\boldsymbol{\sigma}_2$ has to be integrated in the local feedback loop.

Note that analogous to Fig. 4.5.4, a fictitious force acting on the slave could be integrated by an additional remote virtual environment. The extended model mediated teleoperation promises an increase in performance since the operator receives not only delayed force feedback or imprecise fictitious force feedback but a combination of both. Also, the delayed haptic feedback can contain information that is often not considered in models as the ground friction causing wheel slip or little obstacles that were not recognized by the sensors but hinder the wheel motion. The predictive fictitious force feedback applied here does not consider the current slope in the robot environment. In such setups, haptic feedback calculated from the IMU of the remote slave can support the operator's perception of the robot dynamics. Regarding such possible additional haptic cues, a fusion of local and remote force feedback seems highly reasonable. Hereby, the remote feedback can be measured, computed or fictitious. Still, permanent remote force feedback may disturb the operator's perception, such that e.g. computed force feedback from a velocity controller that is gravely affected by the robot inertia is not recommended.

The network representation of an extended model mediated teleoperation architecture for WMRs can be seen in Fig. 4.5.9. The master subsystem in this network representation equals the one of the agent presented in Fig. 3.3.6 of Section 3.3.2. The scaling σ^j ($j \in \{1, 2\}$) as an intrinsically passive functionality is represented by an additional subsystem in the track. A time delay is considered via TDPA Approach 1 (presented in Section 2.3.2.3). A PCU allows the coupling of both feedback channels to the master. The PC_{VE} will be presented in Section 4.5.3.

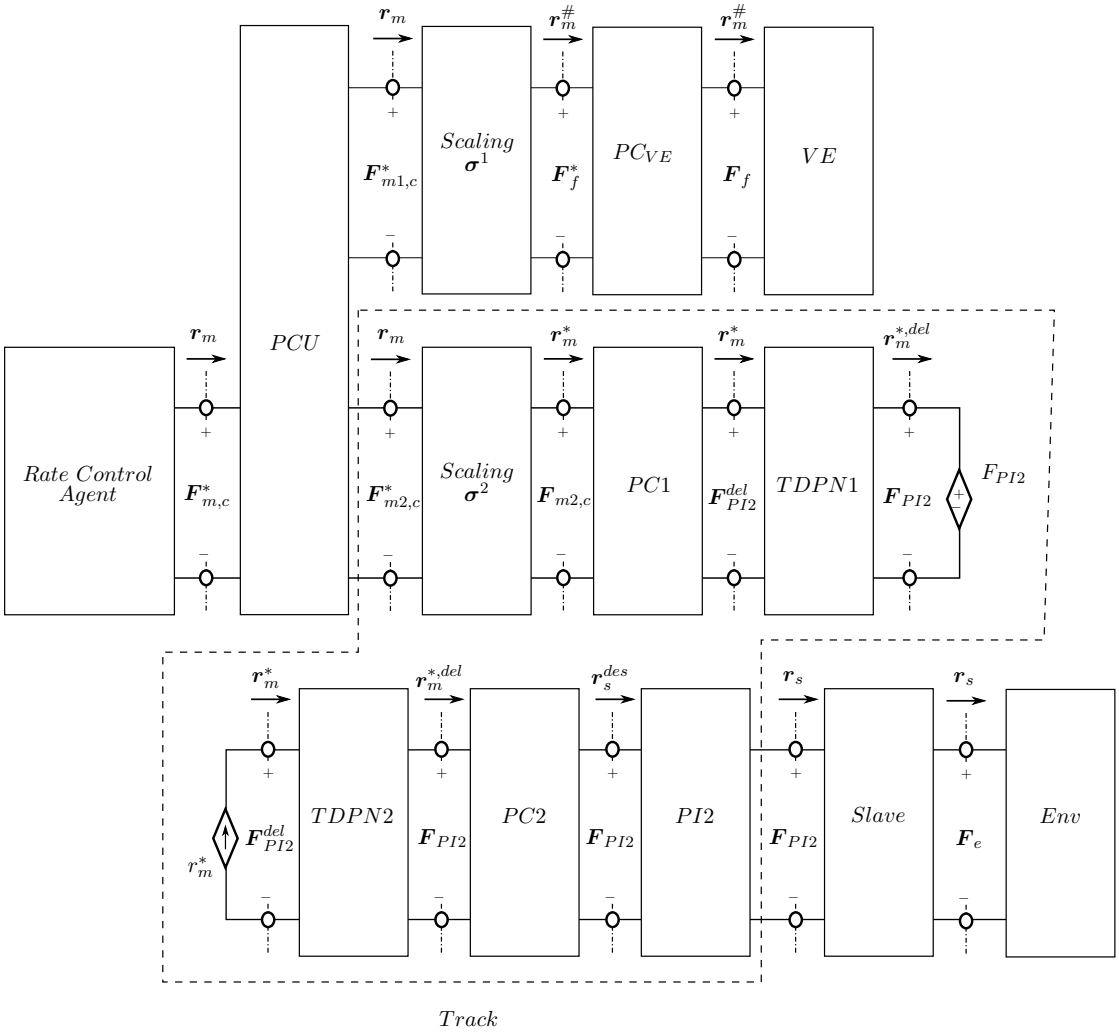

Figure 4.5.9: Network Representation of an Extended Model Mediated Teleoperation Architecture for WMRs
The PCU at the rate control agent fuses the local fictitious force feedback from the passivity controlled VE and the remote computed force feedback.

4.5.3 Stability Proof

A variety of stability concepts have been applied in the literature on teleoperation of WMRs. The respective focus in this thesis is the applicability of the control approach to the MPMT. For example, the Routh-Hurwitz criterion applied in [31] does not suite to the desired passive network. Also the Llewellyn approach of [90] is not useful since passive communication channels (TDPA, wave variables) can not be integrated. The approach of [177] is based on the network representation but does not sufficiently analyze the passivity of rate control agents and measured force feedback. The fictitious force has been modeled as a perturbation in [162] but was later neglected in the passivity and Lyapunov analysis. In [27], it was shown that a force vector resulting from a springlike repulsion can be easily proven to be passive. Still, the overall passivity was not guaranteed and the fictitious force feedback focused here is more complicated since the two slave DoFs are coupled. Also in [161], an approach with a virtual potential field was presented, and a Lyapunov control approach was applied. Still, this stability proof did not consider the feedback loop of the measured force to the operator.

The following stability analysis is based on the network representation and the passivity concept to suite the MPMT. Similar to [90], the r-passivity approach assures passivity under rate control and a PC renders the interaction with the virtual environment passive. In contrast, in order to allow a time delay in the communication channel, here the absolute stability criterion can not be applied.

4.5.3.1 WMR Control

Considering the dynamic equations of the bicycle model in terms of sideslip angle and yaw-rate, the authors of [169] have shown that the map of wheel steering angle δ_{WMR} to yaw-rate $\dot{\psi}$

$$\delta_{WMR} \rightarrow \dot{\psi} \tag{4.83}$$

is strictly passive. This holds analogously for the map of curvature κ to yaw-rate $\dot{\psi}$

$$\kappa \rightarrow \dot{\psi}. \tag{4.84}$$

Thus, the controller $PI2$ acting as spring-damper system on the linear velocity error and the curvature or yaw-rate error respectively is passive.

4.5.3.2 Rate Control

As has been introduced in 3.3.2, the master's passivity in rate control systems can be achieved via the r-passivity concept [81, 83]. Applying a two DoF master device, the r-passivity approach of [81] has to be applied in mode II, whereas the r-passivity approach of [83] for rate-control of multi-dimensional Lagrangian systems has to be applied for mode I. The definition of $\boldsymbol{r}_m$ in Equ. 4.80 is analogous to [83]. The parameter $\boldsymbol{\mu}_j = [0; 1]$ ($j \in \{1, 2\}$) has been introduced to present position control ($\mu = 0$, $\lambda = 1$) and rate control within one equation. Assuming that the joystick can be regarded as two separate 1-DoF linear systems with diagonal mass matrix $\boldsymbol{M} = diag[m_1, m_2]$ and zero Coriolis matrix $\boldsymbol{C}$, $\boldsymbol{\lambda}$, $\boldsymbol{B}$ and $\boldsymbol{K}$ have to be chosen such that

$$b_i \geq \lambda_i m_i, \qquad k_i \geq 0. \tag{4.85}$$

4.5.3.3 Fictitious Force Feedback

The calculation of the fictitious force according to Section 4.5.1 can result in a non-passive behavior. At zero velocity, the lateral motion of the master device may lead to an overlap of the polygon area and obstacles in the map. The resulting force feedback is approximately passive since the environment acts as a spring. But, the discretization of the map and the delay of the force calculation may introduce energy into the system.

The two coupled DoFs can be considered together in the passivity analysis. Overall, the VE subsystem may be passive since no energy can leave on the longitudinal DoF of the master. In this DoF, the force is always acting against the velocity command such that the power flow is unidirectional. Thus, an energy storage can be calculated for the VE subsystem. The power leaving on the lateral DoF of the joystick has to be limited by a passivity controller PC_{VE} if this energy storage is violated.

For example, the energy storage $E_{VE}(k)$ of the VE subsystem of Fig. 4.5.9 can be calculated as follows:

$$E_{VE}(k) = E_{VE}(k-1) + (P^{L2R,1}(k) + P^{L2R,2}(k))T_s \tag{4.86}$$

with the power $P^{L2R,i}$ flowing from left to right in the first (longitudinal, $i = 1$) and second (lateral, $i = 2$) DoF

$$P^{L2R,i}(k) = \begin{cases} -r^{\#}_{m,i}(k)F^{*}_{f,i}(k) & \text{,if } r^{\#}_{m,i}(k)F^{*}_{f,i}(k) \leq 0, \\ 0 & \text{,if } r^{\#}_{m,i}(k)F^{*}_{f,i}(k) > 0. \end{cases} \tag{4.87}$$

If the sum of desired output $P^{R2L}(k) = P^{R2L,1}(k) + P^{R2L,2}(k)$, with

$$P^{R2L,i}(k) = \begin{cases} r^{\#}_{m,i}(k)F^{*}_{f,i}(k) & \text{,if } r^{\#}_{m,i}(k)F^{*}_{f,i}(k) \geq 0, \\ 0 & \text{,if } r^{\#}_{m,i}(k)F^{*}_{f,i}(k) < 0, \end{cases} \tag{4.88}$$

violates the storage $E_{VE}(k)$, energy has to be dissipated by PC_{VE}

$$P^{PC_{VE},1}_{diss}(k) = \begin{cases} P_{diss}(k)\frac{P^{R2L,1}(k)}{P^{R2L}(k)}, & \text{if } E_{VE}(k) < P^{R2L}(k)T_s \\ 0, & \text{if } E_{VE}(k) \geq P^{R2L}(k)T_s \end{cases}, \tag{4.89}$$

$$P^{PC_{VE},2}_{diss}(k) = \begin{cases} P_{diss}(k)\frac{P^{R2L,2}(k)}{P^{R2L}(k)}, & \text{if } E_{VE}(k) < P^{R2L}(k)T_s \\ 0, & \text{if } E_{VE}(k) \geq P^{R2L}(k)T_s \end{cases}, \tag{4.90}$$

with the power P_{diss} that has to be dissipated

$$P_{diss}(k) = E_{VE}(k)/T_s - P^{R2L}(k). \tag{4.91}$$

$P^{PC_{VE},i}_{diss}$ has to be dissipated by an impedance PC in the first and second DoF respectively. The functionality of impedance type PCs is explained in Section 2.2.

Then, the energy storage $E_{VE}(k)$ needs to be updated since the power $P^{R2L}(k)$ left the VE

$$E_{VE}(k) = E_{VE}(k-1) + (P^{L2R,1}(k) + P^{L2R,2}_{2}(k) - P^{R2L,1}(k) - P^{R2L,2}(k))T_s. \tag{4.92}$$

Through the dissipation of impedance type PC_{VE} according to Section 2.3.2.3, the passivity of the interaction with the VE can be assured. Thus, the passivity of all setups presented in this section can be assured.

4.5.3.4 Time Delay

As depicted in the network representation of Fig. 4.5.5, Fig. 4.5.7 and Fig. 4.5.9, the time delay in the communication channels can be considered by the TDPA Approach 1 presented in Section 2.3.2.3. Also, the time delay control Approach 3 (Section 4.1.2) can be applied considering the PI controller of the WMR.

The position drift resulting from admittance type PCs is only affecting the curvature command in mode II, such that a position drift compensation becomes necessary. In contrast, the commanded longitudinal velocity and the yaw-rate in mode I are not affected by integration such that the effect of position drift is concealed.

4.5.4 Discussion on Rate Control and Fictitious Force Feedback

In this section, a method to calculate a fictitious force feedback from a height grid map has been proposed. The passivity of the designed virtual environment interaction can be assured via a passivity controller and applied to the presented variety of control architectures.

Different interfaces to the lateral dynamics have been developed. The two modes of yaw-rate and curvature command respectively, exhibit different behavior with respect to position drift and dependency on the linear velocity.

A multilateral extension of the model mediated teleoperation concept was proposed. Experiments on the respective approach are presented in Section 6.3.

4.6 Discussion on Passive Coupling Architectures

Different agent interaction schemes concerning time delay, coupling signals and rate control have been developed or adapted for the MPMT in the preceding sections. In this context, it was shown that also passively designed PF_{meas}, 3-*Channel* and 4-*Channel* architectures can provide better performance than the standard PP and PF_{comp} architectures. Also, the advantages and disadvantages of three TDPA methods guaranteeing passivity despite time delay have been analyzed. Furthermore, the network representation with the respective passivity proof for different wheeled mobile robot teleoperation schemes involving rate control and different coupling signals has been introduced.

In contrast to the approaches in Sections 4.2 to 4.4 where the PI controller energy was considered to limit the measured force feedback, the environment one port is passivity controlled in the rate control system of Section 4.5. This is necessary since the fictitious force feedback does not correspond to the energy behavior of the WMR controller. In the previous Sections 4.2 to 4.4, another approach was favored that promises to be less conservative. In position controlled systems, an energy injection from the slave side can be desired which would be dissipated if the environment one port would be passivity controlled analogously to Section 4.5.

The developed tracks serve as a basis for novel haptic augmentation concepts that are introduced in the subsequent chapter and underline the modularity and the wide-ranging applicability of the MPMT. In the next chapters different approaches are applied to the respective presented concepts and experimental scenarios. This is due to the fact, that the outline of this thesis does not follow the chronology of developments. Also, to focus on the novel approaches, to reduce the complexity and to ease the comprehension, the

basic PF_{comp} or PP architecture respectively has been applied in the following more complex setups.

Chapter 5

Haptic Augmentation based on the MPMT

This chapter introduces different haptic augmentation approaches that can be realized in the modular framework of the MPMT. Analogous to the well-known visual augmentation, the term haptic augmentation refers to any aid for the operator that is implemented in the haptic channel.
One of the simplest forms of haptic augmentation is a teleoperation training with a bilateral interaction between a mentor and a trainee operator. The haptic training can be improved through an authority allocation realized by scaling of the force feedback. Introducing a slave into this control loop, a trilateral haptic augmentation can be realized.
A more sophisticated haptic augmentation concept makes use of a virtual grasping point. This concept is meaningful in tasks in that the slave is grasping an object distantly from a point on the object in which the interaction with the environment takes place. Bilateral and multilateral systems can be designed with such virtual grasping points and combined with a task allocation similar to the authority allocation principle.
Also, the cooperation of two bilateral teleoperators can be eased through a haptic aid. E.g. the interaction forces of one human operator and his/her master device can be displayed at the other master device. Thus, each operator perceives the motion intention of the respective other operator more precisely.

The majority of the following concepts are multi-DoF systems. Note that the gravity compensation that was implemented for each applied robotic system is not explicitly mentioned in the presented control concepts. For the sake of clarity, vectors are considered instead of scalar signals in the simplified network representation diagrams (compare Section 3.3.4).

5.1 Virtual Grasping Points

An application that can benefit from multilateral control and augmented telepresence is the manipulation and assembly of large structures. The dexterity that an operator can achieve with one single master device is often insufficient for a precise object handling. For instance, placing a long pipe in a hole requires high precision in rotatory motions at one pipe end since the position (close to the hole) of the other end of the pipe should be steady. Another significant application for multilateral haptic augmentation setups is the manipulation of medical probes over patients' bodies. The point of contact of the probe has to follow the contour of the body. At the same time, a specific angle between the probe and the tissue surface has to be realized. This is challenging since e.g. disturbances caused by the cables hanging from the other end influence the task performance. Manipulating such work objects by grasping at one single grasping point (the point at which the slave hand grasps an object) can be tedious due to coupling forces and torques (rotating one end of the object causes unwanted translations at the other, and translational motion of the probe over the body causes rotations due to the moments created by the cables). The described tasks can be drastically simplified by defining a virtual, second grasping point at some other location on the object (or even outside in the environment). Two master devices can be used to control these two grasping points (real and virtual).

Besides the improvement of rotational precision (Section 5.1.1) the virtual grasping point (VG) concept has the capability to provide rotational feedback for underactuated devices via opposing forces (Section 5.1.2). Furthermore, the VG concept can be applied to a Single-Master-Dual-Slave setup with kinematically coupled slaves. The interaction point can be placed e.g. on the line connecting the TCPs of the two slave robots (compare Section 5.1.3).

5.1.1 Rotational Precision Concept

Clearly, the dexterity levels of an operator that is performing a telemanipulation is influenced by the telerobotic platform being used. The methods presented in this section aim at increasing the skillfulness of an operator in manipulating large objects through the distance in unstructured and narrow environments allowing only for compact robotic systems. The addressed scenario consists of a teleoperation system with a single slave and two masters that can be controlled by one operator bimanually. Thereby, one master serves the control of the slave robot's hand whereas the second master controls a virtual grasping point such that the rotational precision can be improved.

The approach can be applied to haptic devices with rotational force feedback. A task allocation for the same scenario is proposed in Section 5.2.2. Experiments and a user study are presented in Section 6.1.

5.1.1.1 System Description

In the following, a system with a bimanual input device and one slave robot arm grasping a pipe (see Fig. 5.1.1 and Fig. 5.1.2) is considered. The task is the insertion of a large pipe into a hole in a wall in the slave's environment. The typical procedure to plug in the pipe is firstly positioning the pipe end near the hole, then reorienting the pipe

perpendicular to the wall and pushing the pipe into the hole. In a general teleoperation system, this has to be solved with only one master robot M1 that is coupled to the slave's hand (grasping point G). The pipe end (PE) as the point of interest is far away from the robotic hand (tool center point, TCP) which makes the task rather difficult. Especially, it is demanding to keep the pipe end position steady during the reorientation of the object. The proposed setup addresses such difficulties by the use of a bimanual

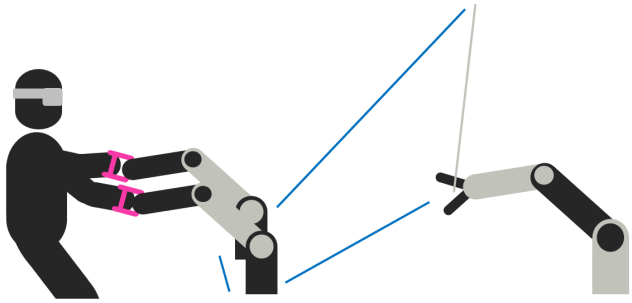

Figure 5.1.1: Multi-Master-Multi-Slave: Rotational Precision Setup for Cooperative Manipulation

haptic device with two master robots (see Fig. 5.1.3). The additional master device M2 is coupled to a virtual grasping point - the main feature of this approach - in the environment of the slave. The human operator can thus manipulate the pipe with two hands. The benefit of the VG or the bimanual manipulation is that the pipe can be rotated via counteracting forces. Thus, a rotation of the robotic hand can be commanded by an opposing translational motion of the master devices. The bimanual approach can be assumed to allow for a more accurate and intuitive manipulation, as it gives the operator a feeling of direct bimanual manipulation of the pipe without a teleoperation system.

Still, the proposed system is generic in that the VG approach can also be implemented in a single master setup. In contrast to a standard bilateral scenario, then, the master does not control the slave hand (grasping point G) but the pose of the VG. Note that in this single master scenario, the rotational motions have to be commanded via torques.

The virtual grasping point can be chosen arbitrarily in the slave's environment. In the considered task, the pipe end is the optimal location. The VG can be set automatically through computer vision and object recognition. Another possibility is to set the VG position via the master device. A visual augmentation in the slave environment might be required for that. For the sake of simplicity the VG was not matched automatically for the experiments later presented. The coupling between the devices through the virtual grasping point is depicted in Fig. 5.1.4. The master M1 (${}^{W}H_{G}^{des}$) and the slave S (${}^{W}H_{G}$) are connected directly by the PI controller $PI_{\Gamma 2}$ of $Track$ $\Gamma 2$. Master M1 (${}^{W}H_{\tilde{VG}}$) is coupled with master M2 (${}^{W}H_{VG}^{des}$) through $PI_{\Gamma 1}$ of $Track$ $\Gamma 1$ indirectly over the virtual grasping point. The same holds for the linkage of master M2 (${}^{W}H_{VG}^{des}$) with slave S

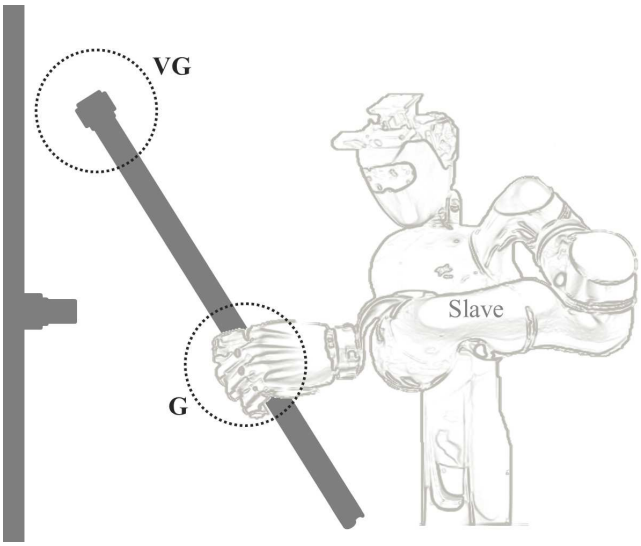

Figure 5.1.2: Slave Robot Grasping Pipe
The slave robot hand grasps a long object in the grasping point G. The point of interaction with the environment on the object is located at the end of the long object. Therefore, a virtual grasping point VG is defined there.

(${}^{W}H_{VG}$). $PI_{\Gamma 1}$ and $PI_{\Gamma 3}$ live in the pipe end. The projections (PR) of master M1 and slave S are represented by dashed coordinate frames. The transformation $\bar{T}$ transforms the controller wrench into the coordinate frames of the master M1 and slave S. Note that the VG of $Track$ $\Gamma 3$ is not equivalent to the one of $Track$ $\Gamma 1$ since the VGs depend on the slave and master M1 pose respectively.

5.1.1.2 Implementation

The position of the virtual grasping point can be defined relative to the slave frame with a scalar distance d and a vector g

$$g = \begin{bmatrix} g_1 \\ g_2 \\ g_3 \end{bmatrix}. \tag{5.1}$$

The orientation of the slave has to be projected onto the axis connecting G and VG through the rotation matrix R_{Pr} into the grasping frame ${}^{W}R_{G}$:

$${}^{W}R_{G} = {}^{W}R_{S}R_{Pr} \tag{5.2}$$

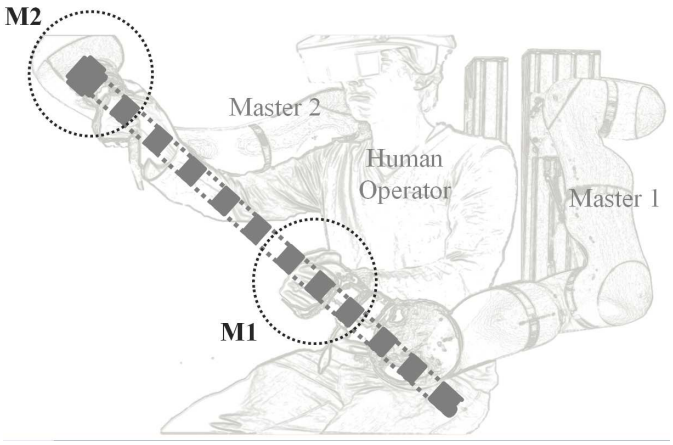

Figure 5.1.3: Operator with Two Masters and Virtual Pipe
A human operator controls the TCP of master M1 with the left and the TCP of master M2 with the right hand. Initially, master M1 is located in the grasping point G and master M2 is located in the virtual grasping point VG.

with

$$R_{Pr} = \left[\frac{r_1}{\|r_1\|_2}, \frac{r_2}{\|r_2\|_2}, \frac{r_3}{\|r_3\|_2} \right], \quad \text{with} \tag{5.3}$$

$$r_1 = g \tag{5.4}$$

$$r_2 = \begin{bmatrix} 0 \\ -r_{1,3} \\ r_{1,2} \end{bmatrix} \tag{5.5}$$

$$r_3 = r_1 \times r_2. \tag{5.6}$$

The pose ${}^{W}H_{VG}$ of the virtual grasping point can be calculated with the distance d as follows

$${}^{W}H_{VG} = \begin{bmatrix} {}^{W}R_G & {}^{W}p_S + {}^{W}R_G d e_1 + {}^{W}R_G a e_1 \\ 0 & 1 \end{bmatrix}, \quad \text{with} \tag{5.7}$$

$$e_1 = \begin{bmatrix} 1 \\ 0 \\ 0 \end{bmatrix}. \tag{5.8}$$

Via the scalar a, the distance of the virtual grasping point can be varied online, e.g. via an additional input device as a pair of buttons. The desired positions of the grasping ${}^{W}p_G^{des}$ and virtual grasping point ${}^{W}p_{VG}^{des}$ are

$${}^{W}p_G^{des} = {}^{W}p_S^{t_0} + {}^{W}p_{M_L} - {}^{W}p_{M_L}^{t_0}, \tag{5.9}$$

$${}^{W}p_{VG}^{des} = {}^{W}p_{VG} + {}^{W}p_{M_R} - {}^{W}p_{M_R}^{t_0}. \tag{5.10}$$

With ${}^{W}R_{VG}^{t_0} = {}^{W}R_G^{t_0}$ and

$${}^{W}R_{VG}^{des} = {}^{W}R_{M_R}\, {}^{M_R}R_W^{t_0}\, {}^{W}R_{VG}^{t_0}, \tag{5.11}$$

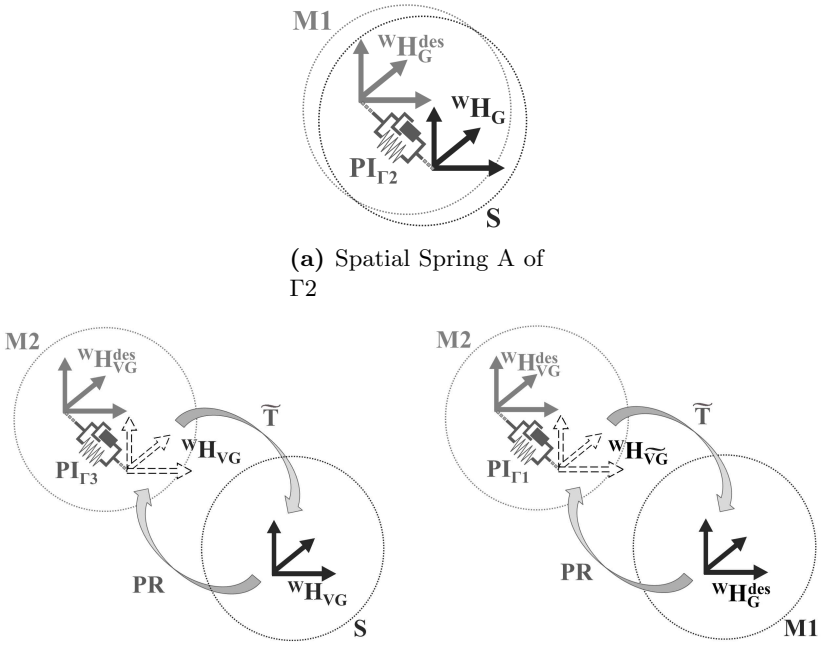

(a) Spatial Spring A of Γ2

(b) Spatial Spring B of Γ3

(c) Spatial Spring C of Γ1

Figure 5.1.4: Device Coupling with Virtual Grasping Point Concept
Master M1 and slave S are coupled in the grasping frame G, whereas master M2 and slave S and master M1 and M2 are coupled in the virtual grasping point VG. Since master M1 and slave S are located in the grasping point, the wrenches of the springs B and C need to be transduced into the grasping frame to calculate the force feedback to slave and master M1.

the current pose of the right master ${}^{W}H_{VG}^{des}$ is

$$ {}^{W}H_{VG}^{des} = \begin{bmatrix} {}^{W}R_{VG}^{des} & {}^{W}p_{VG}^{des} \\ 0 & 1 \end{bmatrix}. \tag{5.12} $$

The current pose of the left master projected into the grasping frame ${}^{W}H_{VG}^{des}$ is

$$ {}^{W}H_{G}^{des} = \begin{bmatrix} {}^{W}R_{G}^{des} & {}^{W}p_{G}^{des} \\ 0 & 1 \end{bmatrix}, \text{ with} \tag{5.13} $$

$$ {}^{W}R_{G}^{des} = {}^{W}R_{M_L}\, {}^{M_L}R_{W}^{t_0}\, {}^{W}R_{G}^{t_0}. \tag{5.14} $$

For the controller connecting the two master devices the pose of the virtual grasping point with respect to the left master ${}^{W}H_{\bar{VG}}$ has to be calculated:

$$ {}^{W}H_{\bar{VG}} = \begin{bmatrix} {}^{W}R_{\bar{VG}} & {}^{W}p_{\bar{VG}} + {}^{W}R_{\bar{VG}} a e_1 \\ 0 & 1 \end{bmatrix}, \tag{5.15} $$

with

$$ {}^{W}H_{\bar{VG}} = {}^{W}H_{G}^{des}\, {}^{G}H_{W}\, {}^{W}H_{VG}. \tag{5.16} $$

The reference frames ${}^{W}H_1$ and ${}^{W}H_2$ of the three coupling springs A,B,C of Fig. 5.1.4 are listed in Table 5.1. The desired pose of the first device ${}^{W}H_{1}^{des}$ is calculated from the pose of the second device ${}^{W}H_2$:

$$ {}^{W}H_{1}^{des} = {}^{W}H_2\, {}^{2}H_{W}^{t_0}\, {}^{W}H_{1}^{t_0}. \tag{5.17} $$

Thus, the wrench in the tool frame of device 1 can be calculated with the controller input ΔH^{des}:

$$ \Delta H^{des} = {}^{1}H_{W}^{des}\, {}^{W}H_1 = {}^{1}H_{W}^{t_0}\, {}^{W}H_{2}^{t_0}\, {}^{2}H_{W}\, {}^{W}H_1. \tag{5.18} $$

Note that the spring A is located in the grasping point G whereas the springs B and C

Table 5.1: Virtual Grasping Point Springs 1

Spring	${}^{W}H_1$	${}^{W}H_2$	Track
A	${}^{W}H_G$	${}^{W}H_{G}^{des}$	$Track\ \Gamma 2$
B	${}^{W}H_{VG}$	${}^{W}H_{VG}^{des}$	$Track\ \Gamma 3$
C	${}^{W}H_{\bar{VG}}$	${}^{W}H_{VG}^{des}$	$Track\ \Gamma 1$

are located in the virtual grasping point VG.

As the springs' wrench output W^A, W^B and W^C is in the frame of ${}^{W}H_1$, the wrench has to be transformed into base frame in order to calculate the wrench commanded to

the hardware:

$$ {}^{S}W^{A} = {}^{S}\bar{T}_{W}\,{}^{W}\bar{T}_{G}\,{}^{G}W^{A}, \tag{5.19} $$

$$ {}^{M_L}W^{A} = {}^{M_L}\bar{T}_{W}\,{}^{W}\bar{T}_{G}\,{}^{G}\tilde{W}^{A}, \tag{5.20} $$

$$ {}^{S}W^{B} = {}^{S}\bar{T}_{W}\,{}^{W}\bar{T}_{\tilde{VG}}\tilde{T}\,{}^{VG}W^{B}, \tag{5.21} $$

$$ {}^{M_R}W^{B} = {}^{M_R}\bar{T}_{W}\,{}^{W}\bar{T}_{VG}\,{}^{VG}\tilde{W}^{B}, \tag{5.22} $$

$$ {}^{M_R}W^{C} = {}^{M_R}\bar{T}_{W}\,{}^{W}\bar{T}_{\tilde{VG}}\,{}^{\tilde{VG}}W^{C}, \tag{5.23} $$

$$ {}^{M_L}W^{C} = {}^{M_L}\bar{T}_{W}\,{}^{W}\bar{T}_{\tilde{VG}}\tilde{T}\,{}^{\tilde{VG}}\tilde{W}^{C}. \tag{5.24} $$

with

$$ \tilde{W}^{i} = -W^{i}. \tag{5.25} $$

Note that transformation matrices $\bar{T}$ do only contain rotatory elements:

$$ {}^{n}\bar{T}_{m} = \begin{bmatrix} {}^{n}R_{m} & 0 \\ 0 & {}^{n}R_{m} \end{bmatrix} \tag{5.26} $$

and transformation matrix $\tilde{T}$ assures the power consistency in the force mapping to the grasping frame:

$$ \tilde{T} = \left[\begin{array}{ccc|c} & \mathbf{I}_3 & & \mathbf{0}_3 \\ \hline 0 & 0 & 0 & \\ 0 & 0 & d & \mathbf{I}_3 \\ 0 & -d & 0 & \end{array}\right], \tag{5.27} $$

with the zero matrix $\mathbf{0}_3$ and the unity matrix $\mathbf{I}_3 \in R^{3x3}$. With the upper setup, the rotation of the pipe can be commanded via rotations at the master devices. Still, a real pipe can be rotated via a translation of one hand e.g. when the second hand remains steady. To implement this behavior in the robotic system, two additional springs (see 5.2) have to be introduced into the system. The orientation R_{VP} of the virtual pipe (VP) connecting the two master devices has to be calculated:

$$ m = {}^{W}p^{des}_{VG} - {}^{W}p^{des}_{G}, \tag{5.28} $$

$$ R_{VP} = \left[\ \tfrac{u_1}{\|u_1\|_2}, \tfrac{u_2}{\|u_2\|_2}, \tfrac{u_3}{\|u_3\|_2}\ \right], \tag{5.29} $$

with the euclidean 2-norm of a vector v

$$ \|v\|_2 = \sqrt{\sum_{i=1}^{n}(v_i)^2} \quad \text{and} \tag{5.30} $$

$$ u_1 = m, \tag{5.31} $$

$$ u_2 = \begin{bmatrix} 0 \\ -m_{1,3} \\ m_{1,2} \end{bmatrix}, \tag{5.32} $$

$$ u_3 = u_1 \times u_2. \tag{5.33} $$

The reference frame for the right ${}^{W}_{VP}H^{des}_{M_R}$ and left master ${}^{W}_{VP}H^{des}_{M_L}$ can be found to be

$$ {}^{W}_{VP}H^{des}_{M_R} = \begin{bmatrix} R_{VP} & {}^{W}p^{des}_{VG} \\ 0 & 1 \end{bmatrix}, \tag{5.34} $$

$$ {}^{W}_{VP}H^{des}_{M_L} = \begin{bmatrix} R_{VP} & {}^{W}p^{des}_{G} \\ 0 & 1 \end{bmatrix}. \tag{5.35} $$

The springs should not have an effect on the translations and the rotation around the pipe frame. Therefore, the spring has to be positioned in the pipe frame and the respective forces and torques have to be canceled through the scaling $v^{VP} = [0, 0, 0, 0, 1, 1]$. The first input ${}^{W}H_1$ to the additional springs D and E equal the reference frames ${}^{W}_{VP}H^{des}_{M_R}$ and ${}^{W}_{VP}H^{des}_{M_L}$. The torques sent to the master devices result in:

Table 5.2: Virtual Grasping Point Springs 2

Spring	${}^{W}H_1$	${}^{W}H_2$	Track
D	${}^{W}_{VP}H^{des}_{M_R}$	${}^{W}H^{des}_{VG}$	$Track\ \Gamma1$
E	${}^{W}_{VP}H^{des}_{M_L}$	${}^{W}H^{des}_{G}$	$Track\ \Gamma1$

$$ {}^{M_R}W^{D} = {}^{M_R}\bar{T}_{W}\ {}^{W}\bar{T}_{VG} v^{VP\ VG}\tilde{W}^{D}, \tag{5.36} $$

$$ {}^{M_L}W^{E} = {}^{M_L}\bar{T}_{W}\ {}^{W}\bar{T}_{G} v^{VP\ G}\tilde{W}^{E}. \tag{5.37} $$

The springs D and E can be integrated into $Track\ \Gamma1$.

5.1.1.3 Passivity

As discussed above, the passivity of the track is crucial for the chosen stability approach. The virtual grasping point method can be represented as projection subsystems PR in the MPMT. Note that for the ease of comprehension the PR blocks are presented separately from the track in Fig. 5.1.5 although they could be integrated into the track. Fig. 5.1.5 shows that PR blocks are added in $Track\ \Gamma1$ and $\Gamma3$ respectively next to the PCU of master 1 and slave such that the PI controllers of those tracks are located in the virtual grasping point.

The large object represented by a pipe in the chosen application can be regarded as a rigid object and thus as a passive tool. The projection block can be regarded as a fix coupling of two frames that have a distance of δH (e.g. between frame $K = {}^{W}H^{des}_{G}$ and frame $Q = {}^{W}H_{\tilde{VG}}$). The virtual coupling has been designed such that the two frames Q and K have the same orientation and lie on the same x-axis (compare equations (5.8)-(5.7)). Since a rotation of a translationally steady frame K results in a translation and rotation of frame Q, the power consistency of the force transformation is not obvious.

Still, transforming the force and torque with matrix $\tilde{T}$ (compare equation (5.27))

$$\begin{bmatrix} F_x \\ F_y \\ F_z \\ M_x \\ M_y \\ M_z \end{bmatrix}^Q = \left[\begin{array}{ccc:c} & \mathbf{I}_3 & & \mathbf{0}_3 \\ \hdashline 0 & 0 & 0 & \\ 0 & 0 & d & \mathbf{I}_3 \\ 0 & -d & 0 & \end{array}\right] \begin{bmatrix} F_x \\ F_y \\ F_z \\ M_x \\ M_y \\ M_z \end{bmatrix}^K \tag{5.38}$$

and the linear and angular velocities according to the distance d

$$\begin{bmatrix} v_x \\ v_y \\ v_z \\ \omega_x \\ \omega_y \\ \omega_z \end{bmatrix}^Q = \left[\begin{array}{c:ccc} & 0 & 0 & 0 \\ \mathbf{I}_3 & 0 & 0 & d \\ & 0 & -d & 0 \\ \hdashline \mathbf{0}_3 & & \mathbf{I}_3 & \end{array}\right] \begin{bmatrix} v_x \\ v_y \\ v_z \\ \omega_x \\ \omega_y \\ \omega_z \end{bmatrix}^K, \tag{5.39}$$

the passivity of the transformation is guaranteed:

$$\begin{aligned} P^Q &= F_x^Q v_x^Q + F_y^Q v_y^Q + F_z^Q v_z^Q + M_x^Q \omega_x + M_y^Q \omega_y + M_z^Q \omega_z = \\ &= F_x^K v_x^K + F_y^K (v_y^K + \omega_z d) + F_z^K (v_z^K - \omega_y d) + M_x^K \omega_x \\ &\qquad + (M_y^K + F_z^K d)\omega_y + (M_z^K - F_y^K d)\omega_z = \\ &= F_x^K v_x^K + F_y^K v_y^K + F_z^K v_z^K + M_x^K \omega_x + M_y^K \omega_y + M_z^K \omega_z = P^K \end{aligned} \tag{5.40}$$

Experiment Exp. 5.1 presents the coupling of a bilateral system with master M_R in VG and M_L in G. The power leading to the motion is introduced at master M_R. The position following in the xy-plane is satisfactory and the last plot shows the passivity check. Since the energy E_{PP} is always positive, the passivity of the combination of spatial spring and projection subsystem is guaranteed. The experiment plot Exp. 5.2 shows the equivalent proof for a motion demand at master M_L.

Besides the projection, also, the change in coordinate frame rotation is a simple lossless transformation as can be shown with the energy preservation of the fixed coupling between a frame Y and the projection frame Z. The condition in index notation

$$\sum_{i=1}^{6} ({}^Y W_i \, {}^Y \dot{q}_i) = \sum_{i=1}^{6} ({}^Z W_i \, {}^Z \dot{q}_i), \tag{5.41}$$

with the generalized velocities $\dot{q}$ and index $i \in \mathbb{Z}$, holds. Equations (5.42) and (5.43)

$${}^Y W_i = \sum_{j=1}^{6} (\bar{T}_{ji} \, {}^Z W_j), \tag{5.42}$$

$${}^Z \dot{q}_i = \sum_{j=1}^{6} (\bar{T}_{ij} \, {}^Y \dot{q}_j), \tag{5.43}$$

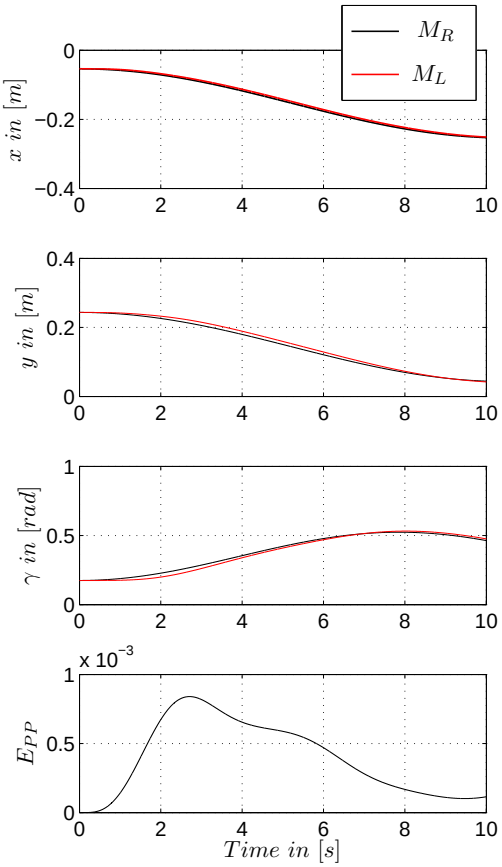

Experiment 5.1: Passivity Check of PR with Input at VG
A planar motion is performed. The trajectory of motion is commanded through the device in the virtual grasping point VG. Since the plot E_{PP} is never negative, the passivity is proven.

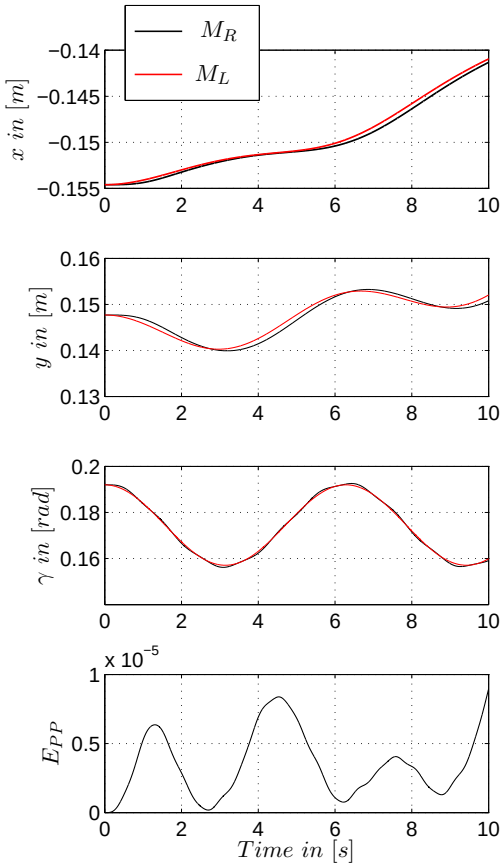

Experiment 5.2: Passivity Check of PR with Input at G
A planar motion is performed. The trajectory of motion is commanded through the device in the grasping point G. Since the plot E_{PP} is never negative, the passivity is proven.

with index $j \in \mathbb{Z}$, fulfill condition (5.41):

$$\sum_{i=1}^{6}(\sum_{j=1}^{6}(\bar{T}_{ji}\ {}^{Z}W_j)\ {}^{Y}\dot{q}_i) = \sum_{i=1}^{6}(\ {}^{Z}W_i \sum_{j=1}^{6}(\bar{T}_{ij}\ {}^{Y}\dot{q}_j)).$$

Thus, the projection block PR is another passive network subsystem.

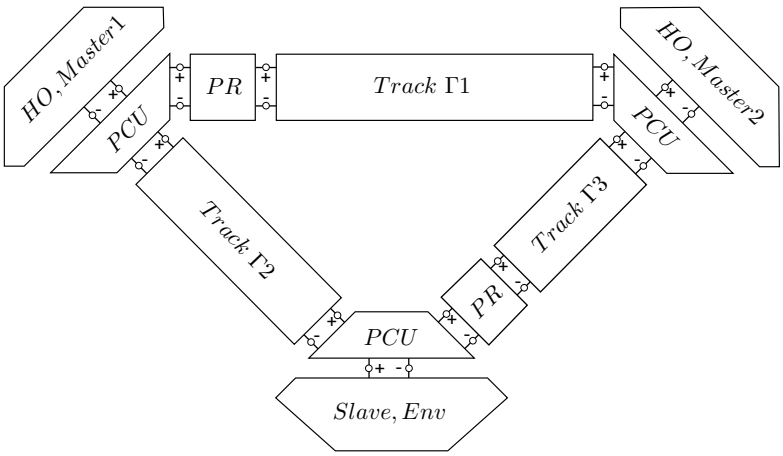

Figure 5.1.5: Multilateral System with Virtual Grasping Point Projection
Since the springs of *Track* Γ1 and *Track* Γ3 are located in the VG, the projection subsystems PR have to be integrated in these tracks next to master M1 and slave S respectively.

5.1.2 Concept for Underactuated Devices

The concept of the preceding Section 5.1.1 is restricted to devices with rotational (torque) feedback. In a large part of teleoperation applications cheap devices can be used that mostly do not provide feedback in the rotational DoFs. In this section, a virtual grasping point Dual-Master-Single-Slave concept is presented that can be applied to devices with and without rotational force feedback as the Geomagic Touch (formerly Sensable Phantom Omni, [39]) or the Force Dimension Omega.7 [26]. A more precise rotational command can be achieved by commanding two rotational DoFs via the relative translations of two master devices. In the same manner, the force feedback of these two master devices results in an artificial torque feedback. For the Novint Falcon haptic device [102], a similar mechanically coupled concept has been proposed in [152].

The proposed approach is presented in Fig. 5.1.6. Two master devices M_L and M_R are used to control one slave robot S. The right master device M_R controls the slave's tool frame directly, whereas the left master device M_L controls a virtual grasping point VG. The virtual grasping point can be positioned randomly. The presented work considers a VG lying on the extension of the hand's x-axis.

Three spatial springs couple the three devices. Master M_R is directly coupled to the slave tool frame, master M_L is coupled to the virtual grasping point VG and master M_L is coupled to the virtual grasping point $\bar{VG}$ (determined by master M_R). The orientation of the slave hand is determined by the relative motion of master M_R and M_L. As only two rotations can be represented by the translation of the master devices, another interface has to be considered to access the third rotational DoF (rotation around the axis connecting M_L and M_R).

The drawbacks of the setup compared to the concept of Section 5.1.1 are that the rotation around the axis connecting the master devices can not be commanded and that the respective torque can not be displayed at the master devices. If one of the master devices provides rotational force feedback, these problems can easily be solved since

the orientation of that device can be coupled to the relative motion of the two master devices by a spatial spring. If no master device provides torque feedback, an additional two button interface can be used or the virtual grasping point position can be reselected iteratively for better manipulability.

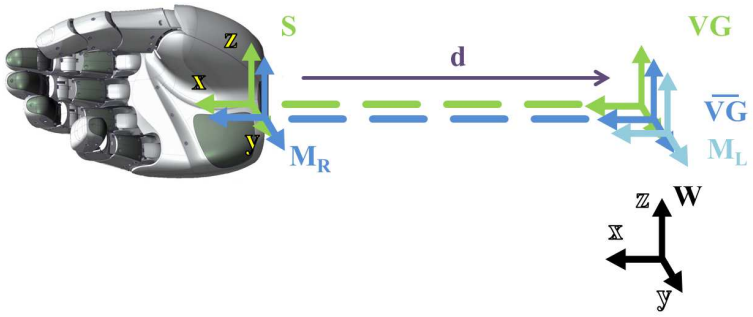

Figure 5.1.6: MMSS Concept for Underactuated Devices
The right master M_R controls the slave's tool center point and the left master M_L controls a virtual grasping point VG in distance d from the slave frame on the x-axis. This method promises higher rotatory precision. If the rotation of the master devices are not actuated, a torque around y-axis and z-axis can be displayed via a combination of counteracting forces at the master devices.

5.1.2.1 Implementation

The pose ${}^{W}H_{VG}$ of the virtual grasping point VG can be calculated with the desired distance d (see Fig. 5.1.6) as follows

$$ {}^{W}H_{VG} = \begin{bmatrix} {}^{W}R_S & {}^{W}p_S + {}^{W}R_S de \\ 0 & 1 \end{bmatrix}, \text{ with} \tag{5.44} $$

$$ e = \begin{bmatrix} 1 \\ 0 \\ 0 \end{bmatrix}. \tag{5.45} $$

Note that the vector e determines the axis of the slave frame on which the VG lies. Thus, the transform from slave to virtual grasping point in base frame ${}^{S}H_{VG}$ can be found:

$$ {}^{S}H_{VG} = {}^{W}H_{VG}\,{}^{S}H_{W}. \tag{5.46} $$

The desired slave and VG position depends on the position of the master devices:

$$ {}^{W}p_S^{des} = {}^{W}p_S^{t_0} + \Delta\,{}^{W}p_{M_R}, \tag{5.47} $$

$$ {}^{W}p_{VG}^{des} = {}^{W}p_{VG}^{t_0} + \Delta\,{}^{W}p_{M_L}. \tag{5.48} $$

$\Delta\,{}^{W}p_{M_i}$ $(i \in \{L, R\})$ is calculated as the difference between the initial and the current master positions:

$$ \Delta\,{}^{W}p_{M_i} = {}^{W}p_{M_i} - {}^{W}p_{M_i}^{t_0}. \tag{5.49} $$

The desired rotation of slave ${}^{W}R_{S}^{des}$ and VG ${}^{W}R_{VG}^{des}$ is found in three steps. The first step leads to ${}^{W}\tilde{R}_{VG}^{des}$ and ${}^{W}\tilde{R}_{S}^{des}$:

$$ {}^{W}\tilde{R}_{S}^{des} = {}^{W}R_{S}^{t_0}, \tag{5.50} $$

$$ {}^{W}\tilde{R}_{VG}^{des} = {}^{S}R_{VG}^{t_0}\,{}^{W}R_{S}^{t_0}. \tag{5.51} $$

Here, ${}^{S}R_{VG}^{t_0}$ is assumed to be the identity matrix $\mathbf{I}_3$.
In the second step the desired rotation in the slave y- and z-axis R^{YZ} can be computed with the angle α between the link of the master devices and the initial first column vector ${}^{W}r_{1,S}^{t_0}$ of the slave frame ${}^{W}R_{S}$:

$$ \alpha = cos^{-1}\left(\frac{({}^{W}p_{VG}^{des} - {}^{W}p_{S}^{des}) \circ {}^{W}r_{1,S}^{t_0}}{|{}^{W}p_{VG}^{des} - {}^{W}p_{S}^{des}||{}^{W}r_{1,S}^{t_0}|}\right). \tag{5.52} $$

With the vector of this rotation k

$$ k = ({}^{W}p_{VG}^{des} - {}^{W}p_{S}^{des}) \times {}^{W}r_{1,S}^{t_0} \tag{5.53} $$

or its skew-symmetric cross-product matrix K respectively

$$ K = \begin{bmatrix} 0 & -k_3 & k_2 \\ k_3 & 0 & -k_1 \\ -k_2 & k_1 & 0 \end{bmatrix} \tag{5.54} $$

and the Rodriguez equation

$$ R^{YZ} = I + sin(\alpha)K + (1 - cos(\alpha))K^2 \tag{5.55} $$

an equivalent rotation matrix can be calculated.
In the third step the desired rotation in the slave x-axis R^X (due to equation (5.45)) is considered:

$$ R^X = \begin{bmatrix} 1 & 0 & 0 \\ 0 & cos\beta & -sin\beta \\ 0 & sin\beta & cos\beta \end{bmatrix}, \tag{5.56} $$

with the angle β that can be demanded by a separate device (e.g. buttons of the master).
Finally, the desired orientation of slave and VG can be found:

$$ {}^{W}R_{S}^{des} = R^{YZ}\,{}^{W}\tilde{R}_{S}^{des}R^{X}, \tag{5.57} $$

$$ {}^{W}R_{VG}^{des} = R^{YZ}\,{}^{W}\tilde{R}_{VG}^{des}R^{X}. \tag{5.58} $$

Note that there are three co-existing positions of the virtual grasping point. The first is defined directly by the motion of master M_L, the second is defined by the extension of the slave position ${}^{W}H_{VG}$ and the third (${}^{W}H_{\bar{VG}}$) depends on the motion of master M_R:

$$ {}^{W}H_{\bar{VG}} = {}^{S}H_{VG}\,{}^{W}H_{S}^{des}. \tag{5.59} $$

If another input m as a pair of buttons is available, the virtual distance between the grasping point and the virtual grasping point can be varied online via the variable m:

$$ {}^{W}\check{H}_{V}^{des} = \begin{bmatrix} {}^{W}H_{VG}^{des} & {}^{W}p_{VG}^{des} + {}^{W}R_{VG}^{des} me \\ 0 & 1 \end{bmatrix}, \tag{5.60} $$

$$ {}^{W}\check{H}_{VG} = \begin{bmatrix} {}^{W}H_{VG} & {}^{W}p_{VG} + {}^{W}R_{VG} me \\ 0 & 1 \end{bmatrix}, \tag{5.61} $$

$$ {}^{W}\check{H}_{\bar{V}G} = \begin{bmatrix} {}^{W}H_{\bar{V}G} & {}^{W}p_{\bar{V}G} + {}^{W}R_{\bar{V}G} me \\ 0 & 1 \end{bmatrix}. \tag{5.62} $$

The reference frames of the three coupling springs are listed in Table 5.3. The spatial spring equations are analogous to equations (5.17)-(5.18). The wrench output of

Table 5.3: Spring Inputs

Spring	${}^{W}H_1$	${}^{W}H_2$
A	${}^{W}H_S$	${}^{W}H_S^{des}$
B	${}^{W}\check{H}_{VG}$	${}^{W}\check{H}_{VG}^{des}$
C	${}^{W}\check{H}_{\bar{V}G}$	${}^{W}\check{H}_{VG}^{des}$

the spring is calculated in the frame of ${}^{W}H_1$. Therefore, the wrench is first transformed into base frame to find the wrench that has to be commanded to the devices.

$$ {}^{S}W^{A} = {}^{S}W^{A} \tag{5.63} $$

$$ {}^{M_R}W^{A} = {}^{M_R}\bar{T}_{W}\, {}^{W}\bar{T}_{S}\, {}^{S}\tilde{W}^{A}, \tag{5.64} $$

$$ {}^{S}W^{B} = {}^{S}\bar{T}_{W}\, {}^{W}\bar{T}_{VG}\tilde{T}\, {}^{VG}W^{B}, \tag{5.65} $$

$$ {}^{M_L}W^{B} = {}^{M_L}\bar{T}_{W}\, {}^{W}\bar{T}_{VG}\, {}^{VG}\tilde{W}^{B}, \tag{5.66} $$

$$ {}^{M_R}W^{C} = {}^{M_R}\bar{T}_{W}\, {}^{W}\bar{T}_{\bar{V}G}\tilde{T}\, {}^{\bar{V}G}W^{C}, \tag{5.67} $$

$$ {}^{M_L}W^{C} = {}^{M_L}\bar{T}_{W}\, {}^{W}\bar{T}_{\bar{V}G}\, {}^{\bar{V}G}\tilde{W}^{C}, \tag{5.68} $$

with

$$ \tilde{W}^{i} = -W^{i}. \tag{5.69} $$

and

$$ \tilde{T} = \left[\begin{array}{ccc:c} & \mathbf{I}_3 & & \mathbf{0}_3 \\ 0 & 0 & 0 & \\ 0 & 0 & d & \mathbf{I}_3 \\ 0 & -d & 0 & \end{array}\right]. \tag{5.70} $$

Note that transformation matrices $\bar{T}$ do only contain rotatory elements:

$$ {}^{n}\bar{T}_{m} = \begin{bmatrix} {}^{n}R_{m} & 0 \\ 0 & {}^{n}R_{m} \end{bmatrix}. \tag{5.71} $$

5.1.2.2 Passivity

The network representation of the presented setup for underactuated devices equals the concept for rotational precision in the preceding section depicted in Fig. 5.1.5. However, it has to be considered that the rotational DoFs present an open-loop system since the torque feedback is zero in rotationally underactuated devices ($F_{24} = F_{25} = F_{26} = 0$ in Fig. 3.3.9). Still, as has been discussed in Section 3.3.3, open-loop teleoperation can be regarded as a passive control architecture due to the visual feedback to the operator. Thus, the overall system is passive.

5.1.2.3 Coupling Rigidity

In order to achieve a more symmetric and rigid system, two additional PI controllers can be implemented in the slave S and master M_R position respectively. In Fig. 5.1.7 and Fig. 5.1.8, the rotational stiffness of the linkage between the two master devices is presented exemplary. If only a spatial spring in the position of master M_R is implemented, the translational flexibility of master M_L is much higher than the one of master M_R. Another spatial spring in the position of master M_L renders the coupling symmetric and leads to a higher coupling rigidity. Note that this dual coupling is not applicable if a cartesian task allocation (compare Section 5.2.2) is implemented. As shown in Fig. 5.1.9, two tracks $\Gamma 1, R2L$ and $\Gamma 3, R2L$ have to be added. Note that in the coupling of

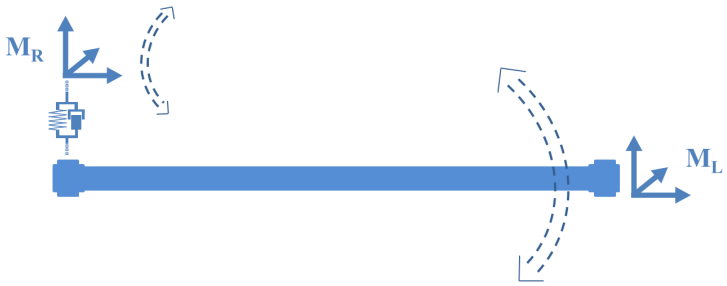

Figure 5.1.7: Interaction between Master M_R and M_L with one Spring
If only a spatial spring in the position of master M_R is implemented, the translational flexibility of master M_L is much higher than the one of master M_R.

Figure 5.1.8: Interaction between Master M_R and M_L with two Springs
Two spatial springs in the positions of master M_L and master M_R render the coupling symmetric and lead to a higher coupling rigidity.

Fig. 5.1.9 each device receives only feedback from two of the tracks it is connected to.

Since the PCU, tracks and the projection subsystems (compare Section 5.1.1.3) are passive, the overall system is passive.

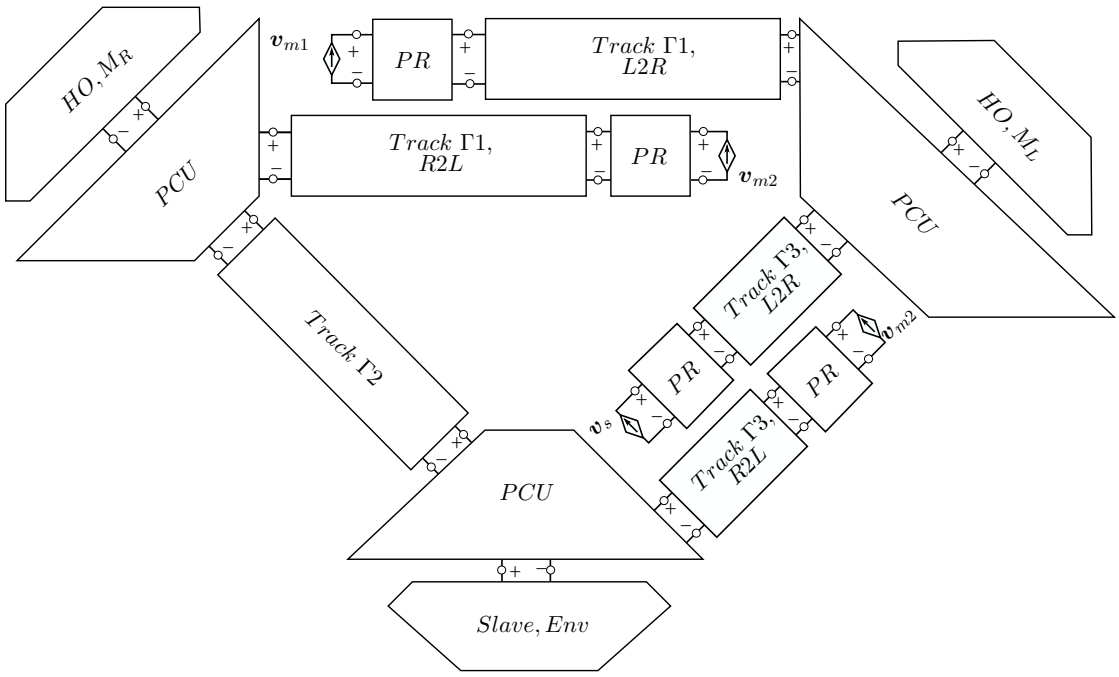

Figure 5.1.9: Multilateral Setup for Underactuated Devices with Additional Spatial Springs
The slave and master M_R are coupled in the slave's tool center point such that no PR subsystem is needed in *Track* Γ2. The L2R and R2L parts of *Track* Γ1 and *Track* Γ3 and the PR subsystems are designed such that one spatial spring is located in the position of both coupled agents of one track.

5.1.2.4 Experiments

The following experiments were performed with the setup presented in Appendix A.4. Two Omega.7 have been applied as master devices and one LWR served as the slave robot. The multilateral coupling was implemented according to Fig. 5.1.5.

To ease the comprehension of the multilateral coupling, master M_R (compare Fig. 5.1.6) has been deactivated in the first experiment Exp. 5.3. Therefore, during the motion of master M_L, the slave translations remain constant (see plot Exp. 5.3) whereas the rotation of the slave changes according to the link of master M_R and M_L. The line color changes with time.

In the second experiment Exp. 5.4, master M_L remains steady. The slave follows the motion of master M_R and the rotations of the slave change analogously to the link of the master devices.

In the third experiment Exp. 5.5, the slave device is rotated by the human hand to test stability considering an active slave environment. The right master device M_R was deactivated. As can be seen in plots Exp. 5.5a and Exp. 5.5b, master M_L follows the motion of the virtual grasping point ${}^W p_{VG}$ well. The forces that push master M_L to the right position can be interpreted as a torque acting in master M_R although the rotation of the master devices are not actuated.

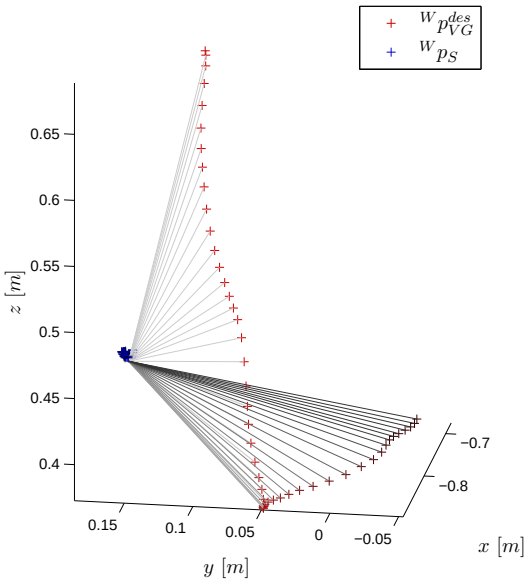

Experiment 5.3: 3D Motion of a Dual-Master-Single-Slave System and Steady Master M_R
During the motion of master M_L, the slave translations remain constant whereas the rotation of the slave changes according to the link of master M_R and M_L.

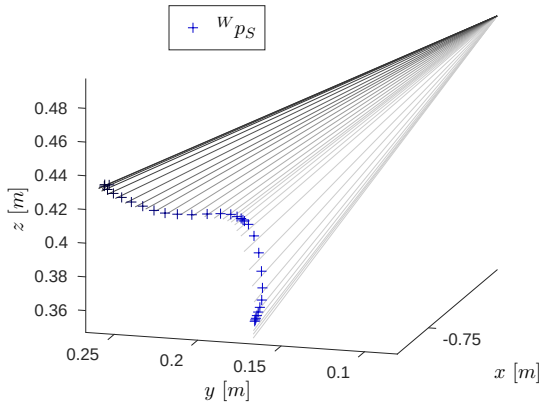

Experiment 5.4: 3D Motion of a Dual-Master-Single-Slave System and Steady Master M_L
The slave follows the motion of master M_R and the rotations of the slave change analogously to the link of the master devices.

In the fourth experiment Exp. 5.6, both master devices are moved. As can be analyzed from plots Exp. 5.6a and Exp. 5.6b, the position of master M_R is constant ($t = [67.5s - 69.5s]$) first and master M_L rotates around M_R. Then both master device move synchronously down ($t = [69.5s - 71s]$) such that the rotation of the slave remains nearly constant. Plot Exp. 5.6a presents the satisfactory position tracking of master M_R ($^W p_G^{des}$) and slave S ($^W p_G$). As depicted in plot Exp. 5.6c, no torque is sent to master M_L. Since the slave is not in contact with the environment, master M_L perceives no resistance in z-direction. In contrast, the coupling springs act on the devices in x-direction to lead master M_L on a sphere around master M_R during the downward motion.

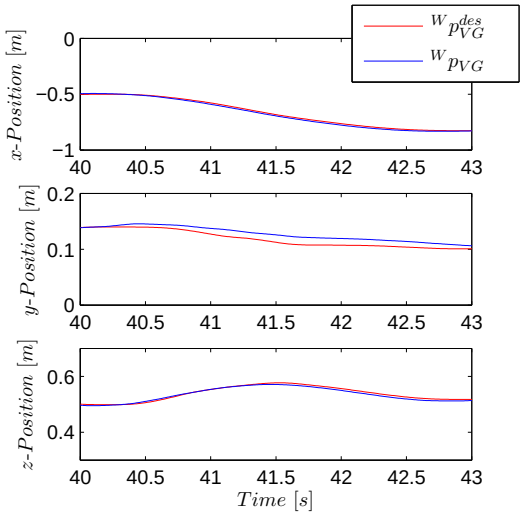

(a) Position Tracking

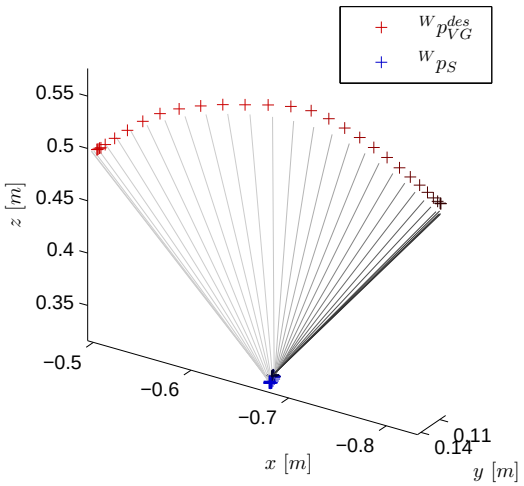

(b) 3D Motion Plot

Experiment 5.5: Dual-Master-Single-Slave System with Active Slave Environment
The actuators of master M_R are deactivated while the slave hand is moved by the operator. Master M_L follows the motion of the virtual grasping point $^W p_{VG}$ well. The forces that push master M_L to the right position can be interpreted as a torque acting in master M_R though the rotation of the master devices are not actuated.

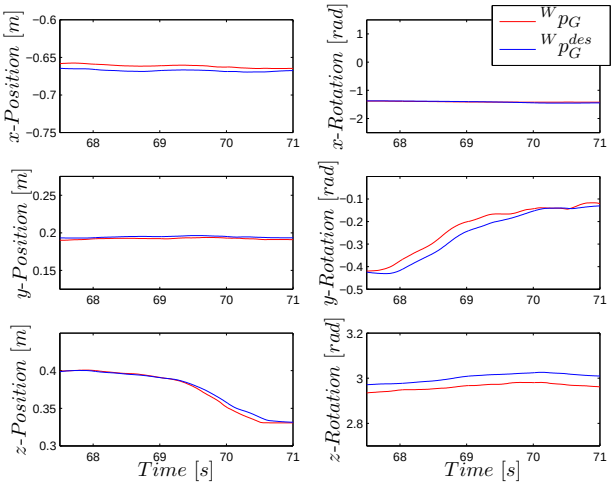

(a) Position Tracking

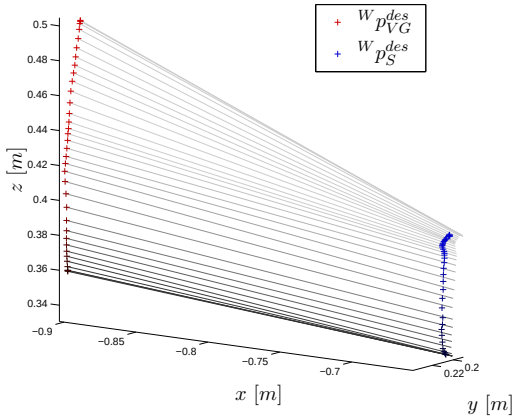

(b) 3D Motion Plot

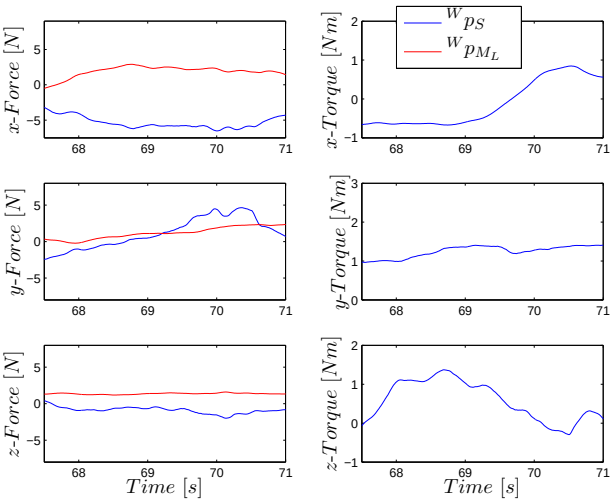

(c) Wrenches

Experiment 5.6: Dual-Master-Single-Slave System with Motion of all Devices
First, the position of master M_R is constant ($t = [67.5s - 69.5s]$) and master M_L rotates around M_R. Then both master device move synchronously down ($t = [69.5s - 71s]$) such that the rotation of the slave remains nearly constant. The position tracking of master M_R ($^W p_G^{des}$) and slave S ($^W p_G$) is satisfactory. No torque is sent to master M_L. The coupling springs act on the devices mainly in x-direction to lead master M_L on a sphere around master M_R during the downward motion.

5.1.3 Cooperatively Grasping Slaves

In the preceding sections, the virtual grasping point method was applied in Multi-Master-Single-Slave systems to improve the rotational performance. In the following, the virtual grasping point concept will be applied to control two slave hands via one master device in a Single-Master-Multi-Slave system [69]. This approach promises higher robustness in the cooperative grasp of one object since the slave robots have a fix kinematic coupling. In contrast, the grasp quality is disturbed, if the operator does not synchronously move two master devices controlling one slave robot each [80].

Two robots are often applied to manipulate one object cooperatively since thus, the load capacity, rigidity and dexterity of the system can be increased [72]. Also, in a MMSS setup, the robustness to single point failure is improved and the level of safety is increased due to the distribution of kinetic energy on two robotic systems [82].

The concept is similar to [55]. The passivity criterion assures stability in the present work whereas in [55] no stability proof has been accomplished. As depicted in Fig. 5.1.10 one master device M controls the left S_L and right slave S_R at the grasping point G located at a distance d_1 from the center of the slave connecting axis D. The transform between the slave devices is constant such that the grasping positions on the manipulated object are not varied.

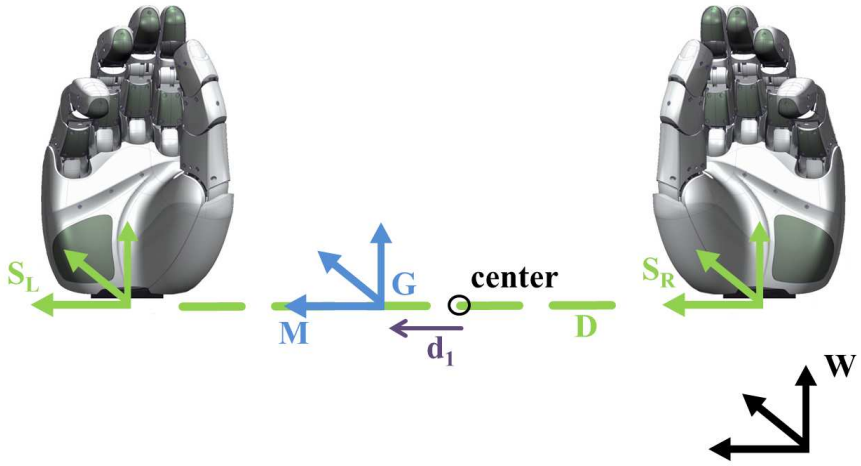

Figure 5.1.10: Kinematically Coupled Slaves in a SMMS System
A master M controls the grasping point G on the link D between the two slave robots S_L and S_R. G is located at a distance d_1 from the center of link D.

5.1.3.1 Implementation

The grasping point position G between the left S_L and the right slave S_R can be calculated as follows:

$$^{W}p_{G}^{t_0} = {}^{W}p_{S_L}^{t_0} - ({}^{W}p_{S_L}^{t_0} - {}^{W}p_{S_R}^{t_0})(0.5 + d_1) \tag{5.72}$$

with the distance from the center d_1 (see Fig. 5.1.10). The rotation matrix ${}^{W}R_{G}^{t_0}$ of the homogenous transform ${}^{W}H_{G}^{t_0}$

$$ {}^{W}H_{G}^{t_0} = \begin{bmatrix} {}^{W}R_{G}^{t_0} & {}^{W}p_{G}^{t_0} \\ 0 & 1 \end{bmatrix}, \tag{5.73} $$

can be calculated with two arbitrary vectors and one vector parallel to the slave connecting axis D through ${}^{W}p_{S_L}^{t_0}$ and ${}^{W}p_{S_R}^{t_0}$ (compare Fig. 5.1.10):

$$ b_1 = {}^{W}p_{S_L}^{t_0} - {}^{W}p_{S_R}^{t_0}, \tag{5.74} $$

$$ b_2 = \begin{bmatrix} 0 \\ -b_1(3) \\ b_2(2) \end{bmatrix}, \tag{5.75} $$

$$ b_3 = b_1 \times b_2 \text{ and} \tag{5.76} $$

$$ {}^{W}R_{G}^{t_0} = [b_1/\|b_1\|_2, b_2/\|b_2\|_2, b_3/\|b_3\|_2]\,. \tag{5.77} $$

The desired pose of the grasping point ${}^{W}H_{G}^{des}$ has to be calculated with respect to the incremental motion of the master M:

$$ {}^{W}p_{G}^{des} = {}^{W}p_{G}^{t_0} + {}^{W}p_{M} - {}^{W}p_{M}^{t_0}, \tag{5.78} $$

$$ {}^{W}R_{G}^{des} = {}^{W}R_{M}\,{}^{M}R_{W}^{t_0}\,{}^{W}R_{G}^{t_0}, \tag{5.79} $$

$$ {}^{W}H_{G}^{des} = \begin{bmatrix} {}^{W}R_{G}^{des} & {}^{W}p_{G}^{des} \\ 0 & 1 \end{bmatrix}. \tag{5.80} $$

The slave poses ${}^{W}H_{S_i}$ ($i \in \{L, R\}$) have to be transformed into the right coordinate frame ${}^{W}H_{\tilde{S}_i}$:

$$ {}^{W}H_{\tilde{S}_i} = \begin{bmatrix} {}^{W}R_{\tilde{S}_i} & {}^{W}p_{S_i} \\ 0 & 1 \end{bmatrix}, \text{ with} \tag{5.81} $$

$$ {}^{W}R_{\tilde{S}_i} = {}^{S_i}R_{G_i}^{t_0}\,{}^{W}R_{S_i}, \tag{5.82} $$

where ${}^{S_i}R_{G_i}^{t_0}$ is the rotation matrix from the respective slave to the grasping frame

$$ {}^{S_i}R_{G_i}^{t_0} = {}^{W}R_{G}^{t_0}\,{}^{S_i}R_{W}^{t_0}. \tag{5.83} $$

The desired positions of the slaves ${}^{W}H_{\hat{S}_i}^{des}$ can be calculated with the initial distance of the respective slave ${}^{W}H_{\tilde{S}_i}^{t_0}$ and desired grasping point ${}^{W}H_{G}^{des,t_0}$ in base frame:

$$ {}^{W}H_{\hat{S}_L}^{des} = {}^{W}H_{G}^{des}\,{}^{G}H_{W}^{des,t_0}\,{}^{W}H_{\tilde{S}_L}^{t_0}, \tag{5.84} $$

$$ {}^{W}H_{\hat{S}_R}^{des} = {}^{W}H_{G}^{des}\,{}^{G}H_{W}^{des,t_0}\,{}^{W}H_{\tilde{S}_R}^{t_0}. \tag{5.85} $$

With a separate input s (e.g. a pair of buttons), the desired slave positions can be moved

on axis D to perform the grasping:

$$ {}^{W}H^{des}_{S_L} = \begin{bmatrix} {}^{W}R^{des}_{\hat{S}_L} & {}^{W}p^{des}_{\hat{S}_L} + {}^{W}R^{des}_{\hat{S}_L} se \\ 0 & 1 \end{bmatrix}, \tag{5.86} $$

$$ {}^{W}H^{des}_{S_R} = \begin{bmatrix} {}^{W}R^{des}_{\hat{S}_R} & {}^{W}p^{des}_{\hat{S}_R} - {}^{W}R^{des}_{\hat{S}_R} se \\ 0 & 1 \end{bmatrix}, \quad \text{with} \tag{5.87} $$

$$ e = \begin{bmatrix} 1 \\ 0 \\ 0 \end{bmatrix}. \tag{5.88} $$

Two springs are sufficient in this SMMS system. Spring A couples master M with slave S_L and the second spring B couples the master M with slave S_R. The respective reference frames of the two coupling springs are listed in Table 5.4. As the wrench output

Table 5.4: Spring Inputs

Spring	${}^{W}H_1$	${}^{W}H_2$
A	${}^{W}H_{\tilde{S}_L}$	${}^{W}H^{des}_{S_L}$
B	${}^{W}H_{\tilde{S}_R}$	${}^{W}H^{des}_{S_R}$

is in the frame of ${}^{W}H_1$, the wrench has to be transformed into base frame in order to calculate the wrench commanded to the hardware

$$ {}^{S_L}W^A = {}^{S_L}\bar{T}_W \, {}^{W}\bar{T}_{\tilde{S}_L} \, {}^{\tilde{S}_L}W^A, \tag{5.89} $$

$$ {}^{M}W^A = {}^{M}\bar{T}_W \, {}^{W}\bar{T}_{\tilde{S}_L} \tilde{T} \, {}^{\tilde{S}_L}\tilde{W}^A, \tag{5.90} $$

$$ {}^{S_R}W^B = {}^{S_R}\bar{T}_W \, {}^{W}\bar{T}_{\tilde{S}_R} \, {}^{\tilde{S}_R}W^B, \tag{5.91} $$

$$ {}^{M}W^B = {}^{M}\bar{T}_W \, {}^{W}\bar{T}_{\tilde{S}_R} \tilde{T} \, {}^{\tilde{S}_R}\tilde{W}^B, \tag{5.92} $$

with

$$ \tilde{W}^i = -W^i. \tag{5.93} $$

and

$$ \tilde{T} = \left[\begin{array}{ccc:c} & \mathbf{I}_3 & & \mathbf{0}_3 \\ 0 & 0 & 0 & \\ 0 & 0 & d_1 & \mathbf{I}_3 \\ 0 & -d_1 & 0 & \end{array}\right]. \tag{5.94} $$

5.1.3.2 Passivity

As depicted in Fig. 5.1.11, the network representation of the multilateral system for cooperative slaves is based on the formerly presented passive subsystems. Therefore, no additional stability proof is needed.

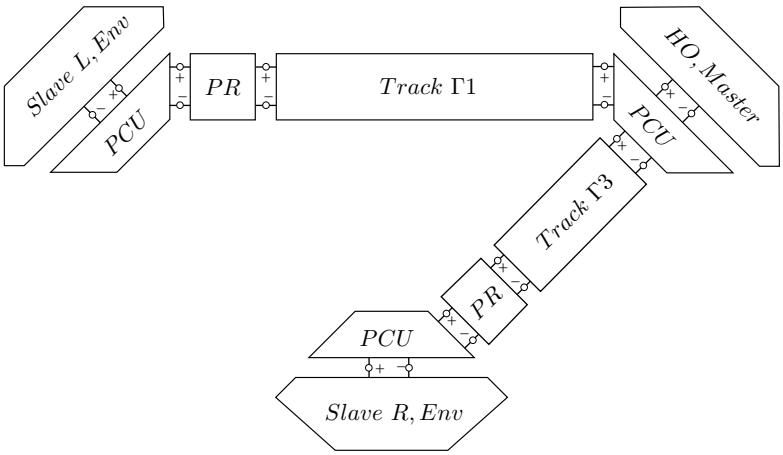

Figure 5.1.11: Single-Master-Multi-Slave System for Cooperative Slave Grasping
Two PR subsystems are introduced such that the coupling springs are located in the position of master M.

Analogous to Section 5.1.2.3, additional PI controllers or tracks respectively can be added to stiffen the control loop as shown in Fig. 5.1.12. Then, the master is coupled to each device by one spring in the master position and a second in the position of the respective slave.

5.1.3.3 Experiments

The following experiment was performed with the setup presented in Appendix A.4. One Omega.7 served as the human machine interface to control two LWR slave robots. The coupling was implemented with four spatial springs according to Fig. 5.1.12.

In Exp. 5.7, a rotation around the x-axis and a translational motion on the x-axis were commanded by the master device. Plot Exp. 5.7a depicts the position tracking of the right slave robot ${}^{W}p_{S_R}$ and the desired slave robot pose ${}^{W}p_{S_R}^{des}$. The commanded rotation around the x-axis is well tracked by the slave device. The translational position accuracy is lower which might result from workspace related disturbances. Plot Exp. 5.7b presents the 3D motion of the multilateral system. The kinematic coupling via four spatial springs provides the desired performance.

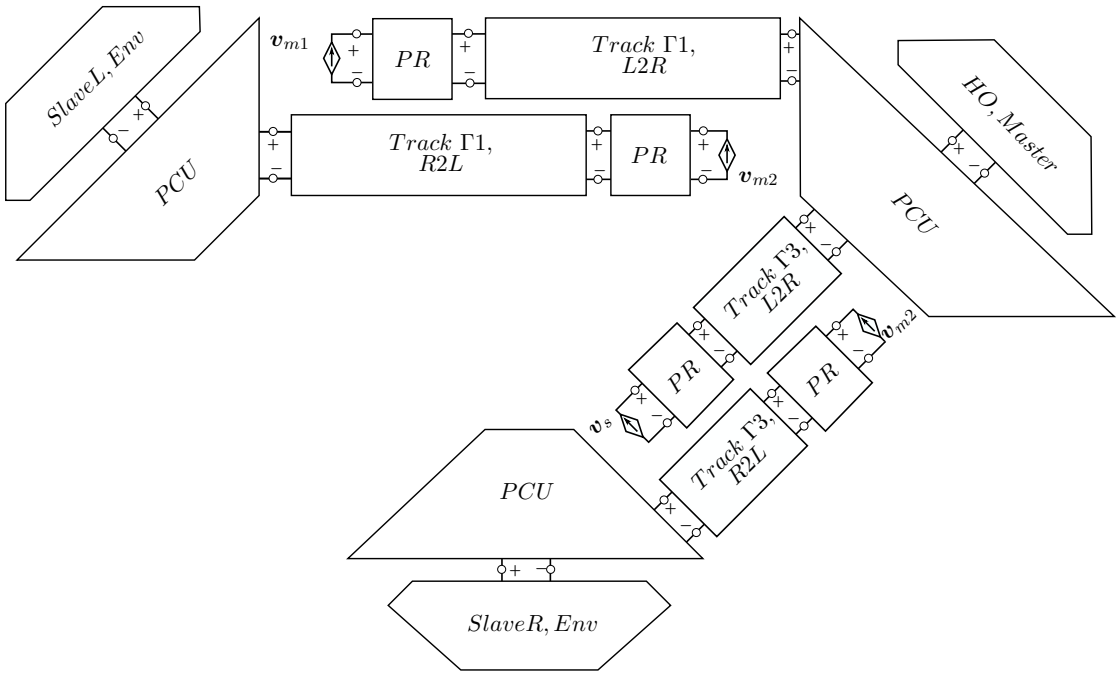

Figure 5.1.12: Single-Master-Multi-Slave System for Cooperative Slave Grasping with Additional Spatial Springs
To increase the coupling rigidity, one spatial spring can be added in the position of each slave. Therefore, *Track* Γ1 and *Track* Γ2 need to be split up and additional PR subsystems need to be integrated.

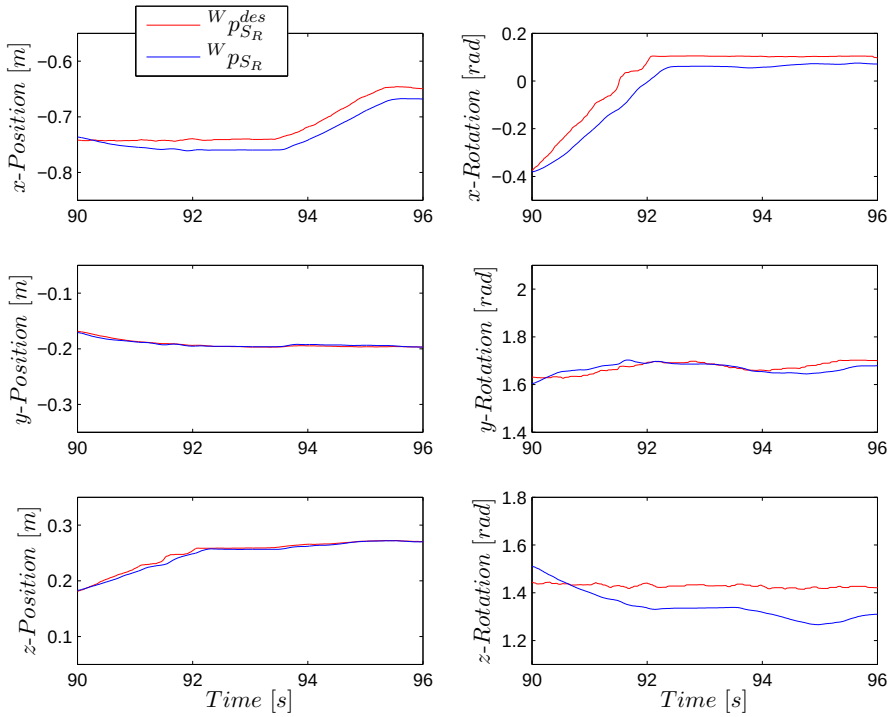

(a) Position Tracking

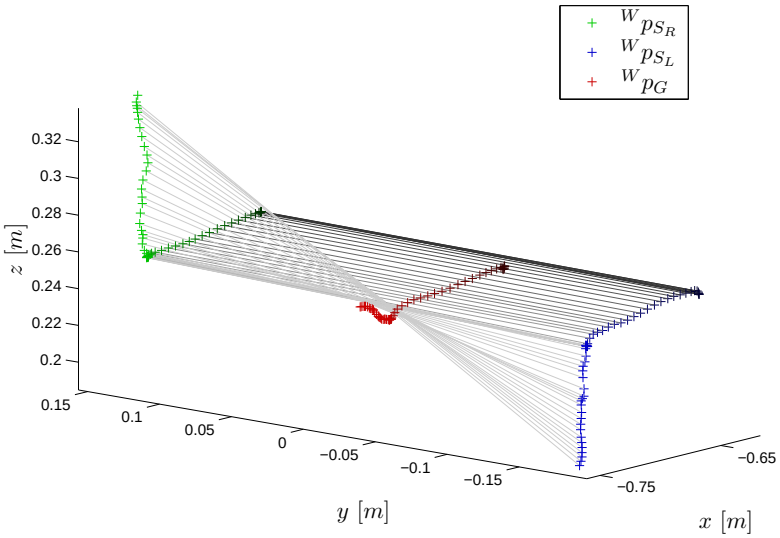

(b) 3D Motion

Experiment 5.7: Kinematically Coupled Slave Robots
A rotation around the x-axis and a translational motion on the x-axis were commanded by the master device in a setup with four coupling springs. The position tracking of slave S_R pose $^W p_{S_R}$ and the desired slave S_R pose $^W p^{des}_{S_R}$ is presented. The commanded rotation around the x-axis is well tracked by the slave devices. The translational position accuracy is lower which might result from workspace related disturbances.

5.1.4 Dual-Master-Dual-Slave

The advantages of the previously discussed concepts for increased rotational precision are also beneficial in the control of cooperatively grasping slave robots especially if underactuated master devices are applied. Therefore, in this section the two concepts are merged to a Multi-Master-Multi-Slave system. The setup is depicted in Fig. 5.1.13. The right master device controls the grasping point G whereas the additional left master device is coupled to a virtual grasping point VG at a distance d_2 from the grasping point G.

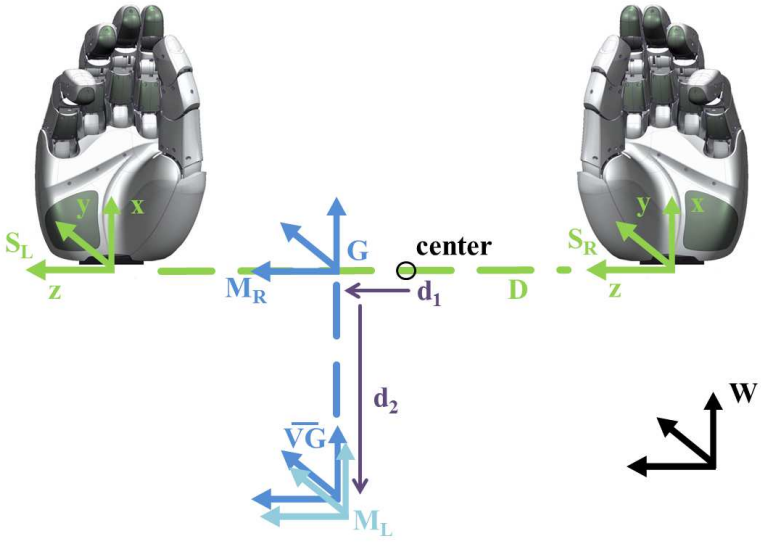

Figure 5.1.13: Coupled Manipulation via MMMS
To increase the rotational precision, two master devices that can be underactuated can be used to control one grasping point G on a link D between to slave devices.

5.1.4.1 Implementation

The calculation of the initial grasping point pose in the Multi-Master-Multi-Slave setup is analogous to Section 5.1.2 (see equations (5.72)-(5.77)). Still, to ease the calculation of the virtual grasping point pose ${}^{W}H_{VG}$, the calculation b_2 (see equation (5.75)) should be adapted. b_2 is the vector of the grasping point frame on which the virtual grasping point should be positioned. The design goal is to find an axis connecting the grasping point with the virtual grasping point that is as parallel to S_L's x-axis as possible (compare equation (5.72)). Still, one axis of the frame should be parallel to the axis D (vector p^a) connecting the slaves. Therefore, the vector b_2 has to lie in one plane with b_1 and the x-axis of the left hand frame and b_2 has to be orthogonal to b_1 (compare Fig. 5.1.14).

The first scalar $b_{2,1}$ of vector b_2 can be chosen randomly but negative to assure that the axis points in direction to the robots torso:

$$b_{2,1} = -1. \tag{5.95}$$

As the vector should be in one plane with axis-vector p^a and the x-vector of the hand

p^b, the vector v must be linearly dependent on p^a and p^b:

$$xp_1^a + yp_1^b = b_{2,1}, \tag{5.96}$$
$$xp_2^a + yp_2^b = b_{2,2}, \tag{5.97}$$
$$xp_3^a + yp_3^b = b_{2,3}. \tag{5.98}$$

Furthermore, the vector b_2 must be orthogonal to p^a:

$$b_{2,1}p_1^a + b_{2,2}p_2^a + b_{2,3}p_3^a = 0. \tag{5.99}$$

With euqation (5.96)-(5.99), we receive

$$b_{2,2} = \frac{p_2^b b_{2,1} {p_1^a}^2 - p_2^a p_1^b b_{2,1} p_1^a + p_2^b b_{2,1} {p_3^a}^2 - p_2^a p_3^b b_{2,1} p_3^a}{p_1^b {p_2^a}^2 - p_1^a p_2^b p_2^a + p_1^b {p_3^a}^2 - p_1^a p_3^b p_3^a} \tag{5.100}$$
$$b_{2,3} = \frac{p_3^b b_{2,1} {p_1^a}^2 - p_3^a p_1^b b_{2,1} p_1^a + p_3^b b_{2,1} {p_2^a}^2 - p_3^a p_2^b b_{2,1} p_2^a}{p_1^b {p_2^a}^2 - p_1^a p_2^b p_2^a + p_1^b {p_3^a}^2 - p_1^a p_3^b p_3^a} \tag{5.101}$$

such that the initial rotation matrix in the grasping point becomes

$${}^W R_G^{t_0} = \left[b_1/\|b_1\|_2, b_2/\|b_2\|_2, b_3/\|b_3\|_2 \right], \tag{5.102}$$

with

$$b_3 = b_1 \times b_2. \tag{5.103}$$

Then, the initial pose of the virtual grasping point can be computed:

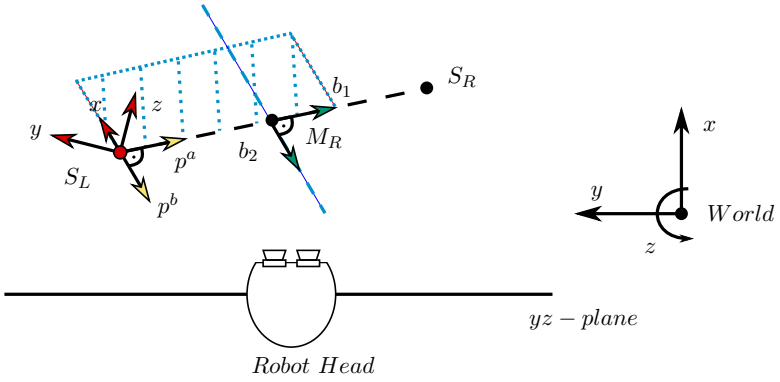

Figure 5.1.14: Design Goal of Second Vector
The axis connecting the grasping point G with the virtual grasping point VG should be as parallel to S_L's x-axis as possible. Still, one axis of the frame should be parallel to the axis D (vector p^a) connecting the slaves. Therefore, the vector b_2 has to lie in one plane with b_1 and the x-axis of the S_L frame and b_2 has to be orthogonal to b_1.

$${}^W H_{VG}^{t_0} = \begin{bmatrix} {}^W R_G^{t_0} & {}^W p_G^{t_0} + {}^W R_G^{t_0} d_2 e \\ 0 & 1 \end{bmatrix} \text{ with} \tag{5.104}$$

$$e = \begin{bmatrix} 0 \\ 1 \\ 0 \end{bmatrix}. \tag{5.105}$$

The pose of the slaves have to be mapped into the same frame

$$ {}^{W}H^{t_0}_{\tilde{S}_i} = \begin{bmatrix} {}^{W}R_{S_i}\, {}^{S_i}R^{t_0}_{W}\, {}^{W}R^{t_0}_{G} & {}^{W}p_{S_i} \\ 0 & 1 \end{bmatrix}, \tag{5.106} $$

with $i \in \{L, R\}$. The desired position of the grasping point can be calculated with the position increment of the master M_R

$$ {}^{W}p^{des}_{G} = {}^{W}p^{t_0}_{G} + {}^{W}p_{M_R} - {}^{W}p^{t_0}_{M_R}, \tag{5.107} $$

whereas the desired position of the virtual grasping point is defined by the position increment of master M_L

$$ {}^{W}p^{des}_{VG} = {}^{W}p_{M_L} - {}^{W}p^{t_0}_{M_L} + {}^{W}p^{t_0}_{G} + {}^{W}R^{t_0}_{G} d_2. \tag{5.108} $$

The rotation around x- and z-axis of the grasping frame can be commanded from the position change of the master devices. The angle α between the initial b_2 (link of the master devices) and the link between the current master positions as well as the vector k of rotation have to be calculated as follows:

$$ \alpha = cos^{-1}\left(\frac{({}^{W}p^{des}_{VG} - {}^{W}p^{des}_{G}) \circ b^{t_0}_{2}}{|\,{}^{W}p^{des}_{VG} - {}^{W}p^{des}_{G}||b^{t_0}_{2}|} \right) \quad \text{and} \tag{5.109} $$

$$ k = ({}^{W}p^{des}_{VG} - {}^{W}p^{des}_{G}) \times b^{t_0}_{2}. \tag{5.110} $$

With the skew-symmetric cross-product matrix K

$$ K = \begin{bmatrix} 0 & -k_3 & k_2 \\ k_3 & 0 & -k_1 \\ -k_2 & k_1 & 0 \end{bmatrix} \tag{5.111} $$

and the Rodriguez equation, the equivalent rotation matrix R^{XZ} can be found

$$ R^{XZ} = I + sin(\alpha)K + (1 - cos(\alpha))K^2. \tag{5.112} $$

Finally, the rotation R^{Y} around the axis b_2 with angle β can be formulated:

$$ R^{Y} = \begin{bmatrix} cos\beta & 0 & sin\beta \\ 0 & 1 & 0 \\ -sin\beta & 0 & cos\beta \end{bmatrix}. \tag{5.113} $$

An additional input device can serve as an interface to this angle β determining the rotation around the axis connecting G and VG. Thus, the desired rotation of grasping point and virtual grasping point frame can be calculated:

$$ {}^{W}R^{des}_{G} = R^{XZ}\, {}^{W}R_{G} R^{Y}, \tag{5.114} $$

$$ {}^{W}R^{des}_{VG} = R^{XZ}\, {}^{W}R_{VG} R^{Y}. \tag{5.115} $$

The desired slave frame can be found as

$$ {}^{W}H^{des}_{\hat{S}_i} = {}^{W}H^{des}_{G}\, {}^{G}H^{des,t_0}_{W}\, {}^{W}H^{t_0}_{\tilde{S}_i}, \tag{5.116} $$

with $i \in \{L, R\}$. With a separate input s (e.g. a button), the desired slave positions can be moved on the D axis to perform the grasping:

$$ {}^{W}H_{S_L}^{des} = \begin{bmatrix} {}^{W}R_{\hat{S}_L} & {}^{W}p_{\hat{S}_L} + {}^{W}R_{\hat{S}_L} sc \\ 0 & 1 \end{bmatrix}, \tag{5.117} $$

$$ {}^{W}H_{S_R}^{des} = \begin{bmatrix} {}^{W}R_{\hat{S}_R} & {}^{W}p_{\hat{S}_R} - {}^{W}R_{\hat{S}_R} sc \\ 0 & 1 \end{bmatrix} \quad \text{with} \tag{5.118} $$

$$ c = \begin{bmatrix} 1 \\ 0 \\ 0 \end{bmatrix}. \tag{5.119} $$

Note that there are two co-existing positions of the virtual grasping point. The first is defined directly by the motion of master M_L and the second is defined by the extension of the master M_R position ${}^{W}H_{\bar{VG}}$:

$$ {}^{W}H_{\bar{VG}} = \begin{bmatrix} {}^{W}R_{G}^{des} & {}^{W}R_{G}^{des} d_2 e + {}^{W}p_{G}^{des} \\ 0 & 1 \end{bmatrix}. \tag{5.120} $$

If another input m as a pair of buttons is available, the virtual distance between the grasping point and the virtual grasping point can be varied online:

$$ {}^{W}\check{H}_{VG}^{des} = \begin{bmatrix} {}^{W}H_{VG}^{des} & {}^{W}p_{VG}^{des} + {}^{W}R_{VG}^{des} me \\ 0 & 1 \end{bmatrix}, \tag{5.121} $$

$$ {}^{W}\check{H}_{\bar{VG}} = \begin{bmatrix} {}^{W}H_{\bar{VG}} & {}^{W}p_{\bar{VG}} + {}^{W}R_{\bar{VG}} me \\ 0 & 1 \end{bmatrix}, \quad \text{with} \tag{5.122} $$

$$ e = \begin{bmatrix} 0 \\ 1 \\ 0 \end{bmatrix}. \tag{5.123} $$

Three spatial springs are required in the presented Dual-Master-Dual-Slave system. Spring A couples master M_R to slave S_L, spring B couples master M_R to slave S_R and spring C couples master M_L to slave M_R. The reference frames of the three coupling springs are listed in Table 5.5. Note that transformation matrices $\bar{T}$ do only contain

Table 5.5: Spring Inputs

Spring	${}^{W}H_1$	${}^{W}H_2$
A	${}^{W}H_{\tilde{S}_L}$	${}^{W}H_{S_L}^{des}$
B	${}^{W}H_{\tilde{S}_R}$	${}^{W}H_{S_R}^{des}$
C	${}^{W}\check{H}_{\bar{VG}}$	${}^{W}\check{H}_{VG}^{des}$

rotation matrices. The wrench output of the spring is in the frame of ${}^{W}H_1$. Therefore, the wrench is first transformed into base frame to find the wrench that has to be

commanded to the devices.

$$ {}^{S_L}W^A = {}^{S_L}\bar{T}_W \, {}^{W}\bar{T}_{\tilde{S}_L} \, {}^{\tilde{S}_L}W^A, \tag{5.124} $$

$$ {}^{M_R}W^A = {}^{M_R}\bar{T}_W \, {}^{W}\bar{T}_{\tilde{S}_L} \tilde{T} \, {}^{\tilde{S}_L}\tilde{W}^A, \tag{5.125} $$

$$ {}^{S_R}W^B = {}^{S_R}\bar{T}_W \, {}^{W}\bar{T}_{\tilde{S}_R} \, {}^{\tilde{S}_R}W^B, \tag{5.126} $$

$$ {}^{M_R}W^B = {}^{M_R}\bar{T}_W \, {}^{W}\bar{T}_{\tilde{S}_R} \tilde{T} \, {}^{\tilde{S}_R}\tilde{W}^B, \tag{5.127} $$

$$ {}^{M_R}W^C = {}^{M_R}\bar{T}_W \, {}^{W}\bar{T}_{\bar{VG}} \tilde{T} \, {}^{\bar{VG}}W^B, \tag{5.128} $$

$$ {}^{M_L}W^C = {}^{M_L}\bar{T}_W \, {}^{W}\bar{T}_{\bar{VG}} \, {}^{\bar{VG}}\tilde{W}^B, \tag{5.129} $$

with

$$ \tilde{W}^i = -W^i. \tag{5.130} $$

and

$$ \tilde{T} = \left[\begin{array}{ccc:c} & \mathbf{I}_3 & & \mathbf{0}_3 \\ \hdashline 0 & 0 & 0 & \\ 0 & 0 & d_j & \mathbf{I}_3 \\ 0 & -d_j & 0 & \end{array}\right], \tag{5.131} $$

with ($j \in \{1, 2\}$)

5.1.4.2 Passivity

The network representation of the proposed Dual-Master-Dual-Slave system is depicted in Fig. 5.1.15. As can be seen, the network consists of master and slave subsystems, power control units, projection subsystems and tracks. The passivity of the projection subsystem has been discussed in Section 5.1.1.3 and the tracks can be implemented according to the different architectures presented e.g. in Section 4. Due to the modularity of the MPMT approach, the passivity of the Dual-Master-Dual-Slave system can be concluded from the passivity of the concepts of Section 5.1.2 and 5.1.3.

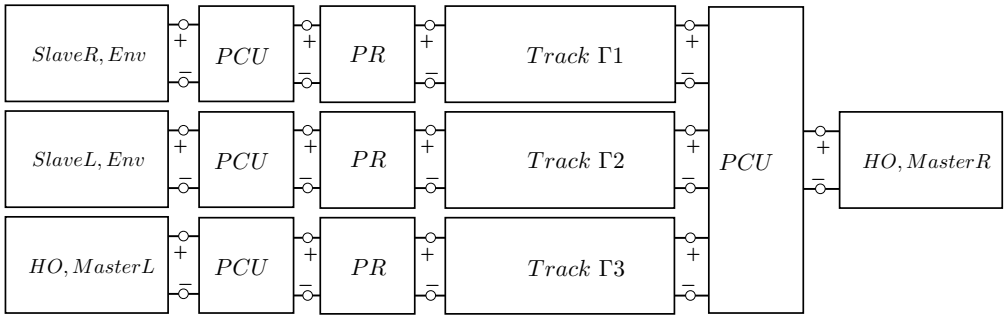

Figure 5.1.15: Network Representation of the Dual-Master-Dual-Slave
The devices S_L, S_R and M_L are not coupled with each other but with the master M_R. The spatial springs are located in the position of master M_R.

The stiffness of the system can be improved analogous to the networks of Fig. 5.1.9 and Fig. 5.1.12. As explained in Fig. 5.1.7 and Fig. 5.1.8, the linkage of two devices

can be improved if one spring is implemented in the tool center point of both devices (coupled via a projection subsystem) each. The corresponding network representation is depicted in Fig. 5.1.16.

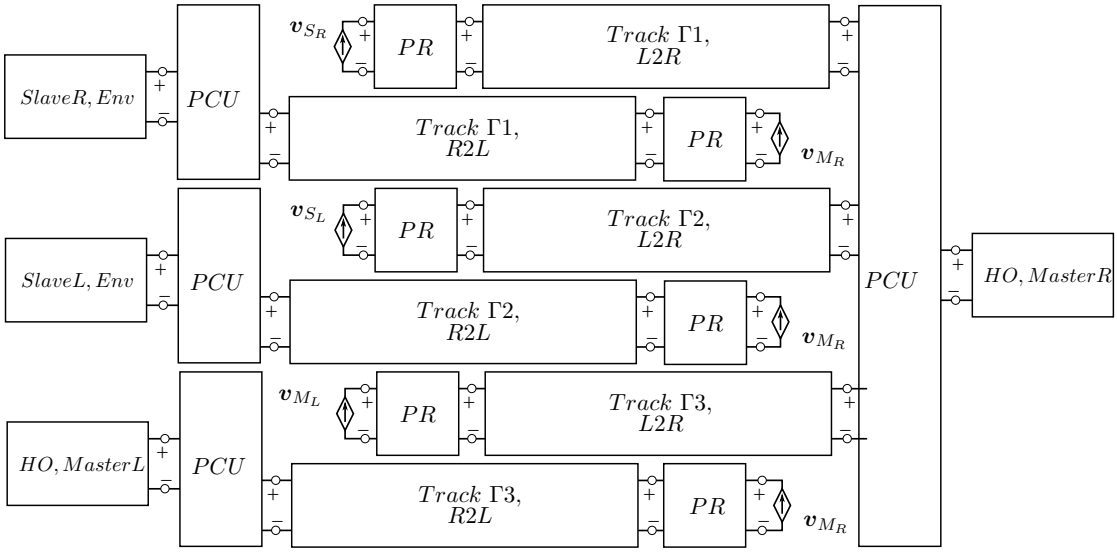

Figure 5.1.16: Network Representation of the Dual-Master-Dual-Slave with Additional Spatial Springs
The coupling rigidity can be improved if two springs are implemented in each coupling track such that one spring is located in each of the two coupled agents.

5.1.4.3 Experiments

The following experiments were performed with the setup presented in Appendix A.4. Two Omega.7 have been applied as master devices and two LWRs served as the kinematically coupled slave robots. The multilateral coupling was implemented according to Fig. 5.1.16.

In the first experiment on the presented Dual-Master-Dual-Slave system Exp. 5.8, master M_L moves on a circle around M_R on the y-axis, such that the positions of M_R, S_R and S_L are steady. The slave robots rotate around their connecting axis D.

In the second experiment Exp. 5.9, master M_R moves on a circle around M_L on the y-axis, such that the position of M_L is steady. As can be seen in plot Exp. 5.9, the position tracking of ${}^W p_{S_R}$ and ${}^W p_{S_L}$ is satisfactory. Additionally, the slave robots rotate around their connecting axis D according to the link of the master devices.

In the third experiment Exp. 5.10, master M_L moves on a circle around M_R around the z-axis, such that the position of M_R is steady. The slaves perform the desired motion well, although workspace disturbances act on the left slave.

In the fourth experiment Exp. 5.11, master M_R moves on a circle around M_L on the z-axis, such that the position of M_L is steady. The multilateral coupling leads to a satisfactory coordination of the kinematically coupled slave robots (compare plot Exp. 5.11).

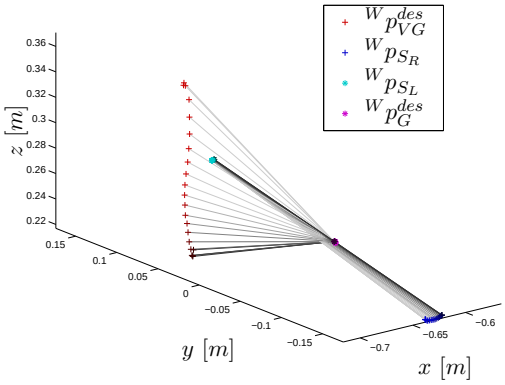

Experiment 5.8: y-Rotation of M_L around M_R
Master M_L moves on a circle around M_R on the y-axis, such that the positions of M_R, S_R and S_L are steady. The slave robots rotate around their connecting axis D.

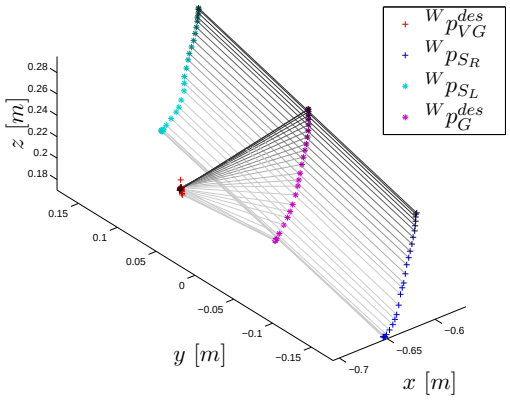

Experiment 5.9: y-Rotation of M_R around M_L
Master M_R moves on a circle around M_L on the y-axis, such that the position of M_L is steady. The slave robots rotate around their connecting axis D according to the link of the master devices. The position tracking of $^W p_{S_R}$ and $^W p_{S_L}$ is satisfactory.

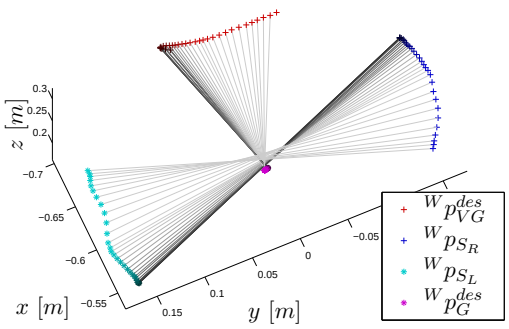

Experiment 5.10: z-Rotation of M_L around M_R
Master M_L moves on a circle around M_R around the z-axis, such that the position of M_R is steady. The slaves perform the desired motion well, though workspace disturbances act on the left slave.

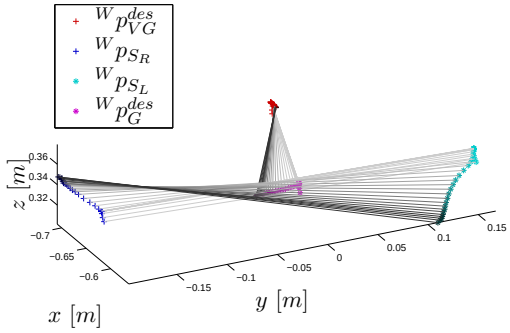

Experiment 5.11: z-Rotation of M_R around M_L
Master M_R moves on a circle around M_L on the z-axis, such that the position of M_L is steady. The coordination of the kinematically coupled slave robots in the multilateral coupling is satisfactory.

5.1.5 Discussion on Virtual Grasping Points

Different applications for the virtual grasping point concept have been presented in this section. Single-Master-Multi-Slave systems as well as Multi-Master-Single-Slave setups and Multi-Master-Multi-Slave systems can benefit from this augmentation method. For example, the steadiness and precision in rotational tasks can be improved via an additional virtual interaction point. Furthermore, it has been shown that the control of two kinematically coupled slave robots requires a virtual interaction point and that the rotational feedback of underactuated input devices can be approximated by counteracting forces in two master devices.

The approach of Section 5.1.1 is extended with a task allocation in Section 5.2.2. Further experiments and a user study on the virtual grasping point approach are presented in Section 6.1.

5.2 Role Distribution of Agents

The role distribution between agents is another concept providing haptic augmentation. In the following, two types of role distributions, the authority and task allocation, are introduced. The task allocation concept [127] is based on the virtual grasping point approach of section 5.1.1. The role distribution is designed in the task-space in that the two master devices have different influence on the motion of the virtual grasping point. In contrast, the authority allocation concept [122] is only reasonable, if two human operators are involved. The authorities on the control of a slave robot are for example shared between a mentor and trainee operator. Also, any shared autonomy concept can be considered as a role distribution between a human operator and an artificial intelligence agent.

5.2.1 Authority Allocation for Training Applications

In the authority allocation (AA) concept, two or more master devices share the control of one or more slave robots. The training application as a typical scenario requiring this method has been presented in literature based on different control concepts (see Section 2.4.1). The first fully connected training scenario with time delay has been presented in [122] based on the TDPA.

In a training scenario, the trainee can observe the mentor's action haptically without influencing the slave robot's motion in the first step. Corresponding to the increase of experience, the authority should be shared between the human operators providing the trainee with progressively higher control. This control adaption is solved by the variation of an authority factor. This concept is in detail described in Fig. 5.2.1. The arrows refer to the ability to control the device or agent towards which the respective arrow points. A time delay is considered such that each agent can be located at a distance to each other.

5.2.1.1 System Description

Fig. 5.2.2 shows the signal flow diagram of a trilateral teleoperation system. In the depicted PF_{comp} architecture velocity (v) and force (F) signals are exchanged between

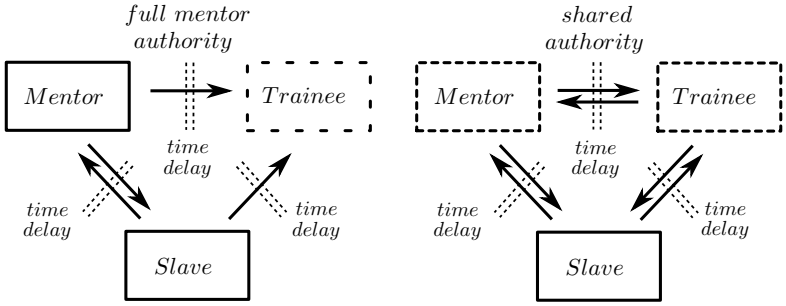

Figure 5.2.1: Trilateral Teleoperation with Authority Allocation and Time Delay
In a training scenario, the trainee can observe the mentor's action haptically without influencing the slave robot's motion in the first step. Corresponding to the increase of experience, the authority should be shared between the human operators providing the trainee with progressively higher control. A time delay may act in the communication channel.

the haptic devices (master M_1, master M_2) and the robot (*Slave*) through the communication channels represented by time delay elements $e^{-T_i s}$. The PI-controllers are corresponding to the PF architecture located on the slave's side of the communication channels (respectively for the operators' track on the trainee's side). The factors γ_{M1} and γ_{M2}, corresponding to mentor and trainee respectively, determine the allocation of authority between the operators through scaling of the delayed PI-controller forces. Those forces correspond to the influence of an agent on the respective other device. The relationship between the two authority variables γ_{M1} and γ_{M2} is given by:

$$\gamma_{M1} = 1 - \gamma_{M2} \quad \text{with} \quad \gamma_i \in \{0...1\} \tag{5.132}$$

($i \in \{M1, M2\}$) indicating that a reduction of the mentor's authority γ_{M1} leads to a correlated increase of the trainee's authority γ_{M2}. Consequently, reducing γ_{M1} from 1 to 0 progressively assigns higher influence on the system to the trainee. In contrast to [65] (complementary linear combination approach), the feedback signals sent from the slave to the master devices remain unaffected by γ_{M1} and γ_{M2} since the slave's position (represented by the feedback force) as the main concern should always be presented correctly to the master devices. The most common approach is the complementary linear combination approach which has been compared to an approach called masters correspondence with environment transfer in [68]. In contrast to these methods, here, the scaling acts only on the force feedback but not on the position information exchanged among the devices [122].

5.2.1.2 Passivity Proof

The authority allocation scaling can be represented by a 2-port module with dependent power source as depicted in Fig. 5.2.3. The authority allocation AA_1 (compare Fig. 5.2.2) is considered in the following.

The gain γ_{M2} scales down the force feedback in $R2L$ direction to the mentor.

$$F_2(t) = \gamma_{M1} F_3(t), \tag{5.133}$$

whereas the velocities equal ($v_2 = v_3$). The force and velocity signals are declared in Fig. 5.2.4. $F_{\gamma_{M2}}$ is the dependent power source of the network representation (compare

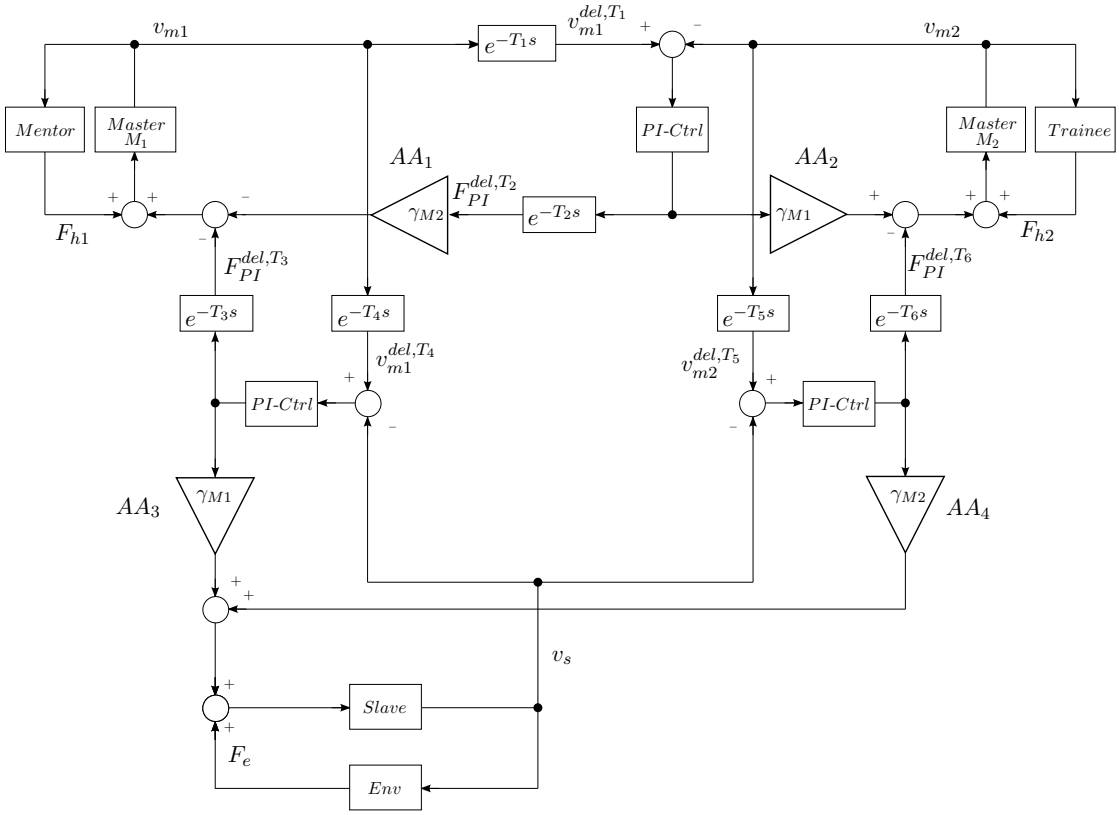

Figure 5.2.2: Signal Flow Diagram of Trilateral PF_{comp} Architecture with Authority Allocation and Time Delay
The authority allocation AA is realized through the scalings γ_{M1} and γ_{M2}. All three devices master $M1$, $M2$ and slave are coupled via PI controllers.

Fig. 5.2.3):

$$F_{\gamma_{M2}}(t) = -(1 - \gamma_{M2})F_3(t). \tag{5.134}$$

A whole track considering time delay controlled by the TDPN approach (Section 2.3.2.3) can be seen in Fig. 5.2.5. The depicted track connects the two master devices. Note that in tracks connecting a master with a slave device, there is only one AA scaling module on the slave side.

Energy that is flowing in R2L direction is reduced by the gain γ_{M2} of authority allocation AA_1:

$$P_2(t) = \gamma_{M2}P_3(t) = v_3(t)\gamma_{M2}F_3(t). \tag{5.135}$$

In contrast, energy is generated by gain γ_{M2} in L2R direction. This energy is dissipated by the force source F_{10}. Thus, the scaling behaves passive in the relevant flow direction of the track.

The energy amount in the coupling PI controller results from the velocities v_{10} and v_{11} and the forces F_{10} and F_{11} that can be calculated from the PI parameters. In the passivity condition, the energy input from the flow sources v_3 and v_{12} and the respective forces F_8 and F_{11} can be considered as the supply rate that represents the input of the human operator and the environment. That energy amount in the spring can be distributed in L2R and R2L direction according to the passivity condition. As analyzed before, in these directions, the authority allocation subsystems behave purely dissipating such that the track remains passive.

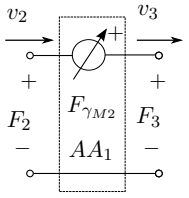

Figure 5.2.3: Network Representation of the Authority Allocation
The authority allocation scaling can be represented by a 2-port module with dependent power source.

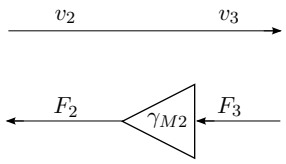

Figure 5.2.4: Signal Flow Diagram of the Authority Scaling

5.2.1.3 Experiments

In this section, experiments will be presented that serve the analysis of the system's performance in dependence of time delay and authority allocation. The technical setup presented in Appendix A.1 has been applied. The mentor controls master M_1 and the trainee master M_2 respectively. The network representation of the system equals the simple trilateral setup presented in Fig. 3.3.3. The tracks were implemented with the PF_{comp} architecture and TDPA Approach 2 (Section 4.1.1). For the experiments, all communication channels have been restrained by one unique time delay. The system has been tuned to go unstable with a delay T_i of 10ms (unique PI parameters: damping $B_{PI} = 0.06\frac{Nms}{rad}$, stiffness $K_{PI} = 3.5\frac{Nm}{rad}$).

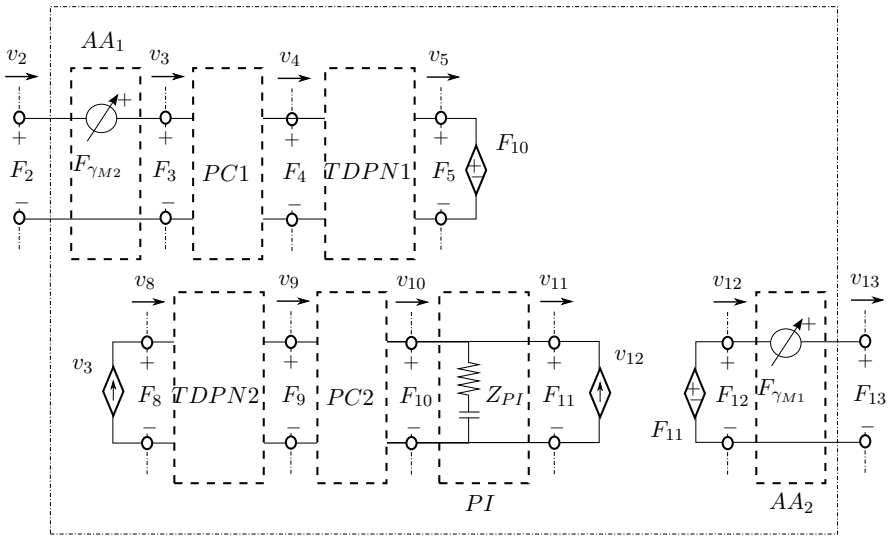

Figure 5.2.5: Network Representation of PF_{comp} architecture with Authority Allocation and Time Delay
In the track, the authority allocation subsystems are located next to the agents (port 2 and port 13) that are coupled by the track such that the scaling does not influence the passivity control of the communication channel.

In the first experiment Exp. 5.12 with a delay of 50ms (roundtrip delay 100ms), the mentor has the full authority ($\gamma_{M1} = 1$). The mentor guides the slave against a wall ($t = [3.5s, 5s]$) marginally penetrating it. The position plot shows that the slave follows the mentor very well. The trainee though resists the motion when the mentor leaves the wall contact. During this resistance, the trainee's PC dissipates a high amount of energy (E_{PC}). The effect of the authority allocation can be recognized looking at the plot of the forces F_{2Sl} sent to the slave. The force sent from trainee to slave is completely canceled by the authority allocation ($\gamma_{M2} = 0$) whereas the mentor's force is entirely received by the slave.

For the passivity proof the sum of energies $E^{R2L}_{\Gamma1,\Gamma2}$ flowing to the mentor in $R2L$ direction of $Track$ $\Gamma1$ and $\Gamma2$ ($\Gamma1$ connects mentor and trainee, $\Gamma2$ connects master and slave) is considered representatively. Since E_{out} is always smaller than E_{in}, the passivity is guaranteed.

With $\gamma_{M1} = 0.75$, the trainee is assigned slightly more authority in the second experiment. The position following can be analyzed in phases of consistent operator movement in plot Exp. 5.13 and is satisfactory despite the delay of 50ms. The position diagram in plot Exp. 5.13 shows that the slave does not stick as well to the mentor as in the first experiment since it is also influenced by the trainee's motion.

In plot Exp. 5.14, the shared authority situation ($\gamma_{M1} = 0.5$) is displayed. The slave is now positioned in the middle of the two operators. Note that no wall contact has been performed. The force F_{2Sl} sent from mentor and trainee are very similar (but inverted) since the operators pull the slave in different directions.

In the last experiment Exp. 5.15 the delay was raised to 200ms per communication channel. The position following of the devices is still satisfactory. At $t = [8s, 9s]$), the operators have the same intention and thus the same position. The slave's position is

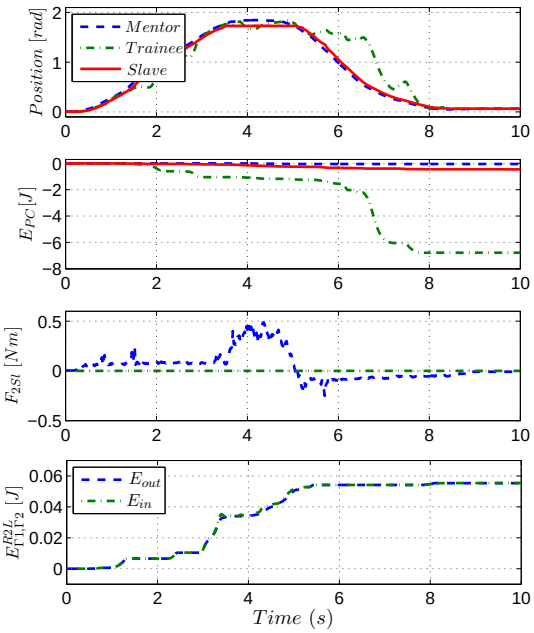

Experiment 5.12: Training Scenario with $T_i = 50ms$ and $\gamma_{M1} = 1$
The mentor guides the slave against a wall ($t = [3.5s, 5s]$) marginally penetrating it. The trainee though resists the motion when the mentor leaves the wall contact. During this resistance, the trainee's PC dissipates a high amount of energy (E_{PC}). The force sent from trainee to slave is completely canceled by the authority allocation ($\gamma_{M2} = 0$) whereas the mentor's force is entirely received by the slave. Since E_{out} is always smaller than E_{in}, the passivity is guaranteed.

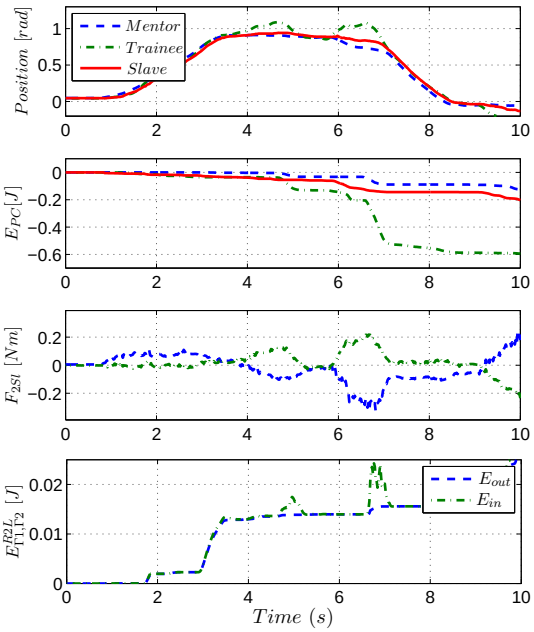

Experiment 5.13: Training Scenario with $T_i = 50ms$ and $\gamma_{M1} = 0.75$
Since the slave is influenced by the trainee's and the mentor's motion, the slave is located between mentor and trainee in this setup during free motion. The position tracking is satisfactory despite the delay of 50ms.

delayed by approximately 0.2s as expected.

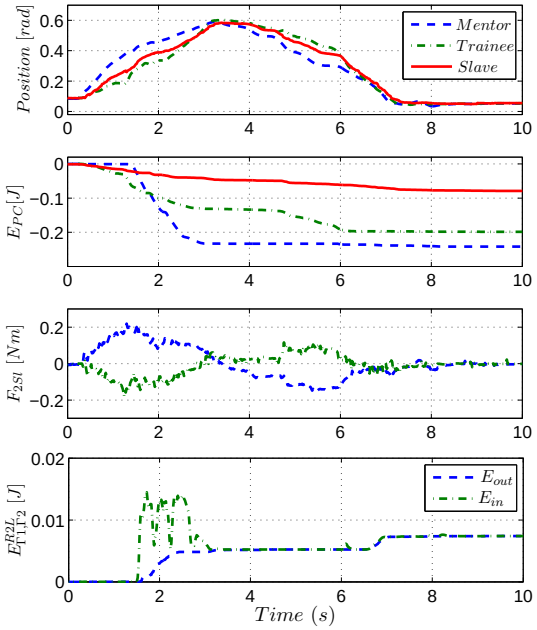

Experiment 5.14: Training Scenario with $T_i = 50ms$ and $\gamma_{M1} = 0.5$
The slave is positioned in the middle of the two operators during free motion. The force F_{2Sl} sent from mentor and trainee are similar, but inverted, since the operators pull the slave in different directions.

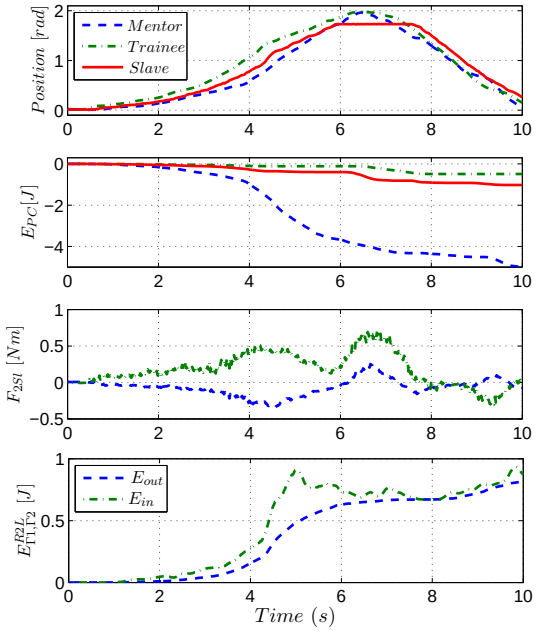

Experiment 5.15: Training Scenario with $T_i = 200ms$ and $\gamma_{M1} = 0.25$
The slave's position is delayed by approximately 0.2s as expected. The position tracking of the devices is still satisfactory.

Comparing the preceding experiments, it is obvious that the amount of dissipated energy (E_{PC}) increases with the delay since the channel's activity rises. Furthermore, it can be seen that the PC of the guiding operator (mentor for $\gamma_{M1} > \gamma_{M2}$ and vice versa) dissipates less energy than the one of the trained operator since energy is introduced mainly by the guiding operator and therefore flowing away from this operator.

5.2.1.4 Discussion on Authority Allocation for Training Applications

Through the force scaling concept, an authority can be allocated to the operators. The network module of the authority allocation contains a dependent power source. The presented experiments underline the adequacy of the setup for a training with focus on the motion of a specific procedure. If the interaction force of the slave and the environment is of higher relevance in the training, a different multilateral setup and the PF_{meas} architecture can be beneficial (as discussed in Section 3.4).

5.2.2 Task Allocation in Multi-DoF systems

In this section, the task allocation (TA) as another virtual feature that provides haptic augmentation is introduced [127, 129]. The virtual grasping point that has been presented in Section 5.1 eases the manipulation of a long object in a unimanually or bimanually controlled system. Especially in the bimanual case, a task allocation to the two masters can further improve the ergonomics of the control. The position of the VG (e.g. pipe end) can be eased if the master device whose TCP is located in the VG has full authority on the translational motions of the VG. The implementation of the task allocation is realized via force feedback scalings analogous to the authority allocation of Section 5.2.1.

5.2.2.1 System Description

Consider the manipulation of a large object (e.g. a long pipe) by a human, without a telerobotic system: The right hand of a human grasping one end of the large object will be affected by the motion of the left hand grasping the pipe at another point. In case of difficult trajectories, or if high forces are necessary for the manipulation, or if not one but two humans do the task, it may happen that the motion of one hand influences the motion of the other hand in an undesired manner since the human may not compensate for all disturbances. This manipulation could be eased e.g. through guide rails or similar fixtures. These structures which support the human in performing the manipulation can be regarded as a non-virtual task allocation.

In the case of teleoperators, the concept of task allocation allows a much broader spectrum of supporting aids to the telemanipulation. These support aids are virtual features which can augment visual and haptic perceptions and thus the telepresent feeling. Note that the task allocation is also reasonable if the master devices are controlled by different operators.

The focused application in this section is the insertion of a pipe into a plug analogous to Section 5.1. The task allocation aims for the following distribution: The task of the right hand (master M2) is to relocate the pipe end and to keep the position until the pipe is correctly oriented (compare Fig. 5.1.3). The task of the left hand (master M1) is the reorientation of the pipe.

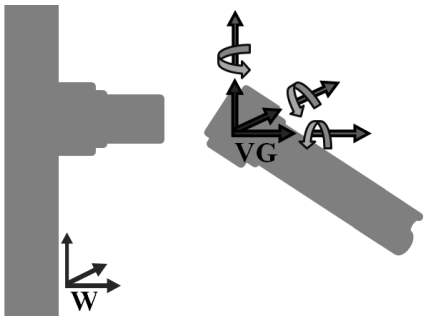

Figure 5.2.6: Task Allocation for Master M2 in Virtual Grasping Point The right hand at master M2 has full authority on the translations in the VG (dark arrows). The authority on the rotations is shared with the distant right hand controlling master M1 (gray arrows).

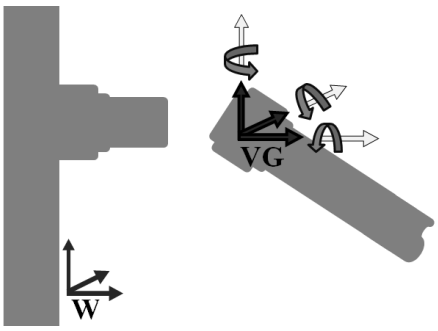

Figure 5.2.7: Task Allocation for Master M1 in Virtual Grasping Point The left hand (master M1) has no control on the VG translations (light-gray arrows). The auhtority on the rotations is shared with master M2 (gray arrows).

A task allocation is designed here which decouples the translational motion of the pipe end from the left hand (master M1) input. In contrast to the real pipe manipulation without teleoperator, the right hand should feel no forces (but torques) caused by the left hand motion. Thus, the control of the pipe end is decoupled from unintentional commands of the left hand and other disturbances. The arrow colors in Fig. 5.2.6 and Fig. 5.2.7 indicate that M2 and M1 share the control of the orientation whereas M2 has more authority on the pipe end's translations than M1.

5.2.2.2 Implementation

Similar to the method proposed in the preceding section, the task allocation can be implemented by parameters γ that scale the stiffness and the damping of the PI-controller or its force and torque feedback respectively (see Fig. 5.2.8):

$$ {}_i\gamma_j \in [0,1], \tag{5.136} $$

$$ {}_i\gamma_{M2} = 1 - {}_i\gamma_{M1}, \tag{5.137} $$

with $i \in \{T, R\}$ and $j \in \{M1, M2\}$ Note that Fig. 5.2.8 presents a generalized track with PP architecture. Since the master devices are controlled by one operator, the delay in the communication channels is zero. The scaling ${}_T\gamma$ acts on the forces (translation T) sent from master M1 or master M2. ${}_R\gamma$ acts on the torques (rotations R) respectively. Since the task allocation is designed in the VG, it is crucial that the PI controllers operate in the VG. Therefore, as depicted in Fig. 5.2.9, two PR blocks need to be added to *Track* Γ2 of Fig. 5.1.5. *Track* Γ2 can be split up into two directions of flow. The PI of the L2R-part is located in the virtual grasping point, whereas the PI in the R2L-part can provide a direct coupling between slave and master M1 in the grasping point G. This renders the setup stiffer and is possible as the slave feedback to the master M1 is not affected by the TA and thus doesn't have to be calculated in the VG.

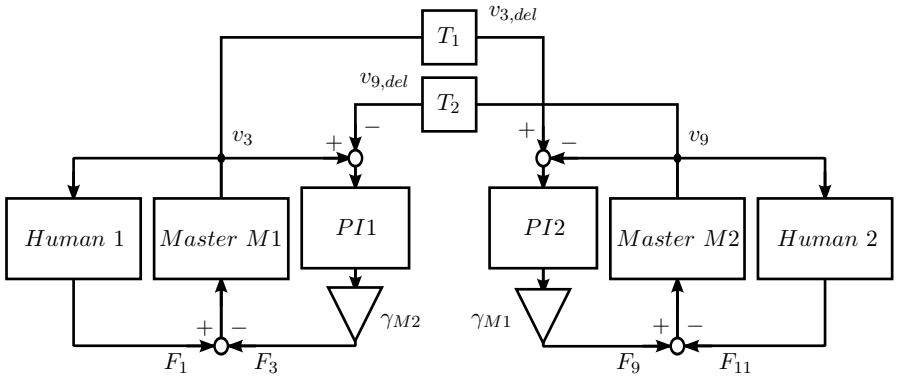

Figure 5.2.8: Signal Flow Diagram of a Teleoperator Training System with Position-Position Architecture and Task Allocation
The task allocation is realized through scalings γ_{M1} and γ_{M2} that reduce the force feedback to master M2 and master M1 respectively.

In contrast to the spring setup in Section 5.1.1.1 and to the task allocation design of [127], this task allocation concept requires six coupling springs A-F (two springs in *Track* Γ2, compare Table 5.6). The spring F is located in the virtual grasping point VG and spring A remains in the grasping point G. The other springs remain as in Table

Table 5.6: TA Springs

Spring	${}^{W}H_1$	${}^{W}H_2$	Track
A	${}^{W}H_G$	${}^{W}H_G^{des}$	Γ2 *R2L*
F	${}^{W}H_{VG}$	${}^{W}H_{\tilde{VG}}$	Γ2 *L2R*

5.1 and Table 5.2. Via the task allocation, the spring outputs will be designed in the following such that the right master M2 has the authority on the translations in the virtual grasping point. Note that the springs D and E are neglected in the following since they are not affected by the TA.

The feedback forces of the springs change:

$$ {}^{S}W^{A} = [0\ 0\ 0\ 0\ 0\ 0]^{T} \tag{5.138} $$

$$ {}^{M_L}W^{A} = {}^{M_L}\bar{T}_{W}\,{}^{W}\bar{T}_{G}\,{}^{G}\tilde{W}^{A}, \tag{5.139} $$

$$ {}^{S}W^{B} = {}^{S}\bar{T}_{W}\,{}^{W}\bar{T}_{\tilde{VG}}\tilde{T}\kappa_{S}^{RC}\kappa_{M2}^{TA}\,{}^{VG}W^{B}, \tag{5.140} $$

$$ {}^{M_R}W^{B} = {}^{M_R}\bar{T}_{W}\,{}^{W}\bar{T}_{VG}\kappa_{M2}^{RC}\,{}^{VG}\tilde{W}^{B}, \tag{5.141} $$

$$ {}^{M_R}W^{C} = {}^{M_R}\bar{T}_{W}\,{}^{W}\bar{T}_{\tilde{VG}}\kappa_{M1}^{RC}\kappa_{M1}^{TA}\,{}^{\tilde{VG}}W^{C}, \tag{5.142} $$

$$ {}^{M_L}W^{C} = {}^{M_L}\bar{T}_{W}\,{}^{W}\bar{T}_{\tilde{VG}}\tilde{T}\kappa_{M2}^{RC}\kappa_{M2}^{TA}\,{}^{\tilde{VG}}\tilde{W}^{C} \tag{5.143} $$

$$ {}^{S}W^{F} = {}^{S}\bar{T}_{W}\,{}^{W}\bar{T}_{VG}\tilde{T}\kappa_{M1}^{TA}\,{}^{VG}W^{D}, \tag{5.144} $$

$$ {}^{M_L}W^{F} = [0\ 0\ 0\ 0\ 0\ 0]^{T}. \tag{5.145} $$

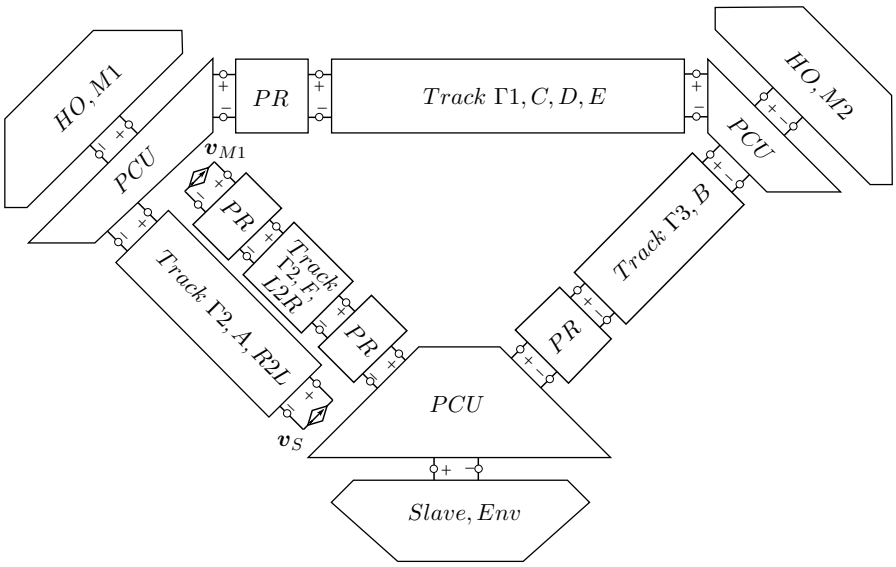

Figure 5.2.9: Multilateral System with Virtual Grasping Point Projection and Task Allocation Since the task allocation is designed in the VG, two PR blocks are added to *Track* Γ2. *Track* Γ2 can be split up into two directions of flow. The spatial spring of the L2R-part is located in the VG, whereas the spatial spring in the R2L-part provides a direct coupling between slave and master M1 in the grasping point G.

The matrices κ_j^{RC} ($j \in [M_R, M_L, S]$) will be used to improve the right robot's workspace limitations in the next step but can be first assumed to be equal to the unity matrix $\mathbf{I}_6 \in R^{6x6}$. The multi-DoF task allocation can be implemented through the matrices κ_{M1}^{TA} and κ_{M2}^{TA}

$$\kappa_{M1}^{TA} = \begin{bmatrix} {}_T\gamma_{M1}\mathbf{I}_3 & \mathbf{0}_3 \\ \mathbf{0}_3 & {}_R\gamma_{M1}\mathbf{I}_3 \end{bmatrix} \tag{5.146}$$

and

$$\kappa_{M2}^{TA} = \begin{bmatrix} {}_T\gamma_{M2}\mathbf{I}_3 & \mathbf{0}_3 \\ \mathbf{0}_3 & {}_R\gamma_{M2}\mathbf{I}_3 \end{bmatrix}, \tag{5.147}$$

with the zero matrix $\mathbf{0}_3 \in R^{3x3}$ and the unitiy matrix $\mathbf{I}_3 \in R^{3x3}$.

In the chosen scenario, the task allocation factors should be chosen as follows:

$${}_T\gamma_{M1} \in [0.7, 1], \tag{5.148}$$

$${}_T\gamma_{M2} = 1 - {}_T\gamma_{M1}. \tag{5.149}$$

If only master M1 would control the rotations, the translations in the right hand could be disturbed by unexpected rotational motions in the operator's right hand. Therefore, the rotational task allocation values remain unaltered (${}_R\gamma_i = 1$) for now. The feedback from the slave to the masters remains unaltered since the slave's motion should always be correctly perceived on the master devices.

5.2.2.3 Robot Workspace Limitations

Especially in robots with serial kinematics, the workspace is constrained by singularities and dynamic nonlinearities. These issues can negatively affect the precision and smoothness of motion when large motions are required. To reduce this, the orientation of an input device can be decoupled from the pipe orientation such that it is able to change its orientation freely without influencing the other device. This allows a variety of robot configurations of that input device, such that singularities or other limitations can be avoided. The only drawback is that this robot can then set a desired orientation only through forces in cooperation with the second input device and not through torques. The torques of the controllers coupling the right master to the other devices have to be set to zero to achieve this behavior. Therefore κ_{M2}^{RC}, κ_{S}^{RC}, κ_{M1}^{RC} have to equal ${}_T\kappa^{RC}$, with

$$ {}_T\kappa^{RC} = \begin{bmatrix} \mathbf{I}_3 & \mathbf{0}_3 \\ \mathbf{0}_3 & \mathbf{0}_3 \end{bmatrix}. \tag{5.150} $$

5.2.2.4 Passivity Proof

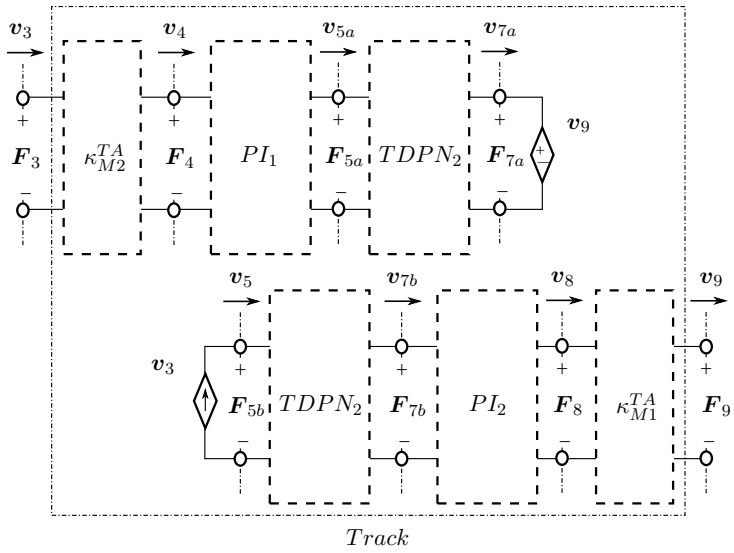

Figure 5.2.10: Network Representation of a PP Architecture Track with Task Allocation The task allocation factors κ_{M2}^{TA} and κ_{M1}^{TA} can be modeled as power sources.

In the MPMT, the allocation factors κ_{M2}^{TA} and κ_{M1}^{TA} can be designed analogous to the authority allocation (Section 5.2.1) as dependent power sources with direction depending energy behavior such that the power P_4 and P_8 are reduced by the task allocation factors (${}_i\gamma_j \in [0,1]$, $i \in \{T,R\}$ and $j \in \{M1,M2\}$) in R2L and L2R direction respectively:

$$ P_3(t) = \kappa_{M2}^{TA} P_4(t) = \boldsymbol{v}_4(t)\kappa_{M2}^{TA}\boldsymbol{F}_4(t), \tag{5.151} $$

$$ P_9(t) = \kappa_{M1}^{TA} P_8(t) = \boldsymbol{v}_8(t)\kappa_{M1}^{TA}\boldsymbol{F}_8(t). \tag{5.152} $$

As discussed in Section 5.2.1.2, the power source κ_{M2}^{TA} in the left part of the track only has an effect in R2L direction. In this direction it has a dissipating characteristic. In contrast,

the same power source κ_{M2}^{TA} has an energy generating behavior in L2R direction but the injected energy is dissipated by the dependent flow source $\boldsymbol{v}_9$ and thus not transmitted to the right part of the track. This holds analogously for the power source κ_{M1}^{TA}.

5.2.2.5 Discussion on Task Allocation

The virtual grasping point concept of Section 5.1.1 has been extended by a method to achieve a Cartesian task allocation in this section. The allocation has been realized via a scaling of the force feedback to the respective master and slave devices. Analogous to the authority allocation in Section 5.2.1, the passivity of the method has been discussed.

Experiments and a user study on the virtual grasping point approach and the task allocation are presented in Section 6.1.

5.2.3 Discussion on Role Distribution

Both, the role distribution for operator training and the one for Cartesian task allocation are designed as scalings that reduce specific force feedback signals to vary the influence of one agent on the others. In contrast, the unidirectional force scaling only varies the coupling stiffness for one of the coupled devices (with higher authority), but preserving the stiffness for the other coupled device (with lower authority). In haptic links, this variation of the force feedback is most reasonable to achieve a role distribution since, alternatively, the velocity or position signal respectively would need to be altered which would disturb the coupling of both coupled devices.

5.3 Haptic Intention Augmentation

For several tasks, the standard bilateral teleoperation of a single robot does not provide sufficient capabilities. Especially, complex tasks require cooperative robots that can be teleoperated by two human operators. Tasks using robotic manipulators can be eased and improved in terms of reliability, adaptability and ergonomics via robot cooperation. For instance, manipulation tasks that require high dexterity, improved handling capability and increased loading capacity favor multi-master-multi-slave systems [157]. Other MMMS scenarios may require a second operator with a different viewpoint. Also, a local supervising operator may need support by a distant expert operator in a MMMS system. The presented approach focuses the cooperative telemanipulation of large or flexible objects by two human operators for scenarios and systems as the walking robot setup of [115], the building of space structures by robots proposed by JAXA [57], the Skyworker proposed in [164] and the constructing rover teams in [149]. Despite visual and haptic feedback, cooperative telemanipulation is challenging due to practical limitations in synchronisation and supervision.

This section introduces a haptic intention augmentation [128] for two human operators that manipulate objects via teleoperation in a cooperative manner. The haptic intention augmentation enhances the force feedback to each operator by information on the motion intention of the other operator that can be observed by a force sensor at the input devices. The result is an active, tight cooperation (compare [84, 54, 57]) of slave robots coupled by a grasped object. The concept of haptic intention augmentation

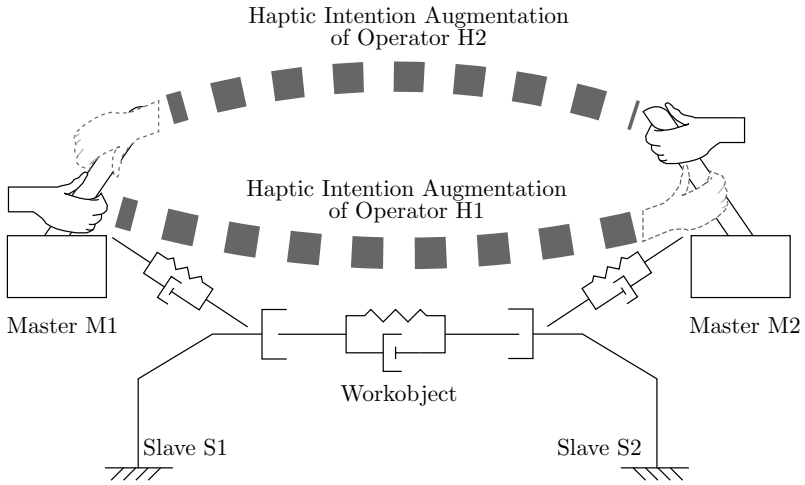

Figure 5.3.1: Functionality of the Haptic Intention Operation
To increase the transparency in terms of intention awareness between cooperative human operators, the feedforward of the interaction forces (and thus the intention of the respective operator) measured at the master device can be exchanged between the operators H1 and H2. This can be regarded as a guidance of the cooperative operator with the second hand as depicted.

presents a $N : N$ system with electronic coupling though it resembles a mechanically coupled cooperation of two teleoperators.

The proposed augmentation provides haptic cues to each operator on the desired direction of motion of the other operator. This solves the following challenges:

- When flexible objects are manipulated, the human operators H1 and H2 may coordinate the motions only via speech. Visual feedback to operator H1 provides just information on the position change of the slave hand controlled by human operator H2 as the applied force/acceleration of operator H2 is not directly visible. As measured force feedback from the slave interaction with a flexible object provides only blurred information, additional force feedback from the cooperating master interaction with its master device is crucial for a good cooperation performance.

- When large objects are manipulated, the inertia of the object and the inertia and damping of the teleoperation system influence the cooperation procedure. For example, if a long object is grasped by one operator at each end, all intended motions apart from the one along the object may not be displayed optimally to the other operator. This holds true for the direct cooperation without a teleoperation system also. If operator H1 intends to move the object up, he has to apply a torque (acting with a lever arm against inertia and damping) at the same time in order to maintain the orientation of the object. In contrast, if only one person lifts an object with two hands she/he knows that both arms need to apply a force in the intended direction.

Among others, these problems can be reduced by the feedforward of the interaction forces (and thus the intention of the respective operator) measured at the master device of operator H1 to operator H2 and vice versa. This can be regarded as a guidance of the cooperative operator with the second hand as depicted in Fig. 5.3.1.

5.3.1 Implementation

Fig. 5.3.2 presents the signal flow diagram of the haptic intention augmentation approach. The system can be divided into two 2-*Channel* teleoperation control loops (upper and lower half) with PF_{comp} architecture. The loops are connected via the delayed (T_3) feedforward of the interaction force $F_{i,h}$ ($i \in \{1,2\}$) of the human operator $H1/H2$ with his/her master device $M1/M2$. These forces are scaled with the constant gains Gh_i. In both teleoperator systems, a time delay T_i is considered in the communication channel. The forward and backward time delays are assumed to be equal for the sake of simplicity. Still, note that the chosen approach allows variable delay, jitter and package loss. A controller $PI1/PI2$ on the slave side $S1/S2$ aims the position tracking of the master and slave robots. The admittance type slave receives the computed controller force $F_{i,sc}$. The master device $M1/M2$ receives the delayed computed controller force $F_{i,sc}$ scaled by Gs_i. With the $PI1$ controller impedance $Z_{PI1}(s) = \frac{Bs+K}{s}$, the force command to slave $S1$ and master $M1$ results in:

$$\begin{aligned} F_{1,sc}(k) =& B(v_{1,m}(k-T_1) - v_{1,s}(k)) + \\ & K(x_{1,m}(k-T_1) - x_{1,s}(k)), \end{aligned} \tag{5.153}$$

$$F_{1,mc}(k) = Gs_1 F_{1,sc}(k-T_1) + Gh_1 F_{2,h}(k-T_3), \tag{5.154}$$

$$F_{1,s}(k) = F_{1,sc}(k) - F_{1,e}(k), \tag{5.155}$$

$$F_{1,m}(k) = F_{1,mc}(k) + F_{1,h}(k). \tag{5.156}$$

The network representation of the multilateral setup is presented in Fig. 5.3.3. The haptic intention augmentation can be designed as a system with four agents and three tracks. *Track* Γ1 and *Track* Γ2 can contain for example a PF_{comp} architecture, whereas *Track* Γ3 exchanges the human interaction forces. Since only the intention of the operator should be transmitted to the cooperative operator, the scalings Gh_i ($i \in \{1,2\}$) have to be designed as follows:

$$\begin{aligned} &\text{If } F_{1,h} > -(F_{1,m2} - F_{1,m1}) \;\&\&\; (F_{1,m2} - F_{1,m1}) < 0 \\ &\qquad Gh_2 = \frac{F_{1,h} + (F_{1,m2} - F_{1,m1})}{F_{1,h}}\, Gh_2^0, \\ &\text{else if } F_{1,h} < -(F_{1,m2} - F_{1,m1}) \;\&\&\; (F_{1,m2} - F_{1,m1}) > 0 \\ &\qquad Gh_2 = \frac{F_{1,h} + (F_{1,m2} - F_{1,m1})}{F_{1,h}}\, Gh_2^0, \\ &\text{else if } F_{1,h} > 0 \;\&\&\; (F_{1,m2} - F_{1,m1}) < 0 \\ &\qquad Gh_2 = Gh_2^0, \\ &\text{else if } F_{1,h} < 0 \;\&\&\; (F_{1,m2} - F_{1,m1}) > 0 \\ &\qquad Gh_2 = Gh_2^0, \end{aligned} \tag{5.157}$$

with the constant scaling Gh_2^0. Through this logic, the control loop between the operators can be decoupled in a way that only the intended accelerations are exchanged in *Track* Γ3. Human operator H2 is informed if human operator H1 acts against the motion of environment and human operator H2 or if he supports this motion. The calculation of Gh_1 is analogous to the logic (5.157).

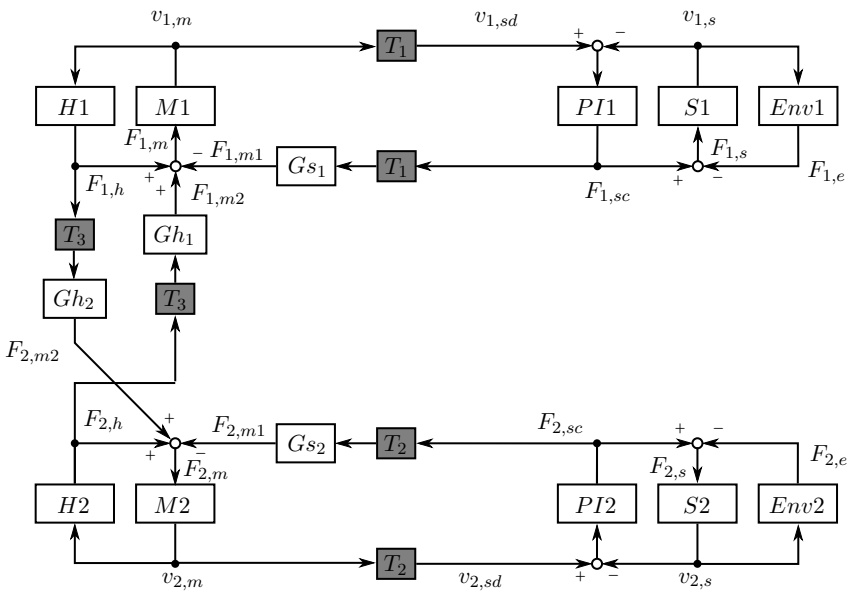

Figure 5.3.2: Signal Flow Diagram of the Haptic Intention Augmentation Setup
In addition to two bilateral systems coupling master $M1$ and slave $S1$ as well as master $M2$ and slave $S2$ respectively, the master-human interaction force is displayed at the master device of the cooperative operator. The scalings Gh_i and Gs_i ($i \in \{1, 2\}$) vary the force feedback.

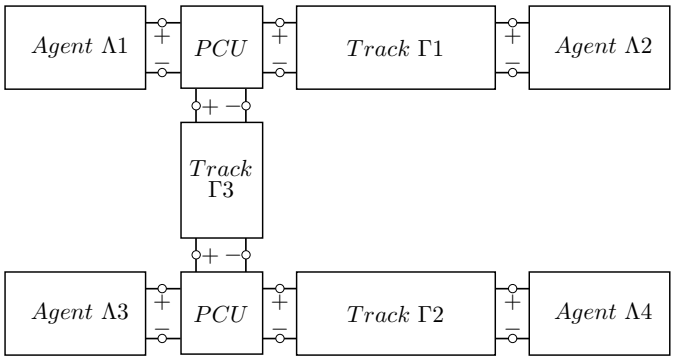

Figure 5.3.3: Simplified Network Representation of the Haptic Intention Augmentation Setup
The haptic intention augmentation can be designed as a system with four agents and three tracks. *Track* Γ1 and *Track* Γ2 can contain for example a PF_{comp} architecture, whereas *Track* Γ3 exchanges the human interaction forces.

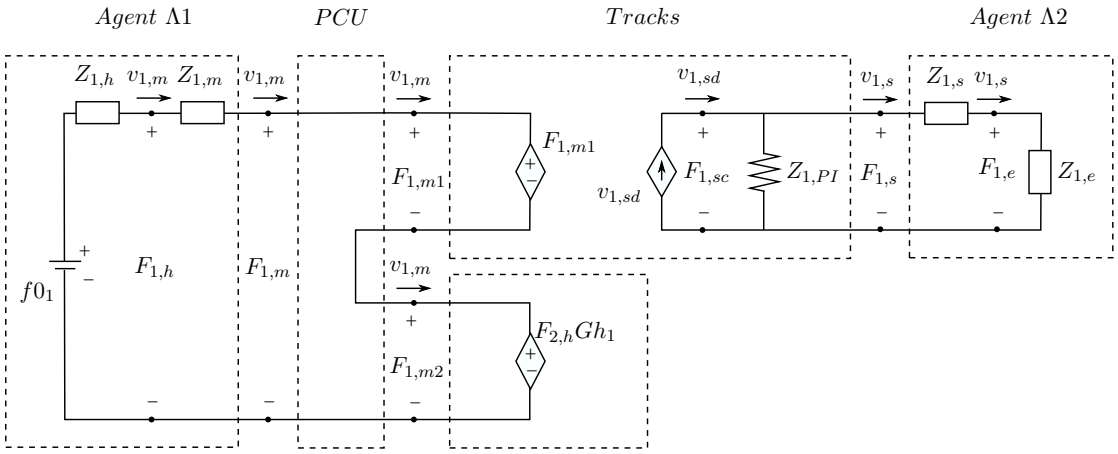

Figure 5.3.4: One Half of the Network Representation of the Haptic Intention Augmentation Setup without Time Delay
The effort sources $F_{1,j}$ $j \in \{m1, m2\}$ inject the force feedback into the circuit of the master side. $F_{1,m1}$ equals the controller force $F_{1,sc}$.

5.3.2 Stability Discussion

The prevalent approaches aiming at the stabilization of teleoperation systems with respect to communication delay are the wave variables method [110] and the time domain passivity approach [144, 143]. In order to analyze the energetic structure of a control loop, its electrical network representation based on the mechanical-electrical analogies is derived. Fig. 5.3.4 represents the upper half teleoperation scheme of the signal flow diagram in Fig. 5.3.2.

An additional communication channel, represented by $F_{1,m2}(t) = F_{2,h}(t - T_3)Gh_1$ has to be added to the PF_{comp} architecture. In order to guarantee that the dual ports of all subsystems have a unique flow, the system is split up into two circuits that are connected with dependent effort and flow sources. The dependent effort sources $F_{1,m1}$ and $F_{2,h}(t - T_3)Gh_1$ establish the feedback of the environmental force, the computed force of the controller $Z_{1,PI}$ and the intention augmentation force of operator H2. The dependent flow source $v_{1,sd}$ transmits the desired slave velocity to the slave side.

The system of Fig. 5.3.4 is passive if all subsystems are passive. Therefore, in the following, the effect of the time delay has to be considered, but also the passivity of the remaining subsystems has to be assured.

5.3.2.1 Time Delay

The haptic intention augmentation setup of Fig. 5.3.4 is extended by a time domain passivity control in Fig. 5.3.5. Via the TDPN, energy flows that are not visible e.g. in the signal flow diagram become apparent such that it becomes obvious with which signals the POs have to be designed. Fig. 5.3.5 presents the network representation considering the TDPNs. The new haptic intention augmentation channel requires the introduction of the $TDPN_1$ B with the conjugate pairs

$$TDPN_1 \text{ B:} \begin{cases} \langle Gh_{1,2}F_{2,h}(k - T_3), v_{1,m}(k)\rangle & \text{at the } H1 \text{ side} \\ \langle Gh_{1,2}F_{2,h}(k), v_{1,m}(k - T_3)\rangle & \text{at the } H2 \text{ side} \end{cases}$$

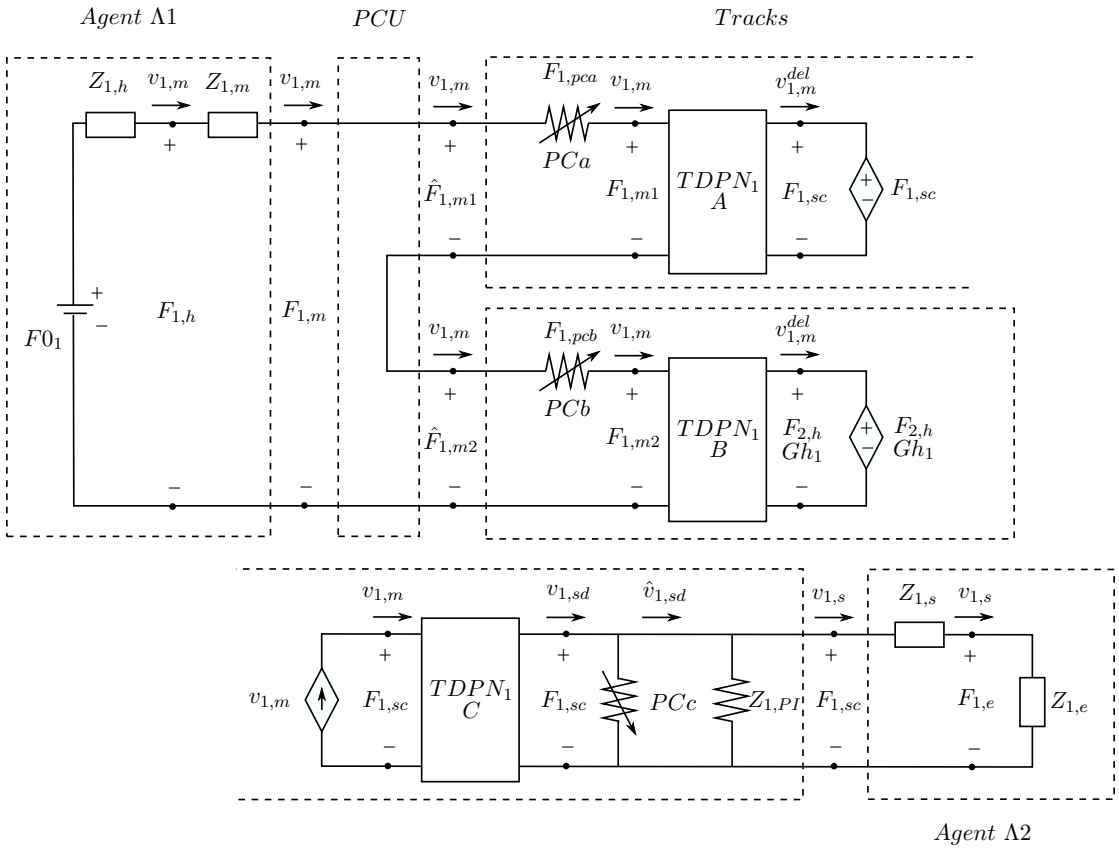

Figure 5.3.5: One Half of the Network Representation of the Haptic Intention Augmentation Setup with Time Domain Passivity Control
To consider a delay in the communication channel, three sets of TDPNs and PCs are integrated in both halfs of the coupled system's network.

The functionality of the TDPN Approach 1 is described in Section 2.3.2.3.

5.3.2.2 Passivity of the Feedforward of Interaction Forces

Besides the passivity of the communication channel, the passivity of the other subsystems has to be proven. The controller as a spring damper system consists of passive modules. As discussed in Section 3.3.2, the agents can be regarded as passive subsystems.

The additional feedforward of the operator interaction forces requires an additional analysis: Clearly, the effort sources $F_{2,h}Gh_1$ and $F_{1,h}Gh_2$ present an energy input to the system. The interaction forces $F_{i,h}$ ($i \in \{1,2\}$) are influenced by the force feeback $F_{i,m1}$ and $F_{i,m2}$. To avoid a complicated coupling caused by the interaction with the environment and the exchange of the intention forces, the scalings Gh_i are designed with the logic (5.157). Due to this logic, no forces are transmitted to the cooperative operator, if the operator wants to keep the pose of the master device. Only the parts of the forces that lead to an acceleration, that is caused by the respective operator, are exchanged in *Track* Γ3. In a perfectly transparent system with perfect gravity and inertia compensation, this is the force that should be felt by the cooperative operator. Therefore, the coupling of *Track* Γ3 can be regarded as a reference for a passive coupling

of the *Agents* Λ1 and Λ3. The *Tracks* Γ1 and Γ2 and the *Agents* Λ2 and Λ4 can be added to this coupling as those are passive subsystems. To guarantee that the energy in the system is lower or equal to the reference case, the forces $F_{1,m1}$ and $F_{1,m2}/Gh_1^0$ have to be scaled down by Gh_1^0 and Gs_1 such that their sum is lower or equal to $F_{2,h}Gh_1/Gh_1^0$. This can be achieved if

$$Gh_i^0 + Gs_i \leq 1 \quad \text{with } Gh_i^0, Gs_i \in [0,1] \text{ and } i \in \{1,2\}. \tag{5.158}$$

Furthermore, the effect of delay in general cooperative teleoperation setups [158] has to be analyzed. Since the delay T_3 is smaller than $T_2 + T_1$, for example master M1 perceives the intention of master M2 earlier and better compared to the pure environmental feedback without haptic intention augmentation. Thus, the proper interaction of the operators is eased also in the delayed case.

5.3.3 Experiments

The following experiments have been performed in the undelayed 6-DoF setup described in Appendix A.3. The evaluation focuses the haptic intention augmentation for the cooperative motion of stiff objects. Further experiments with a space setup considering time delay and flexible objects are presented in Section 6.2. Note that the following experiments were performed in a PF_{meas} architecture (compare [128]) such that Gs_i ($i \in \{1,2\}$) acted on the measured force feedback of the slaves.

The two robotic hands of SpaceJustin grasped a pipe firmly at a distance of about 0.6 meters. Gh_i^0 was set to the value 0.3 and the measured force feedback was scaled with $Gs_i = 0.7$.

Experiment Exp. 5.16 focuses the functionality of the haptic intention augmentation in the translational degrees of freedom. The left operator H1 starts moving the left slave hand upwards ($t = 10.5s$, plot Exp. 5.16a). The right operator H2 follows this motion in order to keep the pipe horizontal as soon as he has perceived the intention of operator H1. Without intention augmentation (plots Exp. 5.16a and Exp. 5.16c), the operator relies on the visual feedback of the slave motion and the force feedback of the slave robot. With active haptic intention augmentation (plots Exp. 5.16b and Exp. 5.16d), the right operator H2 receives the sum $F_{2,FB}$ of the left operator's interaction force $F_{1,h}$ in addition to the force feedback of the slave robot. $F_{i,e,z}$ ($i \in \{1,2\}$) is the interaction force of slave $S1/2$ with the environment in z-direction. Comparing Exp. 5.16a and Exp. 5.16b it is obvious that the operator H2 starts following the translational motion earlier with active augmentation. Also, the average distance in z-direction is lower for that case. The 3D pipe motion during this procedure is visualized in plots Exp. 5.16c and Exp. 5.16d. The line color in the 3D-Plot implies the time. The color turns darker with time. It is obvious that the pipe motion is less horizontal without haptic augmentation.

The second experiment Exp. 5.17 analyzes the benefit of the haptic intention augmentation applied during rotational motions. The left operator H1 intends to rotate the pipe around the right slave robot hand controlled by operator H2. Analogous to the forces, the environmental interaction torques in both experiments with and without intention augmentation (plots Exp. 5.17a and Exp. 5.17b) around the x-axis $\tau_{2,e,\alpha}$ are much lower than the operator's interaction torque $\tau_{1,h,\alpha}$ with the human machine interface. Without the augmentation concept, the operators obviously receive less haptic

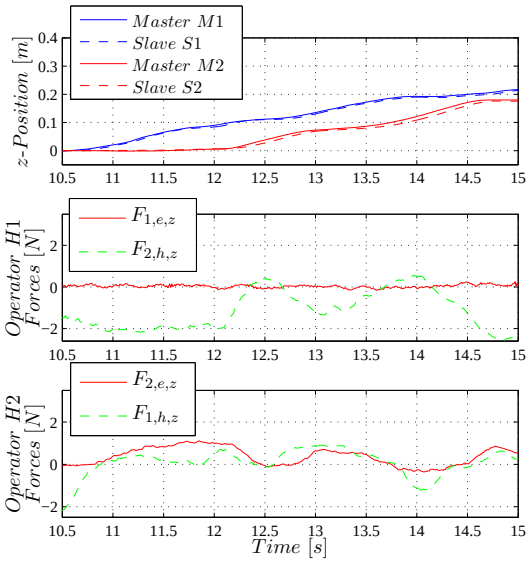

(a) Position and Wrenches without Haptic Intention Augmentation

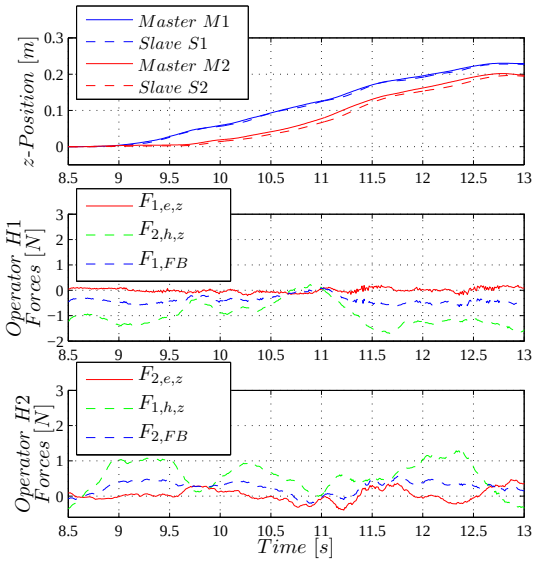

(b) Position and Wrenches with Haptic Intention Augmentation

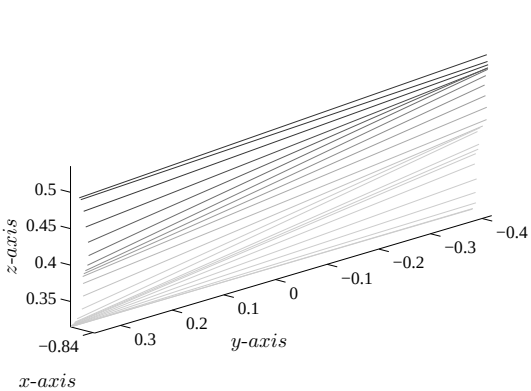

(c) 3D-Motion without Haptic Intention Augmentation

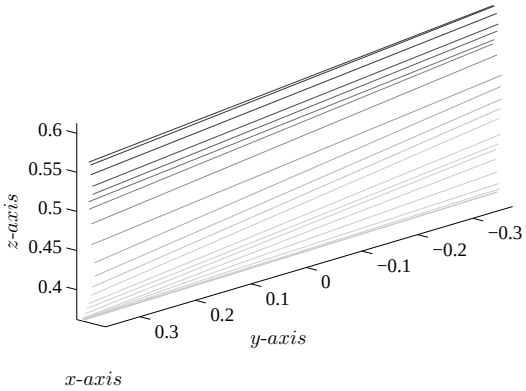

(d) 3D-Motion with Haptic Intention Augmentation

Experiment 5.16: Cooperative Translational Motion
The left operator H1 starts moving the left slave hand upwards ($t = 10.5s$, plot Exp. 5.16a). The right operator H2 follows this motion in order to keep the pipe horizontal as soon as he has perceived the intention of operator H1. Without intention augmentation, the operator relies on the visual feedback of the slave motion and the force feedback of the slave robot. The operator H2 starts following the translational motion earlier with active augmentation. Also, the average distance in z-direction is lower for that case.

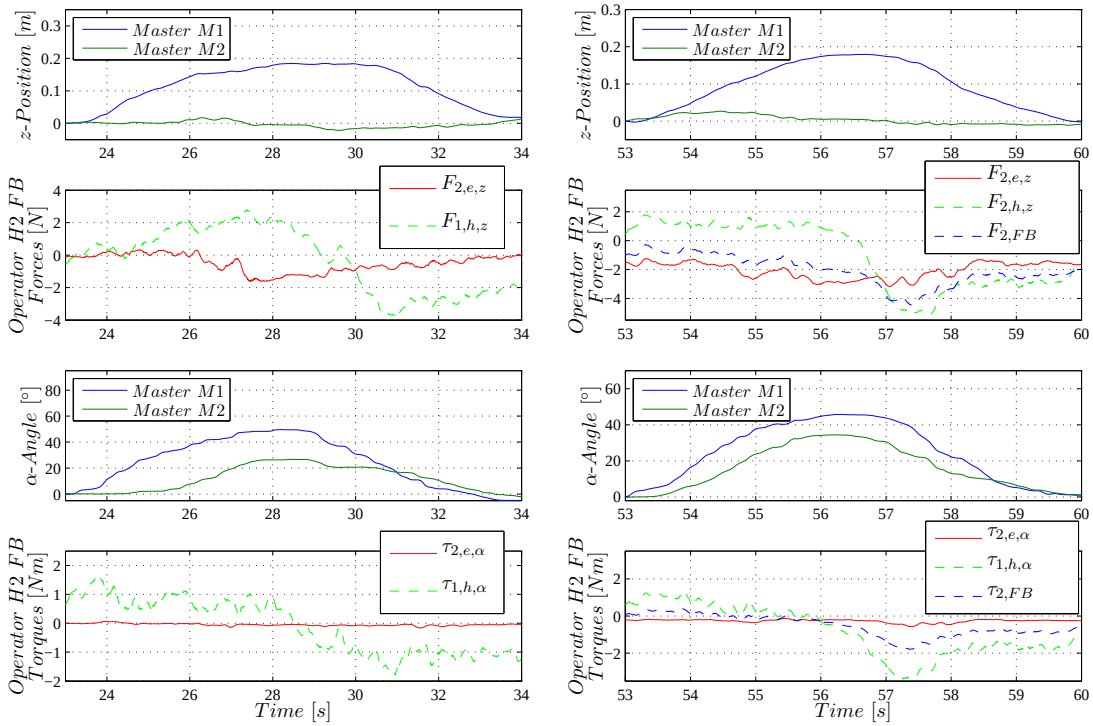

(a) without Haptic Intention Augmentation **(b)** with Haptic Intention Augmentation

Experiment 5.17: Cooperative Rotational Motion
The left operator H1 intends to rotate the pipe around the right slave robot hand controlled by operator H2. The environmental interaction torques in both experiments with and without intention augmentation around the x-axis $\tau_{2,e,\alpha}$ are much lower than the operator's interaction torque $\tau_{1,h,\alpha}$ with the human machine interface. Without the augmentation concept, the operators obviously receive less haptic cues to react on the other operator's motion. Operator H2 reacts earlier on the change in rotation and the average of difference in angle α is lower with haptic intention augmentation though the time of completion is much shorter.

cues to react on the other operator's motion. Comparing plots Exp. 5.17a and Exp. 5.17b, operator H2 reacts earlier on the change in rotation and the average of difference in angle α is lower in Exp. 5.17b with haptic intention augmentation although the time of completion is much shorter.

5.3.4 Discussion on Haptic Intention Augmentation

In this section, a haptic intention augmentation has been introduced that is suitable for the handling of long and/or flexible objects in a tight cooperation manner. Preliminary experiments hint that the haptic intention augmentation brings benefits to cooperative multi-DoF teleoperation. The proposed approach is validated in a setup involving microgravity conditions and real space communication links in Section 6.2.

5.4 Discussion on Haptic Augmentation

Various haptic augmentation methods have been presented in this chapter that extend the standard bilateral teleoperation setup. The three concepts of virtual grasping point, role distribution and haptic intention augmentation provide different aids. Note that different passive architectures can be applied in combination with these concepts, but e.g. measured force feedback is not always reasonable. The haptic intention augmentation provides by far best performance with measured force feedback. In contrast, in the virtual grasping point concept, computed forces are required since these provide accurate position information. In the following chapter, a set of the proposed concepts is evaluated in typical scenarios and a user study.

Chapter 6

Experimental Applications

A variety of control architectures and haptic augmentation modules that can be applied in the MPMT structure have been introduced in the preceding sections. In this chapter, the capabilities of a set of haptic augmentation concepts will be analyzed in more specific and realistic scenarios.
The first set of experiments refers to the virtual grasping point and Cartesian task allocation in a multi-DoF peg-in-hole task involving an industrial pipe. Additionally, a performance evaluation based on quantitative results and statistical analysis, gained in a user study, is presented.
With multilateral robotic setups the reliability and adaptability to different tasks is enhanced when compared to single robot systems. Especially in space applications, these properties provide strong benefits. Therefore, the second experiment refers to a cooperative telemanipulation scenario with an operator in microgravity on the International Space Station. Via this space link, the haptic intention augmentation during cooperative manipulation has been analyzed at low visual feedback quality and delayed communication.
In the final experiment, a multilateral coupling in the teleoperation of remote wheeled mobile robots is investigated. The additional agent is a simulated local model of the WMR at the master side. An extended model-mediated teleoperation setup is realized through a combination of delayed force feedback from the slave robot and artificial force feedback from the simulated WMR.

6.1 Telemanipulation with Virtual Grasping Points (N:1)

The virtual grasping point concept improving the rotational precision (Section 5.1.1) and the Cartesian task allocation (Section 5.2.2) present in combination the most sophisticated haptic augmentation concepts presented in this thesis. Therefore, the approaches are evaluated in the following in a multi-DoF peg-in-hole task [129]. A time delay in a position-position architecture is considered in the final experiment. The experimental

Table 6.1: Control Parameters

Track	K_T [N/m]	B_T [Ns/m]	K_R [Nm/rad]	B_R [Nms/rad]
Γ 1	400	3	15	1
Γ 2	300	6	10	0.45
Γ 3	300	6	10	0.45

setup is the same as presented in the system description in Section 5.1.1. For the sake of an objective analysis, a user study [129] with a simplified virtual setup and two master devices has been performed.

6.1.1 Experiments

In this section, the proposed multilateral system will be analyzed experimentally with focus on the virtual grasping point and the task allocation. The hardware and the applied technical setup with the input device HUG and the humanoid robot SpaceJustin is introduced in Appendix A.2. The DLR HitHand (Wessling Robotics) was used to grasp the pipe. The grasp can thus be assumed to be stable at low to mid range velocities. The Cyberglove served as the hand interface. The grasped pipe was a light plastic pipe made of polypropylene.

All robots have been linked via the presented position-position teleoperation scheme, i.e. no force sensors have been applied in the control loop. The controller constants have been chosen as depicted in Table 6.1. No local damping has been applied.

6.1.1.1 Dual Master Experiments

In the first Exp. 6.1 and second experiment Exp. 6.2, the virtual pipe coupling between master M1 and master M2 ($Track$ Γ1) is analyzed. A rotation around the pipe end at master M2 position is performed and the performance with and without task allocation is compared. Plot Exp. 6.1a (pipe color indicates time) depicts the motion of the virtual pipe without task allocation. Master M1 rotates around master M2 which tries to fix its initial position on the left hand side of the plot. The computed PI controller forces F_c that are demanded from the robots have opposite signs for master M1 and master M2 (compare plot Exp. 6.1b). The force values F_e measured by the force sensor differ, as the operator hands have to counteract e.g. against the link masses. The task allocation is activated for Exp. 6.2. The task allocation values have been chosen according to Table 6.2 (bilateral case). It is obvious that master M2 can maintain its translational position more easily if the task allocation is active. Plot Exp. 6.2b shows that all the forces F_c sent to master M2 are canceled if task allocation is active. The measured forces F_e at the master M2 side are constant during the rotational procedure as the right operator hand does not need to resist against the left hand's demand.

Comparing plots Exp. 6.1b and Exp. 6.2b one can see that in order to rotate the pipe, the right hand at master M2 has to act with a force F_e^z against the rotation only

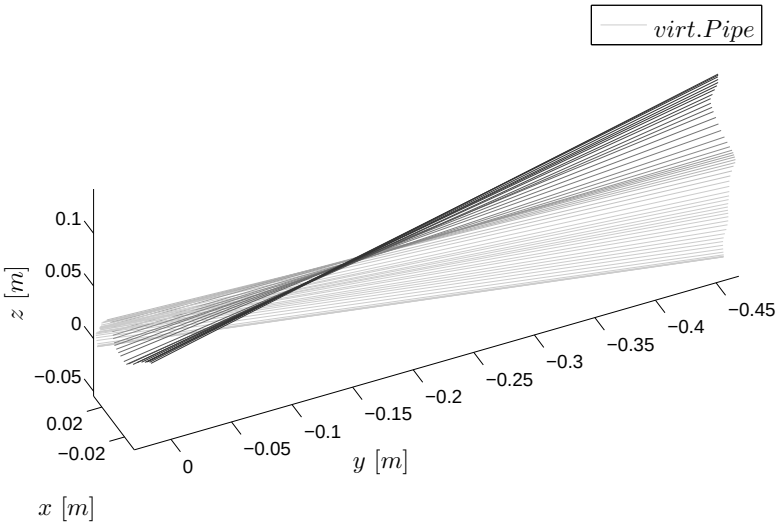

(a) 3D Plot of Virtual Pipe

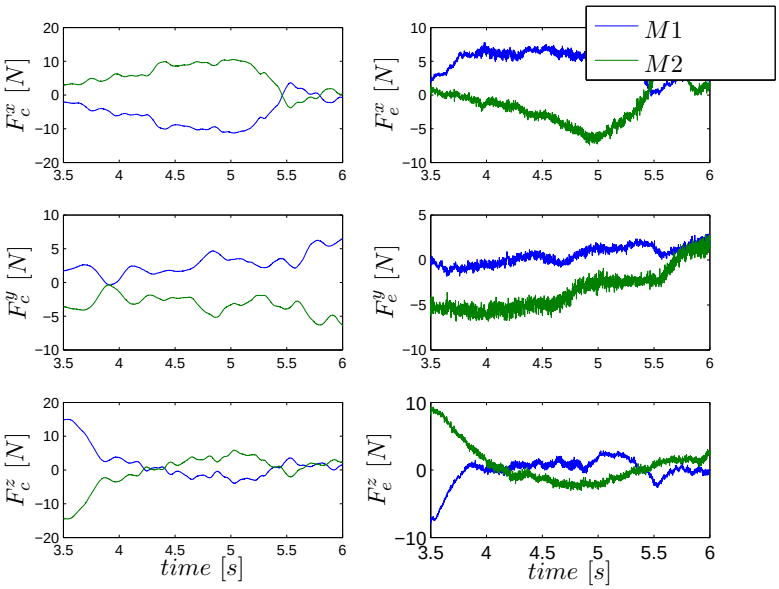

(b) Measured and Computed Forces

Experiment 6.1: Bilateral Virtual Pipe Link without Task Allocation (Devices M1, M2 and Track Γ1)
Master M1 rotates around master M2 which tries to fix its initial position on the left hand side of the 3D plot.

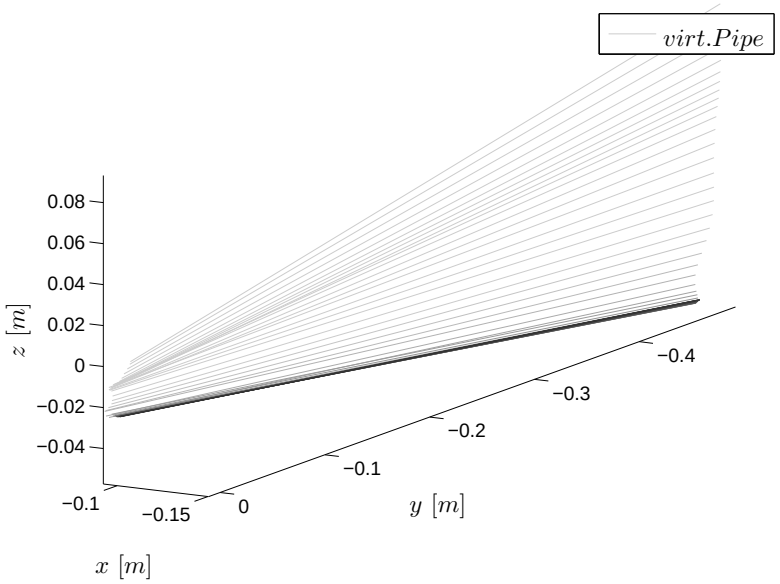

(a) 3D Plot of Virtual Pipe

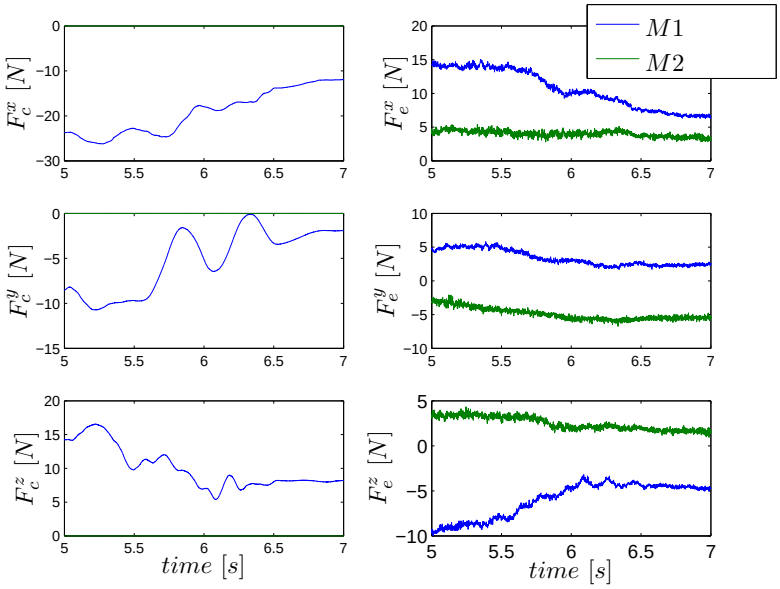

(b) Measured and Computed Forces

Experiment 6.2: Bilateral Virtual Pipe Link with Task Allocation (Devices M1, M2 and Track Γ1)
Master M1 rotates around master M2 which tries to fix its initial position on the left hand side of the 3D plot. Due to the task allocation, the forces sent to master M2 are canceled.

Table 6.2: Task Allocation Settings for Bilateral and Multilateral Experiments

α bilateral	Value	α multilateral	Value
${}_T\alpha_{M1}$	0	${}_T\alpha_{M1}$	0.3
${}_R\alpha_{M1}$	0.5	${}_R\alpha_{M1}$	0.5
${}_T\alpha_{M2}$	1	${}_T\alpha_{M2}$	0.7
${}_R\alpha_{M2}$	0.5	${}_R\alpha_{M2}$	0.5

if the task allocation is not active.

6.1.1.2 Bilateral Experiment

Exp. 6.3 analyzes a bilateral system with direct coupling between master M1 and slave (*Track* Γ2). A rotational motion around the pipe end is performed which is depicted in plot Exp. 6.3a. As the rotational position following (compare α^{Grasp} and α^{PE}) of master M1 and slave is not optimal, the resulting translational position error in the pipe end x^{PE} is high (see plot Exp. 6.3b).

6.1.1.3 Multilateral Experiments

In experiment Exp. 6.4, master M2 is added to the system. *Track* Γ3 and task allocation are still deactivated (Fig. 5.1.5 without *Track* Γ3). There is one indirect coupling between master M1 and master M2 (*Track* Γ1) and one direct coupling from slave to master M1 (*Track* Γ2). An exemplary plugging trajectory of the pipe is depicted in plot Exp. 6.4. The pipe is pushed to the plug position, then the pipe is reorientated around the x-axis and then pushed into the plug in y-axis direction. The rotation around the pipe end is more accurate than in the preceding experiment (compare plot Exp. 6.3a) as the master M1 rotation demand to the slave is stabilized by master M2.

In the next step (Exp. 6.5) the *Track* Γ3 is activated such that a real multilateral coupling as depicted in Fig. 5.1.5 can be evaluated in plot Exp. 6.5a. The task allocation is not active. As the additional coupling via *Track* Γ3 makes the system stiffer, especially the slave's position following is improved compared to Exp. 6.4.

For experiment Exp. 6.6, the task allocation is activated and an additional track corresponding to Fig. 5.2.9 was introduced. Thus the position of the pipe end is more steady in plot Exp. 6.6a. The task allocation values have been chosen according to Table 6.2 (multilateral case) which subjectively evaluated resulted in the best performance. Because of cross couplings caused by the available robot workspace, the task allocation was chosen such that master M1 gained 30% authority ($\alpha^i_{Trans} = 0.30,\ i \in \{\Gamma1, \Gamma2\}$) on the pipe end's translational motion. Comparing plots Exp. 6.6a and Exp. 6.5a, one can see that especially the translational motions along x- and y-axis are more precise if task allocation is active. Another benefit of the task allocation is that the workload of the operator can be reduced, as he needs less forces for the desired motions (compare master M2 forces in plots Exp. 6.6b and Exp. 6.5b).

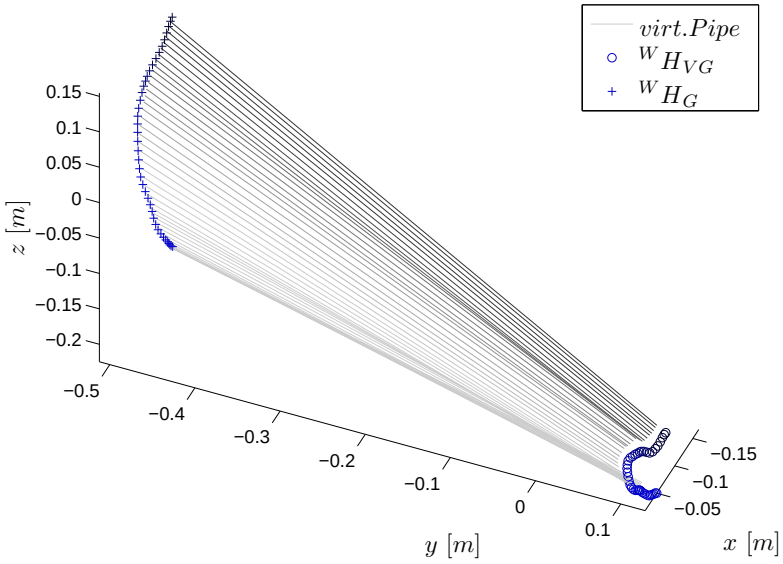

(a) 3D Plot of Virtual Pipe

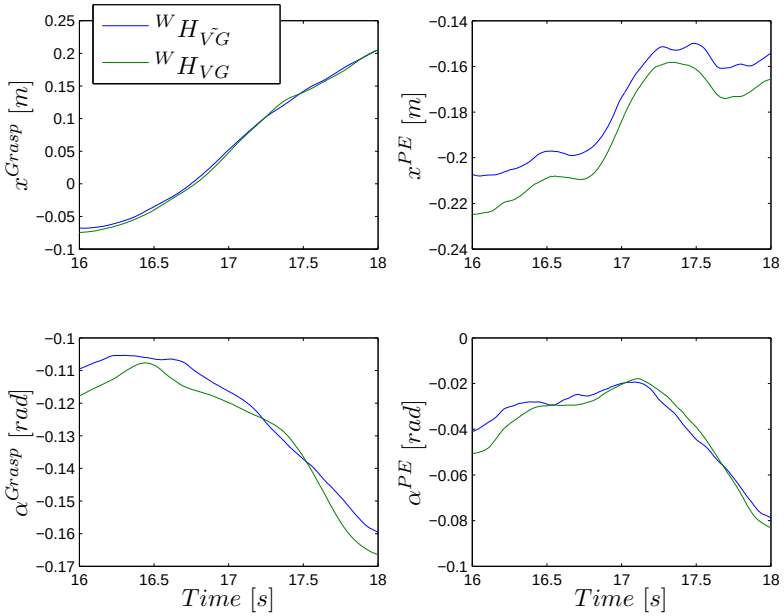

(b) Position Tracking

Experiment 6.3: Direct Bilateral Coupling of Master M1 and Slave (Devices M1, S and Track Γ2)

A rotational motion around the pipe end is performed. As the rotational position following (compare α^{Grasp} and α^{PE}) of master M1 and slave is not optimal, the resulting translational position error in the pipe end x^{PE} is high.

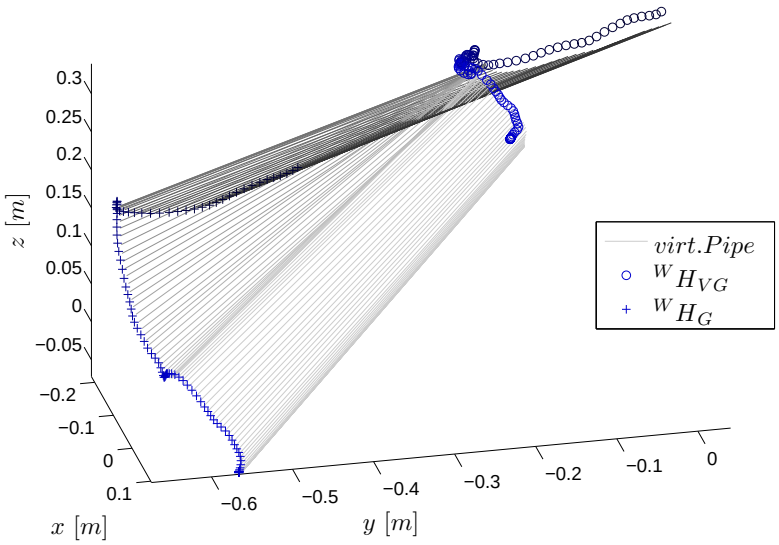

Experiment 6.4: Virtual Pipe Motion with pseudo-multilateral Coupling (Devices M1, M2, S and Tracks Γ1 and Γ2)
First, the pipe is positioned close to the plug location, then the pipe is reorientated around the x-axis and then pushed into the plug in y-axis direction. The pseudo-multilateral coupling with *Tracks* Γ1 and Γ2 improved the accuracy of rotation since the master M1 rotation demand to the slave is stabilized by master M2.

The next set of experiments presents a procedure with rotation in the xy-plane around the virtual grasping point with subsequent plug-in of the pipe into a hole. The experiment with contact forces has been performed in a bilateral setup (direct Master 1 - Slave coupling, Exp. 6.7) as well as in a multilateral setup with task allocation (Tracks Γ1, Γ2 and Γ3, Exp. 6.8). The respective pipe motion plots show that the plug-in is difficult in the bilateral case. In contrast, only one plug-in attempt is necessary with the multilateral setup. The computed forces resulting from one spatial spring in the unimanual setup clearly present three contacts with the wall (compare F_y). Due to the three coupling springs in the multilateral bimanual setup, the force feedback consists not only from the spring deflections resulting from the slave's contact but also from the coupling via the virtual grasping points. Still, the contact forces in y-direction can be recognized in both master devices.

A time delay is considered in the last experiment Exp. 6.9. The slave is assumed to be located distant from the master devices such that the *Tracks* Γ2 and Γ3 contain a roundtrip delay of 40ms. The architecture presented in Fig. 5.2.9 with Time Delay Control Approach 2 (see Section 4.1.1) is chosen. Plot Exp. 6.9a depicts the plug out motion of the pipe (plot Exp. 6.9b, $t = [8.7s, 9.5s]$). Plot Exp. 6.9b shows that delay doesn't reduce the position tracking quality of the three devices during the plug-in and plug-out motion.

6.1.2 User Study

The following study focused the two following hypotheses:

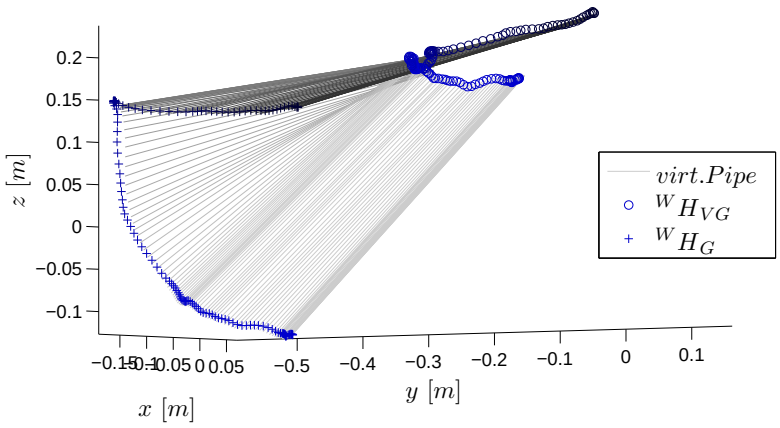

(a) 3D Motion of Pipe

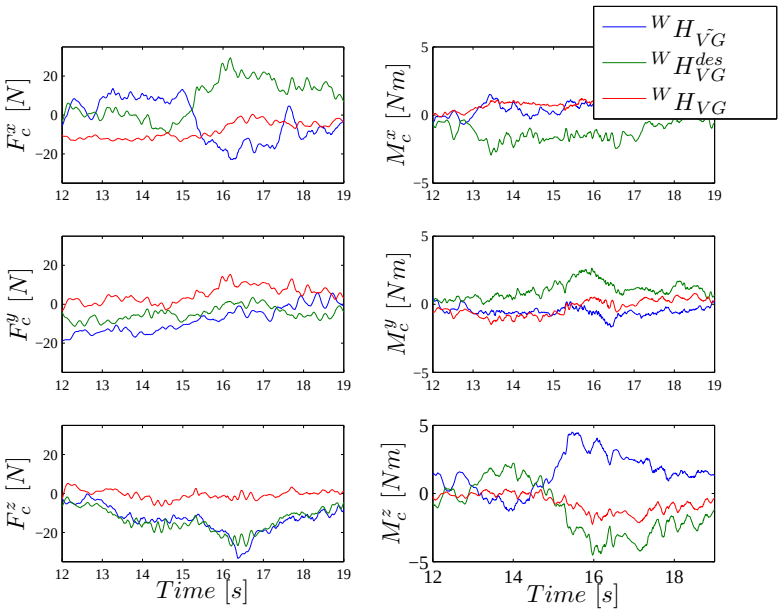

(b) Computed Forces and Torques

Experiment 6.5: Multilateral System without Task Allocation (Devices M1, M2, S and Tracks Γ1, Γ2 and Γ3)
The real multilateral coupling results in a stiff system such that especially the slave's position tracking is improved compared to Exp. 6.4.

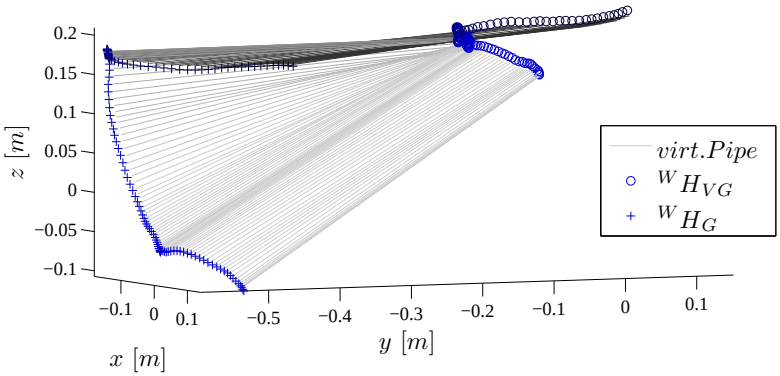

(a) 3D Motion of Pipe

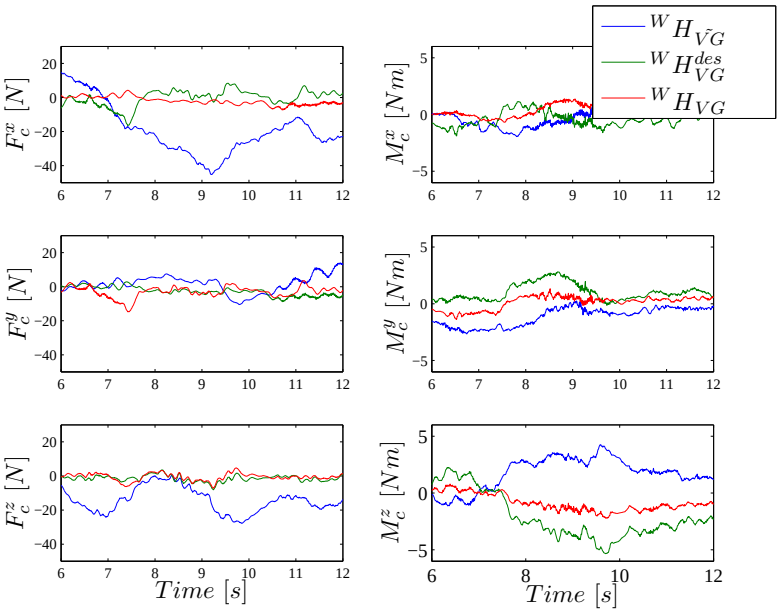

(b) Computed Forces and Torques

Experiment 6.6: Multilateral System with Task Allocation (Devices M1, M2, S and Tracks Γ1, Γ2 and Γ3)
Compared to 6.5, especially the translational motions along x- and y-axis are more precise since task allocation is active. Also, the force plots indicate that the physical workload of the operator can be reduced through the task allocation.

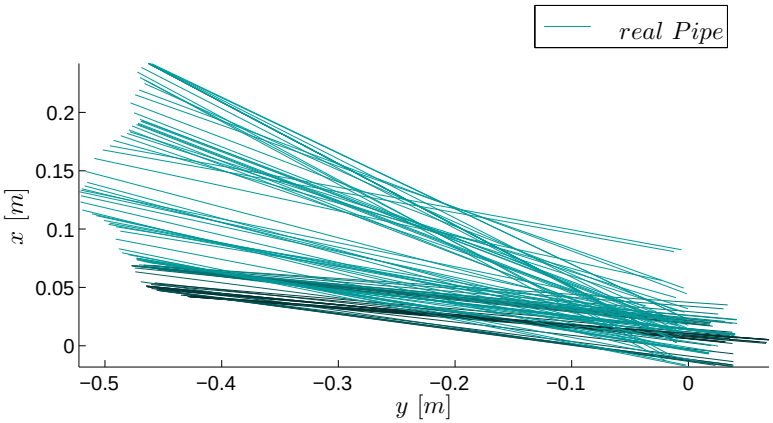

(a) 3D Motion of Pipe

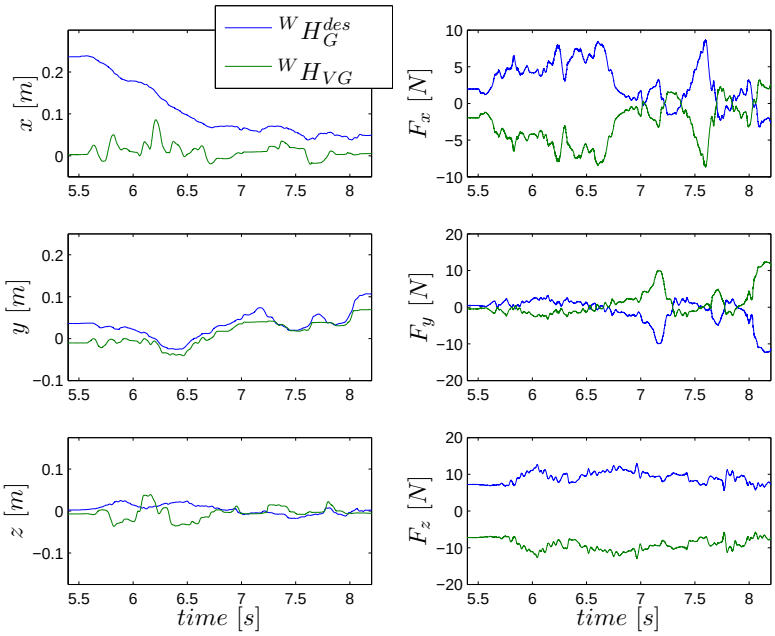

(b) Position Tracking and Forces

Experiment 6.7: Plug-In Procedure in a Bilateral Master-Slave Setup (Devices M1, S and Track Γ2)
In a simple bilateral setup, the plug-in procedure is difficult to perform as the pipe motion plot indicates. The computed forces clearly present three contacts with the wall in y-direction.

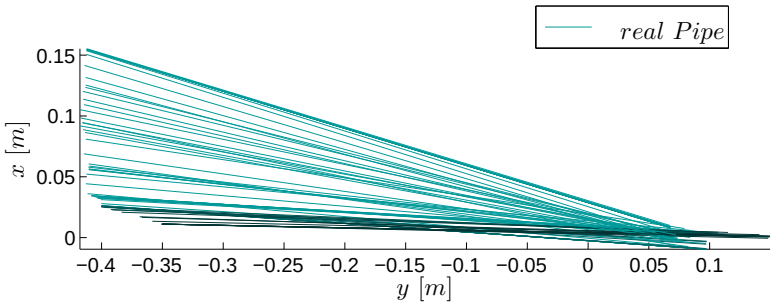

(a) 3D Motion of Pipe

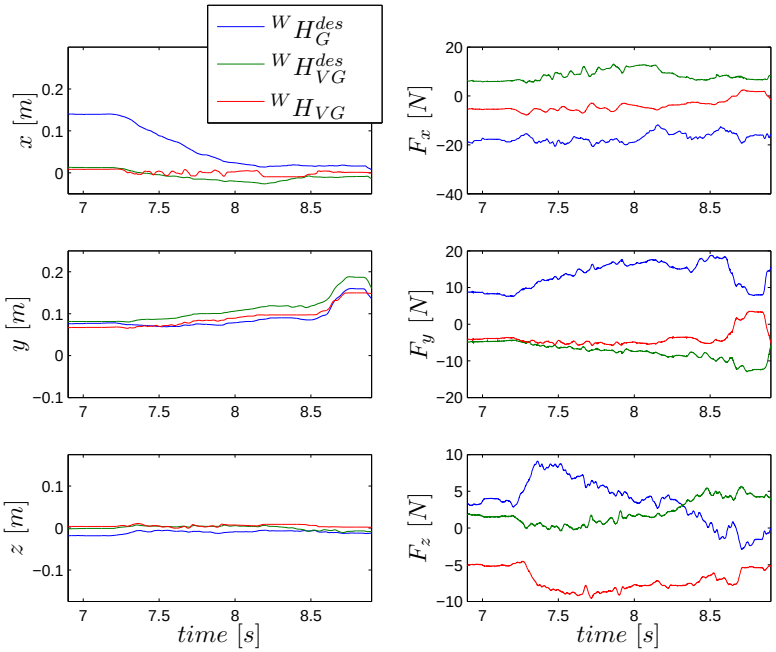

(b) Position Tracking and Forces

Experiment 6.8: Plug-In Procedure in a Multilateral Setup with Task Allocation (Devices M1, M2, S and Tracks Γ1, Γ2 and Γ3)
Due to the three coupling springs in the bimanual setup, the force feedback consists not only from the spring deflections resulting from the slave's contact but also from the coupling via the virtual grasping points. Still, the contact forces in y-direction can be recognized in both master devices.

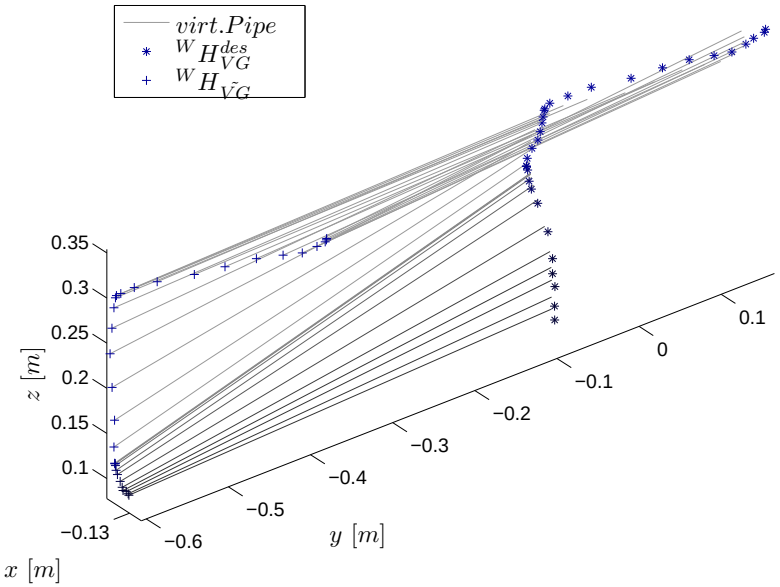

(a) 3D Motion of Pipe

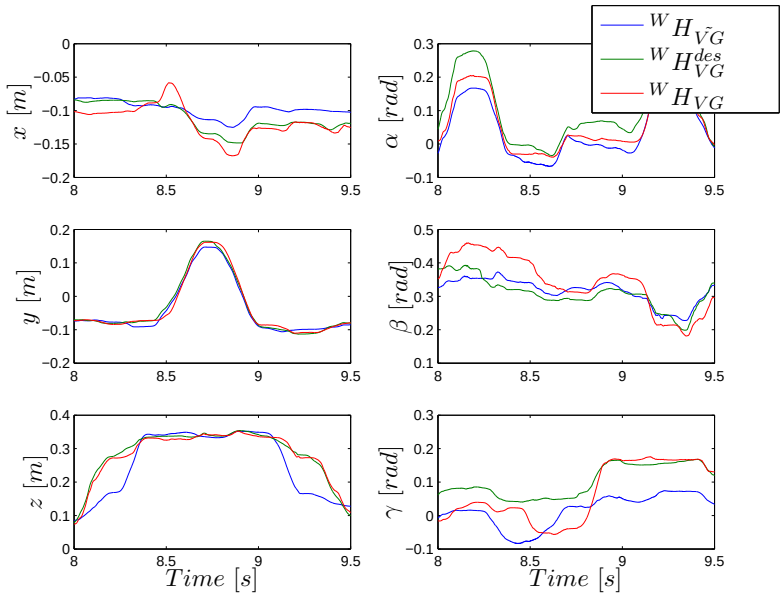

(b) Position Tracking

Experiment 6.9: Multilateral System with Task Allocation at 40ms Roundtrip Delay (Devices M1, M2, S and Tracks Γ1, Γ2 and Γ3)
The delay doesn't reduce the position tracking quality of the three devices during the plug-in and plug-out motion much.

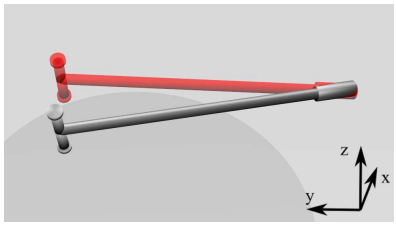

Figure 6.1.1: Virtual Reality Scene of the User Study
The desired pipe position was presented by a red pipe that turned green as soon as the gray controlled pipe reached the target area.

- H1: The proposed bimanual control approach allows a higher level of accuracy then unimanual control when performing a rotational matching task.
- H2: In case of bimanual control, the task allocation approach should lead to higher accuracy compared to an approach without task allocation.

6.1.2.1 Method

The user study was conducted with N=10 participants (9 male, 1 female) with an age between 23 and 35 years (M=28.9; SD=4.1). A within subject design has been chosen such that each participant had to perform the task set with each condition. To reduce undesired effects (e.g. workspace limitations, singularities) of the robot hardware as far as possible, the study was performed with the HUG and a virtual reality instead of a slave robot. Furthermore, the design in the virtual reality allowed clearer instructions and thus a more detailed evaluation of separate tasks.

Technical Setup The controller of the DLR HUG was implemented in Matlab/Simulink and running on a RTLinux system. A pedal served as a deadman switch that activates the robot power. The Instant Player [14] was applied to present the virtual reality to the user. The participants saw the virtual scene on the head mounted display (HMD) nVisorSX60.

Task A set of ten tasks had to be performed with each condition. The virtual reality showed two pipes (see Fig. 6.1.1) The gray pipe was controlled by the operator. The second transparent pipe presented the desired pose of the pipe. When the desired pose was reached, the color of the pipe turned from red to green. After half a second in the desired pose, a new desired pipe pose appeared in red color. The pipe poses have been chosen such that the pipe had to be rotated around the pipe end.

Experimental Design Three conditions have been chosen for the user study:

- Condition 1: unimanual control without haptic augmentation
- Condition 2: bimanual control with virtual grasping point and without task allocation
- Condition 3: bimanual control with virtual grasping point and with task allocation

The set of ten tasks had to be performed once for each condition. The participants started with a training procedure with a condition sequence 1,2,3 to understand the differences of the approaches properly. The order of conditions was randomized for the test subjects to control time effects as fatigue and training.

Another training phase was performed before the accounted task performance in the respective condition. The task set started from a unique initial position. The test subjects were instructed to maintain the pipe end position during the motion of the pipe to the desired position. In addition, the examiner informed that the retention of the pipe end position during the task had higher priority than the time needed for task completion.

Furthermore, the test subjects completed a demographic and an immersive tendency questionnaire [182] to identify correlations with the related performance. Additionally, after the user study a simulator sickness questionnaire [62] had to be filled.

6.1.2.2 Results

The simulator sickness questionnaire indicated that no test subject had to be excluded from the analysis. The following measures have been evaluated:

- The time t needed for one task
- The translational path $path_{PE}$ of the pipe end
- The root mean square (RMS) of the pipe end's translational velocity $RMS(V_{PE})$
- The root mean square of the translational difference of desired and actual pipe end position $RMS(P_{PE}^{diff})$
- The absolute maximum of the translational difference of desired and actual pipe end position $MAX(|P_{PE}^{diff}|)$

The resulting mean value and standard deviation in brackets are presented in Table 6.3. The dimensions x,y and z can be analyzed in Fig. 6.1.1.

The main assumptions for repeated measures ANOVA (rmANOVA), i.e. normality of residuals and sphericity were tested by Shapiro-Wilk's test and Mauchly's test. Only violations of these assumptions are reported in the following analyses. In the case of non-normality the non-parametric Friedman test was chosen. In a first step, the effect of experimental conditions on average completion times t were analyzed in rmANOVA with condition as within factor. Results indicate no significant effect of condition (F (2, 18) = 1.4, n.s.). Next the average path lengths ($path_{PE}$) were explored. Since data were not distributed normally for this variable in condition 1 (Shapiro-Wilk's $W = .84$; $p < .05$), a Friedman test was performed. The results show a highly significant effect of condition, $p = .001$. In subsequent Wilcoxon tests, we found significant differences between condition 1 and 2 as well as 1 and 3 (both $ps < .01$), but no significant difference between condition 2 and 3.

Regarding the empirical distributions for RMS of velocity ($RMS(V_{PE})$) for the three dimensions and conditions also indicated non-normality in four different factor combinations. Thus, three independent Friedman tests with condition as within variable were

Table 6.3: Results

	Condition		
	1	2	3
t	7.29 (2.11)	6.60 (2.30)	6.18 (1.36)
$path_{PE}$	0.541 (0.078)	0.219 (0.069)	0.233 (0.061)
	Dimension x		
$RMS(V_{PE})$	0.064 (0.006)	0.0277 (0.005)	0.0314 (0.006)
$RMS(P_{PE}^{diff})$	0.0288 (0.006)	0.0192 (0.003)	0.0182 (0.004)
$MAX(\|P_{PE}^{diff}\|)$	0.0635 (0.011)	0.0347 (0.008)	0.0342 (0.007)
	Dimension y		
$RMS(V_{PE})$	0.017 (0.002)	0.0106 (0.001)	0.0113 (0.001)
$RMS(P_{PE}^{diff})$	0.0109 (0.002)	0.0115 (0.002)	0.0122 (0.003)
$MAX(\|P_{PE}^{diff}\|)$	0.0208 (0.003)	0.0188 (0.004)	0.0205 (0.004)
	Dimension z		
$RMS(V_{PE})$	0.0763 (0.012)	0.028 (0.004)	0.030 (0.006)
$RMS(P_{PE}^{diff})$	0.0351 (0.005)	0.0260 (0.001)	0.0241 (0.002)
$MAX(\|P_{PE}^{diff}\|)$	0.0721 (0.012)	0.0423 (0.005)	0.043 (0.005)

computed for each dimension. For the x-dimension the Friedman test revealed a significant effect of conditions (p <.001). Contrasting the conditions in Wilcoxon tests showed significant differences between 1 and 2 as well as 1 and 3 (both $ps < .01$) and a non-significant difference between 2 and 3 ($p = .058$). The very same result was found for the y-dimension. Significance was also reached in a Friedman test analyzing data of the z-dimension ($p = .001$). Here only the contrasts between 1 and 2 as well as 1 and 3 reached significance in Wilcoxon's test (both $ps < .01$).

The data for RMS of the position error ($RMS(P_{PE}^{diff})$) also violated the assumption of normality. Again, the above result pattern was evident for the x and the z Dimension with significant Friedman tests (both $ps < .01$) and significant differences between 1-2 and 1-3 (all $ps \leq .01$). Yet, no significant result was found for the y dimension.

Finally, we performed a rmANOVA on the maximum absolute position error ($MAX(|P_{PE}^{diff}|)$) with dimension and condition as within factors. Testing sphericity with Mauchly's procedure indicated a violation of the assumption in the condition factor (Mauchly's $W = .40$; $p < .05$) and the Dimension * Condition interaction (Mauchly's $W = .04$; $p < .01$). Thus the Greenhouse-Geisser correction was applied in these cases. Dimension and condition main effects were highly significant (F (2, 18) = 165.1, p <.001 and F (1.25,11.23) = 63.2, p <.001) as well as the interaction of both factors (F

(2.28,20.48) = 35.4, p <.001). Pairwise comparisons with Bonferroni correction show that results for all three dimensions differ significantly (all $ps < .01$) and that conditions 1-2 and 1-3 differ significantly (both $ps < .001$). The Dimension * Condition Interaction is mainly due to the results for the y-dimension; here, no substantial differences between the conditions are evident in contrast to the x- and z-dimension.

6.1.3 Discussion of Telemanipulation with Virtual Grasping Points

The bilateral and multilateral experiments showed that the manipulation of a long object through one slave robot arm could be eased significantly by the haptic augmentation approaches. Furthermore, the proposed Cartesian task allocation improved the accuracy during the reorientation and the positioning of a pipe additionally, as it helped to maintain the congruence of pipe end and plug position. The position following of the three devices, the virtual and real grasping points was satisfactory even for roundtrip delays of 40ms.

Overall, the results of the user study indicate that the test subjects showed the weakest performance with unimanual control. Thus, hypothesis H1 is clearly substantiated. This result was found for the path length $path_{PE}$, the RMS of the position error of the pipe end $RMS(P_{PE}^{diff})$ and the maximum absolute position error $MAX(|P_{PE}^{diff}|)$. The time t needed for task completion showed no significant effect. I.e. that the test subjects used in average the same time for all three conditions.

No significant effects have been found in dimension y for the position error $RMS(P_{PE}^{diff})$. This can be explained since, in contrast to dimension x and z, the motions in dimension y are less affected by unintended rotations in the left pipe end (grasping point).

The test subjects achieved similar results for both bimanual approaches. Based on statistical analyzes we did not find evidence supporting hypothesis H2. This might be due to the small sample size ($N = 10$) and hence low statistical power. Additional descriptive tests (Cohen's d) at least indicate small effect sizes, for RMS of the position error $RMS(P_{PE}^{diff})$, as the most meaningful criterion, when comparing both bimanual approaches. Comparing the bimanual approaches revealed a small effect size for the x-dimension ($d = 0.28$) and even a large effect size for the z-dimension ($d = 1.20$) providing initial evidence in favor of the task allocation approach.

6.2 Cooperative Manipulation with Haptic Intention Augmentation (N:N)

In addition to the experiments in Section 5.3, the haptic intention augmentation approach [128] has been evaluated in a space setup. Cooperation among space robots has been studied in several works. In [84], the history and the worldwide planned missions for space robot cooperation was reviewed. The analysis yielded that multi-robot systems have advantages in terms of weight reduction and increase of robustness via redundancy. In [33, 38], i.a. NASA analyzed robot cooperation for space applications from the human-robot interaction perspective.

6.2.1 Experimental Setup

A cosmonaut on the International Space Station (ISS) controlled in cooperation with an operator in Russia the two arms of the humanoid robot SpaceJustin located in Germany. The experiment serves the analysis of the approach's capabilities for the cooperative manipulation of flexible objects and in setups with time delay and week quality of video feedback. The experiments have been conducted in the framework of the KONTUR-2 project [141]. The experimental setup and the communication infrastructure are explained in detail in Appendix A.5.

The two operators of the setup used 2-DoF force feedback joysticks (compare Fig. A.5.1) to control SpaceJustin. Since the master devices have only two DoFs, only a sidewards (x) and vertical (z) motion of the arms could be commanded. The remaining four DoFs of the slave robot were fixed to the initial position by a virtual, spatial spring-damper system. The indexing method was implemented to overcome the workspace limitations by an iterative adaption of the workspace of the master device.

The task was to grasp a flexible object cooperatively and to move it synchronously. This procedure is demanding in that this object was not grasped by the hand but only held via opposing forces in horizontal direction from both slave robot arms. Because of the permanent opposing horizontal forces (in x-direction) that hold the object, the haptic intention augmentation approach was only activated in (vertical) z-direction.

6.2.2 Experiments

In Exp. 6.10, the operators first had to approach the ball from the side and hold it with opposing forces. The motion had to be performed as simultaneously as possible in order to not loose the flexible object. The flexible object had to be moved upwards and right with haptic intention augmentation. This procedure can be comprehended from Exp. 6.10a. The color of the trajectory indicates the time.

Gs_i ($i \in \{1, 2\}$) was 0.3 and Gh_i^0 had the value 0.6. As can be seen in plot Exp. 6.10b, the measured environmental interaction force $F_{1,e,z}$ is in absolute value smaller than the operator H2 interaction force $F_{2,h,z}$. The elasticity of the object as well as the damping and the mass of master and slave device blured the intention of the cooperating operator. The elasticity of the object reduces the quality of the perception of the cooperating operator's intention transmitted through conventional force feedback.

As can be seen in plot Exp. 6.10b, the haptic intention augmentation (forces $F_{1,FB}$ and $F_{2,FB}$) enabled the transmission of more interaction information. The disturbances in the motion resulted from robot workspace nonlinearities, indexing and the elasticity of the manipulated object. Despite that and the high initial vertical distance between the grasping positions that can be seen in plot Exp. 6.10a, the cooperation procedure was successful.

6.2.3 Discussion on Cooperative Manipulation with Haptic Intention Augmentation

Despite the low quality of the visual feedback, the experiments in the space setup showed satisfactory results. The cooperation setup showed to be robust to communication channels, affected by high time delay, jitter and high package loss. In future work, the gener-

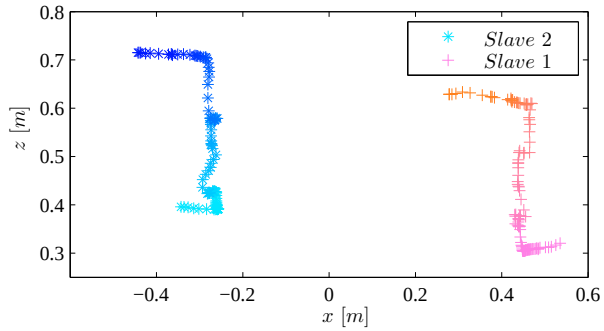

(a) 2D Position Tracking

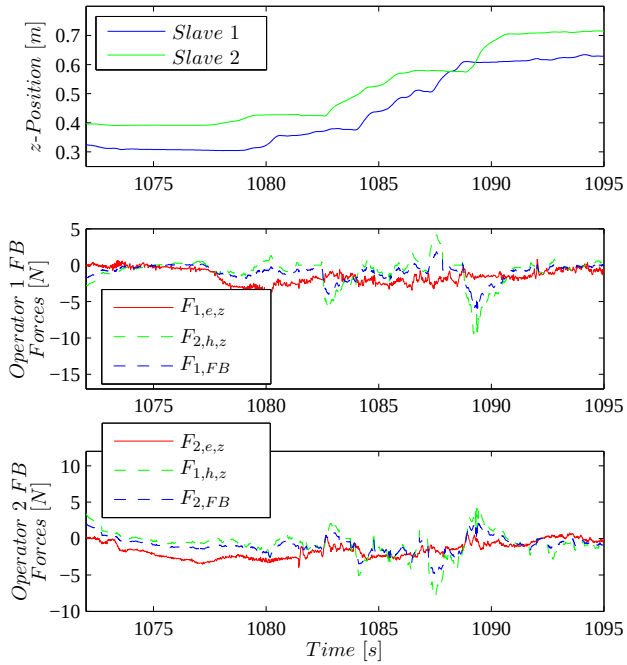

(b) Interaction Forces

Experiment 6.10: 2D Position Tracking with Haptic Intention Augmentation in a space link setup

The haptic intention augmentation (forces $F_{1/2,FB}$) enabled the transmission of more interaction information. The disturbances in the motion resulted from robot workspace nonlinearities, indexing and the elasticity of the manipulated object. Despite that and the high initial vertical distance between the grasping positions, the cooperation procedure was successful.

alization and adaptability of the intention augmentation approach to other tasks should be further analyzed.

6.3 Model-Mediated Teleoperation of WMR (1:N)

The teleoperation of WMR has been in introduced in Section 4.5.2.3. On ground, mobile robots are in general rate controlled in contrast to robot manipulators. In order to compensate for time delay effects to some extent, a local model of the slave robot and/or its environment can provide instantaneous force feedback to the operator. The delayed and the local force feedback can be merged in a multilateral fashion. In the following experiments, the local force feedback is calculated from a virtual environment analogous to Fig. 6.3.1 and Fig. 6.3.2.

6.3.1 Experimental Setup

The first experiments were performed with the RJo joystick presented in Appendix A.5 and a simulation of the lightweight rover unit (LRU) introduced in Appendix A.6. A multi-body simulation of the LRU was implemented in Dymola/Modelica providing a realistic wheel-soil contact in a moon-like 3D-environment. The scene was displayed via SimVis, the visualization toolbox of Dymola/Modelica. The extended model-mediated approach was tested in a real scenario with the LRU.

The map force feedback was determined according to the fictitious force concept in Section 4.5.2.3. The local feedback was calculated from a local map considering the delayed pose of the WMR (compare Fig. 6.3.1).

6.3.2 Experiments

This section presents experiments that serve the evaluation of the passivity control of virtual environments, the comparison of different coupling signals and the analysis of the extended model mediated teleoperation approach.

6.3.2.1 Passivity of Fictitious Force Feedback

The first experiment Exp. 6.11 serves the analysis of the passivity control of the virtual environment and its fictitious force feedback. As can be seen in plot Exp. 6.11, a random motion is commanded to the WMR in a delay-free situation with pure local feedback. Input mode I was applied and considering the system of Fig. 6.3.2, the scaling $\boldsymbol{\sigma}^1$ was set to zero such that only fictitious force feedback from VE was displayed at the master. Especially, in the beginning ($t = [0s, 10s]$) energy is dissipated by PC_{VE^s} since the virtual environment behaves active. The energy plot E_{PP} serving the passivity proof in Exp. 6.11 shows that the passivity controller assures the passivity of the fictitious force feedback.

6.3.2.2 Extended Model Mediated with IMU Force Feedback

The LRU generates the danger map with respect to its horizontal plane without consideration of its own slope. Also, the operator's stereo camera feedback may not provide sufficient information on the slope. Therefore, additional haptic feedback should be provided to the operator to display the inclination of the rover. The WMR controller force or the measured wheel torques contain information on the mobility and slope but also on the WMR's inertia such that the resulting feedback force may be disturbing. Here, a

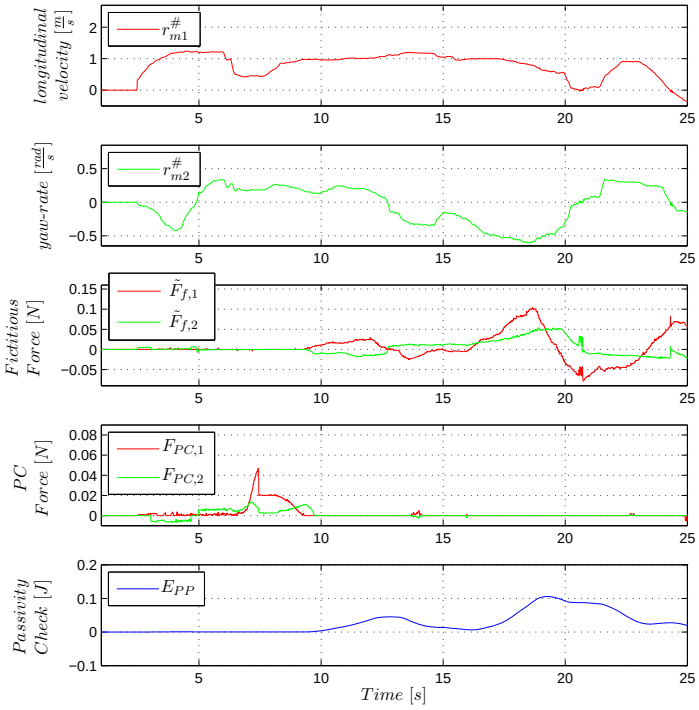

Experiment 6.11: Passivity Proof of Virtual Environment
A random motion is commanded with input mode I to the WMR in a delay-free situation with pure local feedback. Especially in the beginning, energy is dissipated by PC_{VE^s} since the virtual environment behaves active. The positive energy in the passivity proof plot shows that the passivity controller assures the passivity of the fictitious force feedback.

remote feedback generated from the IMU's gravity vector is applied to complement the local model-based feedback [123]. Since the slope measurement through stereo vision is not accurate, the slope can not be well modeled locally in sufficient quality and thus has to be calculated on the remote side.

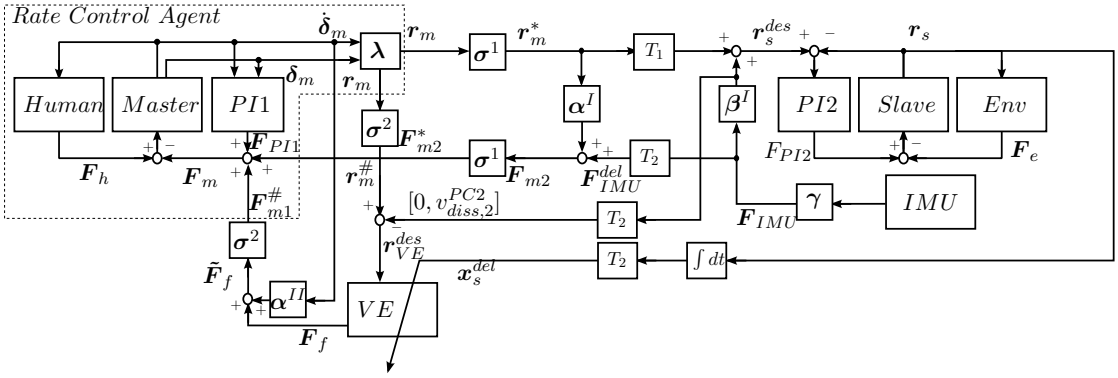

Figure 6.3.1: Signal Flow Diagram of an Extended Model-Mediated Teleoperation Architecture with Passivity Control
The control loop fuses the delayed feedback force F_{m2}^* of the IMU and the local model-based feedback force $F_{m1}^{\#}$. The scalings α^I,α^{II} and β^I represent the passivity controllers' damping. α^I and β^I assure the passivity of the communication channel. The sum of $r_{m,2}^{\#}$ and the delayed integral of $v_{diss,2}^{PC2}$ corrects the mismatch between $r_{m,2}^{\#}$ and $r_{m,2}^*$ resulting from position drift in $r_{m,2}^*$.

Fig. 6.3.1 presents the signal flow diagram of the proposed method applied to rate-controlled WMRs in mode II. The control loop fuses the delayed feedback force F_{m2}^* of the IMU and the local model-based feedback force $F_{m1}^{\#}$. The scalings α^I,α^{II} and β^I represent the passivity controllers' damping. α^I and β^I assure the passivity of the communication channel.

In the position controlled DoF (curvature in the lateral DoF), the passivity controller $PC2$ (β^I) can introduce a position drift in r_s^{des} that can be compensated [8] to some extent. To match the local commanded curvature $r_{m,2}^{\#}$ to r_s^{des}, the velocity $v_{diss,2}^{PC2}$ dissipated by $PC2$ (β^I) needs to be considered in $r_{m,2}^{\#}$. Therefore, a local curvature command to the VE $r_{VE,2}^{des}$ results from the sum of $r_{m,2}^{\#}$ and the delayed integral of $v_{diss,2}^{PC2}$ over time:

$$r_{VE,2}^{des}(k) = r_{m,2}^{\#}(k) + \sum_{i=0}^{k} v_{diss,2}^{PC2}(i - T_2). \tag{6.1}$$

The overall network representation of the extended model-mediated teleoperation architecture for WMRs is depicted in Fig. 6.3.2. Due to the longitudinal rate-control architecture, a RCA $\Lambda 1$ is considered and the scaling subsystems $\boldsymbol{\sigma}^1$ and $\boldsymbol{\sigma}^2$ are integrated.

In contrast to the local VE force feedback, the force F_{IMU} is not affected by discretization or model updates. Since, in addition, the energy exchange with the IMU subsystem is passive, no PC is required for that one-port network. Considering the car-like interface with longitudinal velocity v_x and curvature κ, the passivity of the IMU

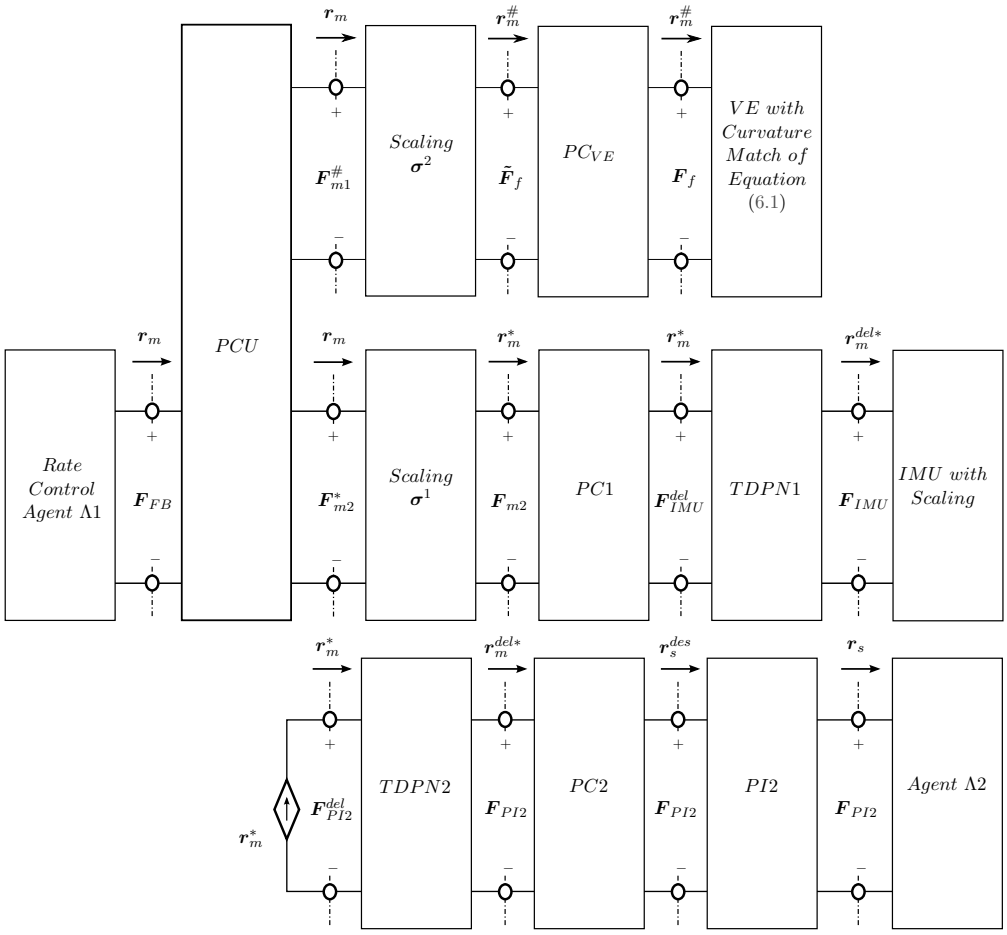

Figure 6.3.2: Network Representation of an Extended Model-Mediated Teleoperation Architecture for Rate Control with Passivity Control
The PCU fuses the local fictitious force feedback of the VE and the remote IMU feedback. In contrast to the VE, the IMU subsystem requires no passivity controller.

subsystem is not obvious. But, analyzing the decoupled interface of v_x and yaw-rate $\dot{\psi}$ ($\dot{\psi} = \kappa v_x$), it is clear that no energy can be introduced by the IMU subsystem that has the energetic behavior of a potential energy storage. Even, the initial potential energy which appears if the WMR starts on a high place is accounted in the passivity criterion.

The following experiments have been performed with the real DLR LRU (see Fig. 6.3.3) and the DLR Force-Feedback Joystick. The mode II curvature command was applied. The control software has been implemented in Matlab/Simulink with a simulated constant delay in a UDP communication. The scalings $\sigma_{1,1}$ and $\sigma_{2,1}$ were set to 4, such that the maximum deflection of 20 degrees was mapped to $1.4m/s$ longitudinal velocity. Whereas the scaling $\sigma_{1,2}$ and $\sigma_{2,2}$ were chosen as 1.5, such that maximally a curvature of approximately $0.5/m$ could be commanded. Since the joystick's moment of inertia equals $0.0003\frac{kg}{m^2}$ and $\gamma_1 = 1$, $\lambda_1 = 10$, a damping of $b_1 = 0.07\frac{Nms}{rad}$ and a stiffness of $k_1 = 0.1\frac{Nm}{rad}$ were chosen.

In experiment Exp. 6.12, a longitudinal motion is commanded to the WMR which is standing on an inclined surface in front of an obstacle as depicted in Fig. 6.3.3.

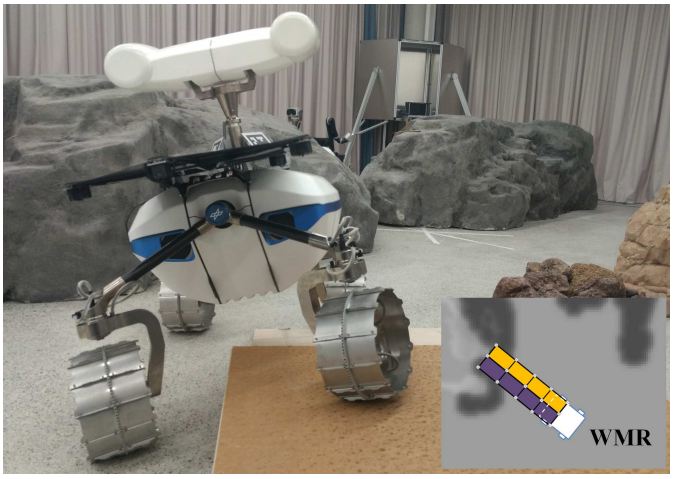

Figure 6.3.3: LRU Scenario with Grid Map and Polygon
The LRU drives on a slope into a canyon-like structure. The top-view visualizes the overlap of polygon and obstacles in the danger map.

Especially, when driving downwards, the IMU feedback and the fictitious feedback might act in opposing directions. Here, the force scalings were designed such that $max(\tilde{F}_{f,1})/max(F_{IMU,1}) = 2$. Therefore, the fictitious force feedback $\tilde{F}_{f,1}$ outweighs the IMU feedback $F_{IMU,1}$ significantly when coming close to the obstacle. In addition, a nonlinear, obstacle distance dependent force weight in the VE force generation can be considered. Also, a top view visualization of the LRU motion and the polygons in the danger map support the operator's awareness of impeding obstacles. The fictitious force feedback $\tilde{F}_{f,1}$ and the IMU feedback $F_{IMU,1}$ have different signs such that the perception of the obstacle through $\tilde{F}_{f,1}$ is constrained ($t = [0s, 30s]$). It can be analyzed from Fig. 6.12 that the operator is pushed away from the obstacle and that the IMU feedback pushes the operator down the slope during standstill ($t = 0s$). The velocity command $r_{s,1}^{des}$ as well as the force feedback $F_{FB,1}$ are not heavily affected by the passivity controllers $PC1$ and $PC2$ respectively such that the current velocity of the slave $r_{s,1}$ is close to the commanded value $r_{s,1}^{des}$. The energies in the passivity controlled TDPN1 and TDPN2 are purely positive which confirms the passivity of the communication channels. The velocity and force signals closing the control loop do not show any oscillations which promises a good operating performance despite a roundtrip-delay of 400ms. Therefore, the setup can be applied even with a high delay KU-Forward link with geostationary satellites. Here, we present a proof of concept in a simplified environment. In case of higher slopes which are within the maneuverability range of the WMR, the IMU scaling can be adjusted without violating the passivity condition.

In experiment Exp. 6.13 ($\gamma_2 = 0$, $\lambda_2 = 1$, $b_2 = k_2 = 0$) a combined longitudinal and lateral motion was performed at 800ms roundtrip-delay. The LRU is driving down a slope and enters a canyon-like structure (compare Fig. 6.3.3). The curvatures $r_{s,2}^{des}$ and $r_{VE,2}^{des}$ equal thanks to the functionality of equation (6.1). Therefore, the local VE provides reasonable force feedback in the lateral DoF. Especially in free motion, the IMU feedback is clearly perceived by the operator. The force plots in Fig. 6.13 show that, as desired, the obstacles are displayed with higher priority to the operator.

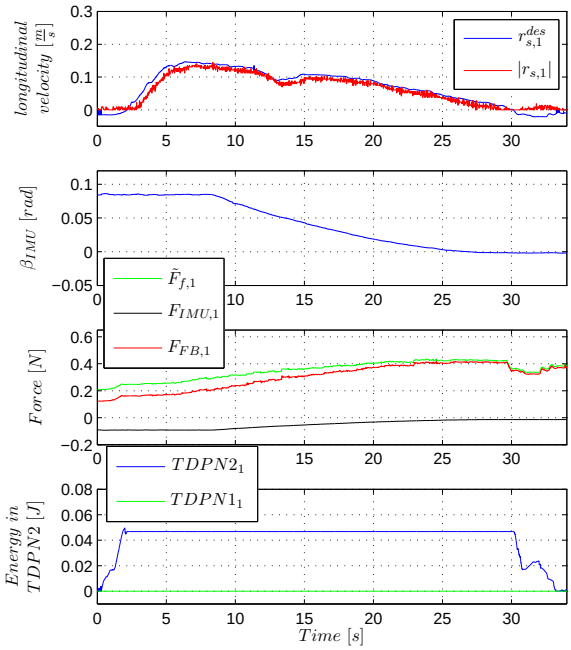

Experiment 6.12: Pure Longitudinal Motion at 400ms Roundtrip-Delay

Therefore, the fictitious force feedback $\tilde{F}_{f,1}$ outweighs the IMU feedback $F_{IMU,1}$ significantly when coming close to the obstacle. The fictitious force feedback $\tilde{F}_{f,1}$ and the IMU feedback $F_{IMU,1}$ have different signs such that the perception of the obstacle through $\tilde{F}_{f,1}$ is constrained ($t = [0s, 30s]$). It can be analyzed from Fig. 6.12 that the operator is pushed away from the obstacle and that the IMU feedback pushes the operator down the slope during standstill ($t = 0s$). The velocity command $r_{s,1}^{des}$ as well as the force feedback $F_{FB,1}$ are not heavily affected by the passivity controllers $PC1$ and $PC2$ respectively such that the current velocity of the slave $r_{s,1}$ is close to the commanded value $r_{s,1}^{des}$. The energies in the passivity controlled TDPN1 and TDPN2 are purely positive which confirms the passivity of the communication channels.

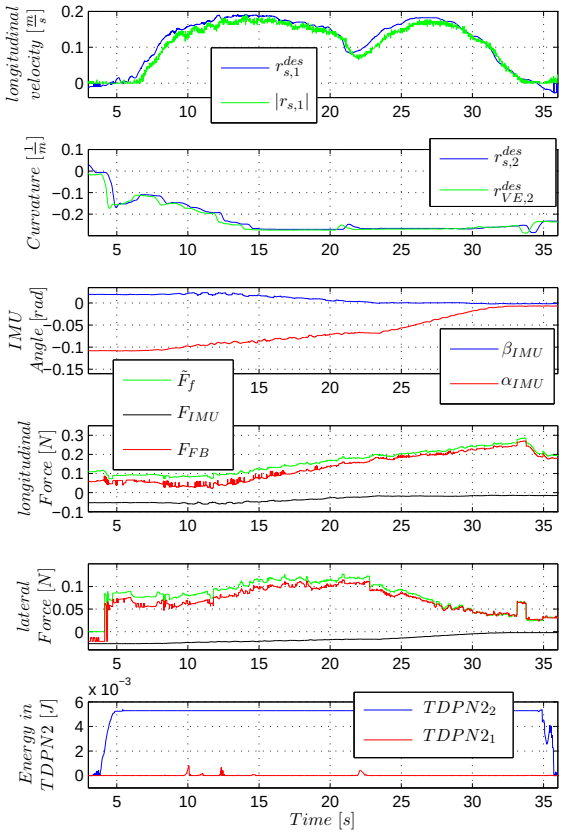

Experiment 6.13: Combined Longitudinal and Lateral Motion at 800ms Roundtrip-Delay
The LRU is driving down a slope and enters a canyon-like structure. Especially in free motion, the IMU feedback is clearly perceived by the operator. The force plots in Fig. 6.13 show that, as desired, the obstacles are displayed with higher priority to the operator. Again, the passivity controllers $PC1$ and $PC2$ do not seriously disturb the velocity and curvature commands r_s^{des} and the force feedback F_{FB}. The positive energy plots of the communication channel TDPN2 prove the passivity despite time delay.

Again, the passivity controllers $PC1$ and $PC2$ do not seriously disturb the velocity and curvature commands r_s^{des} and the force feedback F_{FB}. The positive energy plots of the communication channel TDPN2 prove the passivity despite time delay.

6.3.3 Discussion on Model-Mediated Teleoperation of WMR

In this section, it could be shown that the MPMT is an adequate tool for the control of wheeled mobile robots. The lateral motion control through curvature demand was investigated. Furthermore, the passivity of the fictitious force feedback calculated from a virtual environment could be guaranteed via time domain passivity control. The virtual environment model was applied in an extended model mediated teleoperation setup with merged local and remote force feedback which promises better performance than pure delayed or local feedback. In future work, the rate control approach should be tested in combination with the time delay control Approach 3 which promises higher position accuracy.

6.4 Discussion on the Experimental Evaluation

The benefits of the virtual grasping point and role distribution concept, evaluated in the user study, underline the usefulness of haptic augmentation concepts. Further experiments proofed the robustness with respect to negative communication properties as delay, jitter and package loss. The successful application of the MPMT in an experiment involving a wheeled mobile robot underlined the modularity and adaptability of the approach.

Considering the presented applications, the model independence of the MPMT, which is crucial for high modularity and universality of the approach, did not lead to increased conservatism. The discretization effects have the biggest influence on the controller parametrization, since the continuous controller itself is intrinsically passive. As for any other control approach, a local or controller damping has to be implemented, if the hardware intrinsic damping is not sufficient to neutralize the discretization effects. Furthermore, since the TDPA assures passivity of the communication channel in the time domain through a variable damping, the framework is not conservative. Thus, overall, the MPMT can be regarded as a control approach with low conservatism.

Chapter 7

Conclusion

The toolbox for passivity-based multilateral teleoperation (MPMT) depicts a framework-like guideline for the design of multilateral robotic systems. Due to its modularity various interactions between electronically coupled robotic agents can be set up in a highly adaptive manner. The majority of the approaches collected in a thorough literature review can be designed with the MPMT. From the application point of view, i.a. training scenarios, rehabilitation and cooperative setups can be realized. With the tools of the (MPMT), these applications can be in detail optimized regarding ergonomics and transparency with novel haptic concepts that provide e.g. virtual grasping points, role distribution among agents or haptic intention augmentation.

The network representation as the main design tool of the MPMT allows for an intuitive energy-based analysis of the system behavior. The transfer of the mechanical energy concepts in teleoperation systems is obvious to the engineer and can be straightforward translated into an electrical circuit via the respective analogies. The modular nature of the passivity theorem allows for the separate energy analysis of the network subsystems. Thus, even different tools for passivity analysis can be applied in one system. For example, the time delay can be controlled via the time domain passivity approach or the wave variables method without influence on the other parts of the multilateral system. Within this thesis, new network modules as the track connecting two agents bilaterally, the PCU that allows the fusion of different force feedback signals, the projection subsystems PR for the virtual grasping point methods, scaling subsystems and the network representation of rate control agents have been introduced and their passivity has been discussed.

With these new modules a variety of multilateral haptic augmentation concepts were developed, implemented and validated. Therefore, different coupling setups with varying numbers of master and slave devices in 1:N, N:1 and M:N configurations were designed. With a role distribution concept, it was shown that training scenarios and Cartesian task allocations can be realized through the MPMT. The virtual grasping point and the task allocation concept as well as the haptic intention augmentation for cooperative setups were tested in a delayed scenario. Also, an extended model-mediated teleoperation approach was proposed and tested with a delayed communication channel.

Besides the contribution of novel concepts for multilateral control, this thesis provided improvements of standard passivity controlled bilateral architectures in terms of conservatism and thus transparency. It was shown that time domain passivity control

can be applied not only for the control of delayed communication but also to render a controller structure passive. A passivity control for 2-*Channel* architectures with measured force feedback has been proposed that allows for far higher feedback gains and therefore promises to improve the feeling of immersion to the operator compared to the existing passive or absolutely stable solutions. Based on that, a 3-*Channel* architecture with merged computed and measured force feedback has been implemented. Also, a novel passivity control for the 4-*Channel* architecture has been proposed.

A variety of experiments and applications have been presented in this thesis. Each proposed concept was thoroughly analyzed through experiments. Multi-DoF experiments and a user study allow the evaluation of a set of novel concepts in a realistic scenario. The teleoperation from the International Space Station hint that the control approaches are meaningful in case of communication channels that are limiting the quality of visual and haptic feedback.

In future work, the extended model-mediated teleoperation approach should be applied to robotic manipulation and the multilateral approaches have to be validated in further user studies. Furthermore, the novel energy reflection based TDPA has to be extended to 3- and 4-Channel architectures and an analytical calculation of the storage energy in the monitoring unit should be tested. Due to the chronological order of developments, among others the energy reflection based TDPA has not yet been applied in complex multilateral setups, which remains for future work.

This thesis presented several novel technical solutions to increase the dexterity, robustness and reliability of robotic applications through multilateral control. The virtual grasping point method for increased rotational precision can bring benefits in general teleoperation applications but also especially to medical robotics since medical probes can be manipulated with dual-hand precision. Furthermore, the virtual grasping point method for under-actuated devices additionally extends the force feedback capabilities of those low-cost devices and thus makes a high-end teleoperation setup more achievable. The intention augmentation concept for cooperative applications is especially valuable in civil engineering constructional tasks and the extended model-mediated teleoperation of mobile robots can take humans out of the danger zone for example when applied to teleoperated food supply trucks in war areas.

Appendix A

Experimental Setups

A.1 1DoF Master-Slave-System

The 1DoF Master-Slave-System developed by SENSODRIVE GMbH [151] (compare Fig. A.1.1) allows the precise evaluation of new control methods since the hardware produces only negligible disturbances. The direct drive brushless DC motors with a nominal torque of 0.7Nm are optimized for haptic applications and equipped with a high-precision position sensor. A 10bit torque sensor with dynamic range of 1.7Nm can be attached to the output between motor and handle. The product data is listed in Table A.1. The control software runs on a real time system (QNX). For the communication with the hardware a s-function has been developed for the Real-Time Workshop of Matlab/Simulink.

Figure A.1.1: 1DoF Master-Slave-System [151]

Dimensions (WxHxD)	350x215x280 mm
Max. Torque	2Nm
Max. force at the handle	12N
Max. position resolution	16383 Ink/360°
Supply voltage	24...48V
Communication	CAN
Implemented effects	Spring stiffness, damping, friction

Table A.1: SENSODRIVE Master-Slave-System

Bilateral Setup In bilateral experiments, two Master-Slave-Systems are connected to one Peak CAN card. The control software is compiled for QNX and runs in real-time with 1kHz sampling rate. The communication between hardware and software and between master and slave is delayed by less than 1ms.

Multilateral Setup In multilateral experiments, two devices are connected to one QNX machine each. The delay in the network link between two QNX systems is lower than one sampling step of 1ms. The two Simulink models communicate via UDP.

A.2 7DoF DLR Light Weight Robots

The redundant DLR Light Weight Robot (LWR [50]) has seven joints and is built in a modular way. A joint module contains a brushless DC motor, Harmonic Drive Gears, a torque sensor and two position sensors. Its Robodrive ILM motors have been specially developed for the LWR. The robots size, power and manipulation capabilities have been designed to match those of a human arm (compare Table A.2). The light weight of the LWR is achieved by the carbon-fiber structure. The software can run on RT Linux or VxWorks systems. A passivity-based control framework for position, torque and impedance control for flexible joint robots has been designed in [4].

Table A.2: DLR Light Weight Robot Specifications

Dynamic mass	14kg
Max. Payload	14kg
Max. Joint Speed	120°/s
Number of Axes	7 revolute joints
Maximum reach	936mm
Power supply	48 V DC
Control	Position-, Torque-, Impedance Control
Sampling Rates	40kHz current 3kHz joint 1kHz cartesian

A.2.1 DLR SpaceJustin

The humanoid upper body DLR SpaceJustin (see Fig. A.2.1) is build of two LWR arms, a torso and a head. The head of SpaceJustin can be moved in two degrees of freedom and is equipped with two Prosilica cameras. SpaceJustin is equipped with two DLR HitHand II with five identical fingers and an aluminum open skeleton structure. Further product data is listed in Table A.3.

Table A.3: DLR HitHand II Specifications

Number of fingers	5
Joints per finger	4
DoFs per finger	3
Active finger tip force	10N
Weight	1.5kg
Joint velocity	$\approx 360°/s$

A.2.2 DLR HUG

The DLR HUG, depicted in Fig. A.2.2, is a haptic input device with two DLR LWR. The physical data is listed in Table A.4. In addition to the kinesthetic input device, a

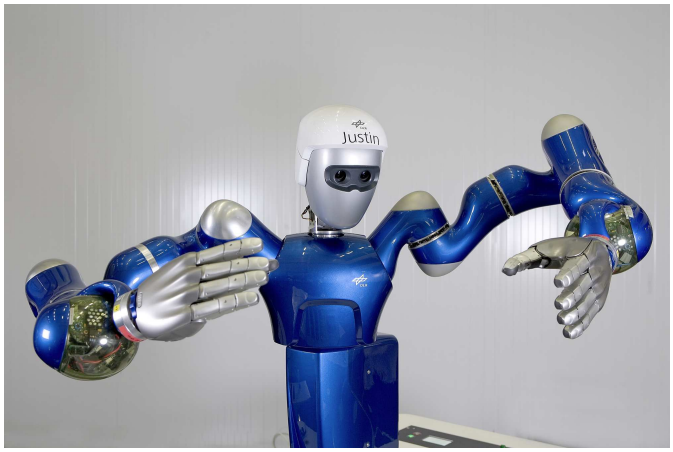

Figure A.2.1: DLR SpaceJustin

pair of cyberglove serves the control of the finger motion. Also, the telepresence station is equipped with the head mounted display (HMD) nVisorSX60. The head tracking via a VICON tracking system allows the control of the slave robot's head motion. A deadman switch is implemented as a foot pedal. Another three-pedal interface allows to move e.g. the torso of SpaceJustin. The HUG robots are applied as impedance type devices. Via a 6DoF FT-sensor and feed-forward control, the weight of the LWR can be artificially reduced such that backdrivability is improved and the robot can be easily moved. The big advantages of the HUG design are high feedback forces and a big interaction workspace.

Figure A.2.2: DLR HUG Haptic Input Device

Table A.4: DLR HUG Specifications

Dynamic mass	2x14kg
Peak force	2x150N
Maximum span	2x936mm
Number of DoF	2x7 revolute joints
Sensors in each joint	2 position sensors 1 torque sensor
Additional sensors	2x6DoF FT-Sensor

A.3 HUG - Space Justin

The control of SpaceJustin (see section A.2.1) via the HUG (see section A.2.2) promises good operator immersion in terms of workspace configuration. This master-slave combination has been applied for example in the 6DoF experiments on the haptic intention augmentation approach in section 5.3. Both slave robot hands grasped one stiff long object (pipe) at the two end positions (see Fig. A.3.1). The two operators used one arm of HUG each as an input device. In the experimental evaluation of virtual grasping point and task allocation concept in section 6.1, two arms of the HUG and the left arm of SpaceJustin have been applied (see Fig. 5.1.2 in section 5.1.1). In both applications, the master side controller was implemented on the RT Linux host of HUG and the slave side controller ran on the RT Linux host of SpaceJustin. The real time models ran at a sampling rate of 1kHz. The communication between the host computers was established with the UDP protocol.

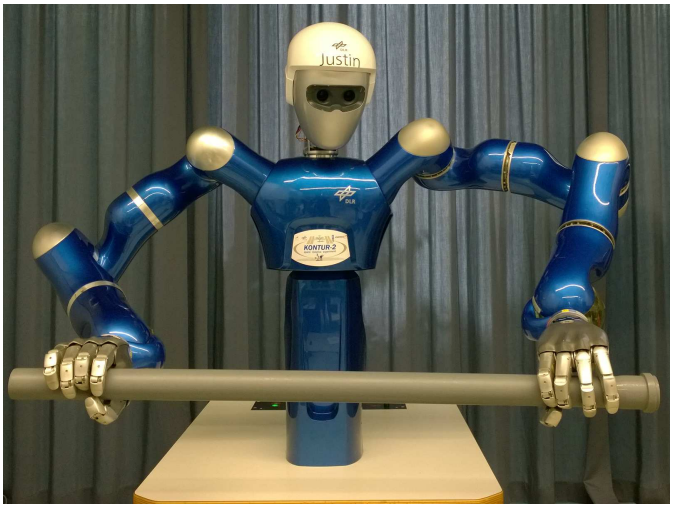

Figure A.3.1: DLR HUG Haptic Input Device

A.4 Omega.7 - HUG

The underactuated device Omega.7 has been applied for the teleoperation of the HUG in a set of experiments of section 5.1. The Omega.7 of force dimension [26], depicted in Fig. A.4.1, is a 7DoF haptic input device. In the Omega.7 device, the three translational but not the three rotational degrees of freedom are actuated. The seventh DoF is an actuated grasping input device in the handle. The device communicates via a standard USB 2.0 connection with the QNX host machine at refresh rates up to 4kHz. Further specifications are listed in Table A.5.

In the experiment, the QNX host computer communicated with the HUG RT Linux host via UDP protocol. The control software of master and slave have been implemented on the slave host. The real time models ran at a sampling rate of 1kHz.

Figure A.4.1: Force Dimension Omega.7 [26]

Workspace	Translation	⌀ 160mmx220mm
	Rotation	240°x140°x180°
	Grasping	25mm
Forces	Translation	12.0N
	Grasping	±8N
Resolution	Translation	<0.01mm
	Rotation	0.09°
	Grasping	0.006mm
Dimension	Height	270mm
	Width	300mm
	Depth	350mm
Power	110V - 240V	

Table A.5: Omega Specifications

A.5 Space Link Setup

In the experiment on the evaluation of the haptic intention augmentation concept with space link (see section 6.2), the two human operators used one RokvissJoystick (DLR RJo, Fig. A.5.1) each to control the arms of SpaceJustin. The humanoid robot was located in Oberpfaffenhofen, Germany. As depicted in Fig. A.5.3, a cosmonaut controlled its right arm from ISS and an operator in Saint-Petersburg teleoperated the left arm.

The master side of the control software was implemented on the on-board computer of the DLR RJo. The host computer of SpaceJustin (see Fig. A.5.2) is a RT Linux system that runs the slave side controller. The real time models ran at a sampling rate of 1kHz.

The DLR RJo (see Fig. A.5.1) was developed for the KONTUR-2 project [141] that serves the feasibility analysis of teleoperation of robots for planetary exploration by an operator from a spacecraft and the related weightlessness effects on sensorimotor performance [179]. For the employment on the ISS, the joystick had to be ISS-qualified with EMC, electical, thermal, structural, offgassing and flammability tests. The DLR RJo has an ethernet interface. Additional technical data is listed in Table A.6.

The communication from Oberpfaffenhofen (Germany) to Saint-Petersburg was a standard internet connection (Fig. A.5.4, 70ms roundtrip delay). The link to ISS in-

Figure A.5.1: DLR RJo

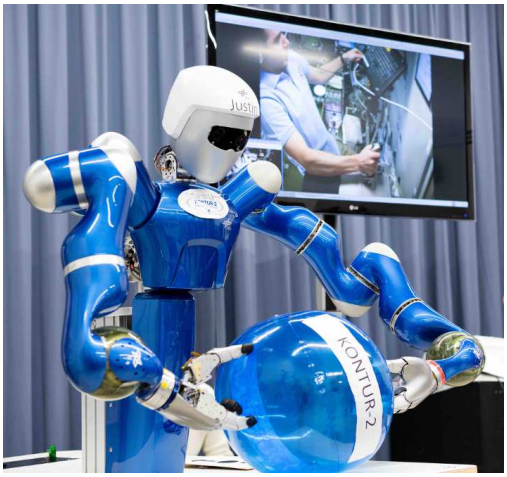

Figure A.5.2: DLR SpaceJustin with Flexible Object and Cosmonaut on ISS

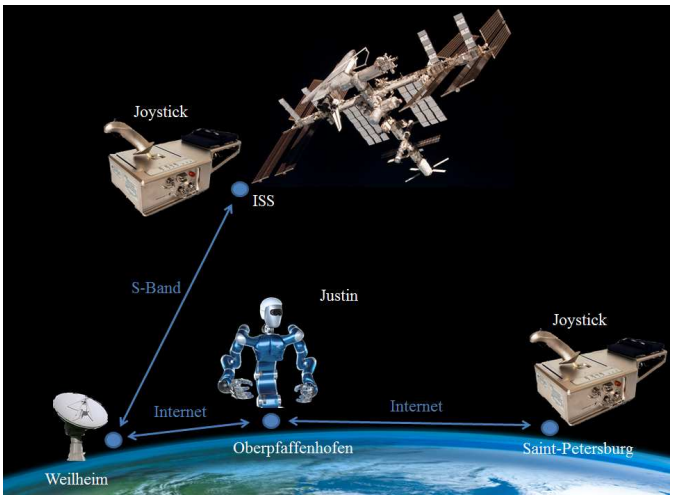

Figure A.5.3: Communication Infrastructure

cluded a high-speed internet link from Oberpfaffenhofen to Weilheim (Germany) and a S-band communication to the ISS (Fig. A.5.5, 25ms roundtrip delay). The communication was affected by delay, jitter and package loss. As can be analyzed from Fig. A.5.4 and Fig. A.5.5, the ISS-Link had less delay and package loss than the link to Russia. Still, the bandwidth of the ISS-Link is more limited.

Table A.6: DLR RJo Specifications

Max. Force at the handle	15N
Workspace	2x±20°
Number of DoF	2
Sensors in each joint	2 position sensors 1 torque sensor
Additional sensors	2x6DoF FT-Sensor

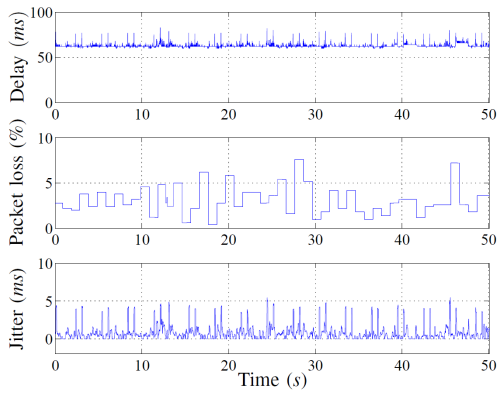

Figure A.5.4: Communication Properties Internet-Link to Russia [7]

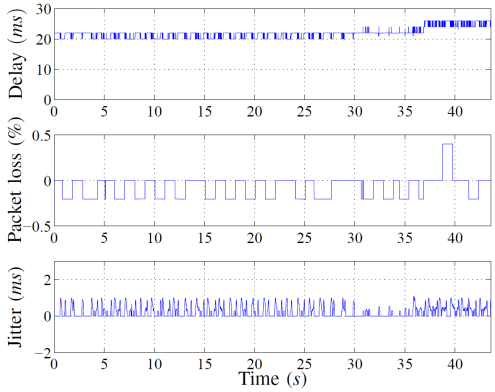

Figure A.5.5: Communication Properties ISS-Link [7]

A.6 Lightweight Rover Unit

The DLR Lightweight Rover Unit (LRU, see Fig. A.6.1) is the prototype of a mobile robot tailored for the exploration of unknown, rough and hard-to-reach terrain. Its envisaged applications are planetary exploration and terrestrial search and rescue scenarios. A very high traffic ability, terrainability and overall maneuverability performance are achieved through advanced kinematics and the unique combination of active and passive chassis elements. The lightweight design, a total mass of 30 kg and a payload of 5kg renders the LRU a promising concept for any future lunar mission. A detailed list of the LRU's specifications can be found in Table A.7.

The LRU is equipped with a monochrome stereo-camera set and a color camera on a pan-tilt unit (compare Fig. A.6.2). The stereo-camera and the Semi-Global-Matching-Algorithm (SGM) allow the WMR to perceive its environment in 3D. Thus, the rover is able to calculate area maps and to drive to predetermined waypoints in unknown and rough terrain autonomously.

Figure A.6.1: DLR LRU

Figure A.6.2: Pan-Tilt Camera Unit of the LRU

Table A.7: DLR LRU Specifications

Size	114cm x 74cm x94cm
Weight	ca. 30kg
Additional Payload	5kg
max. Velocity	1.11m/s
max. Velocity	28.8V, 5Ah, >120min
DoFs	4 steering actuators 4 traction actuators 2 serial elastic joints 2 pan tilt joints
Sensors	Inertial Measurement Unit FPGA-based stero vision

Nomenclature

$1Ch$ 1-*Channel*

$2Ch$ 2-*Channel*

$3Ch$ 3-*Channel*

$4Ch$ 4-*Channel*

AA Authority Allocation

BIBO Bounded-Input Bounded-Output

CC Communication Channel

CP Consensus Problem

DoF Degree of Freedom

FT Force-Torque

fps Frames per Second

G Grasping Point

HMD Head Mounted Display

HUG Haptic User Device

HMI Human Machine Interface

IoT Internet of Things

IPC Intrinsically Passive Controller

ISS International Space Station

JAXA Japan Aerospace Exploration Agency

khz Kilohertz

L2R Left To Right

LRU Lightweight Rover Unit

LWR Light Weight Robot

MISO Multi-Input-Single-Output

MMMS Multi-Master-Multi-Slave

MMSS Multi-Master-Single-Slave

MTF Modulated Transformer

NASA National Aeronautics and Space Administration

PC Passivity Controller

PCU Power Control Unit

PCS Passivity Controlled Subsystems

PE Pipe End

PF Position-Force

PF_{comp} Position-Computed Force

PF_{meas} Position-Measured Force

PHCD Port-Controlled Hamiltonian System with Dissipation

PO Passivity Observer

PP Position-Position

PR Projection

PSPM Passive Set-Position Modulation

R2L Right To Left

RCA Rate Control Agent

RJo Rokviss Joystick

RMS Root Mean Square

SISO Single-Input-Single-Output

SGM Semi-Global-Matching-Algorithm

SMC Sliding-Mode Control

SMMS Single-Master-Multi-Slave

TA Task Allocation

TCP Tool Center Point

MPMT Methodology for Passivity-based Multilateral Teleoperation

TDPA Time Domain Passivity Approach

TDPN Time Delay Power Networks

TSP Tracking Synchronization Problem

UAV Unmanned Air Vehicle

UDP User Datagram Protocol

VE Virtual Environemnt

UGV Unmanned Ground Vehicle

VG Virtual Grasping Point

VP Virtual Pipe

WMR Wheeled Mobile Robot

List of Figures

1.2.1 Single-Master-Multi-Slave: Sequential Setup 3
1.2.2 Single-Master-Multi-Slave: Synchronous Motion Setup 3
1.2.3 Single-Master-Multi-Slave: Cooperative Manipulation Setup 4
1.2.4 Single-Master-Multi-Slave: Extended Model-Mediated Setup 4
1.2.5 Multi-Master-Single-Slave: Training Setup 5
1.2.6 Multi-Master-Single-Slave: Rotational Precision Setup 5
1.2.7 Multi-Master-Multi-Slave: Rotational Precision Setup for Cooperative Manipulation 5
1.2.8 Multi-Master-Multi-Slave: Intention Augmentation Setup 5

2.1.1 Signal Flow Diagram of the PF_{comp} Architecture without Delay 11
2.1.2 Signal Flow Diagram of the PF_{comp} Architecture with Delay 13
2.1.3 Signal Flow Diagram of the PF_{meas} Architecture with Delay 14
2.1.4 Signal Flow Diagram of the PP Architecture with Delay 15
2.1.5 Signal Flow Diagram of a 3-*Channel* Architecture with Delay 15
2.1.6 Signal Flow Diagram of a 4-*Channel* Architecture with Delay 16
2.1.7 2-port of a H-Matrix Representation 17
2.1.8 Linear Fraction Representation of a General Control Configuration [159] 17
2.1.9 2-port of a RLC Circuit 19
2.1.10 Mass, Damper and Spring Diagram 19
2.1.11 Energy Flow at a 1-port Network 20
2.1.12 Energy Flow at a 2-port Network 20
2.1.13 Mechanical Representation of a PI controller 21
2.1.14 Electrical Representation of a PI controller 21
2.1.15 Signal Flow Diagram of a Bilateral Teleoperator without Delay 22
2.1.16 Mechanical 1DoF Model of a Bilateral Teleoperator 22
2.1.17 Electrical 1DoF Model of a Bilateral Teleoperator 22
2.1.18 Bond Graph of Ideal Operation 23
2.1.19 Bond Graph of Human-Master Interaction 24
2.1.20 Bond Graph of Slave-Environment Interaction 24
2.2.1 Multi-Master-Single-Slave: Virtual Grasping Point Concept 25
2.2.2 Multi-Master-Single-Slave: Nullspace Control 25
2.2.3 Multi-Master-Single-Slave: Cooperation of two Separate Teleoperators . 26
2.3.1 Bond Graph of the Impedance Adaption of the Transmission Line [166] . 29
2.3.2 Bilateral Teleoperator with Wave Variables Approach in Network Representation 30
2.3.3 Time Domain Passivity Approach 32
2.3.4 Energy Flow at a 2-port Network with Time Delay 32

2.3.5 Track with PF_{comp} Architecture and TDPN Approach 34
2.3.6 Track with PP Architecture and TDPN Approach 35
2.3.7 Bond Graph Representation of a Trilateral Teleoperation System 37
2.3.8 One Degree of Freedom Feedback Configuration [159] 40
2.3.9 S/T Mixed Sensitivity Optimization in Standard Form [159] 41
2.3.10 Ring Network 42
2.3.11 Connected Network 42
2.3.12 Hub Network 42
2.4.1 Fully Connected Topology 47
2.4.2 Arbitrary M:N Topology 47
2.4.3 Star Topology 47
2.4.4 Line Topology 47

3.3.1 Signal Flow Diagram of a Trilateral PF_{comp} Architecture without Delay 61
3.3.2 Network Representation of a Trilateral PF_{comp} Architecture without Delay 61
3.3.3 Generalized Modular Framework [127] 62
3.3.4 Signal Flow Diagram of a Power Control Unit 62
3.3.5 Master Agent for Teleoperation Setups with Position Control 64
3.3.6 Master Agent Preserving Passivity in Teleoperation with Rate Control . 65
3.3.7 Network Representation of a Track with PF Architecture 66
3.3.8 Network Representation of PP Architecture 68
3.3.9 Network Representation of a Bilateral n-DoF Teleoperation System . . . 70
3.3.10 Simplified Network Representation of a Bilateral Multi-DoF Tel. System 70
3.4.1 Network Representation of a Pseudo Trilateral Line Topology without $Track$ $\Gamma 3$ 72
3.4.2 Network Representation of a Pseudo Trilateral Line Topology without $Track$ $\Gamma 1$ 73

4.1.1 Energy Observation and Passivity Control of Approach 1 79
4.1.2 Energy Observation and Passivity Control of Approach 2 80
4.1.3 Network representation of a Track with PP Architecture with Time Delay Control Approach 2 81
4.1.4 Assembly of Tracks to a Multilateral System 84
4.1.5 Energy Observation and Passivity Control Considering Energy Reflection (Approach 3) 89
4.1.6 Time Delay Control Approach 3 for a PF_{comp} Architecture 90
4.1.7 Comparison of Real and Ideal Potential Energy Storages 91
4.1.8 Technical Setup of Comparative Study 97
4.2.1 Network Representation of a PF architecture without Time Delay . . . 102
4.2.2 Network Representation of the 1-port Teleoperator Proposed in [180] . . 103
4.2.3 Network Representation of a Passive PF_{meas} Architecture without Time Delay 104
4.2.4 Network Representation of a passive PF_{meas} Architecture with Time Delay 107
4.3.1 Network Representation of a 3-$Channel$ Architecture with Passivity Control 111
4.3.2 Passive 3-$Channel$ Architecture with Time Delay 114
4.4.1 Free Motion 118

4.4.2 Contact . . . 118
4.4.3 Network Representation of a 4-*Channel* Architecture with Passivity Control . . . 119
4.4.4 Network Representation of a 2-*Channel* Architecture . . . 120
4.4.5 Passive 4-*Channel* Architecture with Time Delay . . . 123
4.5.1 Exemplary Height Map . . . 127
4.5.2 Grid Map with Curvature Polygon . . . 128
4.5.3 Curves of Weighting Functions at Different Velocities . . . 130
4.5.4 Signal Flow Diagram of a WMR Teleoperator with Computed Force Feedback . . . 132
4.5.5 Network Representation of a WMR Teleoperator with Computed Force Feedback and Time Delay . . . 133
4.5.6 Signal Flow Diagram of a WMR Teleoperator with Fictitious Force Feedback . . . 133
4.5.7 Network Representation of a WMR Teleoperator with Measured Force Feedback and Time Delay . . . 134
4.5.8 Signal Flow Diagram of an Extended Model Mediated Teleoperation Architecture for WMRs . . . 135
4.5.9 Network Representation of an Extended Model Mediated Teleoperation Architecture for WMRs . . . 136

5.1.1 Multi-Master-Multi-Slave: Rotational Precision Setup for Cooperative Manipulation . . . 143
5.1.2 Slave Robot Grasping Pipe . . . 144
5.1.3 Operator with Two Masters and Virtual Pipe . . . 145
5.1.4 Device Coupling with Virtual Grasping Point Concept . . . 146
5.1.5 Multilateral System with Virtual Grasping Point Projection . . . 152
5.1.6 MMSS Concept for Underactuated Devices . . . 153
5.1.7 Interaction between Master M_R and M_L with one Spring . . . 156
5.1.8 Interaction between Master M_R and M_L with two Springs . . . 156
5.1.9 Multilateral Setup for Underactuated Devices with Additional Spatial Springs . . . 157
5.1.10 Kinematically Coupled Slaves in a SMMS System . . . 161
5.1.11 Single-Master-Multi-Slave System for Cooperative Slave Grasping . . . 164
5.1.12 Single-Master-Multi-Slave System for Cooperative Slave Grasping with Additional Spatial Springs . . . 165
5.1.13 Coupled Manipulation via MMMS . . . 167
5.1.14 Design Goal of Second Vector . . . 168
5.1.15 Network Representation of the Dual-Master-Dual-Slave . . . 171
5.1.16 Network Representation of the Dual-Master-Dual-Slave with Additional Spatial Springs . . . 172
5.2.1 Trilateral Teleoperation with Authority Allocation and Time Delay . . . 175
5.2.2 Signal Flow Diagram of Trilateral PF_{comp} Architecture with Authority Allocation and Time Delay . . . 176
5.2.3 Network Representation of the Authority Allocation . . . 177
5.2.4 Signal Flow Diagram of the Authority Scaling . . . 177

5.2.5 Network Representation of PF_{comp} architecture with Authority Allocation and Time Delay . . . 178
5.2.6 Task Allocation for Master M2 in Virtual Grasping Point . . . 182
5.2.7 Task Allocation for Master M1 in Virtual Grasping Point . . . 182
5.2.8 Signal Flow Diagram of a Teleoperator Training System with Position-Position Architecture and Task Allocation . . . 183
5.2.9 Multilateral System with Virtual Grasping Point Projection and Task Allocation . . . 184
5.2.10 Network Representation of a PP Architecture Track with Task Allocation 185
5.3.1 Functionality of the Haptic Intention Operation . . . 187
5.3.2 Signal Flow Diagram of the Haptic Intention Augmentation Setup . . . 189
5.3.3 Simplified Network Representation of the Haptic Intention Augmentation Setup . . . 189
5.3.4 One Half of the Network Representation of the Haptic Intention Augmentation Setup without Time Delay . . . 190
5.3.5 One Half of the Network Representation of the Haptic Intention Augmentation Setup with Time Domain Passivity Control . . . 191

6.1.1 Virtual Reality Scene of the User Study . . . 209
6.3.1 Signal Flow Diagram of an Extended Model-Mediated Teleoperation Architecture with Passivity Control . . . 218
6.3.2 Network Representation of an Extended Model-Mediated Teleoperation Architecture with Passivity Control . . . 219
6.3.3 LRU Scenario with Grid Map and Polygon . . . 220

A.1.1 1DoF Master-Slave-System [151] . . . 227
A.2.1 DLR SpaceJustin . . . 229
A.2.2 DLR HUG Haptic Input Device . . . 229
A.3.1 DLR HUG Haptic Input Device . . . 230
A.4.1 Force Dimension Omega.7 [26] . . . 231
A.5.1 DLR RJo . . . 232
A.5.2 DLR SpaceJustin with Flexible Object and Cosmonaut on ISS . . . 232
A.5.3 Communication Infrastructure . . . 232
A.5.4 Communication Properties Internet-Link to Russia [7] . . . 233
A.5.5 Communication Properties ISS-Link [7] . . . 233
A.6.1 DLR LRU . . . 234
A.6.2 Pan-Tilt Camera Unit of the LRU . . . 234

List of Tables

2.1 Analogies . . . 18
2.2 Notification of Stability Approaches . . . 45

2.3 Notification of Communication Delay Control Approaches 45
2.4 Application and Task Space DoFs 46
2.5 Multi-Robot Configuration 46
2.6 Network Topology 47
2.7 Stability Approach and Considered Models 49
2.8 Stability Approach and Coupling Signals 50
2.9 Communication Delay Control Approach 51

5.1 Virtual Grasping Point Springs 1 147
5.2 Virtual Grasping Point Springs 2 149
5.3 Spring Inputs 155
5.4 Spring Inputs 163
5.5 Spring Inputs 170
5.6 TA Springs 183

6.1 Control Parameters 198
6.2 Task Allocation Settings for Bilateral and Multilateral Experiments . . . 201
6.3 Results 211

A.1 SENSODRIVE Master-Slave-System 227
A.2 DLR Light Weight Robot Specifications 228
A.3 DLR HitHand II Specifications 228
A.4 DLR HUG Specifications 230
A.5 Omega Specifications 231
A.6 DLR RJo Specifications 233
A.7 DLR LRU Specifications 234

List of Experiments

3.1 Energy Behavior of a PI controller 67
3.2 Position Tracking in a Trilateral Setup with PF_{comp} Architecture with Tracks Γ1-Γ3 72
3.3 Position Tracking in a Pseudo Trilateral Setup with PF_{comp} Architecture without $Track$ Γ3 72
3.4 Position Tracking in a Pseudo Trilateral Setup with PF_{comp} Architecture without $Track$ Γ1 73
3.5 Position Tracking in a Trilateral Setup with 3-$Channel$ Architecture with Tracks Γ1-Γ3 . . 75
3.6 Position Tracking in a Pseudo Trilateral Setup with 3-$Channel$ Architecture without $Track$ Γ1 75

4.1 Unstable Closed-Loop Teleoperation System with 30ms Roundtrip Delay 78
4.2 Limitation of $W_{obs}^{R2L,PI1}$ 82
4.3 30ms Roundtrip Delay with Passivity Control 85
4.4 200ms Roundtrip Delay with Passivity Control 86
4.5 Simulation of Multilateral Teleoperation 87
4.6 Wall Contact with 30ms roundtrip delay in Approach 3 92
4.7 Wall Contact with 400ms roundtrip delay in Approach 3 92
4.8 Energy Behavior of a Controller with Energy Storage Element 94
4.9 Free Motion and Wall Contact with 30ms roundtrip delay in Approach 1 95
4.10 Free Motion and Wall Contact with 200ms roundtrip delay in Approach 1 96
4.11 System Comparison at $f \in [0.2Hz]$ 100
4.12 System Comparison at $f \in [0.2Hz - 1.4Hz]$ 101
4.13 Free Motion and Wall Contact with Computed Force Feedback 108
4.14 Free Motion and Wall Contact with Measured Force Feedback 108
4.15 Wall Contact with Measured Force Feedback at 100ms Roundtrip Delay 109
4.16 Position Tracking in a Multilateral Setup (Forces and Energy Behavior of $Track$ Γ2) 110
4.17 Free Motion and Wall Contact with Hybrid Force Feedback in a 3-$Channel$ Architecture 114
4.18 Free Motion and Wall Contact with Hybrid Force Feedback in a 3-$Channel$ Architecture at 30ms roundtrip delay 115
4.19 Position Tracking in a Trilateral Setup with Hybrid Force Feedback . . . 116
4.20 Position Tracking in a Trilateral Setup with Hybrid Force Feedback at 30ms Roundtrip Delay 116
4.21 Free Motion and Wall Contact of a Bilateral Teleoperator with 4-$Channel$ Architecture 124
4.22 Free Motion and Wall Contact of a Bilateral Teleoperator with 4-$Channel$ Architecture at 100ms Roundtrip Delay 124

5.1 Passivity Analysis of PR with Input at VG 151
5.2 Passivity Analysis of PR with Input at G 151
5.3 3D Motion of a Dual-Master-Single-Slave System and Steady Master M_R 158
5.4 3D Motion of a Dual-Master-Single-Slave System and Steady Master M_L 158
5.5 Dual-Master-Single-Slave System with Active Slave Environment 159
5.6 Dual-Master-Single-Slave with Motion of all Devices 160
5.7 Kinematically Coupled Slave Robots 166
5.8 y-Rotation of M_L around M_R 173
5.9 y-Rotation of M_R around M_L 173
5.10 z-Rotation of M_L around M_R 173
5.11 z-Rotation of M_R around M_L 173
5.12 Training Scenario with $T_i = 50ms$ and $\gamma_{M1} = 1$ 179
5.13 Training Scenario with $T_i = 50ms$ and $\gamma_{M1} = 0.75$ 179
5.14 Training Scenario with $T_i = 50ms$ and $\gamma_{M1} = 0.5$ 180
5.15 Training Scenario with $T_i = 200ms$ and $\gamma_{M1} = 0.25$ 180
5.16 Cooperative Translational Motion 193
5.17 Cooperative Rotational Motion 194

6.1 Bilateral Virtual Pipe Link without Task Allocation 199
6.2 Bilateral Virtual Pipe Link with Task Allocation 200
6.3 Direct Bilateral Coupling of Master M1 and Slave 202
6.4 Virtual Pipe Motion with pseudo-multilateral Coupling 203
6.5 Multilateral System without Task Allocation 204
6.6 Multilateral System with Task Allocation 205
6.7 Plug-In Procedure in a Bilateral Master-Slave Setup 206
6.8 Plug-In Procedure in a Multilateral Setup with Task Allocation with Tracks Γ1, Γ2 and Γ3 207
6.9 Multilateral System with Task Allocation at 40ms Roundtrip Delay . . . 208
6.10 2D Position Tracking with Haptic Intention Augmentation in a space link setup 214
6.11 Passivity Proof of Virtual Environment 217
6.12 Pure Longitudinal Motion at 400ms Roundtrip-Delay 221
6.13 Combined Longitudinal and Lateral Motion at 800ms Roundtrip-Delay . 222

Bibliography

[1] Richard J Adams and Blake Hannaford. A two-port framework for the design of unconditionally stable haptic interfaces. In *International Conference on Intelligent Robots and Systems*, volume 2, pages 1254–1259. IEEE, 1998.

[2] Richard J Adams and Blake Hannaford. Stable haptic interaction with virtual environments. *IEEE Transactions on Robotics and Automation*, 15(3):465–474, 1999.

[3] Richard J Adams and Blake Hannaford. Control law design for haptic interfaces to virtual reality. *IEEE Transactions on control systems technology*, 10(1):3–13, 2002.

[4] Alin Albu-Schäffer, Christian Ott, and Gerd Hirzinger. A unified passivity-based control framework for position, torque and impedance control of flexible joint robots. *The International Journal of Robotics Research*, 26(1):23–39, 2007.

[5] Robert J Anderson and Mark W Spong. Bilateral control of teleoperators with time delay. *Transactions on Automatic control*, 34(5):494–501, 1989.

[6] Jordi Artigas, Ribin Balachandran, Marco De Stefano, Michael Panzirsch, Roberto Lampariello, Alin Albu-Schaeffer, Jan Harder, and Juergen Letschnik. Teleoperation for on-orbit servicing missions through the astra geostationary satellite. In *Aerospace Conference*, pages 1–12. IEEE, 2016.

[7] Jordi Artigas, Ribin Balachandran, Cornelia Riecke, Martin Stelzer, Bernhard Weber, Jee-Hwan Ryu, and Alin Albu-Schaeffer. Kontur-2: force-feedback teleoperation from the international space station. In *International Conference on Robotics and Automation*, pages 1166–1173. IEEE, 2016.

[8] Jordi Artigas, Jee-Hwan Ryu, and Carsten Preusche. Position drift compensation in time domain passivity based teleoperation. In *International Conference on Intelligent Robots and Systems*, pages 4250–4256. IEEE, 2010.

[9] Jordi Artigas, Jee-Hwan Ryu, Carsten Preusche, and Gerd Hirzinger. Network representation and passivity of delayed teleoperation systems. In *International Conference on Intelligent Robots and Systems*, pages 177–183. IEEE, 2011.

[10] Jordi Artigas, Jee-Hwan Ryu, Carsten Preusche, and Gerd Hirzinger. Network representation and passivity of delayed teleoperation systems. In *International Conference on Intelligent Robots and Systems*, pages 177–183. IEEE, 2011.

[11] U.A. Bakshi and Bakshi A.V. *Network Theory*. Technical Publications Pune, 2007.

[12] Ribin Balachandran, Jordi Artigas, Jee-Hwan Ryu, and Usman Mehmood. Performance comparison of wave variable transformation and time domain passivity approaches for time-delayed teleoperation: Preliminary results. In *International Conference on Intelligent Robots and Systems*. IEEE, 2016.

[13] William F. Ballhaus and John Casani. James webb space telescope (jwst) independent comprehensive review panel (icrp) final report. *ser. NASA contractor report*, 2010.

[14] Johannes Behr, Ulrich Bockholt, and Dieter Fellner. Instantrealitya framework for industrial augmented and virtual reality applications. In *Virtual Reality & Augmented Reality in Industry*, pages 91–99. Springer, 2011.

[15] E. Folke. Bolinder. Survey of some properties of linear networks. *Transactions on Circuit Theory*, 4:70–78, 1957.

[16] Craig R. Carignan and Pontus A. Olsson. Cooperative control of virtual objects over the internet using force-reflecting master arms. In *International Conference on Robotics and Automation*, volume 2, pages 1221–1226. IEEE, 2004.

[17] Vinay Chawda, Ha Van Quang, Marcia K O'Malley, and Jee-Hwan Ryu. Compensating position drift in time domain passivity approach based teleoperation. In *IEEE Haptics Symposium*, pages 195–202. IEEE, 2014.

[18] Alvin I Chen, Max L Balter, Timothy J Maguire, and Martin L Yarmush. Real-time needle steering in response to rolling vein deformation by a 9-dof image-guided autonomous venipuncture robot. In *Int. Conference on Intelligent Robots and Systems*, pages 2633–2638. IEEE, 2015.

[19] Jessie YC Chen, Ellen C Haas, and Michael J Barnes. Human performance issues and user interface design for teleoperated robots. *IEEE Transactions on Systems, Man, and Cybernetics, Part C (Applications and Reviews)*, 37(6):1231–1245, 2007.

[20] Robert A Chipman. *Transmission lines*. McGraw-Hill Schaums Outline Series, 1968.

[21] Nak Young Chong, Tetsuo Kotoku, Kohtaro Ohba, and Kiyoshi Komoriya. Remote coordinated controls in multiple telerobot cooperation. *International Conference on Robotics And Automation*, pages 3138 – 3143, 2000.

[22] Nikhil Chopra, Mark W Spong, and Rogelio Lozano. Synchronization of bilateral teleoperators with time delay. *Automatica*, 44(8):2142–2148, 2008.

[23] CL Clover, Greg R Luecke, James J Troy, and William A McNeely. Dynamic simulation of virtual mechanisms with haptic feedback using industrial robotics equipment. In *International Conference on Robotics and Automation*, volume 1, pages 724–730. IEEE, 1997.

[24] RW Daniel and PR McAree. Fundamental limits of performance for force reflecting teleoperation. *The International Journal of Robotics Research*, 17(8):811–830, 1998.

[25] Marco De Stefano, Jordi Artigas, and Cristian Secchi. An optimized passivity based method for simulating satellite dynamics on a position controlled robot in presence of latencies. In *International Conference on Intelligent Robot and System*. IEEE, 2016.

[26] Force Dimension. Omega.7 overview. *URL http://www.forcedimension.com/products/omega-7/overview*, 2017.

[27] Nicola Diolaiti and Claudio Melchiorri. Teleoperation of a mobile robot through haptic feedback. In *Haptic Virtual Environments and Their Applications*, pages 67–72. IEEE, 2002.

[28] Singh Diwas and Christian Terwiesch. Impact of workload on service time and patient safety: An econometric analysis of hospital operations. *Management Science*, 55(9):1486–1498, 2009.

[29] Anjali M Diwekar and Rama K Yedavalli. Stability of matrix second-order systems: new conditions and perspectives. *Transactions on Automatic Control*, 44(9):1773–1777, 1999.

[30] Nam Duc, Yusuke Yamashina, and Toru Namerikawa. Multiple cooperative bilateral teleoperation with time-varying delay. *SICE Journal of Control, Measurement, and System Integration*, 4(2):89–96, 2011.

[31] Ildar Farkhatdinov and Jee-Hwan Ryu. Improving mobile robot bilateral teleoperation by introducing variable force feedback gain. In *International Conference on Intelligent Robots and Systems*, pages 5812–5817. IEEE, 2010.

[32] Liu Fei, Arnaud Lelevé, Damien Eberard, and Tanneguy Redarce. A dual-user teleoperation system with online authority adjustment for haptic training. In *International Conference of the IEEE Engineering in Medicine and Biology Society*, volume 2015, page 1168, 2015.

[33] Jeffrey Ferketic, Loel Goldblatt, Edward Hodgson, Sean Murray, Robert Wichowski, Arthur Bradley, TW Fong, John Evans, Wendell Chun, Randy Stiles, et al. Toward human-robot interface standards II: An examination of common elements in human-robot interaction across the space enterprise. In *AIAA Space*, 2006.

[34] Manuel Ferre, Rafael Aracil, Carlos Balaguer, Martin Buss, and Claudio Melchiorri. *Advances in telerobotics*, volume 31. Springer, 2007.

[35] Daniela Feth, Binh An Tran, Raphaela Groten, Angelika Peer, and Martin Buss. Shared-control paradigms in multi-operator-single-robot teleoperation. In *Human Centered Robot Systems*, pages 53–62. Springer Berlin Heidelberg, 2009.

[36] Floyd A Firestone. A new analogy between mechanical and electrical systems. *The Journal of the Acoustical Society of America*, 4(3):249–267, 1933.

[37] T Fjallbrant. Activity and stability of linear networks. *IEEE Transactions on Circuit Theory*, 12(1):12–17, 1965.

[38] Terrence Fong and Illah Nourbakhsh. Interaction challenges in human-robot space exploration. *NASA technical report*, 2005.

[39] Geomagic. Geomagic touch haptic device. *URL http://www.geomagic.com/en/products/phantom-omni/overview/*, 2017.

[40] Charles M Gewertz et al. Synthesis of a finite, four-terminal net-work from its prescribed driving-point functions and transfer function. *Journal of Mathematics and Physics*, 12(1):1–257, 1933.

[41] A Ghorbanian, SM Rezaei, AR Khoogar, M Zareinejad, and K Baghestan. A novel control framework for nonlinear time-delayed dual-master/single-slave teleoperation. *ISA transactions*, 52(2):268–277, 2013.

[42] Jorge Juan Gil and Emilio Sanchez. Control algorithms for haptic interaction and modifying the dynamical behavior of the interface. In *2nd international conference on Enactive Interfaces*, pages 17–18, 2005.

[43] Blake Hannaford. A design framework for teleoperators with kinesthetic feedback. *Transactions on Robotics and Automation*, 5(4):426–434, 1989.

[44] Blake Hannaford and Robert Anderson. Experimental and simulation studies of hard contact in force reflecting teleoperation. In *IEEE International Conference on Robotics and Automation*, pages 584–589. IEEE, 1988.

[45] Blake Hannaford and Jee-Hwan Ryu. Time-domain passivity control of haptic interfaces. *IEEE Transactions on Robotics and Automation*, 18(1):1–10, 2002.

[46] K Hashtrudi-Zaad and SE Salcudean. On the use of local force feedback for transparent teleoperation. In *International Conference on Robotics and Automation*, volume 3, pages 1863–1869. IEEE, 1999.

[47] Keyvan Hashtrudi-Zaad and Septimiu E Salcudean. Analysis of control architectures for teleoperation systems with impedance/admittance master and slave manipulators. *The International Journal of Robotics Research*, 20(6):419–445, 2001.

[48] S. S. Haykin. *Active Network Theory*. Addison-Wesley Publishing Company, 1970.

[49] InTouch Health. Rp-vita^{TM} robot. *URL http://www.intouchhealth.com/*, 2017.

[50] Gerd Hirzinger, Norbert Sporer, A Albu-Schaffer, M Hahnle, Rainer Krenn, A Pascucci, and Markus Schedl. Dlr's torque-controlled light weight robot iii-are we reaching the technological limits now? In *International Conference on Robotics and Automation*, volume 2, pages 1710–1716. IEEE, 2002.

[51] Ralph L Hollis, Septimiu E Salcudean, and A Peter Allan. A six-degree-of-freedom magnetically levitated variable compliance fine-motion wrist: design, modeling, and control. *IEEE Transactions on Robotics and Automation*, 7(3):320–332, 1991.

[52] John Hu, Aaron Edsinger, Yi-Je Lim, Nick Donaldson, Mario Solano, Aaron Solochek, and Ronald Marchessault. An advanced medical robotic system augmenting healthcare capabilities-robotic nursing assistant. In *International Conference on Robotics and Automation*, pages 6264–6269. IEEE, 2011.

[53] Thomas Hulin, Katharina Hertkorn, Philipp Kremer, Simon Schätzle, Jordi Artigas, Mikel Sagardia, Franziska Zacharias, and Carsten Preusche. The dlr bimanual haptic device with optimized workspace. In *IEEE International Conference on Robotics and Automation*, pages 3441–3442. IEEE, 2011.

[54] Terry Huntsberger, Paolo Pirjanian, Ashitey Trebi-Ollennu, H Das Nayar, Hrand Aghazarian, Anthony J Ganino, Michael Garrett, Shirish S. Joshi, and Paul S Schenker. CAMPOUT: A control architecture for tightly coupled coordination of multirobot systems for planetary surface exploration. *Transactions on Systems, Man, and Cybernetics-Part A: Systems and Humans*, 33(5):550–559, 2003.

[55] Gilgueng Hwang, Peter Tamas Szemes, Noriaki Ando, and Hideki Hashimoto. Development of a single-master multi-slave tele-micromanipulation system. *Advanced Robotics*, 21(3-4):329–349, 2007.

[56] Petros A Ioannou and Jing Sun. *Robust adaptive control*. Courier Corporation, 2012.

[57] Yoshiyuki Ishijima, Dimitrios Tzeranis, and Steven Dubowsky. The on-orbit maneuvering of large space flexible structures by free-flying robots. In *Proceedings of i-SAIRAS Conference*, 2005.

[58] T. Kanno and Y. Yokokohji. Multilateral teleoperation control over time-delayed computer networks using wave variables. *Haptics Symposium*, pages 125–131, 2012.

[59] John J Karakash. *Transmission lines and filter networks*. Macmillan, 1950.

[60] Seiichiro Katsura and Kouhei Ohnishi. A realization of haptic training system by multilateral control. *Transactions on Industrial Electronics*, 53(6):1935–1942, 2006.

[61] Seiichiro Katsura, Toshiyuki Suzuyama, and Kiyoshi Ohishi. A realization of multilateral force feedback control for cooperative motion. *Transactions on Industrial Electronics*, 54:3298 – 3306, 2007.

[62] Robert S Kennedy, Norman E Lane, Kevin S Berbaum, and Michael G Lilienthal. Simulator sickness questionnaire: An enhanced method for quantifying simulator sickness. *The International Journal of Aviation Psychology*, 3(3):203–220, 1993.

[63] B. Khademian and K. Hashtrudi-Zaad. A four-channel multilateral shared control architecture for dual-user teleoperation systems. In *International Conference on Intelligent Robots and Systems*, pages 2660–2666, Oct 2007.

[64] B. Khademian and K. Hashtrudi-Zaad. Kinesthetic performance analysis of dual-user teleoperation systems. In *International Conference on Systems, Man and Cybernetics*, pages 228–233, Oct 2007.

[65] Behzad Khademian. Control of dual-user teleoperation systems design, stability analysis, and performance evaluation. *Queen's University*, 2010.

[66] Behzad Khademian and Keyvan Hashtrudi-Zaad. A robust multilateral shared controller for dual-user teleoperation systems. In *Canadian Conference on Electrical and Computer Engineering*, pages 001871–001876. IEEE, 2008.

[67] Behzad Khademian and Keyvan Hashtrudi-Zaad. Novel shared control architectures for enhanced users' interaction in haptic training simulation systems. In *International Conference on Intelligent Robots and Systems*, pages 886–892. IEEE, 2009.

[68] Behzad Khademian and Keyvan Hashtrudi-Zaad. Shared control architectures for haptic training: Performance and coupled stability analysis. *The International Journal of Robotics Research*, pages 1627–1642, 2011.

[69] A Kheddar, C Tzafestas, P Coiffet, T Kotoku, S Kawabata, K Iwamoto, K Tanie, I Mazon, C Laugier, and R Chellali. Parallel multi-robots long distance teleoperation. In *International Conference on Advanced Robotics*, pages 1007–1012. IEEE, 1997.

[70] Kiho Kim, Hohee Lee, Jangjin Park, and Myungseung Yang. Robotic contamination cleaning system. In *International Conference on Intelligent Robots and Systems*, volume 2, pages 1874–1879. IEEE, 2002.

[71] Wolfhard Kliem and Christian Pommer. Stability and response bounds of non-conservative linear systems. *Archive of Applied Mechanics*, 73(9-10):627–637, 2004.

[72] K Kosuge, J Ishikawa, K Furuta, and M Sakai. Control of single-master multi-slave manipulator system using vim. In *International Conference on Robotics and Automation*, pages 1172–1177. IEEE, 1990.

[73] Andreas Kugi. *Non-linear control based on physical models*. Springer, 2001.

[74] Andreas Kugi and Kurt Schlacher. Analysis and synthesis of non-linear dissipative systems: An overview (part 1). *at-Automatisierungstechnik Methoden und Anwendungen der Steuerungs-, Regelungs-und Informationstechnik*, 50(2/2002):63, 2002.

[75] R. Kumar, B. Hoffman, G. Prisco, D. Larkin, W. Nowlin, F. Moll, S. Blumenkranz, G.D. Niemeyer, J.K. Salisbury, Y. Wang, et al. Multi-user medical robotic system for collaboration or training in minimally invasive surgical procedures, September 3 2013. US Patent 8,527,094.

[76] Anthony R. Lanfranco, Andres E. Castellanos, Jaydev P. Desai, and William C. Meyers. Robotic surgery: a current perspective. *Annals of surgery*, 239(1):14–21, 2004.

[77] D. A. Lawrence. Stability and transparency in bilateral teleoperation. *IEEE Transactions on Robotics and Automation*, 9(5):624–637, 1993.

[78] Heath LeBlanc, Emeka Eyisi, Nicholas Kottenstette, Xenofon Koutsoukos, and Janos Sztipanovits. A passivity-based approach to deployment in multi-agent networks. In *Informatics in Control, Automation and Robotics*, pages 135–149. Springer Berlin Heidelberg, 2011.

[79] Dong Gun Lee, Gun Rae Cho, Min Su Lee, Byung-Su Kom, Sehoon Oh, and Hyoung II Son. Human-centered evaluation of multi-user teleoperation for mobile manipulator in unmanned offshore plants. In *International Conference on Intelligent Robots And Systems*, pages 5431–5438. IEEE, 2013.

[80] Dongjun Lee, Oscar Martinez-Palafox, and Mark W Spong. Bilateral teleoperation of multiple cooperative robots over delayed communication networks: Application. In *International Conference on Robotics and Automation*, pages 366–371, 2005.

[81] Dongjun Lee, Oscar Martinez-Palafox, and Mark W Spong. Bilateral teleoperation of a wheeled mobile robot over delayed communication network. In *International Conference on Robotics and Automation*, pages 3298–3303. IEEE, 2006.

[82] Dongjun Lee and Mark W Spong. Bilateral teleoperation of multiple cooperative robots over delayed communication networks: theory. In *International Conference on Robotics and Automation*, pages 360–365. IEEE, 2005.

[83] Dongjun Lee and Daye Xu. Feedback r-passivity of lagrangian systems for mobile robot teleoperation. In *Robotics and Automation (ICRA), 2011 IEEE International Conference on*, pages 2118–2123. IEEE, 2011.

[84] Jürgen Leitner. Multi-robot cooperation in space: A survey. In *Advanced Technologies for Enhanced Quality of Life*, pages 144–151, 2009.

[85] J. Li, M. Tavakoli, and Q. Huang. Stability analysis of trilateral haptic collaboration. *World Haptics Conference*, 5, 2013.

[86] Jian Li, M. Tavakoli, V. Mendez, and Qi Huang. Conservatism of passivity criteria for stability analysis of trilateral haptic systems. In *World Haptics Conference*, pages 633–638, April 2013.

[87] Jian Li, Mahdi Tavakoli, and Qi Huang. Absolute stability of a class of trilateral haptic systems. *Transactions on Haptics*, 7(3):301–310, 2014.

[88] Jian Li, Mahdi Tavakoli, and Qi Huang. Absolute stability of multi-dof multilateral haptic systems. *Transactions on Control Systems Technology*, 22(6):2319–2328, 2014.

[89] Jian Li, Mahdi Tavakoli, Victor Mendez, and Qi Huang. Passivity and absolute stability analysesof trilateral haptic collaborative systems. *Journal of Intelligent & Robotic Systems*, 78(1):3–20, 2015.

[90] Weihua Li, Zhen Liu, Haibo Gao, Xuefeng Zhang, and Mahdi Tavakoli. Stable kinematic teleoperation of wheeled mobile robots with slippage using time-domain passivity control. *Mechatronics*, 39:196–203, 2016.

[91] Zhijun Li, Liang Ding, Haibo Gao, Guangren Duan, and Chun-Yi Su. Trilateral teleoperation of adaptive fuzzy force/motion control for nonlinear teleoperators with communication random delays. *Transactions on Fuzzy Systems*, 21(4):610–624, 2013.

[92] Zhijun Li, Yuanqing Xia, and Xiaoqing Cao. Adaptive control of bilateral teleoperation with unsymmetrical time-varying delays. *Journal of Innovative Computing, Information and Control*, 9(2):753–767, 2013.

[93] Qingping Lin and Chengi Kuo. Virtual tele-operation of underwater robots. In *International Conference on Robotics and Automation*, volume 2, pages 1022–1027. IEEE, 1997.

[94] F.B. Llewellyn. Some fundamental properties of transmission systems. *Proceedings of the IRE*, 40(3):271 –283, march 1952.

[95] Lei Ma and Klaus Schilling. Survey on bilateral teleoperation of mobile robots. In *International conference on Robotics and Applications*, pages 489–494. ACTA Press, 2007.

[96] Pawel Malysz. A kinematic control framework for asymmetric semi-autonomous teleoperation systems. *PhD*, 2012.

[97] Pawel Malysz and Shahin Sirouspour. Dual-master teleoperation control of kinematically redundant robotic slave manipulators. In *International Conference on Intelligent Robots And Systems*, pages 5115 – 5120. IEEE, 2009.

[98] Pawel Malysz and Shahin Sirouspour. Cooperative teleoperation control with projective force mappings. In *Haptics Symposium*, pages 301 – 308. IEEE, 2010.

[99] Pawel Malysz and Shahin Sirouspour. A kinematic control framework for single-slave asymmetric teleoperation systems. *Transactions on Robotics*, 27:901 – 917, 2011.

[100] Pawel Malysz and Shahin Sirouspour. Trilateral teleoperation control of kinematically redundant robotic manipulators. *The International Journal of Robotics Research*, 30:1643–1664, 2011.

[101] Pawel Malysz and Shahin Sirouspour. Task performance evaluation of asymmetric semiautonomous teleoperation of mobile twin-arm robotic manipulators. *Transactions on Haptics*, 6:484 – 495, 2013.

[102] Steven Martin and Nick Hillier. Characterisation of the novint falcon haptic device for application as a robot manipulator. In *Australasian Conference on Robotics and Automation*, pages 291–292. Citeseer, 2009.

[103] Thomas H Massie, J Kenneth Salisbury, et al. The phantom haptic interface: A device for probing virtual objects. In *Proceedings of the ASME winter annual meeting, symposium on haptic interfaces for virtual environment and teleoperator systems*, volume 55, pages 295–300. Citeseer, 1994.

[104] V. Mendez and M. Tavakoli. A passivity criterion for n-port multilateral haptic systems. *Conference on Decision and Control*, 49:274–279, 2010.

[105] Victor Mendez, Mahdi Tavakoli, and Jian Li. A method for passivity analysis of multilateral haptic systems. *Advanced Robotics*, 28(18):1205–1219, 2014.

[106] Probal Mitra and Günter Niemeyer. Model-mediated telemanipulation. *The Int. Journal of Robotics Research*, 27(2):253–262, 2008.

[107] Reza Mohajerpoor, Iman Sharifi, Heidar Ali Talebi, and Seyed Mehdi Rezaei. Adaptive bilateral teleoperation of an unknown object handled by multiple robots under unknown communication delay. *International Conference on Advanced Intelligent Mechatronics*, pages 1158 – 1163, 2013.

[108] Marta Mora-Rillo, Marta Arsuaga, Germán Ramírez-Olivencia, Fernando de la Calle, Alberto M Borobia, Paz Sánchez-Seco, Mar Lago, Juan C Figueira, Belén Fernández-Puntero, Aurora Viejo, et al. Acute respiratory distress syndrome after convalescent plasma use: treatment of a patient with ebola virus disease contracted in madrid, spain. *The Lancet Respiratory Medicine*, 3(7):554–562, 2015.

[109] Günter Niemeyer and J-JE Slotine. Stable adaptive teleoperation. *Journal of Oceanic Engineering*, 16(1):152–162, 1991.

[110] Günter Dieter Niemeyer. *Using wave variables in time delayed force reflecting teleoperation*. PhD thesis, Massachusetts Institute of Technology, 1996.

[111] S.S. Nudehi, R. Mukherjee, and M. Ghodoussi. A shared-control approach to haptic interface design for minimally invasive telesurgical training. *Transactions on Control Systems Technology*, 13(4):588–592, 2005.

[112] E. Nuno, R. Ortega, L. Basanez, and D. Hill. Synchronization of networks of nonidentical euler-lagrange systems with uncertain parameters and communication delays. *Transactions on Automatic Control*, 56:935–941, 2011.

[113] Emmanuel Nuño, Luis Basañez, and Miguel Prada. Asymptotic stability of teleoperators with variable time-delays. In *International Conference on Robotics and Automation*, pages 4332–4337. IEEE, 2009.

[114] Emmanuel Nuño, Romeo Ortega, and Luis Basañez. An adaptive controller for nonlinear teleoperators. *Automatica*, 46(1):155–159, 2010.

[115] Mitsushige Oda and Masahiro Mori. Stepwise development of SSPS; JAXAs current study status of the 1GW class operational SSPS and its precursor. *International Astronautical Congress of the International Astronautical Federation*, 1(10), 2003.

[116] Reza Olfati-Saber, J Alex Fax, and Richard M Murray. Consensus and cooperation in networked multi-agent systems. *Proceedings of the IEEE*, 95(1):215–233, 2007.

[117] Reza Olfati-Saber and Richard M Murray. Consensus problems in networks of agents with switching topology and time-delays. *Transactions on Automatic Control*, 49(9):1520–1533, 2004.

[118] World Health Organization et al. Health worker ebola infections in guinea, liberia and sierra leone: a preliminary report. *World Health Organization*, 2015.

[119] Christian Ott, Jordi Artigas, Carsten Preusche, and Gerd Hirzinger. Subspace-oriented Energy Distribution for the Time Domain Passivity Approach. In *International Conference on Intelligent Robots And Systems*, San Francisco, CA, USA, 2011. IEEE.

[120] Oscar M Palafox and Mark W Spong. Bilateral teleoperation of a formation of non-holonomic mobile robots under constant time delay. In *International Conference on Intelligent Robots and Systems*, pages 2821–2826. IEEE, 2009.

[121] M. Panzirsch, J. Artigas, Jee-Hwan Ryu, and Manuel Ferre. Multilateral control for delayed teleoperation. *International Conference on Advanced Robotics*, pages 1–6, 2013.

[122] M. Panzirsch, J. Artigas, A. Tobergte, P. Kotyczka, C. Preusche, A. Albu-Schaeffer, and G. Hirzinger. A peer-to-peer trilateral passivity control for delayed collaborative teleoperation. *EuroHaptics*, 12:395–406, 2012.

[123] M. Panzirsch, H. Singh, M. Stelzer, M. J. Schuster, C. Ott, and M. Ferre. Extended Predictive Model-Mediated Teleoperation of Mobile Robots through Multilateral Control. *Intelligent Vehicles Symposium*, 2018.

[124] M. Panzirsch, J. Artigas T. Hulin, C. Ott, and M. Ferre. Integrating measured force feedback in passive multilateral teleoperation. *EuroHaptics*, page accepted, 2016.

[125] M. Panzirsch, B. Weber, L. Rubio, S. Coloma, M. Ferre, and J. Artigas. Tele-Healthcare with Humanoid Robots: A User Study on the Evaluation of Force Feedback Effects. *World Haptics Conference*, 2017.

[126] Michael Panzirsch. Trilaterale Regelung für einen Telechirurgietrainer. *TU Munich*, 2010.

[127] Michael Panzirsch, Ribin Balachandran, and Jordi Artigas. Cartesian task allocation for cooperative, multilateral teleoperation under time delay. In *International Conference on Robotics and Automation*, pages 312–317. IEEE, 2015.

[128] Michael Panzirsch, Ribin Balachandran, Jordi Artigas, Cornelia Riecke, Manuel Ferre, and Alin Albu-Schaeffer. Haptic intention augmentation for cooperative teleoperation. In *International Conference on Robotics and Automation*, pages 5335–5341. IEEE, 2017.

[129] Michael Panzirsch, Ribin Radhakrishna Balachandran, Bernhard Weber, Manuel Ferre, and Jordi Artigas. Haptic augmentation for teleoperation through virtual grasping points. *IEEE Transactions on Haptics*, 2018.

[130] Michael Panzirsch and Bernhard Weber. A 3dof-sidestick user interface for four wheel independent steering vehicles. In *Intelligent Vehicles Symposium*, pages 1310–1315. IEEE, 2015.

[131] Hyung-Soon Park and Pyung Hun Chang. Causality analysis using bond-graph and its significance in bilateral teleoperation. In *International Conference on Intelligent Robots and Systems*, volume 3, pages 2991–2998. IEEE, 2002.

[132] Jong Hyeon Park and Hyun Chul Cho. Sliding-mode controller for bilateral teleoperation with varying time delay. In *International Conference on Advanced Intelligent Mechatronics*, pages 311–316. IEEE, 1999.

[133] SI Part. Impedance control: An approach to manipulation. *Journal of dynamic systems, measurement, and control*, 107:17, 1985.

[134] Angelika Peer, Sandra Hirche, Carolina Weber, Inga Krause, and Martin Buss. Intercontinental multimodal tele-cooperation using a humanoid robot. *International Conference on Intelligent Robots and Systems*, pages 405 – 411, 2008.

[135] Carsten Preusche, Gerd Hirzinger, Jee H. Ryu, and Blake Hannaford. Time Domain Passivity Control for 6 Degrees of Freedom Haptic Displays. In *International Conference on Intelligent Robots and Systems*, pages 2944–2949, October 2003.

[136] Ha Van Quang and Jee-Hwan Ryu. Stable multilateral teleoperation with time domain passivity approach. In *International Conference on Intelligent Robots And Systems*, pages 5890 – 5895. IEEE, 2013.

[137] G. Raisbeck. A definition of passive linear networks in terms of time and enregy. *Journal fo Applied Physics*, 25:1510 –1514, 1954.

[138] Kamran Razi and Keyvan Hashtrudi-Zaad. Extension of zeheb-walach absolute stability criteria for robot-human interactions. In *Conference on Decision and Control*, pages 1186–1191. IEEE, 2012.

[139] Kamran Razi and Keyvan Hashtrudi-Zaad. Analysis of coupled stability in multilateral dual-user teleoperation systems. *Transactions on Robotics*, 30(3):631–641, 2014.

[140] Joao Rebelo and Andre Schiele. Time domain passivity controller for 4-channel time-delay bilateral teleoperation. *Transactions on Haptics*, 8(1):79–89, 2015.

[141] C. Riecke, J. Artigas, R. Balachandran, R. Bayer, A. Beyer, B. Brunner, H. Buchner, T. Gumpert, R. Gruber, F. Hacker, K. Landzettel, G. Plank, S. Schtzle, H.-J. Sedlmayr, N. Seitz, B.-M. Steinmetz, M. Stelzer, J. Vogel, B. Weber, B. Willberg, and A. Albu-Schffer. Kontur-2 mission: the dlr force feedback joystick for space telemanipulation from the iss. In *Proceedings of i-SAIRAS Conference*, 2016.

[142] Otto J Rösch, Klaus Schilling, and Hubert Roth. Haptic interfaces for the remote control of mobile robots. *Control Engineering Practice*, 10(11):1309–1313, 2002.

[143] Jee-Hwan Ryu, Jordi Artigas, and Carsten Preusche. A passive bilateral control scheme for a teleoperator with time-varying communication delay. *Mechatronics*, 20(7):812–823, 2010.

[144] Jee-Hwan Ryu, Dong-Soo Kwon, and Blake Hannaford. Stable teleoperation with time-domain passivity control. *Transactions on Robotics and Automation*, 20(2):365–373, 2004.

[145] Jee-Hwan Ryu and Carsten Preusche. Stable bilateral control of teleoperators under time-varying communication delay: time domain passivity approach. In *International Conference on Robotics and Automation*, pages 3508–3513. IEEE, 2007.

[146] Septimiu E Salcudean. Control for teleoperation and haptic interfaces. In *Control problems in robotics and automation*, pages 51–66. Springer, 1998.

[147] Septimiu E Salcudean, S Ku, and G Bell. Performance measurement in scaled teleoperation for microsurgery. In *CVRMed-MRCAS'97*, pages 789–798. Springer, 1997.

[148] H Santacruz-Reyes, LG Garcia-Valdovinos, H Jimenez-Hernandez, T Salgado-Jimenez, and LA Garcia-Zarco. Higher order sliding mode based impedance control for dual-user bilateral teleoperation under unknown constant time delay. In *International Conference on Intelligent Robots and Systems*, pages 5209–5215. IEEE, 2015.

[149] Paul S Schenker, Terry L Huntsberger, Paolo Pirjanian, Eric T Baumgartner, and Eddie Tunstel. Planetary rover developments supporting mars exploration, sample return and future human-robotic colonization. *Autonomous Robots*, 14(2-3):103–126, 2003.

[150] Olivier Sename and Anas Fattouh. Robust H^{∞} control of bilateral teleoperation systems under communication time-delay. In *Applications of time delay systems*, pages 99–116. Springer, 2007.

[151] SENSODRIVE. Master-slave-system overview. *URL https://www.sensodrive.de/DE/Produkte/Master-Slave-Systeme.php*, 2017.

[152] Aman V Shah, Scott Teuscher, Eric W McClain, and Jake J Abbott. How to build an inexpensive 5-dof haptic device using two novint falcons. In *International Conference on Human Haptic Sensing and Touch Enabled Computer Applications*, pages 136–143. Springer, 2010.

[153] M. Shahbazi, H.A. Talebi, and M.J. Yazdanpanah. A control architecture for dual user teleoperation with unknown time delays. *International Conference on Advanced Intelligent Mechatronics*, pages 1221–1226, 2010.

[154] Kamran Shamaei, Lawrence H Kim, and Allison M Okamura. Design and evaluation of a trilateral shared-control architecture for teleoperated training robots. In *International Conference of the IEEE Engineering in Medicine and Biology Society*, pages 4887–4893. IEEE, 2015.

[155] Alan Sherman, Murat Cenk Çavusoglu, and Frank Tendick. Comparison of teleoperator control architectures for palpation task. In *Proceedings of the ASME Dynamic Systems and Control Division*, pages 1261–1268, 2000.

[156] Shahin Sirouspour. Modeling and control of cooperative teleoperation systems. *Transactions on Robotics*, 21:1220 – 1225, 2005.

[157] Shahin Sirouspour. Robust control design for cooperative teleoperation. *International Conference on Robotics and Automation*, pages 1133–1138, 2005.

[158] Shahin Sirouspour and Peyman Setoodeh. Adaptive nonlinear teleoperation control in multi-master/multi-slave environments. *International Conference on Control Applications*, pages 1263 – 1268, 2005.

[159] Sigurd Skogestad and Ian Postlethwaite. *Multivariable feedback control: analysis and design*, volume 2. Wiley New York, 2007.

[160] Emanuel Slawiñski, S García, L Salinas, and V Mut. Pd-like controller with impedance for delayed bilateral teleoperation of mobile robots. *Robotica*, 34(09):2151–2161, 2016.

[161] Emanuel Slawiñski, Vicente Mut, Lucio Salinas, and Sebastian García. Teleoperation of a mobile robot with time-varying delay and force feedback. *Robotica*, 30(01):67–77, 2012.

[162] Emanuel Slawinski, Vicente A Mut, Paolo Fiorini, and Lucio R Salinas. Quantitative absolute transparency for bilateral teleoperation of mobile robots. *IEEE Transactions on Systems, Man, and Cybernetics-Part A: Systems and Humans*, 42(2):430–442, 2012.

[163] FM Smith, DK Backman, and Stephen C Jacobsen. Telerobotic manipulator for hazardous environments. *Journal of Robotic Systems*, 9(2):251–260, 1992.

[164] Peter J Staritz, Sarjoun Skaff, Chris Urmson, and William Whittaker. Skyworker: a robot for assembly, inspection and maintenance of large scale orbital facilities. In *International Conference on Robotics and Automation*, volume 4, pages 4180–4185, 2001.

[165] Stefano Stramigioli. Geometric modeling of mechanical systems for interactive control. In *Advances in the control of nonlinear systems*, pages 309–332. Springer, 2001.

[166] Stefano Stramigioli. *Modeling and IPC Control of Interactive Mechanical Systems: A Coordinate-Free Approach*. Springer-Verlag New York, Inc., Secaucus, NJ, USA, 2001.

[167] Da Sun, Fazel Naghdy, and Haiping Du. Enhancing flexibility of the dual-master-dual-slave multilateral teleoperation system. In *Conference on Control Applications*, pages 300–305. IEEE, 2015.

[168] Da Sun, Fazel Naghdy, and Haiping Du. Stability control of force-reflected nonlinear multilateral teleoperation system under time-varying delays. *Journal of Sensors*, 2016, 2015.

[169] Gilles Tagne, Reine Talj, and Ali Charara. Passivity analysis and design of passivity-based controllers for trajectory tracking at high speed of autonomous vehicles. In *Intelligent Vehicles Symposium Proceedings, 2014 IEEE*, pages 1151–1156. IEEE, 2014.

[170] Ran Tao and Mahdi Tavakoli. Multilateral haptic system stability analysis: The effect of activity or passivity of terminations via a series-shunt approach. In *Haptics Symposium*, pages 203–208. IEEE, 2014.

[171] M Tavakoli, A Aziminejad, R Patel, and M Moallem. Enhanced transparency in haptics-based master-slave systems. *Proceedings of the American control conference*, 8(9):10, 2007.

[172] U. Tumerdem and K. Ohnishi. Haptic consensus in multilateral teleoperation. In *International Symposium on Industrial Electronics*, pages 1335–1340, June 2008.

[173] U. Tumerdem, T. Shimono, and K. Ohnishi. Micro-macro multilateral teleoperation through scaled information flow. In *Conference on Industrial Electronics*, pages 2911–2916, Nov 2008.

[174] Ugur Tumerdem and Kouhei Ohnishi. Multi-robot teleoperation under dynamically changing network topology. In *International Conference on Industrial Technology*, pages 1–6. IEEE, 2009.

[175] Richard Q Van der Linde, Piet Lammertse, Erwin Frederiksen, and B Ruiter. The hapticmaster, a new high-performance haptic interface. In *Proc. Eurohaptics*, pages 1–5, 2002.

[176] Arjan Van der Schaft. *L2-gain and passivity techniques in nonlinear control*. Springer Science & Business Media, 2012.

[177] Ha Van Quang, Ildar Farkhatdinov, and Jee-Hwan Ryu. Passivity of delayed bilateral teleoperation of mobile robots with ambiguous causalities: Time domain passivity approach. In *International Conference on Intelligent Robots and Systems*, pages 2635–2640. IEEE, 2012.

[178] Yuji Wang, Fuchun Sun, Huaping Liu, and Zidi Li. Passive four-channel multilateral shared control architecture in teleoperation. In *International Conference on Cognitive Informatics*, pages 851–858. IEEE, 2010.

[179] Bernhard Weber, Simon Schätzle, Cornelia Riecke, Bernhard Brunner, Sergey Tarassenko, Jordi Artigas, Ribin Balachandran, and Alin Albu-Schäffer. Weight

and Weightlessness Effects on Sensorimotor Performance During Manual Tracking. In *International Conference on Human Haptic Sensing and Touch Enabled Computer Applications*, pages 111–121. Springer, 2016.

[180] Bert Willaert, Brecht Corteville, Dominiek Reynaerts, Hendrik Van Brussel, and Emmanuel B. Vander Poorten. Bounded environment passivity of the classical position-force teleoperation controller. In *International Conference on Intelligent Robots and Systems*, pages 4622–4628, 2009.

[181] Jan C Willems. Dissipative dynamical systems part i: General theory. *Archive for rational mechanics and analysis*, 45(5):321–351, 1972.

[182] Bob G Witmer and Michael J Singer. Measuring presence in virtual environments: A presence questionnaire. *Presence: Teleoperators and virtual environments*, 7(3):225–240, 1998.

[183] John L Wyatt Jr, Leon O Chua, Joel W Gannett, Izzet C Goknar, and Douglas N Green. Energy concepts in the state-space theory of nonlinear n-ports: Part i-passivity. *Transactions on Circuits and Systems*, 28(1):48–61, 1981.

[184] Joseph Yan and SE Salcudean. Teleoperation controller design using h-optimization with application to motion-scaling. *Transactions on Control Systems Technology*, 4(3):244–258, 1996.

[185] Yasuyoshi Yokokohji, Teruhiro Tsujioka, and Tsuneo Yoshikawa. Bilateral control with time-varying delay including communication blackout. In *Symposium on Haptic Interfaces for Virtual Environment and Teleoperator Systems*, pages 285–292. IEEE, 2002.

[186] George Zames. Feedback and optimal sensitivity: Model reference transformations, multiplicative seminorms, and approximate inverses. *Transactions on Automatic Control*, 26(2):301–320, 1981.

[187] Ezra Zeheb and Eugene Walach. Necessary and sufficient conditions for absolute stability of linear n-ports. *International Journal of Circuit Theory and Applications*, 9(3):311–330, 1981.

[188] Zhiyuan Zuo and Dongjun Lee. Haptic tele-driving of a wheeled mobile robot over the internet: a pspm approach. In *Conference on Decision and Control*, pages 3614–3619. IEEE, 2010.